



SCUOLA DOTTORALE IN GEOLOGIA DELL' AMBIENTE E DELLE
RISORSE
DOTTORATO DI RICERCA IN GEOLOGIA DELLE RISORSE
NATURALI

CICLO DEL CORSO DI DOTTORATO XXVII

Exploration of medium- and low-enthalpy geothermal resources in the
sub-Andean area for the sustainable development of the cities of the
Salta province (northwestern Argentina)

ROBERTA MAFFUCCI
Nome e Cognome del dottorando


firma


SVEVA CORRADO
Docente Guida/Tutor: Prof.


Sveva CORRADO
firma

GUIDO GIORDANO
Co-Tutor: Prof.


firma

SABINA BIGI
Co-Tutor: Prof.


firma

CLAUDIO FACCENNA
Coordinatore: Prof


firma

ACKNOWLEDGEMENTS

This dissertation would not have been possible without the guidance and the help of some close people who accompanied me during the years of this research project.

First of all, I would like to express my deeply gratitude to my supervisor Prof. Sveva Corrado for her constant guidance, support, enthusiasm and inspiration that allowed me to develop this project.

I am extremely grateful to my co-supervisor Prof. Sabina Bigi. She accompanied me step by step in these years. I thank her for the continuous help, teaching and for the confidence she put in me to undertake the PhD project.

I am also indebted to my co-supervisor Prof. Guido Giordano. His teachings and comments highly enhanced this Thesis.

My sincere gratitude goes to Dr. Lea Di Paolo for her precious help in the field and for her support and scientific contribution.

Thanks to Prof. Chiara Invernizzi and Prof. Pietropaolo Pierantoni for their precious help in the field and for the useful discussions. They have contributed significantly to the results presented in Chapter 6 of this Thesis.

I would also like to thank Prof. Josè Viramonte, Dr. Agostina Chiodi and Dr. Walter Baez for their scientific contribution and also for their help during the fieldwork and their warm hospitality in Argentina.

Thanks to the company Geotermia Andina that provided the inspiration for this project.

Thanks to Dr. Carlo Ungarelli for the useful discussions on the integration with audiomagnetotelluric data presented in the Chapter 6.

Thanks to Dr. Luca Aldega and Dr. Chiara Caricchi for their encouragement and for the discussions on the burial and exhumation history results of the stratigraphic succession involved in the Sierra de La Candelaria anticline.

Thanks are also due to Prof. Stefano Mazzoli and Prof. Massimiliano Barchi who provided stimulating and helpful reviews of my Thesis.

I am indebted to my many colleagues with whom I shared the office or who I met in these years at Roma Tre: Marco, Gabriele, Francesco, Silvia, Andrea, Gabriele, Andrea, Luca, Massimo, Ileana, Ines, Giorgia, Sandro, Danilo, and Lorenzo.

Thanks also to all the people who I met in Argentina. They made a travel job an amazing life experience: Mama Julia y su hermosa familia, Florencia, Tato, Nesth, Emilce, Gabriela, Raul and Rodriguez.

Thanks also to my dear friends Raffaella, Chiara, Marco, Eloisa, Roberta.

Many thanks to my relatives, parents and sister for their love, and in particular, to my mother and my mother-in-law. Without their extraordinary help, this work would not have been finalized.

Finally, special thanks to my husband and my son. They are the reason of my life and to them, I would like to dedicate this Thesis.

TABLE OF CONTENTS

ABSTRACT	iv
RIASSUNTO	viii
CHAPTER I - INTRODUCTION	1
1.1 Problem	1
1.2 Aims of the thesis and methodology	2
1.3 Outline of the Thesis	4
CHAPTER II - PREVIOUS STUDIES AND OPEN PROBLEMS	6
2.1 Introduction	6
2.2 Geodynamic framework	8
2.2.1 The Central Andes	8
2.2.2 The Santa Barbara System	9
2.2.3 The Metán basin	12
2.3 Sierra de La Candelaria anticline	14
2.4 Rosario de La Frontera geothermal system	17
CHAPTER III - TECTONIC MODEL OF SIERRA DE LA CANDELARIA ANTICLINE	22
3.1 Introduction	22
3.2 Structural analysis at the outcrop scale	22
3.2.1 Southwestern Backlimb	24
3.2.2 Northeast nose of Balboa anticline	26
3.2.3 Northern nose of Termas anticline	28
3.2.3.1 Backlimb	29
3.2.3.2 Periclinal closure area	30
3.2.3.3 Forelimb	33
3.3 Structural setting of the Sierra de La Candelaria	33
3.4 Tectonic interpretation of the deformation sequence	35
CHAPTER IV - 3-D MODEL OF THE RESERVOIR AND FRACTURE MODELLING	40
4.1 Introduction	40
4.2 Methodology	40
4.3 Lithological components of the geothermal system	43
4.4 3-D reservoir model	45
4.5 Reservoir discrete fracture network model	46

4.5.1 Fracture data elaboration	47
4.5.1.1 Type and orientation	48
4.5.1.2 Intensity	50
4.5.1.3 Size (height, length and aperture)	53
4.5.2 Problems in data modelling	54
4.5.3 Results	56
4.6 DFN upscaling	57
4.7 Geothermal potential	59
CHAPTER V - EVALUATION OF THE CAP-ROCK EFFECTIVENESS	62
5.1 Introduction	62
5.2 Methods and materials	62
5.2.1 Optical study of organic matter dispersed in sediments for thermal evolution of sedimentary basins	63
5.2.1.1 Generalities	63
5.2.1.2 Thermal maturity parameters used in this Thesis	66
5.2.1.2.1 Vitrinite Reflectance	66
Sample preparation and analysis	68
5.2.2 XRD study of clay minerals	69
5.2.2.1 Generalities	69
Sample preparation and analysis	72
5.2.3. Fluid Inclusion Studies	72
5.2.3.1. Generalities	72
5.2.3.1.1 Phase changes in Fluid Inclusions	74
Single component system H ₂ O	75
Two component system H ₂ O-NaCl	76
5.2.3.1.2 Fluid Inclusions petrography	77
5.2.3.1.3 Fluid Inclusions microthermometry	79
Sample preparation and analysis	80
5.2.4 - Thermo-structural modelling	80
5.3 Results	81
5.3.1 Structural data	81
5.3.2 X-ray diffraction of clay minerals	83
5.3.3 Vitrinite reflectance data	85
5.3.4 Fluid inclusions microthermometry and petrography	85
5.3.5 Burial and thermal modelling	87
5.4 Discussion	90
5.4.1 Geothermal gradient	91
5.4.2 Thermal interpretation of the tectono-stratigraphic units	91
5.4.2.1 Pirgua Subgroup	91
5.4.2.2 Balbuena and Santa Barbara Subgroups	92
5.4.2.3 Metán Subgroup	92
CHAPTER VI - DISCUSSION	94
<i>References cited</i>	105

Abstract

Exploration methodologies commonly applied in oil and gas research can provide important information also in the perspective of exploitation and reservoir management of medium- and high-enthalpy geothermal systems.

The purpose of this study has been to evaluate the possibility of exploitation of the Rosario de La Frontera geothermal system through a multidisciplinary approach based on the integration of different methodologies: structural analyses at the outcrop scale, a reservoir fracture modelling performed with the software MoveTM (Midland Valley Exploration Ltd.), and paleo-thermal analyses (organic matter optical analysis - vitrinite reflectance: Ro%, clay mineralogy by means of X-ray analyses, fluid inclusions analyses on veins and mono-dimensional thermal and burial modelling with the aid of Basin Mod 1-D software).

The geothermal system of Rosario de La Frontera belongs to the Sierra de La Candelaria anticline, one of the positively inverted structures cropping out in the Sub-Andean foreland of the northwestern Argentina. Despite of the occurrence of different thermal sites along the frontal structures of the Andean retro-wedge, the high temperatures of the thermal fluids of this system makes it as the most promising site for potential exploitation. Such a development could contribute to improve the sustainable growth of the cities of the Salta province.

This active geothermal system is characterized by several hot springs that mainly occur near the town of Rosario de La Frontera, at the northern edge of the regional Sierra de La Candelaria anticline, with temperatures ranging between 24° and 90°C. Fractured sandstones of the Cretaceous syn-rift deposits (Pirgua Subgroup) provide the reservoir of the geothermal system. Differently, the low permeable post-rift and the syn-orogenic deposits (respectively, Balbuena and Santa Bárbara subgroup, and Metán subgroup) mainly act as cap-rock. These deposits are deformed in the N-S trending hanging wall anticline (Sierra de La Candelaria) and dissected by subsequent strike-slip and normal fault planes. The anticline and the associated structures (faults and fractures) represent the structural context of the geothermal system.

The current study employs a multidisciplinary approach in order to assess the quality of the reservoir and cap-rock of the geothermal system. Special regard is devoted to explore

how faults and fractures affect fluids circulation at depth, and control their natural upwelling to the surface. The adopted methodological approach provide new data on the evolution of this Sub-Andean foreland structure, previously poorly investigated, constraining also the burial and thermal history experienced by the studied sedimentary succession from Barremian to Quaternary ages. Moreover, the integration with published hydrogeological, geochemical and geophysical (audiomagnetotellurics) data (CUIA project 2010 – International University Cooperation Italy-Argentina) addressed to the elaboration of a conceptual model of thermal fluids circulation, identifying the best area for drilling-purposes in perspective of undirect heat uses (electricity production).

Structural and stratigraphic analyses conducted at the outcrop scale allowed to reconstruct the tectonic evolution of the Sierra de La Candelaria anticline (CHAPTER 3) highlighting the type and intensity of the deformation that affected the anticline in the different structural positions. Two main deformation phases were identified: an extension happened during the Cretaceous rifting and a positive inversion and folding occurred since Upper Miocene times. Accordingly, the regional anticline formed at the hanging wall of a N-S Cretaceous normal fault. This high-angle normal fault was reactivated as an oblique reverse fault since it had an oblique trend with respect to the WNW-ESE Andean shortening direction. The event of positive inversion can be divided into an early, intermediate and mature sub-stages of deformation. At the outcrop scale, tectonic stylolites and shears fractures mainly testify the early develop of the regional anticline. Progressively, in the intermediate stage, an oblique NNW-SSE fault plane enhanced the development of the minor Termas and Balboa anticlines. In correspondence of these anticlines, fault planes, with the associated Riedel shears, shear fractures, calcite- and gypsum-filling veins and deformation bands record both the strike-slip kinematics and the folding process related to inversion. E-W and ENE-WSW normal faults and extensional fractures are mainly associated to the mature stage of the deformation, recording the final stage of the folding process.

The performed three-dimensional model of the anticline together with the reservoir fracture modelling (CHAPTER 4) addressed to reservoir evaluation: i.e. lateral extent, thickness and volume, tectonic features, porosity/permeability patterns, possible reservoir compartments.

The results show a reservoir volume of 53 Km³ with a mean thickness of 450 m, confined to the east by the main high angle thrust fault that borders the anticline on the eastern side

and to the west by a continuous, almost N-S oriented, lineament well visible on remote sensing images. To the north, it is delimited by a normal fault plane trending E-W and dipping to the north. Whereas, to the south, the reservoir is confined by its outcrops and by a NE-SW strike-slip fault occurring in the Ceibal area. In the northern sector of the anticline, at the northern edge of Termas and Balboa anticlines, the reservoir deposits reach the maximum depths of ~2,100 m and ~2,400 m, respectively.

Focusing on this northern portion of the regional anticline considered as the most interesting for different heat uses since the thermal fluids reach the highest temperatures, a reservoir volume of 28 Km³ with a fracture portion of 0.001 Km³ were computed. Furthermore, 1.89×10^{17} J of extractable geothermal heat was calculated from the reservoir portion where temperature exceeds 60°C, at least for direct heat uses.

The reservoir fracture modelling confirm the interest for this area because of the high values of the computed secondary permeability and porosity (4.2E-04 and until ~20mD, respectively) as a result of the intensive brittle deformation that affect this portion of the anticline. The modelling also shows the highest secondary permeability values in the direction parallel to the strike of the main NNW-SSE fault plane. These results allow considering this fault plane as the main structure controlling the migration path of hot fluids at depth and their upwelling from the reservoir to the surface, as also demonstrated by associated calcite-filled veins. At the same time, the NNW-SSE fault plane may act as a barrier to fluid flow, producing a reservoir compartmentalization.

Paleo-thermal analyses conducted on the cap-rock of the geothermal system (CHAPTER 5), well exposed in this northern portion of the regional anticline, suggest that it acts as a good insulator. Clay mineralogy analyses indicate a low thermal maturity of these deposits with low amounts of illite in I-S mixed layers, comparable with the thermal maturity detected on the same deposits exposed along the western limb of the anticline, far away from the influence of the hot springs. Thermal and burial models reconstructed in the two investigated areas of the anticline, far away and close to the area of the hot springs, demonstrate that this thermal maturity represents the result of the burial history experienced by the cap-rock under a geothermal gradient of about 40 °C/Km stabilised after the rifting event. Furthermore, as demonstrated by vitrinite reflectance data computed for the post-rift Yacoraite Formation (0.6-0.7%), the rift succession experienced a thermal evolution compatible with late diagenetic conditions in the early stages of hydrocarbon generation during Upper Miocene times.

A high degree of the cap-rock thermal alteration (80% of illite in I-S mixed layers) occurs in correspondence of its most fractured portions. The R3 structures do not fit the performed purely conductive 1D thermal models. These results together with fluid inclusion analyses, that indicate an entrapment temperature (T_h) of 115°C on the same fractured outcrops, suggest that hot fluids circulation may have played a key role in the thermal alteration of the cap rock only where it was intensely fractured. In this framework, deformation due to strike-slip kinematics rather than to folding process may have focused hot fluids and driven localized thermal alteration of the cap-rock.

Coupling these results together with the recently published geochemical, hydrogeological and audiomagnetotelluric data (Barcelona et al., 2013; Invernizzi et al., 2014; Chiodi et al., 2015) (CHAPTER 6), I suggest that the most favourable site for a potential future exploitation of the thermal fluids is located along the northern buried plunge of the Balboa anticline. The high temperatures reached by the thermal fluids in this area (~120°C) suggest that an undirect heat use for electric power generation could be feasible. Furthermore, the compartmentalization ruled by the NNW-SSE fault plane may guarantee, at the same time, the sustainability of the geothermal resource exploited at present by the Hotel Termas, in correspondence of the Termas anticline.

Riassunto

Le metodologie di esplorazione comunemente applicate nella ricerca di olio e gas, possono fornire importanti informazioni anche quando applicate nella prospezione di sistemi geotermici a media ed alta entalpia nella prospettiva di un loro sfruttamento e di una corretta gestione del reservoir.

L'obiettivo di questa Tesi è stato quello di valutare la possibilità di sfruttamento del sistema geotermico di Rosario de La Frontera attraverso un approccio di studio multidisciplinare basato sull'integrazione di differenti metodologie: indagini strutturali condotte alla scala dell'affioramento, modellazione delle rete di fratture nel reservoir geotermico attraverso il software MoveTM (Midland Valley Exploration Ltd.) e analisi paleo-termiche (analisi ottiche della materia organica dispersa nei sedimenti, quali la riflettanza della vitrinite: Ro%, analisi diffrattometriche a raggi X delle argille, studio microtermometrico delle inclusioni fluide, e modellazioni monodimensionali della storia termica e di seppellimento della successione in esame attraverso il software Basin Mod 1-D).

Il sistema geotermico di Rosario de La Frontera appartiene all'anticlinale Sierra de La Candelaria, una delle strutture invertite positivamente, affiorante nell'avampaese Sub-Andino in Argentina nordoccidentale. Nonostante la presenza di differenti siti termali situati lungo le strutture frontali della retrocatena andina, le alte temperature dei fluidi di questo sistema geotermico lo rendono uno dei siti più promettenti per un suo potenziale sfruttamento al fine di sostenere uno sviluppo sostenibile delle città della provincia di Salta.

Questo sistema geotermico attivo è caratterizzato da diverse manifestazioni termali, con temperature comprese tra 24°C e 90°C, che emergono principalmente in prossimità della cittadina di Rosario de La Frontera, al margine settentrionale dell'anticlinale regionale. Le arenarie fratturate dei depositi Cretacici di sin-rift (Sottogruppo Pirgua) rappresentano il reservoir del sistema geotermico. Differentemente, i depositi di post-rift e sin-orogenici a bassa permeabilità (rispettivamente, Sottogruppo Balbuena e Santa Bárbara, e Sottogruppo Metán) agiscono principalmente come cap-rock. Questi depositi sono deformati in un'anticlinale allungata in senso N-S e tagliati da successivi piani di faglia normali e trascorrenti. L'anticlinale e le strutture associate (faglie e fratture) rappresentano il contesto strutturale del sistema geotermico.

Il presente studio si avvale di un approccio multidisciplinare allo scopo di valutare la qualità del reservoir e della cap-rock del sistema geotermico. Particolare attenzione è rivolta alla comprensione di come le faglie e le fratture influenzano la circolazione dei fluidi in profondità e la loro risalita in superficie. Le indagini applicate forniscono nuovi dati sull'evoluzione di questa struttura dell'avampaese Sub-Andino, precedentemente poco studiata, vincolando anche la storia termica e di seppellimento della successione sedimentaria dal Barremiano fino al Quaternario. Inoltre, l'integrazione con dati idrogeologici, geochimici e geofisici (audiomagnetotellurici) pubblicati (progetto CUIA 2010 – Cooperazione Universitaria Internazionale Italia-Argentina), ha consentito di elaborare un modello concettuale della circolazione dei fluidi termali identificando la migliore area per una potenziale perforazione nella prospettiva di uno sfruttamento indiretto dei fluidi termali (generazione di elettricità).

Le analisi stratigrafiche e strutturali condotte alla scala dell'affioramento hanno permesso di ricostruire l'evoluzione tettonica dell'anticlinale Sierra de La Candelaria (CAPITOLO 3) mettendo in luce il tipo e l'intensità della sua deformazione in diverse posizioni strutturali. Due principali fasi deformative sono state identificate: un'estensione avvenuta durante il rifting Cretacico, e un'inversione positiva e relativo piegamento nell'hanging wall, avvenuti a partire dal Miocene superiore. Secondo questa ricostruzione, l'anticlinale regionale si è sviluppata nell'hanging wall di una faglia cretacica orientata N-S. Tale piano di faglia ad alto angolo è stato riattivato con cinematica transpressiva, con un'orientazione non perfettamente ortogonale rispetto alla direzione WNW-ESE del raccorciamento regionale. L'evento d'inversione positiva è descrivibile in tre stadi evolutivi: precoce, intermedio e maturo. Alla scala dell'affioramento, stiloliti e fratture di taglio testimoniano principalmente il primo stadio di sviluppo dell'anticlinale regionale. Progressivamente, nello stadio intermedio, lo sviluppo di una faglia obliqua orientata NNW-SSE ha favorito la formazione delle due anticlinali minori, Termas e Balboa. In corrispondenza di queste due anticlinali, la cinematica trascorrente e il piegamento legato allo sviluppo di questa faglia obliqua, è registrato da diversi piani di faglia con i piani di riedel associati, fratture di taglio, vene di calcite e di gesso e deformation bands. Faglie normali e fratture estensionali orientate E-W e ENE-WSW sono principalmente associate allo stadio maturo della deformazione.

L'elaborazione di un modello tri-dimensionale dell'anticlinale insieme alla modellazione della fratturazione nel reservoir (CAPITOLO 4) ha consentito una valutazione del reservoir definendone estensione laterale, spessore e volume, caratteristiche strutturali, porosità/permeabilità secondaria e possibile compartimentalizzazione.

I risultati mostrano un volume di reservoir di 53 Km³ con uno spessore medio di 450 m, confinato a est dal piano di faglia ad alto angolo che borda l'anticlinale lungo il suo fianco orientale e a ovest da un lineamento continuo orientato N-S, ben visibile dalle immagini satellitari. A nord il reservoir appare delimitato da un piano di faglia normale immergente a nord e orientato E-W. Mentre, a sud, risulta confinato dai suoi affioramenti e da una faglia trascorrente orientata NE-SW presente nell'area del Ceibal. Nel settore settentrionale dell'anticlinale, all'estremo nord delle anticlinali Termas e Balboa, il reservoir raggiunge le massime profondità rispettivamente di ~2100 m e ~2400 m.

Focalizzandosi su questa porzione settentrionale dell'anticlinale regionale, in quanto considerata la più interessante per differenti utilizzi del calore, è stato calcolato un volume di reservoir di 28 Km³ comprensivo di una porzione fratturata di 0.001 Km³. Inoltre, considerando solo la porzione di questo reservoir dove il calore eccede i 60°C (minima temperatura richiesta almeno per usi diretti del calore), risultano estraibili $1.89 \cdot 10^{17}$ J di calore geotermico.

La modellazione della fratturazione nel reservoir conferma l'interesse per questa area per gli alti valori di porosità e permeabilità secondaria ottenuti (4.2E-04 e fino a ~20mD, rispettivamente), come risultato dell'intensa deformazione fragile che interessa questa porzione dell'anticlinale. La modellazione eseguita mostra anche valori più alti della permeabilità secondaria parallelamente alla direzione del piano di faglia orientato NNW-SSE. Questi risultati portano a considerare questo piano di faglia come il principale tragitto percorso dai fluidi in profondità e lungo il quale risalgono dal reservoir verso la superficie, come dimostrato anche da vene di calcite associate. Allo stesso tempo, il piano di faglia orientato NNW-SSE dovrebbe agire come barriera al flusso del fluido perpendicolarmente alla propria direzione, producendo una compartimentalizzazione del reservoir.

Le analisi paleo-termiche condotte sulla cap-rock del sistema geotermico (CAPITOLO 5), ben esposta nella porzione settentrionale dell'anticlinale, suggeriscono che agisce come un buon isolante termico. L'analisi mineralogica delle argille indica una bassa maturità termica di questi depositi con bassi contenuti di illite negli strati misti I-S, confrontabile alla maturità termica ritrovata negli stessi depositi affioranti lungo il fianco occidentale

dell'anticlinale, lontano dall'influenza delle emergenze calde. I modelli termici e di seppellimento, ricostruiti per le due aree investigate dell'anticlinale, vicino e lontano dai fluidi termali, dimostrano che questa maturità termica è il risultato del seppellimento subito dalla cap-rock con un gradiente geotermico di circa 40 °C/Km stabilitosi dopo l'evento di rifting. Inoltre, come dimostrato dai dati di riflettanza della vitrinite analizzata per la Formazione Yacoraite di post-rift (0.6-0.7%), i depositi di rift subiscono un'evoluzione termica compatibile con le tarde condizioni diagenetiche nei primi stadi di generazione degli idrocarburi durante il Miocene superiore. Un alto grado di alterazione termica della cap-rock (80% di illite negli strati misti I-S) è registrata in corrispondenza delle sue porzioni fratturate. Queste strutture R3 non si adattano con il modello termico elaborato puramente conduttivo. Questi risultati insieme all'analisi delle inclusioni fluide, indicanti una temperatura di intrappolamento (T_h) di 115°C negli stessi affioramenti fratturati, suggerisce che la circolazione dei fluidi deve aver giocato un ruolo chiave nell'alterazione termica della cap-rock solo dove era intensamente fratturata. La deformazione legata alla cinematica trascorrente, più di quella legata al processo di piegamento, deve aver guidato i fluidi caldi, determinandone un'alterazione termica localizzata.

Integrando questi risultati con i dati idrogeologici, geochimici e audio-magnetotellurici recentemente pubblicati (Barcelona et al., 2013; Invernizzi et al., 2014; Chiodi et al., 2015) (CAPITOLO 6), la zona ideale per un potenziale futuro sfruttamento dei fluidi termali risulta localizzata all'estremo nord dell'anticlinale Balboa. Le alte temperature raggiunte dai fluidi termali in quest'area (~120°C) suggeriscono un possibile utilizzo indiretto del calore per produzione di energia elettrica. Inoltre, la compartimentalizzazione prodotta dalla faglia orientata NNW-SSE dovrebbe garantire allo stesso tempo la sostenibilità della risorsa geotermica attualmente sfruttata dalla struttura termale dell'Hotel Termas in corrispondenza dell'anticlinale Termas.

CHAPTER I

INTRODUCTION

1.1 Problem

The basic conceptual model for a convection-dominated geothermal system includes three main elements: a heat source, a reservoir including a cap-rock that limits the heat escape, and a fluid (Dickson and Fanelli, 1994). Convection of the thermal fluids, induced by the heat source or elevated heat flow, transports heat from deeper levels to the surface.

Geological and hydrogeological studies represents the starting point of any geothermal exploration programme. They are mainly devoted to the identification and extension of the areas worth investigating and to the regional characterization of the macro-circulation (Serpen, 2004; La Vigna et al., 2012; Mazza et al., 2013).

Geochemical surveys are commonly applied to detect the composition, the origin, the thermo-baric state of the fluids and their migration paths (Truesdell and Hulston, 1980; Nuti, 1992; D'Amore and Bolognesi, 1994; Minissale et al., 2000; Magro et al. 2003; Minissale, 2004; Chiodini et al., 2005; Pierantoni et al., 2012; Barberi et al., 2013; Mwangi, 2013; Chiodi et al., 2012a, 2012b, 2015). They are commonly integrated with structural investigations in order to detect the structural channels controlling the fluid flow pathways and to analyse the fluid-rock interaction and the implications on permeability of hosting rocks (Liotta et al., 2010; Rossetti et al., 2011; Giordano et al., 2013; Invernizzi et al., 2014; Brogi et al., 2015). Furthermore, numerical models of coupled fluid and heat flow are increasingly used to improve the understanding of hydrothermal systems and their natural evolution, especially in fractured environments (Bertani and Cappetti 1995; Zhang and Sanderson 1996; Kloditz and Clauser 1998; Magri et al., 2010; Shaik et al., 2011; Barchi et al., 2013).

Most of the literature on geothermal exploration is also focused on the characterization of the reservoir by means of petrological and geophysical investigations (Majumdar et al., 2000; Lüschen, 2005; Finetti, 2006; Moeck et al., 2010; Barcelona et al., 2013; Ganguly

and Kumar, 2012, for a review) and on the evaluation of the P-T conditions (Erkan et al., 2008; De Benedetti et al., 2010; De Filippis et al., 2012). In this framework, seismic surveys are also addressed to detect the preferential upward migration paths for magmatic fluids (Brogi et al., 2003, 2005a, 2005b). Since most of the geothermal reservoirs all over the world are hosted in fractured rock media where the main flow occurs through a network of interconnected fractures, special regards is devoted to the modelling of its fracture network (Wang & Ghassemi, 2011; Müller et al., 2010; Maffucci et al., 2012a, 2013, 2015; Deckert and Bauer, 2015; Phillip, 2015).

Less attention has been generally addressed to the characterization of the cap-rock of a geothermal system. Its integrity is mainly analysed by means of soil CO₂ flux and hydrothermal alteration mineralogy (Cox and Browne, 1998; Yang et al., 2001; Todaka and Akasaka, 2004; Battaglia et al., 2007; Timlin, 2009; Todesco and Giordano, 2010; Di Paolo et al., 2012; Maffucci et al., 2012b; Corrado et al., 2014; Carapezza et al., 2015).

In this work, a multidisciplinary approach was applied to study the geothermal system of Rosario de La Frontera located at the northern edge of Sierra de La Candelaria anticline, in the Sub-Andean foreland of the Santa Barbara system (northwestern Argentina) (Fig. 1.1).

Structural and paleo-thermal analyses and a fracture reservoir modelling were applied to investigate its reservoir and cap-rock in order to evaluate the possibility of exploitation of the thermal fluids. Furthermore, the integration with hydrogeological, geochemical and geophysical studies available on this geothermal system (Barcelona et al., 2013; Invernizzi et al., 2014; Chiodi et al., 2015) addressed to the main goal of this research.

1.2 Aims of the thesis and methodology

The studies carried out in this PhD project are aimed to evaluate the possibility of exploitation of potential medium- and low-enthalpy geothermal fields located in the province of Salta (northwestern Argentina) in order to improve the sustainable development of its cities.

Special regard was devoted to the geothermal system of Rosario de La Frontera (Salta province). This active geothermal system is marked by several hot springs with surface temperatures ranging between 24°C and 90°C that occur close to the Hotel Termas thermal spa. One further hot spring (~ 38°C) occurs a few tens of kilometres along the south-western flank of the ridge.

The high temperature of its thermal fluids makes it as the most promising site for the supplying energy in the Sub-Andean foreland of the Salta province.

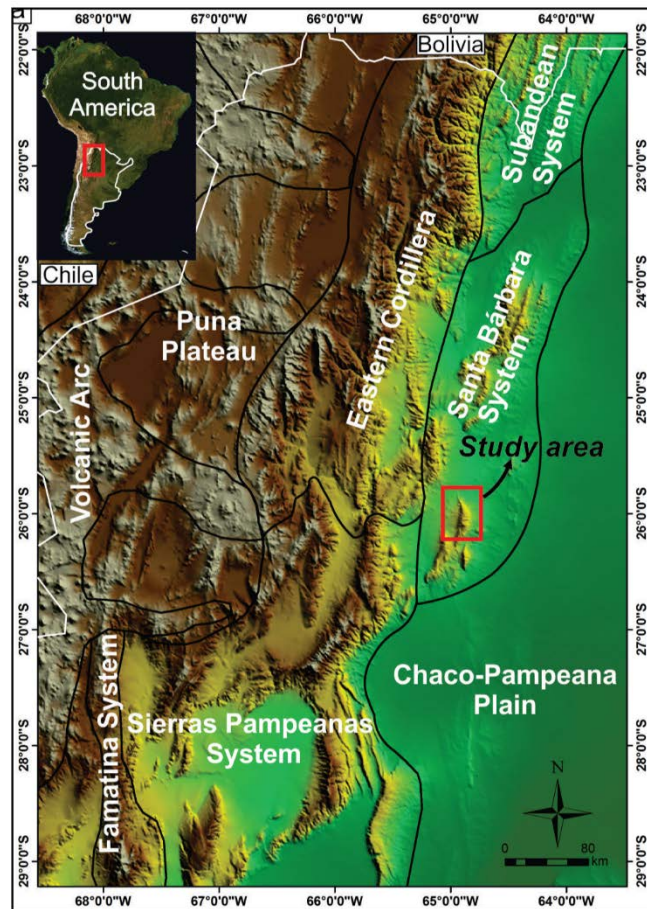


Fig. 1.1 – Location of the study area (from Chiodi et al., 2015)

The Cretaceous deposits of the Salta Group (Pirgua Subgroup) provide the reservoir of this system. They consist of continental deposits, mainly represented by sandstones and conglomerates, related to the syn-rift stage (Late Neocomian – Early Maastrichtian). On the contrary, the low permeable post-rift and the syn-orogenic deposits (respectively, Balbuena and Santa Bárbara subgroup, and Metán subgroup) provide the cap-rock to the system. These deposits are deformed in a N-S trending hanging wall anticline (Sierra de La Candelaria) and dissected by subsequently strike-slip and normal faults. The anticline and the associated structures (faults and fractures) represent the structural context of the studied geothermal system.

The purpose of this research is to assess the quality of the reservoir and cap-rock of this geothermal system through a multidisciplinary approach based on the integration of

different methodologies: paleo-thermal and structural analyses, and modelling of the reservoir fracture network.

Paleo-thermal analyses are typical of the Basin Analyses field, mainly applied by oil companies for exploration. The applied methodology include the optical analyses of the organic matter dispersed in sediments correlated to the X-ray diffraction study of clay minerals, and the fluid inclusions analyses on veins. Results were used to build mono-dimensional thermal and burial models, and allowed to reconstruct the thermal history and the origin of the thermal anomaly of the studied geothermal system. Furthermore, the integration with structural investigations performed at the outcrop scale allowed to assess the quality of its cap-rock as a function of thermal vs fracturing state.

Structural investigations were also useful to elaborate a reliable tectonic model of the studied anticline. Moreover, structural data collected at the outcrop scale were used to model the fracture network in a 3-D volume of the geothermal reservoir reconstructed on the base of the 3-D geological cross-sections with the aid of a dedicated software. The results addressed to reservoir evaluation: i.e. lateral extent, thickness and volume, tectonic features, porosity/permeability patterns and possible reservoir compartments.

In addition, thanks to the cooperation with others research groups working on the same geothermal system (CUIA University Cooperation Italy-Argentina project 2010), the present work was integrated with others exploration methodologies: hydrogeological, geochemical and geophysical (audiomagnetotellurics) analyses. The integration allowed to evaluate the sustainability of the geothermal resource through the elaboration of a conceptual model of the fluid reservoir.

As a result, the most favourable site for drilling purposes, in perspective exploitation and reservoir management, and a possible use of the thermal fluids are indicated.

1.3 Outline of the Thesis

Following this introductory part (Chapter 1), this thesis is divided into other five parts.

In Chapter 2 an overview of the geological and structural evolution of the Sub-Andean foreland is given, with major focus placed on the Santa Barbara System in general and the Sierra de La Candelaria in particular. The contribution of this work to the geological knowledge of the studied area is also explained.

In Chapter 3 a possible model for the tectonic evolution of the Sierra de La Candelaria anticline is proposed, based on the collected structural data. The results presented in this

chapter are also illustrated in the article “Quality assessment of reservoirs by means of outcrop data and discrete fracture network models: The case history of Rosario de La Frontera (NW Argentina) geothermal system” published by Maffucci et al. in *Tectonophysics* (2015).

In Chapter 4 the reservoir evaluation and the modelling of its fracture network is illustrated.

In Chapter 5 the burial and thermal evolution of the studied geothermal system as well as the integrity of its cap-rock is discussed on the base of the paleo-thermal analyses. Theoretical aspects and analytical procedures of the applied methodologies are also explained. The applied methods comprise: i) Organic matter thermal maturity studies; ii) XRD analyses and iii) Fluid Inclusions studies.

In Chapter 6 final remarks on the main results achieved by the entire research are presented.

CHAPTER II

PREVIOUS STUDIES AND OPEN PROBLEMS

2.1 Introduction

The research interest of this study is the geothermal system of Rosario de La Frontera belonging to the Sierra de La Candelaria anticline. This latter represents one of the positively inverted structure cropping out in the Sub-Andean foreland of the Santa Barbara System.

The northwestern Argentine territory (NOA) is characterized by numerous thermal springs along the frontal structures of the Andean retro-wedge (Pesce, 2000). These thermal manifestations are aligned in a N-S direction and can be traced until the Argentina-Bolivia boundary, to the north, and the Santiago del Estero province, to the south (Fig. 2.1).

These manifestations are mainly associated to medium- and low-enthalpy convective geothermal systems. Unlike the high-enthalpy geothermal systems of the Puna plateau (Pesce and Miranda, 2003; Giordano et al., 2013), they are located in populated areas and therefore they have a high potential for exploitation both for therapeutic and bathing purposes, as at present, and for direct use of heat.

In detail, the southernmost thermal area of the NOA is represented by Termas de Rio Hondo (Santiago del Estero province). In this area, fourteen thermal springs occur at surface with temperatures ranging between 35° and 60°C. The thermal complex of Rio Hondo represents the most important centre of health tourism in Argentina.

Northward, the thermal areas of El Saladillo, El Galpón, and El Sauce characterize the Salta province. The temperature of their thermal springs at surface ranges between 18° and 64°C. To the north, in the region of “El Ramal Jujeno”, in the eastern portion of the Jujuy province, occur the thermal areas of Aguas Caliente de Caimancito, Laguna La Quinta and Termas El Palmar. Their thermal springs show surface temperatures between 37°C and 58°C. In this province, are also present the thermal areas of Termas de Reyes, Puesto Viejo and Cachipunco with temperatures of the thermal springs between 24° and 52°C.

In these areas, little thermal complexes offer mainly balneology services for the local populations.

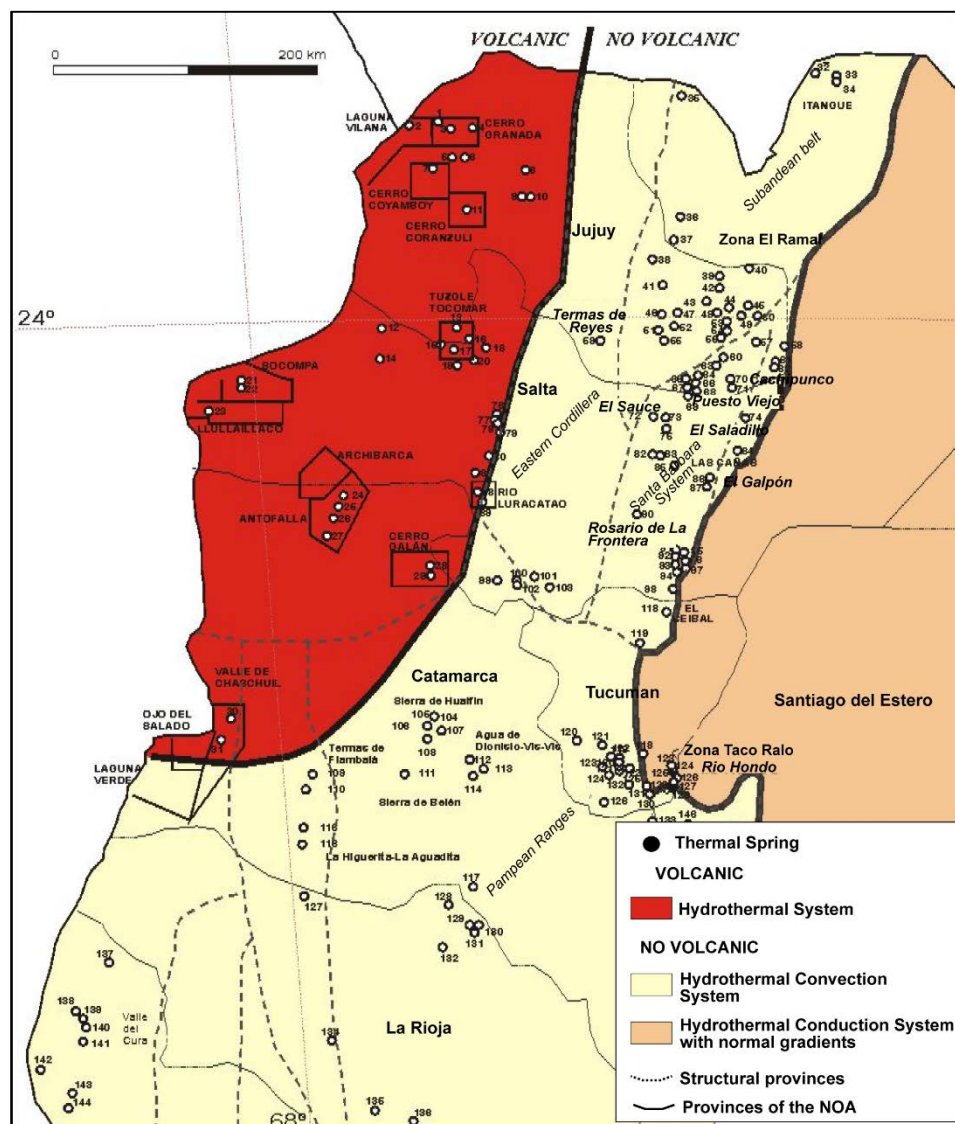


Fig 2.1 – Thermal areas occurring in the northwestern Argentina (Region NOA) (from *Pesce, 2000*).

Among all these thermal manifestations, the springs of Rosario de La Frontera system, located in the southern portion of the Salta province, are characterized by the highest temperatures at surface. This feature makes this site as the most interesting to improve the sustainable development in this area by the exploitation of the hot springs for direct and indirect heat uses such as space heating, greenhouses, industry, aquaculture, domestic use and production of electricity.

At present, its thermal springs are exploited for therapeutic purposes by the Rosario de la Frontera thermal complex, financially supported by the Salta Province government. It

represents the first thermal centre used under a medical criteria in Argentina and in South America, created by the Spanish doctor Antonio Palau in 1878 (Canton, 1896).

Form a geological point of view, the system of Rosario de La Frontera is located in the southernmost portion of the Santa Barbara system, to the south of the Metán basin (Fig.1.1).

Published works on this foreland segment are mainly referred to its northern portion (Ruiz Huidobro 1968; Mingramm et al. 1969; Gebhard et al. 1974; Mon 1976; Gómez Omil and Albariño 1996; Kley and Monaldi 1999; Kley and Monaldi, 2002). Poor available works on the southern area are mainly focused on the Metán depression (Mon, 1971, 1972; Mon and Dinkel, 1974; González and Mon, 1996; Grier et al., 1991; Cristallini et al., 1997; Iaffa et al., 2011, 2013). In particular, previous investigations of the Sierra de La Candelaria anticline are mainly focused on the chemistry and circulation of the thermal springs of Rosario de La Frontera system (Moreno Espelta et al., 1975; Seggiaro et al., 1995, 1997). Poor structural investigations on the anticline provided a kinematic interpretation invoking only a generic model of positive inversion based on structural pieces of evidence collected at regional scale (Moreno Espelta et al., 1975; Seggiaro et al., 1997; Iaffa et al., 2011; Iaffa et al., 2013), and on the base of a geomorphological and morphostructural characterization at local scale (Barcelona et al., 2014).

In this framework, one of the goals of this work is to give a new and recent geological contribute on a structure poorly studied of the Sub-Andean foreland. The original results presented in this work provide a kinematic evolutionary model of the studied anticline in an integrated framework that was missing in the past literature. Furthermore, the implications on the geothermal system object of interest of this work, allow to better understand the mechanisms controlling all the geothermal systems located along the Sub-Andean foreland.

For these aims, the geological framework given below will also refer to the broader studying site, as well as aspects of geodynamic and stratigraphic evolution, and the current structural configuration of the Sub-Andean foreland.

2.2 Geodynamic framework

2.2.1 The Central Andes

The Andean chain represents the result of the crustal deformation produced by the active subduction of the Nazca Plate beneath the South American Plate. This margin was defined as an “Andean type” according to the classification of Dewey & Bird (1970).

Along strike structural differences of the chain have been mainly related to dip changes in the subducted Nazca oceanic plate, to the pre-existing geological structures and lithological composition of the upper crust and to the thermal evolution of the lithosphere (Barazangi & Isacks 1976; Allmendinger et al. 1983, 1997; Allmendinger and Gubbels, 1996; Jordan et al. 1983; Jordan & Alonso 1987; Isacks, 1988; McQuarrie, 2002; Babeyko & Sobolev 2005; Oncken et al. 2006).

In its central portion (in Bolivia, northern Chile and Argentina), where shortening is greatest, the orogen is highest and widest (James, 1971; Isacks, 1988; Kley and Monaldi, 1998; Beck and Zandt, 2002; McQuarrie et al., 2005; Oncken et al., 2006; De Celles et al., 2011).

The Central Andes are characterized by the dominance of protracted magmatic activity in the west (widely distributed around the Western Cordillera, i.e. the arc) and of tectonic shortening in the east (in the Eastern Cordillera and adjacent areas). Eastward from the modern forearc region, at $\sim 25^{\circ}\text{S}$ in the northwest Argentina, the orogen can be divided into four longitudinal structural regions, including the active volcanic arc of the Western Cordillera, the Altiplano-Puna plateau, the Eastern Cordillera (a bivergent fold-thrust belt) and the Santa Barbara System foreland (Allmendinger et al., 1997; Strecker et al., 2007). Eastward of this fold-thrust belt adjoins the flat plain of the Chaco, which forms the recent retroarc foreland basin of the Central Andes (Fig. 2.2a).

2.2.2 The Santa Barbara System

The Santa Barbara System of northwestern Argentina represents a 400 km long segment of the Subandean foreland thrust belt characterized by predominantly west verging high-angle thrust faults with detachment level at mid-crustal depths (10-25 Km) (Allmendinger et al., 1983; Grier et al., 1991; Cristallini et al., 1997; Kley and Monaldi, 2002) (Fig. 2.2a,b).

By contrast, the sub-Andean belt to the north is a thin-skinned fold and thrust belt detached along a Silurian shale unit extended at a regional scale (Mingramm et al., 1979; Allmendinger et al., 1983; Aramayo Flores, 1989; Baby et al., 1989, 1992; Dunn et al., 1995). Furthermore, the Sierras Pampeanas to the south is an extensive province of basement uplifts associated with deep-reaching thrusts or reverse faults that dip moderately eastward and westward (González Bonorino, 1950; Allmendinger et al., 1983; Jordan and Allmendinger, 1986). Differences in the tectonic style along-strike correlates with changes in the dip of the subducted Nazca plate beneath the continental margin, in major paleogeographic structures and sedimentary basins distribution, and with a north-south

change in the upper mantle structure (Pilger, 1981; Allmendinger et al., 1983; Jordan et al., 1983; Withman et al., 1992; Kley et al., 1999).

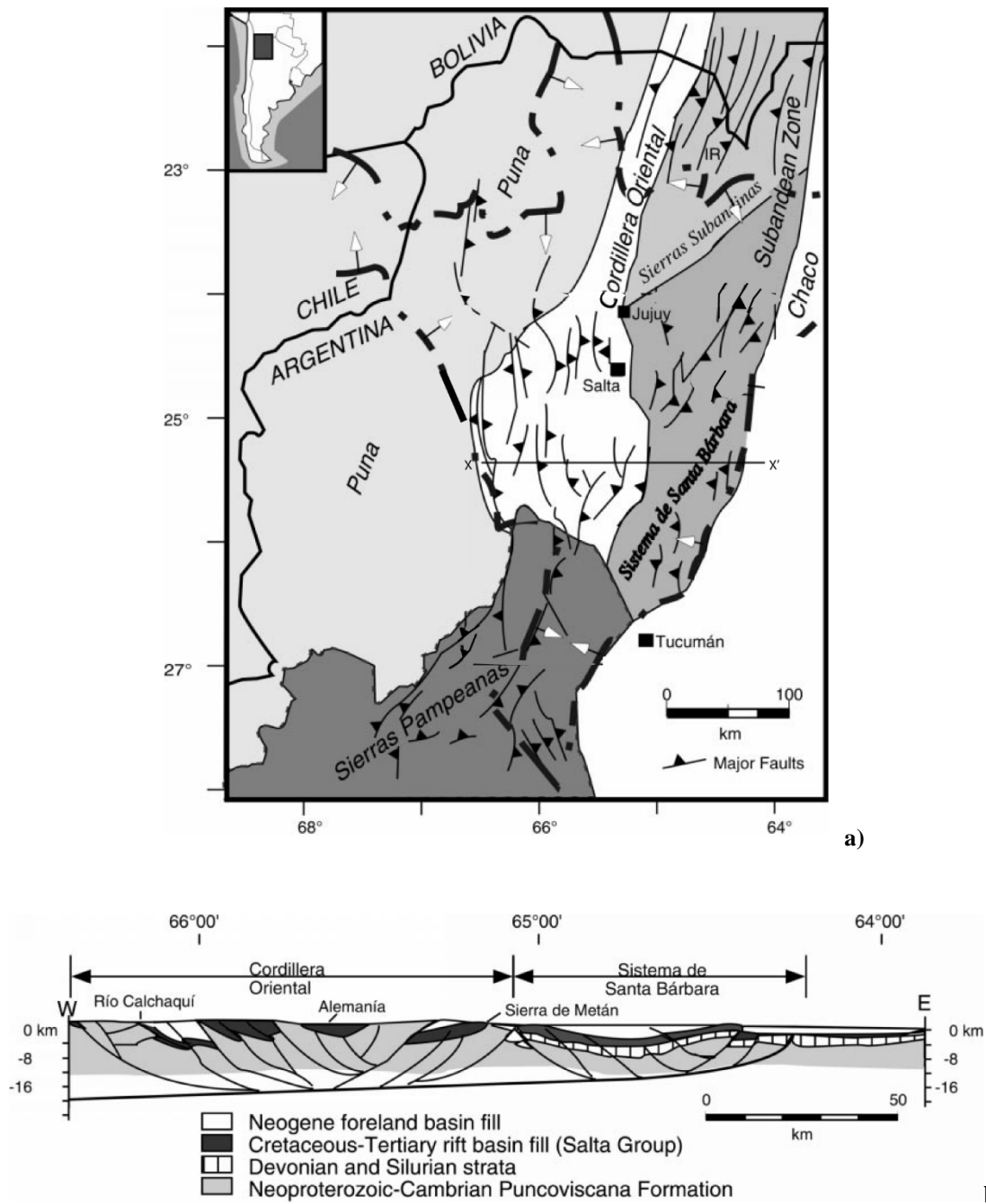


Fig 2.2 – a) Map illustrating the structural provinces in the northwestern Argentina (Region NOA) and b) a balanced cross section of the Transition Zone at 25°30'S. Its trace is indicated in the map. Heavy dashed lines denote the approximate boundaries of the Salta rift (white arrows on down- thrown side) (from Reynolds et al., 2011).

In detail, the Santa Barbara System is located in correspondence of the Transition Zone where the Nazca oceanic plate changes its dip from flat, to the south, to “normal” (about 30° dip) to the north at 27° S latitude (Barazangi and Isacks, 1976; Cahill and Isacks, 1992;

Gutscher et al., 2000; Ramos et al., 2002). Furthermore, the upper crust in the studied region has a strong segmentation that reflects inherited stratigraphic and structural inhomogeneities related to the succession of tectonic events occurred since early Palaeozoic times (Allmendinger et al., 1983; Mpodozis and Ramos, 1989; Kley et al., 1999). From that time on, different reactivation events took place in the area. One major event occurred in Late Cretaceous times, when extension favoured the opening of a back-arc rift basin (Salta Rift) (Salfity & Marquillas 1981; Monaldi et al. 2008) constituted by a series of extensional troughs or sub-basins (e.g. Sey, Tres Cruces, Brealito, Tucumán, Choromoro, El Rey, Lomas de Olmedo, Metán) (Fig. 2.3).

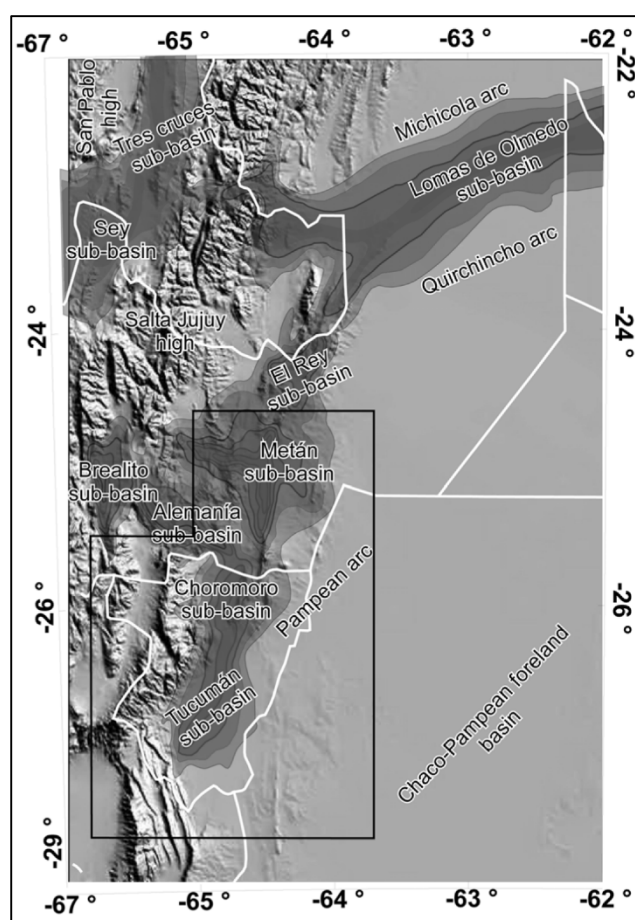


Fig 2.3 - Main sub-basins forming the Cretaceous Salta Rift. The rift basin developed in a series of sub-basins that were partially connected (from *Iaffa et al., 2013*).

The Andean orogeny with its deformation started to imprint its effects in the study region in the Eocene (Coutand et al. 2001; Carrapa et al. 2005; Carrera et al. 2006; Hongn et al. 2007). Since then, deformation has propagated towards the east but with jumps back to the west intercalated in an out-of-sequence deformation (Salfity et al., 1993; Carrera et al. 2006; Carrera & Muñoz, 2008; Hain et al., 2011).

The stratigraphic succession comprises three major sequences (Fig. 2.2b): (1) A basement of Precambrian to early Cambrian low grade metasedimentary rocks (Pankhurst & Rapela, 1998; Omarini et al., 1999; Aceñolaza et al., 2002; Aceñolaza, 2005) is overlain with a regional angular unconformity by (2) a predominantly continental succession of red beds with minor limestone intercalations (Salta Group) including syn-rift, and post-rift deposits. The latter are capped by (3) a thick continental foreland basin fill that was shed from the rising Andes in the west in Eocene to Recent time (Coutand et al. 2001; Carrapa et al. 2005; Carrera et al. 2006; Hongn et al. 2007).

From a structural point of view, the area is dominated by spatially and temporally disparate range trending north to NNE, uplift along steeply dipping inherited faults from the Cretaceous rift (Grier et al., 1991; Mon and Salfity, 1995; Cristallini et al., 1997, Kley and Monaldi, 2002) (Fig. 2.2a). The present topography shows a strong segmented foreland characterized by different interconnected sub-basins. Among them, the Metán Basin is located in the southernmost portion of the Santa Barbara system.

Furthermore, a thin mantle lithosphere and a low flexural rigidity have been shown in this segment of the Sub-Andean foreland (Withman et al., 1992, 1994, 1996). Petrologic data suggest that the thinned foreland lithosphere may in part be inherited from a thermal anomaly established during mantle-activated Cretaceous rifting (Lucassen et al., 1999; Kley and Monaldi, 2002). Accordingly, a relatively high heat flow (100-120 mW/m²) is indicated in the area (Hamza and Muñoz, 1996; Hamza et al., 2005; Cardoso et al., 2010; Vieira and Hamza, 2014) (Fig. 2.4).

2.2.3 The Metán basin

The striking feature of the Metán basin is represented by the variety of structural trends (Kley and Monaldi, 2002; Iaffa et al., 2013). Interaction between the older reactivated faults and the newly generated ones gave rise to a complex pattern of fold interference (Mon, 1976; Grier et al., 1991; Cristallini et al., 1997; Kley and Monaldi, 2002; Carrera et al., 2006; Iaffa et al., 2011, 2013).

Anisotropies produced during the Precambrian to Palaeozoic tectonic cycles shaped the basement fabric, producing discontinuities that were reutilized in posterior tectonic stages (Iaffa et al., 2011). Some of these structures were reactivated during the Salta Rift and others in the different stages of the Andean deformation (Cristallini et al., 1997; Iaffa et al., 2013). As a result, the general structural trend of the area is dominated by N-S, NE-SW and NNE-SSW thrust faults and folds. The oldest Andean compressive structures in the study

area was probably the N-S Sierra de Metán Thrust Fault and its hangingwall anticline, and resulted from W-E shortening (Iaffa et al., 2011).

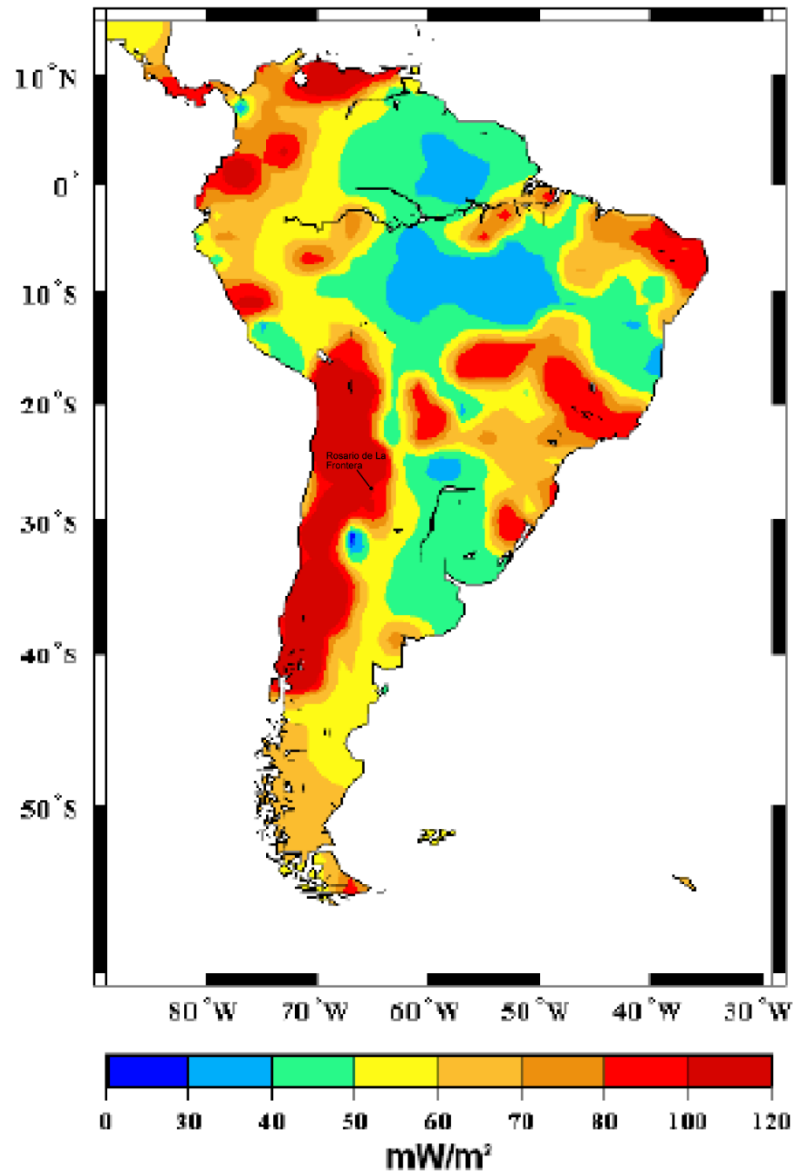


Fig 2.4 – Heat Flow map of the south America (from Cardoso et al., 2010).

In this framework, during the Andean orogeny, pre-existent rift faults with an orientation unfavourable to reactivation acted as a buttress favouring an inward migration of the deformation with the formation of out of sequence thrusts (Iaffa et al., 2011).

The absence of important thicknesses of marine deposits or evaporites in the basins that in posterior compressive stages could act as ductile layers is a factor contributing to the tectonic reactivation of previous structural discontinuities (Iaffa et al., 2011). Shallower

detachment levels only acted in the last stages of the Andean deformation, when intermontane basins were locked by the uplifted basement ranges and the system was buttressed.

The Sierra de La Candelaria anticline represents one of these uplift basement ranges. It delimits to the south the Metán basin.

2.3 Sierra de La Candelaria anticline

Despite some early studies, the Sierra de La Candelaria structure is poorly documented. Moreno Espelta et al. (1975) and Seggiaro et al. (1995, 1997) provided a first description of the stratigraphy and geology of the anticline with the aim to define the structural framework of the thermal springs of Rosario de La Frontera area.

Sierra de La Candelaria ridge consists of a broad anticline bifurcated, in the northern portion, in two minor anticlines both dipping to the north: Termas and Balboa, separated by a NNW-SSE to N-S fault plane (Fig. 2.5).

Its stratigraphic succession covers a wide time span: from pre-Cambrian to Pliocene-Quaternary times (Moreno Espelta et al., 1975) (Fig. 2.5). The oldest stratigraphic unit crops out in the core of the anticline. It is the Precambrian basement made up of low grade metasedimentary rocks (Medina Formation) that, in the northern portion and along the western limb of the anticline, is unconformably overlain by a thick succession of continental Cretaceous to Paleogene strata (Salta Group) related to the Cretaceous rift stage (Turner, 1959; Salfity, 1982; Galliski and Viramonte, 1988; Salfity and Marquillas, 1994; Viramonte et al., 1999; Marquillas et al., 2005).

The Early to Late Cretaceous Pirgua subgroup, marks the syn-rift fill stage (Salfity and Marquillas, 1994), whereas the Balbuena and Santa Bárbara subgroups represent the post-rift thermal subsidence stage (Bianucci et al., 1981; Salfity and Marquillas, 1994; Comnínquez and Ramos, 1995). Post-rift deposits are in turn overlain by a thick continental foreland basin fill, related to the Andean mountain uplift and erosion, that was deposited from Middle Miocene to Pliocene–Quaternary times (Gebhard et al., 1974).

The retrowedge basin fill includes two subgroups (Metán and Jujuy, according to Gebhard et al., 1974) belonging to the Orán Group. The main outcrops of these subgroups cover the northern portion of the Sierra de La Candelaria ridge at the lowest elevations.

The stratigraphic succession cropping out along the Sierra de La Candelaria ridge forms an anticline whose general trend is N-S. It is located in the hanging wall of a N-S high-angle fault that borders the structure along its eastern margin.

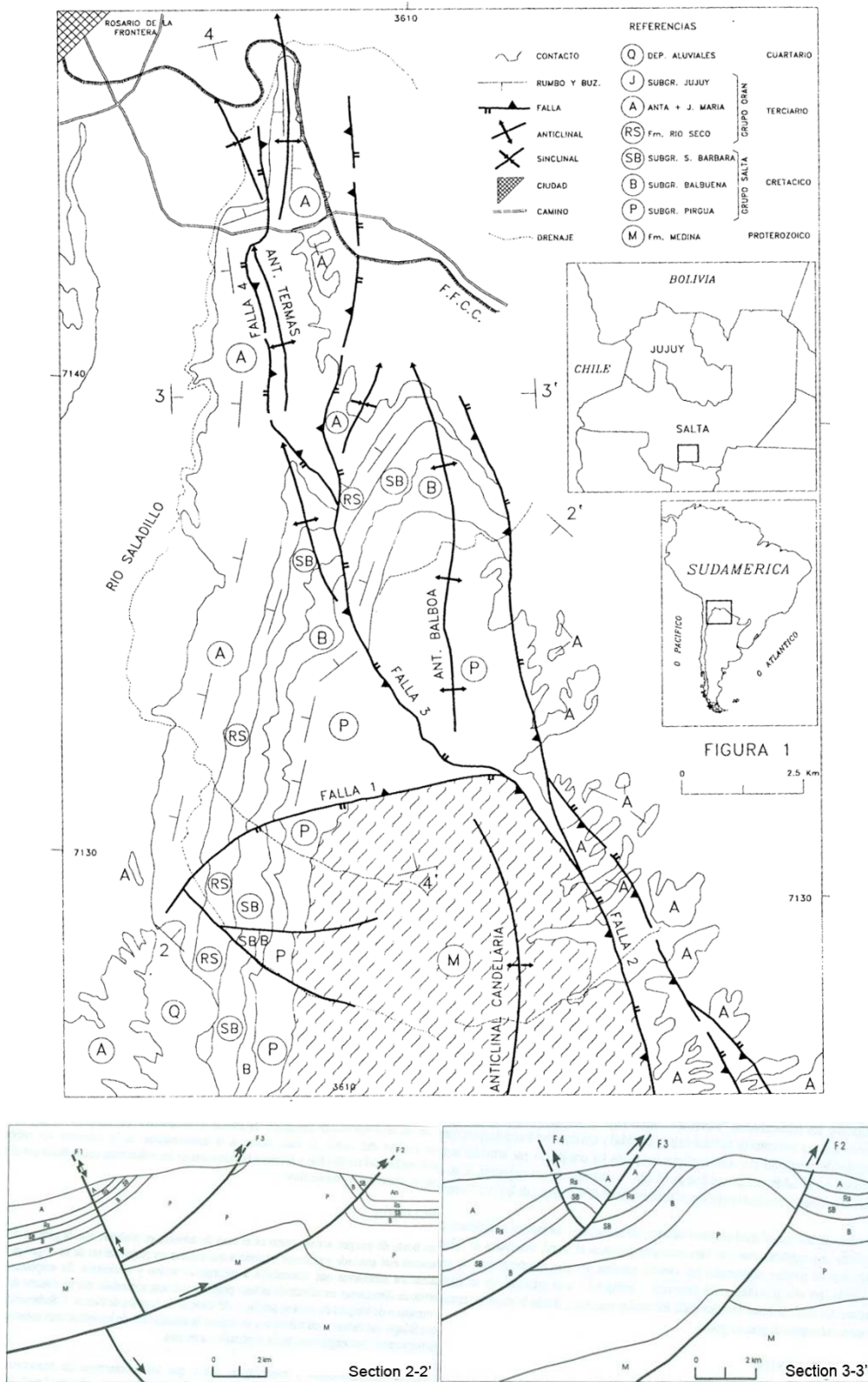


Fig 2.5 – Geological map of the northern portion of the Sierra de La Candelaria anticline from Seggiaro et al. (1997). According to the authors, the reverse fault “falla 2” bordering the anticline along its eastern margin is the responsible of the uplift of the anticline. The reverse fault “falla 3” in the central area, divides the structure in two anticlines: Termas and Balboa. In section 2-2’, the E-W inverted normal fault “falla1” is cut at depth by the N-S thrust fault plane.

Seggiaro et al. (1995), throughout balanced cross sections, constrained the detachment level of this fault plane at 10 Km of depth, in correspondence of the metamorphic basement of Medina Formation (Fig. 2.5). Later, Seggiaro et al. (1997) argued as the central NNW-SSE fault plane, detached within the syn-rift deposits (Pirgua Subgroup), may be the responsible of the uplift of Termas anticline enhanced by a linked N-S backthrust. In their structural interpretation, an E-W inverted normal fault delimits to the south the Balboa anticline and is cut at depth by the N-S thrust fault.

González et al. (2000) were the first to describe the southern portion of the anticline. They defined a left-lateral NE-SW strike-slip fault in the southern area of Ceibal (Fig. 2.6).

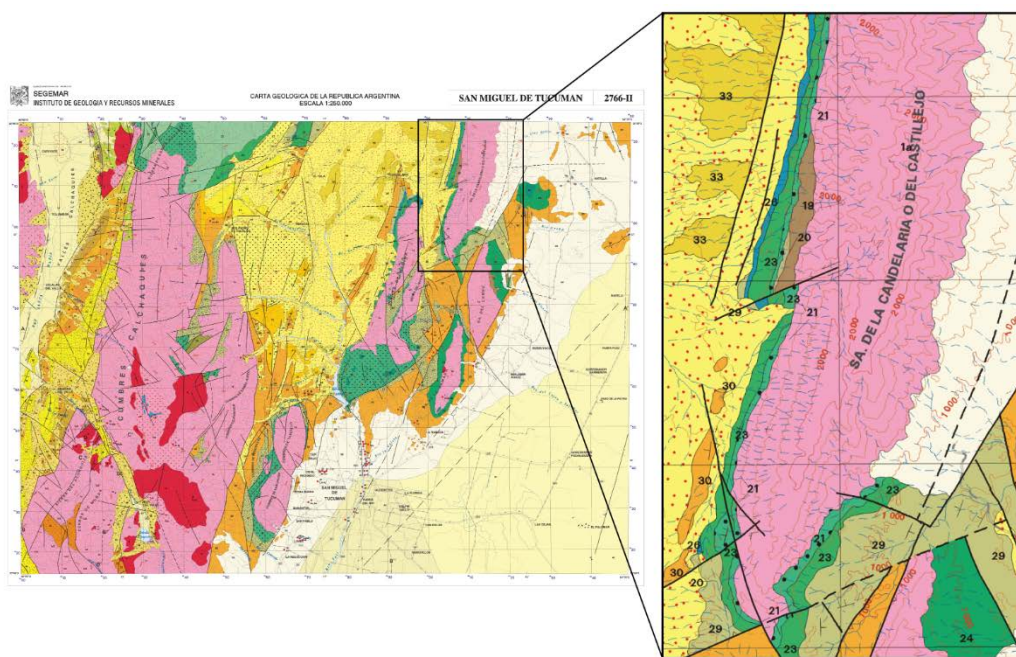


Fig. 2.6 – Geological map of the southern portion of the Sierra de La Candelaria anticline (from González et al., 2000). The structure is dissected by a left-lateral strike-slip fault. Others NNW-SSE and NE-SW fault planes dissect the southernmost portion of the structure with reverse and strike-slip kinematics, respectively.

Later, Salfity and Monaldi (2006) provided a detailed mapping of the northern portion of the anticline. They described the NNW-SSE fault plane dividing the two anticlines as an oblique fault plane. Branches of the fault splay off to the northwest. Two E-W fault planes delimits to the south the Balboa anticline cutting the N-S thrust fault that borders the structure on the eastern side (Fig. 2.7).

Recently, Iaffa et al. (2011) by reconstructing the structural style of this portion of the Sub-Andean foreland on the base of seismic and field data, established that the N-S fault plane flanking the anticline to the east represents a former Salta Rift extensional fault.

A new interpretation of the uplift evolution and growth of this mountain range was proposed by Barcelona et al. (2014) on the base of an integrated analysis of geomorphology and morphostructural characterization. They reconstructed a multi-stage development of the Sierra de La Candelaria range identifying three morpho-structural segments uplifted at different times. The first stage uplifted the central segment. Accordingly, the Balboa anticline might precedes the Termas anticline representing the northern ancient nose of the Sierra de la Candelaria range. After a significant time lapse, the mountain range was subjected to southward thick-skinned growth and northward growth via stepwise thin-skinned deformation. The development of the southern segment of the Sierra de la Candelaria range could have induced a concomitant uplift of the central segment through mechanical coupling, which evolved into a second stage of vertical development of the central segment. This stage of uplift could have been controlled by the development or reactivation of a blind antithetic thrust, forming a pop-up structure style. Progressively, the final northward thin-skinned deformation stage developed the Termas anticline with a detachment zone located in a clay-bearing level of the Pirgua Subgroup, in agreement with the structural model of Seggiaro et al. (1997).

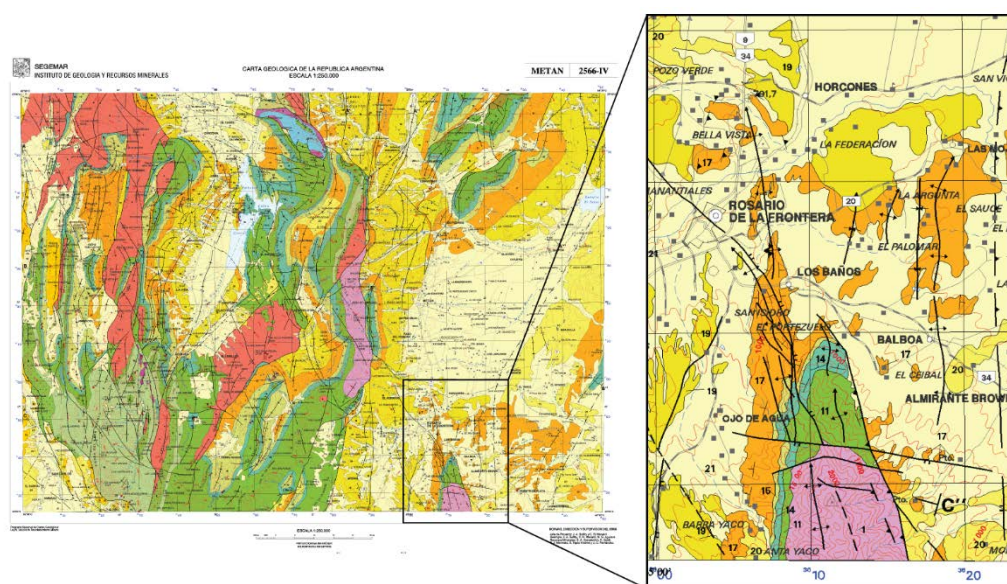


Fig. 2.7 – Geological map of the northern portion of the Sierra de La Candelaria anticline (from Salfity and Monaldi, 2006). See text for details.

2.4 Rosario de La Frontera geothermal system

At the northern edge of Sierra de La Candelaria anticline are located the thermal springs of Rosario de La Frontera geothermal system.

In 1876 Dr. Max Siawert started studying water chemistry in the area, four years later Dr. Antonio Palau began the exploitation of thermal springs for commercial purposes. In 1888, Doctors Doering and Schikendantz, and Dr. Tagliabue in 1895, proved the occurrence of nine different kinds of waters, which turned the “Termas de Salta” (as it was known until the end of the nineteenth century) to be a privileged place for therapeutic purposes (Rivas, 2012).

Seggiaro et al. (1995) were the first to study the chemistry, temperature and pH of the thermal springs providing data for five samples. Only recently Chiodi et al. (2015) have produced an exhaustive dataset of the thermal springs and of the dissolved gases of 13 thermal discharges (hot springs and bubbling pools with temperatures up to 90.5 °C), with the aim to construct a conceptual model of the circulation of the thermal fluids at depth (Fig. 2.8; Tables 2.1, 2.2).

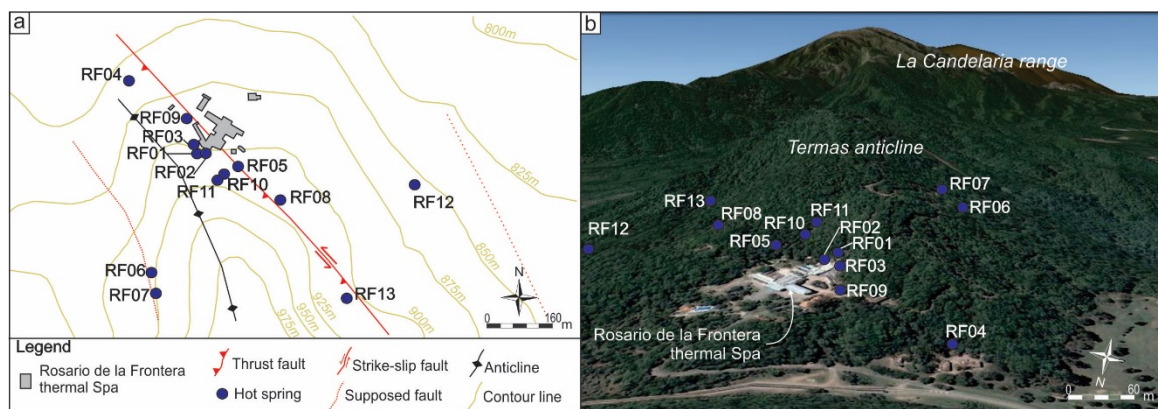


Fig. 2.8 – (a) Morphotectonic map of the Termas anticline and (b) 3D-image of the studied area. Sampled thermal springs are illustrated (from Chiodi et al., 2015).

Their results are in accordance with the occurrence of two aquifer previous detected, at ~2400 and ~150 m depth, by Barcelona et al. (2013) and Invernizzi et al. (2014) on the base of audio-magnetotelluric and hydrogeological investigations, respectively.

The deepest hydrothermal reservoir, hosted within the Cretaceous Pirgua Subgroup deposits, is mainly recharged by meteoric water and shows a Na–HCO₃ composition with significant contributions of crustal CO₂ and He from mantle degassing through the fault systems that dissect the anticline. The uprising thermal fluids mix with a relatively high salinity Na–Cl dominated aquifer produced by the interaction of meteoric water with shallow evaporitic deposits of the Anta Formation (Fig. 2.9).

Table 2.1 – Outlet temperatures (in °C), pH, chemical composition, $\delta^{34}\text{S}\text{-SO}_4$ (expressed as ‰ vs. V-CDT $\delta^{18}\text{O}$ and $\delta^2\text{H}$ (both expressed as ‰ vs. V-SMOW) and $\delta^{11}\text{B}$ (in ‰) values of the RFHS fluid discharges. Concentrations of solutes are in mg/L; n.a.: not analyzed. (from Invernizzi et al. 2014 and Chiodi et al., 2015).

Sample	Lat.	Long.	Altitude (m)	T°	pH	HCO ₃ ⁻	F ⁻	Cl ⁻	Br ⁻	NO ₃ ⁻	SO ₄ ²⁻	Ca ²⁺	Mg ²⁺	Na ⁺	K ⁺	NH ₄ ⁺	B	SiO ₂	$\delta^{34}\text{S}\text{-SO}_4$	$\delta^{18}\text{O}\text{-H}_2\text{O}$	$\delta\text{D}\text{-H}_2\text{O}$	$\delta^{11}\text{B}$
RF01	25,84	64,93	924	74,0	6,75	169	2,3	313	0,06	0,63	128	11	0,5	305	4,3	0,05	0,12	92	n.a.	-7,0	-38	
RF02	25,84	64,93	905	81,2	6,88	156	1,8	682	0,23	0,53	190	10,6	0,5	587	7,4	0,06	0,18	88	6,99	-6,9	-38	
RF03	25,84	64,93	918	71,4	7,06	201	8,8	16000	2,08	0,11	2100	326,1	20,1	11200	80,8	0,07	0,23	47	n.a.	-7,1	-40	0,87
RF04	25,84	64,93	865	24,1	6,84	315	8,7	5340	1,98	6,13	3010	439,7	63,5	4290	17,4	0,05	0,33	54	6,31	-6,4	-38	1,05
RF05	25,84	64,93	948	52,7	6,42	198	1,9	137	0,19	1,17	146	32	1,5	188	2,7	0,05	0,21	94	n.a.	-6,8	-37	
RF06	25,84	64,93	960	64,8	6,09	149	0,7	270	0,24	1,38	104	5,1	0,1	288	4,0	0,07	0,39	89	n.a.	-6,6	-36	
RF07	25,84	64,93	967	58,2	6,73	224	2,5	42	0,11	1,51	103	15	0,7	147	1,7	0,13	0,27	85	n.a.	-6,6	-36	13,8
RF08	25,84	64,93	954	74,9	6,83	219	1,5	122	0,08	0,96	143	22	0,9	193	2,3	0,07	0,15	87	5,87	-6,6	-37	
RF09	25,84	64,93	894	24,2	7,36	279	1,5	2510	1,55	2,72	626	75	10,9	1900	17,4	0,11	0,45	51	5,42	-6,6	-38	
RF10	25,84	64,93	928	90,5	6,12	171	2,5	276	0,15	0,22	187	3,9	0,2	321	5,7	0,09	0,28	102	7,32	-6,9	-39	12,6
RF11	25,84	64,93	942	90,4	6,39	190	8,0	254	0,18	0,85	180	14	0,3	294	5,6	0,28	0,35	108	n.a.	-6,5	-36	
RF12	25,84	64,93	867	45,2	6,77	215	2,3	80	0,07	0,27	155	4,6	0,28	206	4,7	0,26	0,44	116	n.a.	-6,6	-36	
RF13	25,84	64,93	918	72,2	6,26	210	2,0	133	0,11	0,39	140	3,2	0,1	227	5,3	0,20	0,51	124	n.a.	-6,5	-37	

Table 2.2 – Chemical composition, $\delta^{13}\text{C}$ in CO₂ and CH₄ (both expressed as ‰ vs. V-PDB) and R/Ra values of the bubbling and dissolved gases from the RFHS. Concentrations are in mmol/mol; n.d.: not detected. (from Chiodi et al., 2015).

Sample	type	CO ₂	H ₂ S	N ₂	CH ₄	Ar	O ₂	Ne	H ₂	He	C ₂ H ₆	C ₃ H ₈	i-C ₄ H ₁₀	n-C ₄ H ₁₀	i-C ₄ H ₈	i-C ₃ H ₁₂	n-C ₃ H ₁₂	C ₆ H ₆	$\delta^{13}\text{C}\text{-CO}_2$	R/Ra	$\delta^{13}\text{C}\text{-CH}_4$
RF01	dissolved	209	n.d.	756	0,011	17,4	18	0,0093	n.d.	0,0015	n.d.	n.d.	n.d.	n.d.	n.d.	n.d.	n.d.	n.d.	-6,56		
RF02	bubbling	956	3,6	28	0,051	0,59	12	0,0003	0,015	0,0044	0,00061	0,00005	0,00004	0,00003	0,00003	0,00002	0,00003	0,00011	-4,11	1,15	-39,3
RF03	dissolved	168	n.d.	803	0,005	16,9	12	0,009	n.d.	0,0021	n.d.	n.d.	n.d.	n.d.	n.d.	n.d.	n.d.	n.d.	-7,13		
RF04	dissolved	139	n.d.	841	0,087	19	2,3	0,010	n.d.	0,0011	n.d.	n.d.	n.d.	n.d.	n.d.	n.d.	n.d.	n.d.	-5,66		-41,5
RF05	dissolved	575	n.d.	385	0,011	8,9	31	0,005	n.d.	0,0061	n.d.	n.d.	n.d.	n.d.	n.d.	n.d.	n.d.	n.d.	-5,16		
RF06	dissolved	889	n.d.	106	0,051	2,39	2,66	0,0015	n.d.	0,0021	0,00061	0,00002	0,00003	0,00002	0,00005	0,00003	0,00002	0,00018	-4,15		-41,4
RF08	dissolved	212	n.d.	755	0,115	18,5	14	0,010	n.d.	0,0013	n.d.	n.d.	n.d.	n.d.	n.d.	n.d.	n.d.	n.d.	-11,49		
RF09	dissolved	296	n.d.	676	0,009	17,1	11	0,009	n.d.	0,0024	n.d.	n.d.	n.d.	n.d.	n.d.	n.d.	n.d.	n.d.	-4,11		
RF10	dissolved	960	1,2	36	0,087	0,77	2,3	0,0004	0,011	0,0042	0,00077	0,00004	0,00005	0,00002	0,00004	0,00002	0,00003	0,00015	-3,66	0,98	-40,6
RF11	dissolved	550	n.d.	415	0,015	9,8	25	0,006	n.d.	0,0027	n.d.	n.d.	n.d.	n.d.	n.d.	n.d.	n.d.	n.d.	-4,44		
RF13	dissolved	954	n.d.	44	0,069	0,89	1,5	0,0005	0,022	0,0033	0,00078	0,00003	0,00002	0,00004	0,00006	0,00003	0,00004	0,00021	-3,77		-39,8

The temperature of the main hydrothermal reservoir, the deepest one, estimated with water geothermometers, is in the range of 100°-130°C (Seggiaro et al., 1995; Chiodi et al., 2015). A preliminary evaluation of the volume of this aquifer, hosted within Cretaceous sedimentary units, was made by Invernizzi et al. (2014). It accounts for 39 km³. On the base of the integration of hydrogeological, structural and chemical (isotopic analyses) investigations, the same authors provided a preliminary conceptual model of the geothermal fluid reservoir. They constrained the recharge area of the geothermal system of Rosario de La Frontera close to the area of the thermal baths, located in the northern sector of Sierra de la Candelaria. Temperature acquisition are achieved at depth where the infiltrated water reaches the base of the reservoir. A fast water ascent is driven by fracture systems well developed in correspondence of the northern end of the plunging structure. Furthermore, a long residence time of water at depth (over 50 years) is indicating by ³H data suggesting a long timing for the aquifer recharge (Invernizzi et al., 2014).

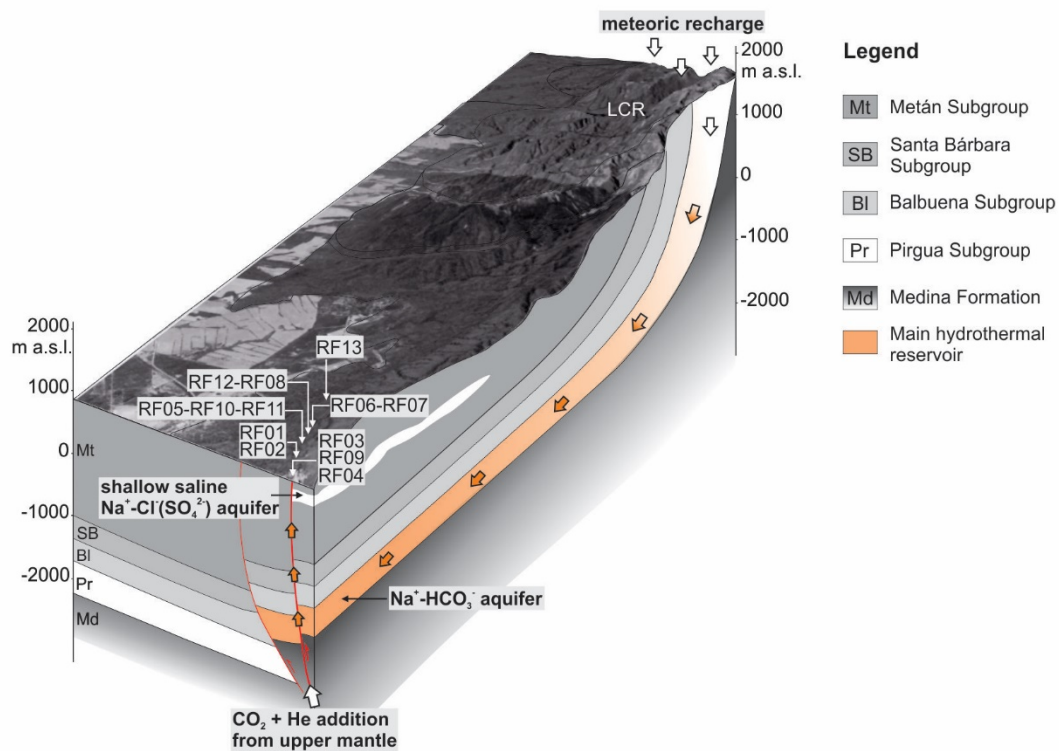


Fig. 2.9 – Three-dimensional conceptual model of the underground fluid circulation of Rosario de La Frontera geothermal system (from Chiodi et al., 2015).

According to this model of circulation, considering a surface water temperature of 20 °C (Invernizzi et al., 2014) and a local geothermal gradient of ~40 °C/km (Seggiaro et al., 1995), recharging meteoric water reaches reservoir temperatures at 2100–2900m depth,

consistent with the difference between the average altitude of the recharge area (1680 m a.s.l.) and the depth of the Pirgua Subgroup (1100-1500 m b.s.l.) (Chiodi et al., 2015).

On the base of this reconstruction, Invernizzi et al. (2014) and Chiodi et al. (2015), considering an average reservoir temperature of $\sim 90^{\circ}\text{C}$ and $\sim 115^{\circ}\text{C}$, respectively, proposed a preliminary evaluation of the energy potential of the Rosario de La Frontera geothermal system estimating the heat stored in the fluid phase in the order of 10^{18} J.

CHAPTER III

TECTONIC MODEL OF SIERRA DE LA CANDELARIA ANTICLINE

3.1 Introduction

The chapter focuses on structural data collected at the outcrop scale along the Sierra de La Candelaria anticline in order to understand their relationships with the main deformation events that affected the anticline and their influence on fluids migration.

The analyses of the collected data, together with the evaluation of the structural relationships between the anticline and the faults mapped in the area, and the geometry of the different stratigraphic units allowed to better constrain the structural setting of the anticline and to elaborate a multi-stage model that explains its formation and evolution.

3.2 Structural analysis at the outcrop scale

Field work was dedicated both to qualitative and quantitative analysis (orientation, dimension, spatial distributions, mode of deformation and spacing) of structural data recorded in the outcropping sedimentary succession. I tried to collect structural data in different areas of the anticline, along the forelimb, the backlimb and in the northern plunging nose, in order to illustrate the relationship of the structural data features to folding and their influence on fluid flow. Unfortunately, the Sierra de La Candelaria structure is densely covered by shrubby vegetation, and exposures are restricted mostly to river beds, river banks, railroad and highway cut. Therefore, the outcrops condition together with the difficulty to catch them very limited the distribution of measure sites along the anticline. Anyway, structural data on faults, cleavages, fractures, and veins were collected at 95 georeferenced field sites (Fig. 3.1).

In detail, structural data were collected in the Guanaco, Jesús María, Anta, Yacoraite, Pirgua and Medina Formations. The first three formations are mainly exposed in the northern portion of the ridge; Anta Formation extensively crops out both in the crestal

sector of Termas anticline and along the western limb of the main anticline. On the contrary, Yacoraite Formation and Pirgua Subgroup are widely exposed along the limbs in the central sector of Balboa anticline and in the southern sector of the ridge.

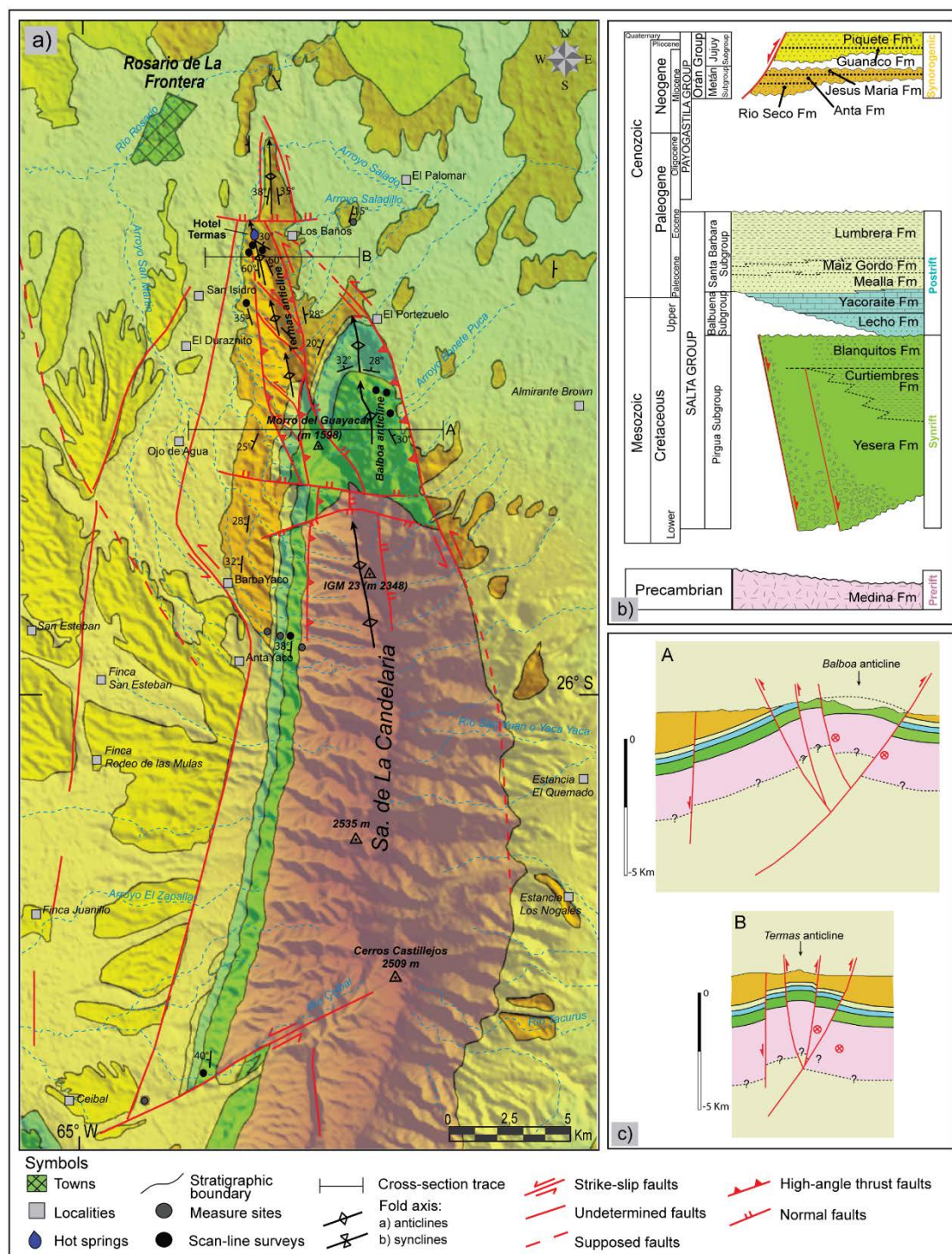


Fig. 3.1 – (a) Geological Map of Sierra de La Candelaria anticline. (b) Chronostratigraphic column showing the tectonostratigraphic units cropping out in the study area, as well as the main tectonic events that controlled their deposition (redrawn by Carrera et al., 2006). (c) Representative cross sections of the anticline. Their location is indicated in the geological map.

I identified in the field faults, generic fractures (e.g. defined as discontinuities with small aperture not sufficient to exclude a shear component during the opening, isolated weathered fracture) (Tavani et al., 2008), shear fractures, deformation bands, gypsum- and calcite-filled veins, and tectonic stylolites.

3.2.1 Southwestern Backlimb

Along the south-western limb of the main Sierra de La Candelaria anticline, structural data were collected in two different sectors: Anta Yaco (north) and Ceibal (south) (Fig. 3.1). In the Anta Yaco area, structural analysis were performed on Anta, Yacoraite, Pirgua and Medina Formations. Conversely, in the Ceibal area structural data were collected from the outcrops of Pirgua Subgroup and Jesús María Formations.

As a whole, the sedimentary succession cropping out along the backlimb strikes N-S, dipping about 40° to the W. The analysed structures include generic fractures, shear fractures, veins and tectonic stylolites representing a spaced disjunctive cleavage produced by pressure solution.

Generic fractures occur in all the mechanical units exposed along the backlimb of the anticline. Poles to generic fractures show four main directions both in their present orientation and after bed rotation: N-S, E-W, NNW-SSE, ENE-WSW and WNW-ESE (Fig. 3.2a, b).

N-S fractures are dominant and well visible in all the outcrops, and have generally high angle of dip (80°). They occur also in the younger strata (Jesús María Fm.) with a constant spacing of about 30cm and a length greater than 2m; the aperture is from few millimeters up to 1.5cm.

E-W fractures occur in the strata of Yacoraite Formation and Pirgua Subgroup, in the area of Anta Yaco and Ceibal; they show a constant spacing of about 30cm; their length varies from 30 cm to several metres and the aperture is mostly lower than 1mm, but in some cases it reach a value of 3mm such as in the strata of Yacoraite Formation (Fig. 3.3).

NNW-SSE and WNW-ESE striking fractures, with high angle of dip, occur mainly in the strata of Medina and Pirgua Formations in the area of Anta Yaco. ENE-WSW generic fractures characterized mainly the strata of Pirgua Subgroup in the Ceibal area. In this latter area, calcite-filled veins are dominant in systematic sets striking along ENE-WSW and NNE-SSW directions (Fig. 3.4a).

They show a variable spacing ranging from several metres down to 30-40cm; their thickness ranges from few millimeters to 2cm.

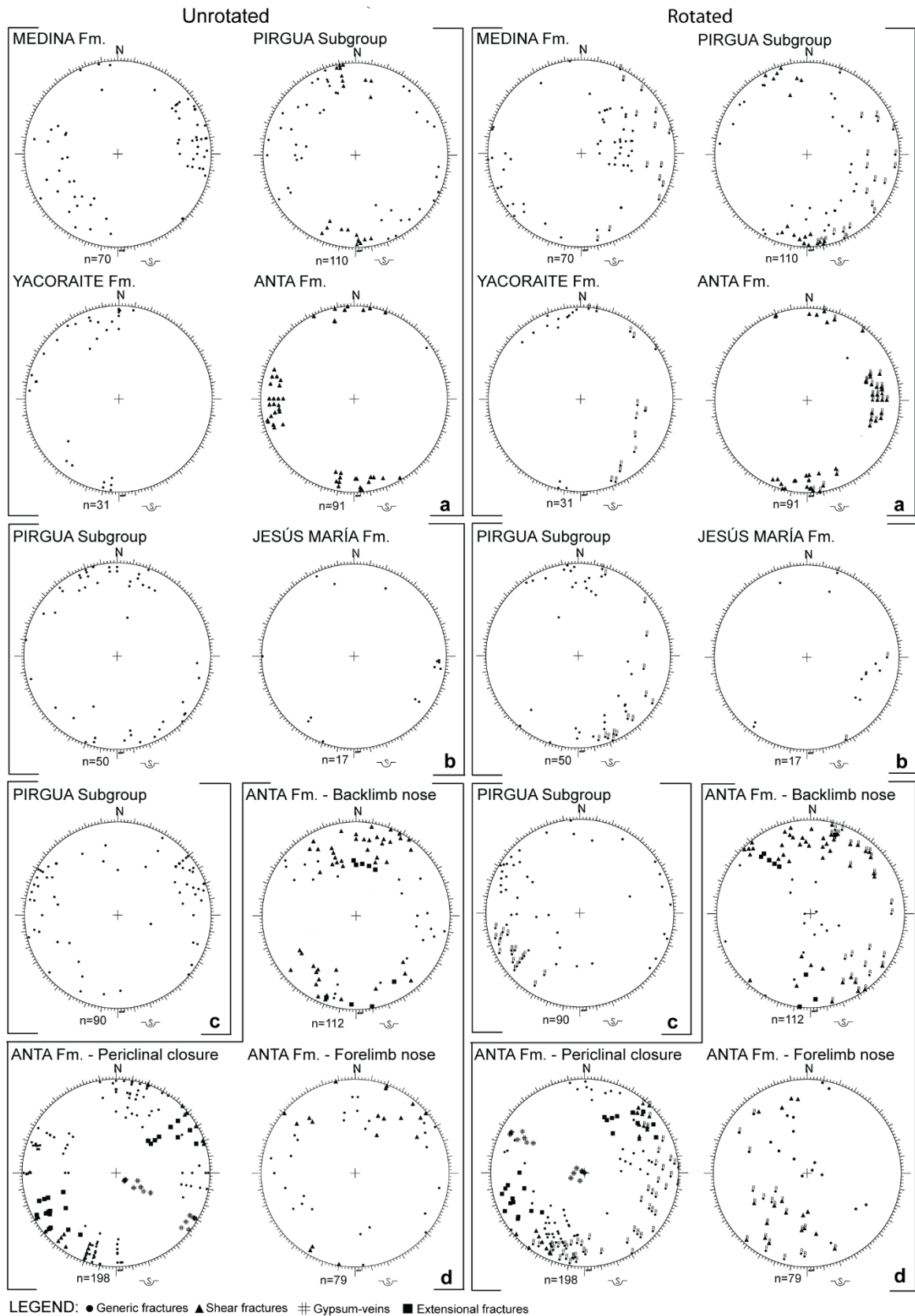


Fig. 3.2 – Stereographic projections (Schmidt net, lower hemisphere) of the structural data collected in the (a) Anta Yaco and (b) Ceibal areas, (c) Balboa and (d) Termas anticlines.

Shear fractures were recognized in the strata of Anta and Pirgua Formations in the area of Anta Yaco. In the Anta Formation, they occur as conjugate strike-slip systems striking NNW-SSE and E-W, steeply dipping and mutually cross cutting, probably related to a contraction parallel to bedding dip (Fig. 3.4b). On the contrary, the strata of Pirgua Subgroup show a pervasive deformation characterized by E-W shear fractures with a right-lateral component of motion and a constant spacing of about 30cm (Fig. 3.4c); they are in accordance with the WNW-ESE shortening Andean direction (Marrett et al., 1994). WNW-ESE left-lateral shear fractures also occur in these deposits. They occur with a low frequency and a length of about 80cm.



Fig. 3.3 – E-W fractures in the strata of Yacoraite Formation in the area of Anta Yaco

Stylolites trending N-S were observed in the strata of Yacoraite Formation (Fig. 3.4d). They occur normal to bedding and are interpreted as contractional structures.

Although the cross cutting relationship are not always consistent, N-S fractures are considered the younger one, because of their occurrence in the younger strata.

3.2.2 Northeast nose of Balboa anticline

Fractures data were collected from this portion of the anticline in the area of Balboa anticline, from the sandstones of Pirgua Subgroup (Fig. 3.2c). In this area, bedding strike rotates from N75°W to N20°W, as a consequence of the shape of the Balboa anticline (Fig. 3.1).

Generic fractures, veins and deformation bands occur in the area. Poles to generic fractures are clustered around two broad maxima corresponding roughly to NNE-SSW and NNW-SSE trends, both in the rotated and unrotated analysis. These fractures are

characterized by an average spacing of 35cm (Fig. 3.5a). Subordinately, N-S generic fractures are also present. These fractures often mutually cross-cut, suggesting that they are essentially coeval.

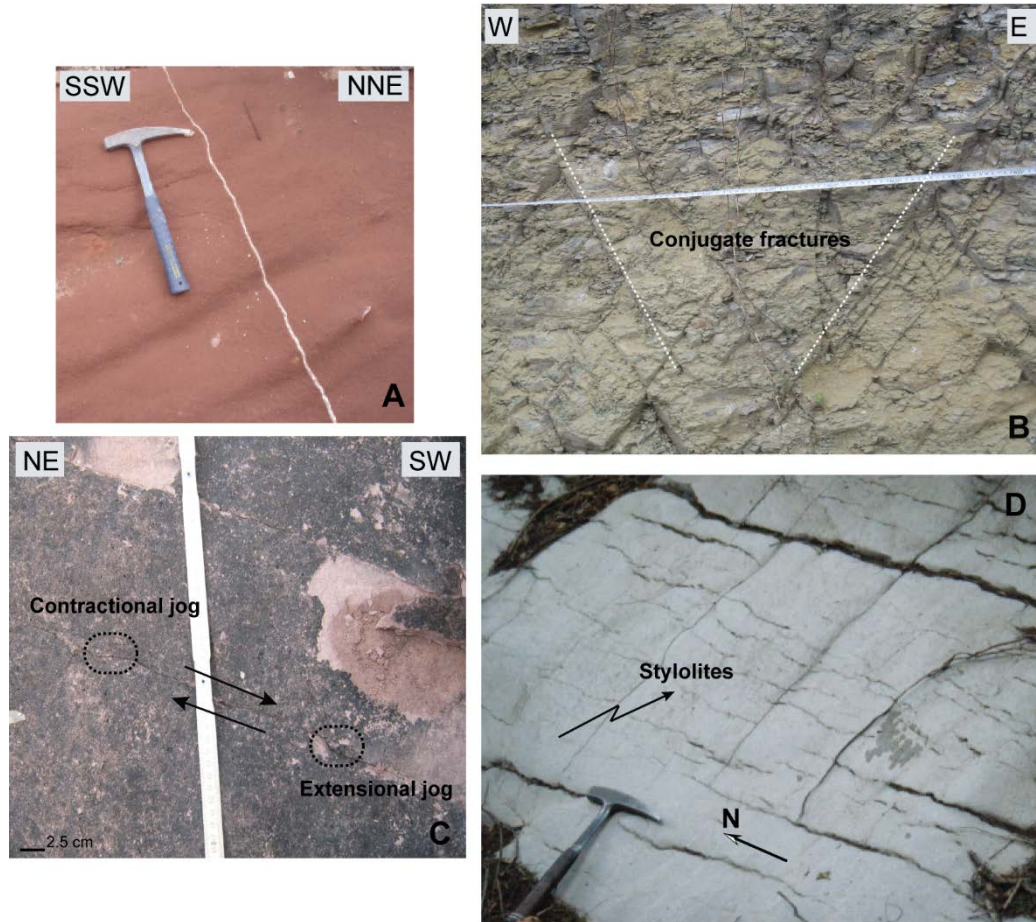


Fig. 3.4 – Examples of the structural discontinuities observed in the field: (a) Calcite-filled vein in the southwestern backlimb of the main anticline (Pirgua Subgroup). (b) Strike-slip conjugate fracture system in the backlimb of the main Sierra de La Candelaria anticline (Anta Formation). (c) Shear fractures in the backlimb of the main anticline (Pirgua Subgroup). (d) Stylolites oriented parallel to the bedding strike in the backlimb of the main anticline (Yacoraite Formation).

NNE-SSW and NNW-SSE calcite-filled veins were also observed with a thickness variable from few millimetres up to 1cm.

In addition, NW-SE and N-S fractures are often characterized by a positive relief with respect to the host rock, suggesting a high resistance to erosion. Their thickness is up to 5mm and the higher compaction observed within, suggests the occurrence of deformation bands (Aydin & Johnson 1978, 1983; Jamison & Stearns 1982; Underhill & Woodcock 1987; Mair et al., 2000; Antonellini et al., 1994; Fossen & Hesthammer 1997; Shipton & Cowie, 2001) (Fig.3.5b).

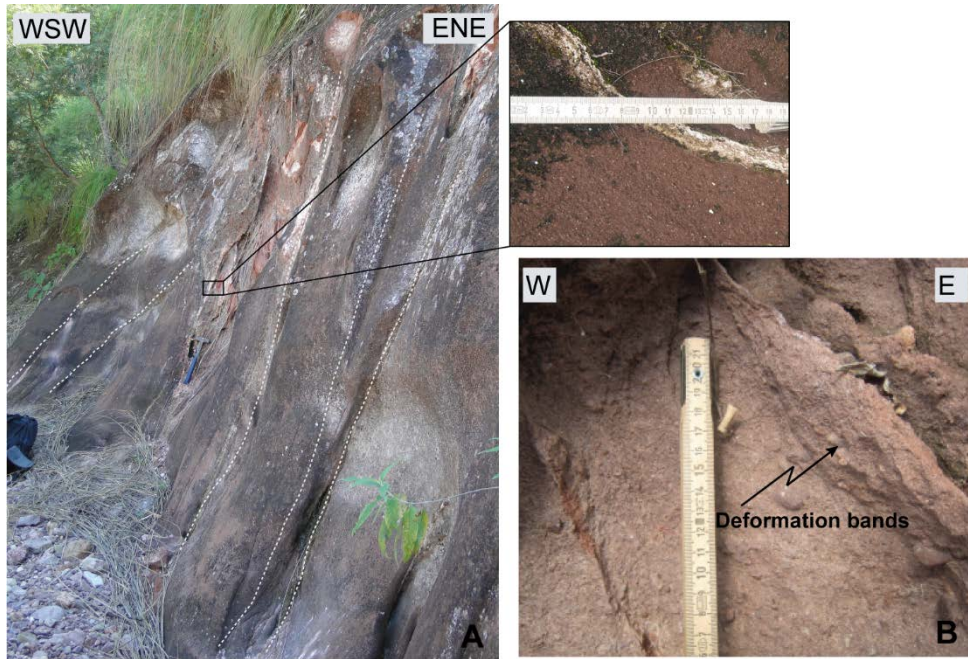


Fig. 3.5 - Examples of structural discontinuities observed in the area of Balboa anticline: (a) NW-SE and NE-SW striking fractures. In the square, a calcite-filled fracture with the same trend. (b) NW-SE deformation bands.

3.2.3 Northern nose of Termas anticline

In the area close to the Hotel Termas, the Anta Formation extensively crops out, and subordinately, Jesús María and Guanaco Formations. In detail, these two younger Formations crop out in the eastern limb of the anticline with a visible unconformity separating them (Fig. 3.6).

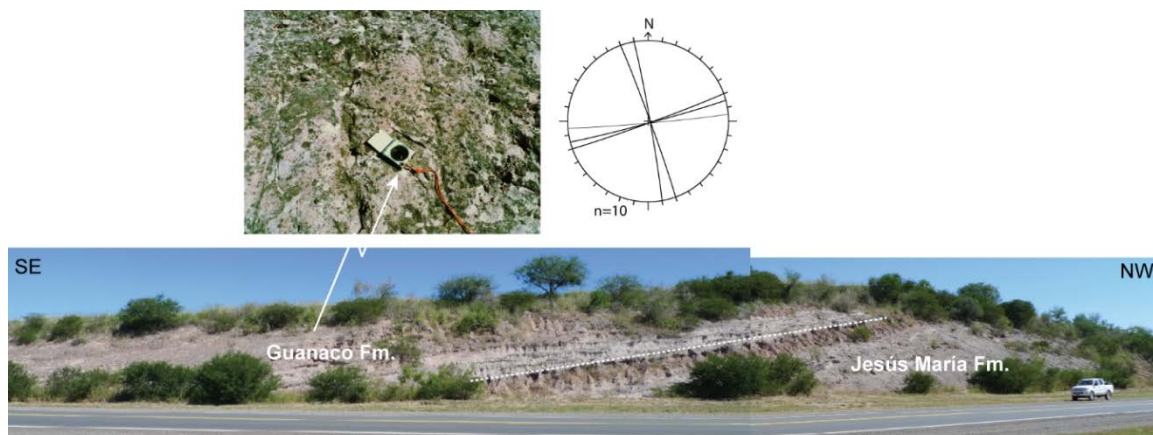


Fig. 3.6 - Guanaco and Jesús María Formations cropping out with a visible unconformity separating them. The stereonet (Schmidt net, lower hemisphere projection) shows the corresponding structural data set collected on the strata of Guanaco Formation.

Brittle deformation is recorded only in the better cemented Guanaco beds that dip 15° to SE. It consists of poorly developed, open fractures striking $N075^\circ E$ and $N015^\circ W$, likely

compatible to the latest strike-slip motion along NNW-SSE lineaments and faults mapped in the Hotel Termas area.

In the same area, the well exposed strata of Anta Formation have different trends (Fig. 3.1). In the backlimb nose of the anticline, bedding strikes ca. N-S, whereas in the forelimb it strikes N030°W, dipping of about 60° in both cases. In the periclinal closure area, bedding strikes from N030°E, with a dip of about 50°, to N060°E with dip decreasing down to 30°. On the base of the qualitative analysis, I recognized on the field generic fractures, shear fractures, faults, gypsum- and calcite-filled veins and deformation bands (Fig. 3.2).

3.2.3.1 Backlimb

In the backlimb nose of the anticline, shear fractures striking NNW-SSE and E-W occur as a strike-slip conjugate system, compatible with the WNW-ESE shortening direction (Fig. 3.7a).

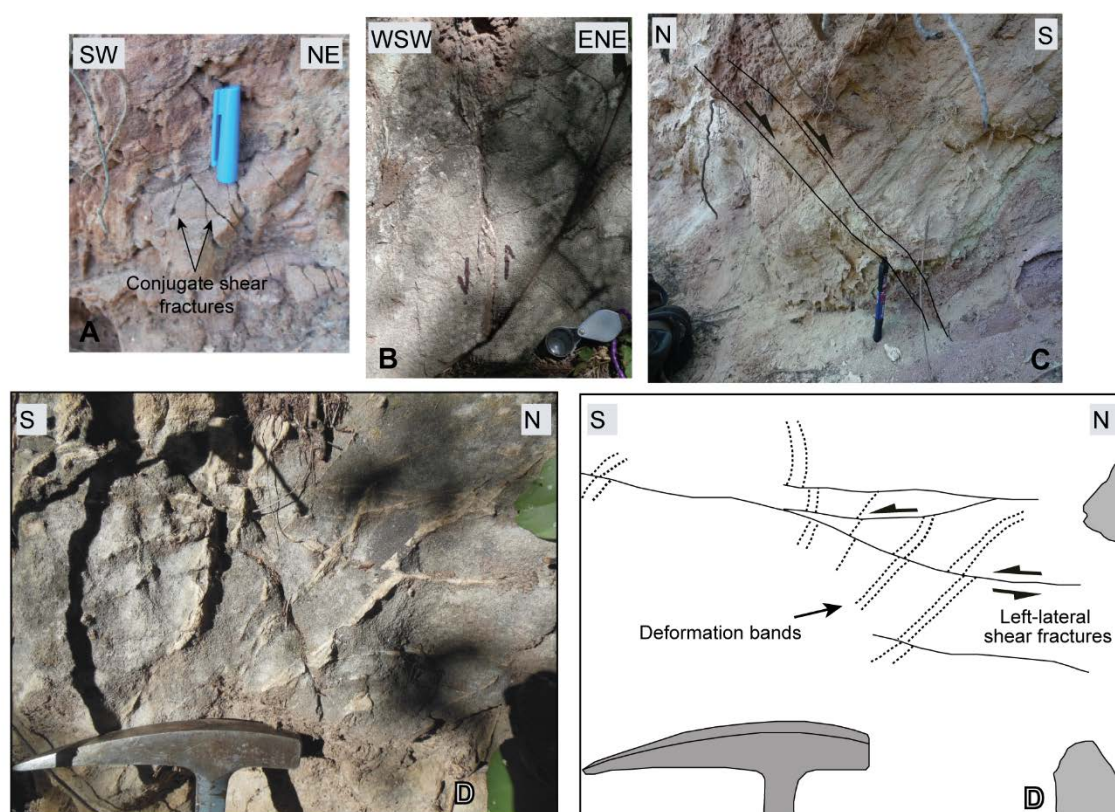


Fig. 3.7 - Examples of structural discontinuities observed in the backlimb of Termas anticline: (a) NNW-SSE and E-W strike-slip conjugate fractures. (b) strike-slip, left-lateral sense of shear on sub-vertical fault plane dipping to 50°. A small pull-apart is formed by extension between the overlapping fault surfaces. (c) Small normal faults dipping 150°. (d) Left-lateral shear fractures.

The occurrence of NNW-SSE left-lateral faults suggests to interpret this association as Type I fracture array of Stearns (1968), indicating a direction of contraction parallel to dip direction of bedding (3.7b). In this interpretation, the Type I fracture set is asymmetrical, because the right-lateral fault system does not occur. ENE-WSW normal fault planes occur in the area (3.7c). In some cases, they show transtensive kinematics with pitch values of about 40°. Northward dipping, E-W striking normal faults and extensional fractures also occur in the area. Slickenlines on fault planes often show the superimposition of a dip-slip motion (slickenlines pitch between 70° and 120°).

A tighter packing of grains was observed in the area within fractures striking NNW-SSE and NE-SW suggesting deformation mechanisms typical of deformation bands. Shear fractures striking WNW-ESE and ENE-WSW cut-off these latter with a left-lateral kinematics (Fig. 3.7d).

In addition, generic fractures are recognized in the area. In their present orientation (i.e. unrotated analysis), the dominant sets strike N-S dipping to the west with angles of 60°. A subordinately set strikes NE-SW dipping at high angle in both directions. No shear or opened mode was observed in the field and the abutting relationship shows as NE-SW fractures post-dates the N-S trending ones.

3.2.3.2 Periclinal closure area

In the periclinal closure area where bedding strikes N60°E, extensional fractures striking NNW-SSE occur with a conjugate system of fractures dipping both to NE and to SW (mutually cross cutting). Therefore, they are interpreted as Type III fracture array of Stearns (1968), with the σ_2 lying parallel to bedding. This interpretation is confirmed by the occurrence of normal faults striking sub-parallel to the fold axis that suggest extension parallel to bedding dip (Fig. 3.8a).

In the area of the Hotel Termas, where bedding strikes N30°E and dips to WNW, a decimetric shear zone occurs. It is composed by a pervasive system of strike-slip fault planes. These fault planes strike N30°W and roughly N-S and they are sub-vertical or highly dipping mainly towards the eastern quadrants. Slickenlines on fault planes have azimuth to N005°. The architecture of the damaged fault zones consists of main shear surfaces and subsidiary Riedel planes striking N50°W with slickenlines striking N20° and N290°. Furthermore, in this shear zone is also present a spaced cleavage folded into Z-shaped folds with steeply plunging axes and asymmetry suggesting a left-lateral motion in

correspondence to the major fault planes (Fig. 3.8b,c,d). Calcite infillings often occur in correspondence to the transtensive WNW-ESE and NNW-SSE fault planes.

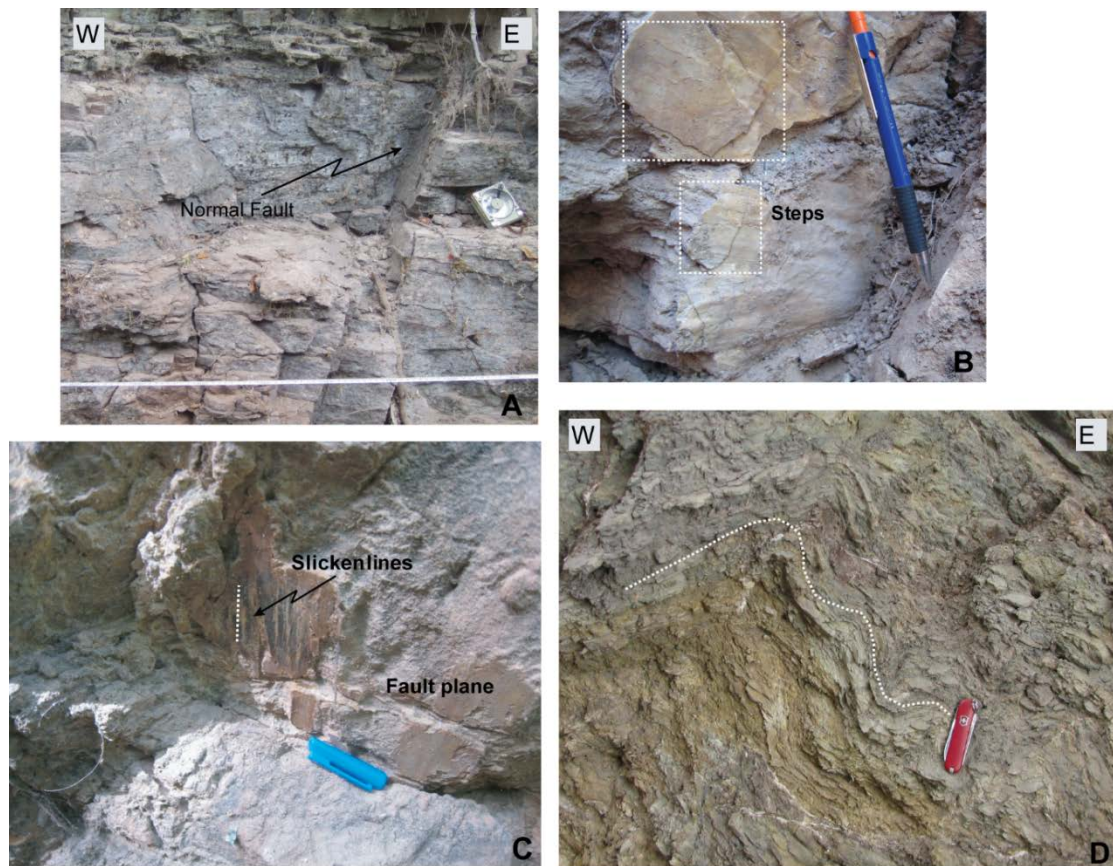


Fig. 3.8 - Examples of structural discontinuities observed in the periclinal closure area of Termas anticline: (a) longitudinal normal fault; (b) Steps on normal fault striking N030°W; (c) Fault plane with slickenlines showing a dip-slip motion in the periclinal closure area; (d) Spaced cleavage folded into Z-shaped folds with steeply plunging axes.

In addition, in this area, in correspondence to the thick pelitic layer that characterized Anta Formation, three families of gypsum-veins occur (Fig. 3.9). They strike NNE-SSW dipping to NW both steeply and gently. Gypsum veins steeply dipping and sub-parallel to bedding are characterized by gypsum crystals both orthogonal and oblique with respect to the fracture walls. Both of these fill types seems to be compatible to shear parallel to bedding, developed during a flexural slip process. The first one, extensional, suggests a first decompression of strata (σ_3 normal to bedding, σ_1 horizontal), related to the first phase of folding, and followed by shear along bedding (flexural slip). A third family of gypsum veins is gently dipping and at high angle to bedding. It is characterized by gypsum crystals oblique of about 30° with respect to the fracture walls indicating a sense of shear

with top to NE. This latter family overprints the other sets and could be related to the final phase of compression (shear planes cutting the fold limbs).

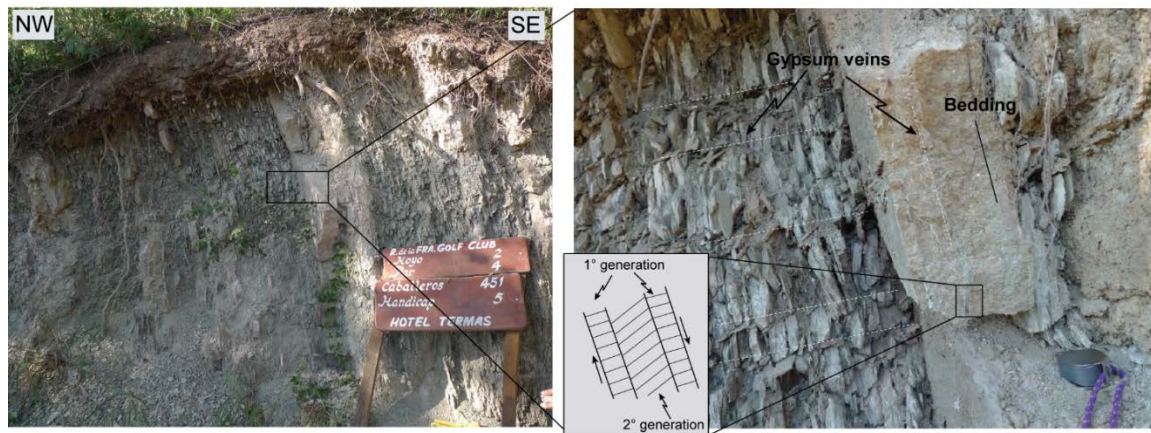


Fig. 3.9 - Three families of gypsum veins in the pelitic layer of Anta Formation (periclinal closure area). In the square, two families sub-parallel to bedding characterized by gypsum crystals orthogonal and oblique with respect to the fracture walls.

Generic fractures are also frequent in the area. Where bedding strikes $N30^{\circ}E$, they occur with a strike WNW-ESE and E-W. They are often open, with an aperture of about 3mm, and often occur in association with gypsum-veins described above; abutting relationship shows that generic fractures striking WNW-ESE cut the system of gypsum-veins (Fig. 3.10).

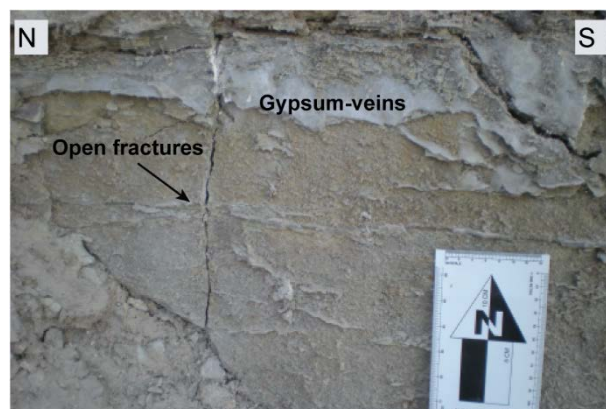


Fig. 3.10 – Open fractures cutting gypsum veins

Generic fractures striking N-S and steeply dipping to both directions represent the most frequent set where bedding strike $N060^{\circ}E$. Even though no open mode was detected in the field, in some cases, the occurrence of calcite-filled veins with the same trend suggests a tensile origin for this fracture set.

3.2.3.3 Forelimb

Generic fractures are organized in this area in three main trends striking E-W (mainly dipping to the south at low angle) and NW-SE (dipping to north-east at a high angle). Subordinately, a N-S fracture trend occurs. It dip to the east at high angle.

Deformation bands striking WNW-ESE and ENE-WSW were recognized in the area. Shear fractures striking WNW-ESE and ENE-WSW occur in the area with a right- and left-lateral kinematics, respectively (Fig. 3.11).

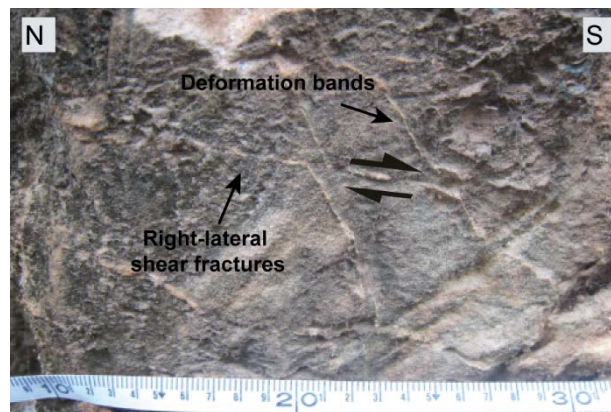


Fig. 3.11 – Shear fractures offset deformation bands with a right-lateral motion

3.3 Structural setting of the Sierra de La Candelaria

Field surveys together with the analyses of the existing maps (Moreno Espelta et al., 1975; Seggiaro et al., 1997; González et al., 2000; Salfity and Monaldi, 2006) and of lineaments and morphostructures identified through satellite data SRTM V2, allowed to better define the structural setting of the Sierra de La Candelaria anticline and to elaborate a revised geological map (Fig. 3.1).

This latter shows the Sierra de La Candelaria as broad anticline elongated in N-S direction for about 55km and with a maximum elevation of about 2,600m a.s.l. Its general trend is N-S but further to the north it turns to a NNW-SSE orientation in the axial plunging of the Hotel Termas area. The eastern limb of the anticline is bounded by a high-angle reverse fault striking N-S with a top-to-the-east sense of transport. The lateral thickness variation (from 400 to 450m) of the syn-rift deposits moving from the area of Anta Yaco to the area of Balboa anticline, allowed to consider it as an inverted Cretaceous normal fault (in agreement with Iaffa et al., 2013). Its oblique trend also suggests a left-lateral strike-slip kinematics component along this fault, compatible with the latest Andean regional WNW-ESE shortening direction (Marrett et al., 1994). This fault plane and a backthrust on the

western limb, striking N-S and dipping to the east, are the main faults responsible of the uplift of the anticline.

Furthermore, the anticline is offset by several minor faults. To the north, the anticline core is truncated by a NNW–SSE trending oblique-slip fault characterized by reverse dip-slip and left-lateral strike-slip components that divides the structure in two anticlines: Termas and Balboa (Moreno Espelta et al., 1975; Seggiaro et al., 1997; Barcelona et al., 2014). In detail, the Balboa anticline, to the east, trends N-S and is characterized by the outcrops of Cretaceous sandstones of the Pirgua subgroup at its core (Fig. 3.1a, b, section A). Whereas the Termas anticline, to the west, trends NNW-SSE. At its core, where Anta Formation crops out, are located the hot springs, close to the thermal complex of the Hotel Termas (Fig. 3.1a, b, section B). A strike-slip component along the NNW-SSE fault that divides the two anticlines is suggested by its geometry, by offset of stratigraphic boundaries, and by kinematic indicators observed in the field.

Furthermore, in the northwestern area, the backlimb is affected by a series of minor NW-SE faults that splay off the NNW-SSE oblique fault in the sense of Riedel shears tending to link to the western backthrust. Despite Seggiaro et al. (1997) interpreted these fault planes as reverse faults, the analyses at the outcrop scale allows me to consider these faults as left-lateral strike-slip faults with a normal component.

Two E-W high-angle faults, dipping both to the north and to the south, border to the south this northern segment of the anticline. A general N-S extension is accommodated along these faults as shown by the offset of stratigraphic boundaries and of the main fault planes. Another E-W normal faults is interpreted to occur in the northernmost portion of the anticline, responsible of the offset of the axial plane of Termas anticline.

Further to the south, along the western fold limb of the regional anticline, a kilometric NE-SW left-lateral strike-slip fault cross cuts the regional anticline (Gonzalez et al., 2000). Furthermore, along its western limb, the anticline is flanked by a NNE-SSW high-angle fault plane. Its southernmost trace was also reported by Gonzalez et al. (2000). Along its trace, the Pliocene alluvial deposits crop out.

The occurrence of this fault has been also highlighted in the northern portion of the anticline, at lower topographic level, by remote sensing analyses (Invernizzi et al., 2014). An offset of this fault could be possible by the occurrence of a NW-SE left-lateral fault plane, also detected by remote sensing analyses.

The latter have been performed with the aim to detect reasonable lineament to constrain the lateral extension of the reservoir for the evaluation of its volume. The analyses allowed

to identify a network of main lineaments (Fig. 3.12) that correspond to the main faults detected in the field and reported on existing geological maps.

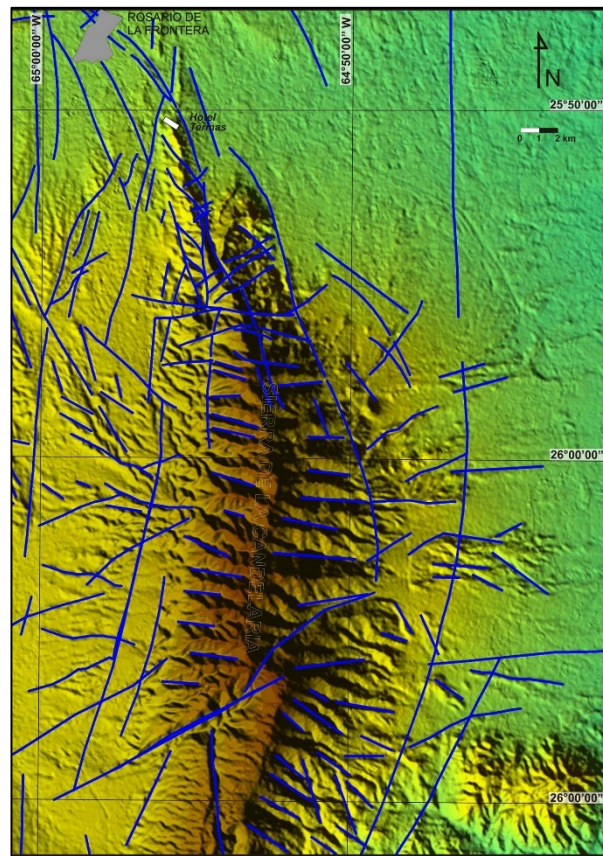


Fig. 3.12 – Structural lineaments detected by qualitative analysis of satellite data (SRTM V2) are drawn on a DEM representation of the studied area and surroundings (from Invernizzi et al., 2014).

Different families of lineaments have been detected: NNE-SSW, represented by continuous lineaments mostly developed in the foothills both to the west and to the east of the Sierra de la Candelaria relief; E-W, WNW-ESE and, subordinately, NW-SE mainly diffused along Sierra de la Candelaria and in the western foothills; NE-SW lineaments concentrated in the northern part and in the middle portion of the Sierra de la Candelaria and both on the western and eastern foothills.

3.4 Tectonic interpretation of the deformation sequence

The kinematic evolution and timing of the studied anticline was deciphered by analyzing (1) the structural relationships with the faults mapped in the area, (2) the geometry of the different stratigraphic units, and (3) the structural data collected at the outcrop scale.

In general, the analysis of the deformation pattern showed that both the attitude and kinematic of most tectonic structures are consistent with two main deformation phases, that can be traced throughout Cretaceous to present day: 1. extension and 2. positive inversion and folding. Data at the outcrop scale allowed refining the timing of deformation of event 2 into early, intermediate and mature sub-stages (Fig. 3.13) (Woodcock and Rickards, 2003). Also the different trending lineaments detected by remote sensing analyses correlate with the recognized deformative events.

Extension due to Cretaceous rifting is recorded by an increase in total thickness (from 400 to 450m) and in beds thickness (from less than 1m up to 5-6m) of the syn-rift deposits (Pirgua Subgroup). Moreover, their clastic facies evolves from mainly arenitic to mainly conglomeratic moving from the area of Anta Yaco to the area of the Balboa anticline. This facies and thickness lateral variation indicates that the area of the Balboa anticline was proximal to a syn-sedimentary normal fault that limited the succession to the east.

This evidence supports the hypothesis that the fault bordering the anticline to the east started as a normal fault during the Cretaceous rifting process and was inverted during the Cenozoic tectonic phase, in agreement with Iaffa et al. (2013) (Fig. 3.13a).

The same high-angle fault may be transpressionally reactivated as an oblique thrust ramp during the thrust system emplacement since it had an oblique trend with respect to the compression direction (i.e. oblique or transpressional inversion; Butler, 1982; Crane, 1987; McClay, 1989; Lacombe & Mouthereau, 2002). Accordingly, it shows a left-lateral strike-slip kinematic component compatible to the latest Andean regional WNW-ESE shortening direction (Marrett et al., 1994). Furthermore, it is responsible of the uplift of the Sierra de La Candelaria structure, deformed in a N-S trending hanging wall anticline (Moreno Espelta et al., 1975; Seggiaro et al., 1997). Accordingly, the Balboa anticline might represent the northern ancient nose of the Sierra de la Candelaria range, in agreement with the reconstruction proposed by Barcelona et al. (2014).

In this early stage of inversion, the deformation is mainly recorded at the outcrop scale by N-S-striking stylolites in the strata of Yacoraite Formation in the southwestern limb of the anticline.

Progressively, the deformation in the hangingwall was accommodated by growing of the regional anticline and activity of a N-S trending backthrust bordering the western limb of the anticline. The latter is likely to be connected at depth to the inverted fault (Fig. 3.13b).

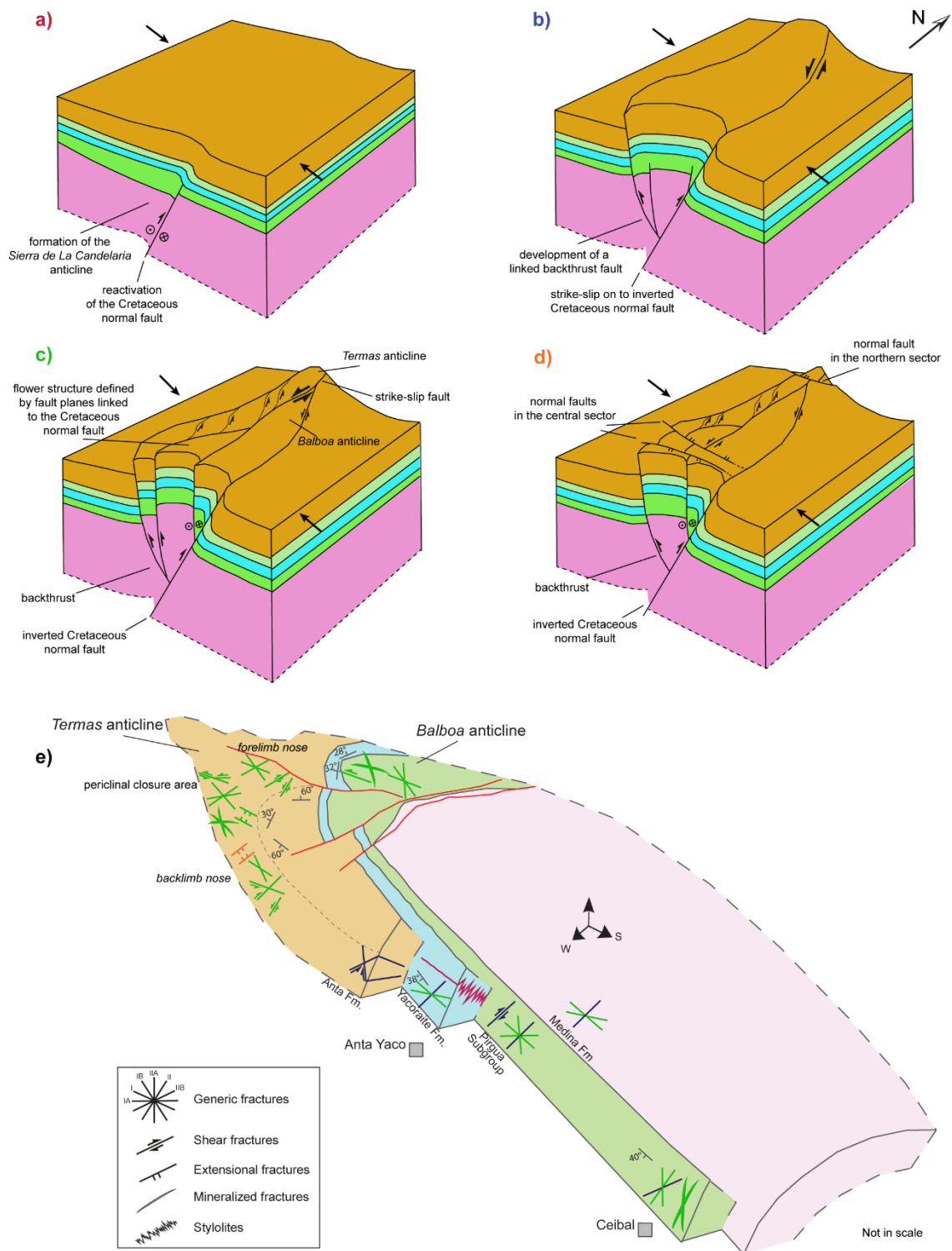


Fig. 3.13 – Schematic interpretation of the kinematic evolution of the Sierra de La Candelaria anticline. It shows the (a, b) early, (c) intermediate and (d) mature stages of the deformation that produced the regional anticline. (e) A scheme of the different mesostructures associated to the early (pink colour), intermediate (blue) and mature deformation stages (green and orange) of the anticline. See text for details.

In the intermediate stage of inversion, the northern portion of the regional anticline was dissected by a NNW-SSE oblique fault plane. It divided the main anticline enhancing the

development of the minor Termas and Balboa anticlines, in agreement with Barcelona et al. (2014). The occurrence of this fault characterized by reverse dip-slip and left-lateral strike-slip components defines a positive flower-like structure with associated minor NW-SE strike-slip faults (Fig. 3.13c).

In the area syn-folding features are represented by:

- Gypsum extensional veins striking NNE-SSW, steeply dipping and at low angle to bedding. They indicate the initial stage of folding under overpressure condition (Shearman et al., 1972; Gustavson et al., 1994; Sibson and Scott, 1998);
- Shear veins in gypsum bearing pelites of Anta Formation. They testify flexural slip on both limbs;
- NNW-SSE and E-W conjugate shear fractures occurring in the backlimb. They are interpreted as Type I fracture array of Stearns (1968);
- N-S-trending joint and calcite filled veins in the periclinal closure area. They record an extension sub-parallel to the fold axis trend;
- NNW-SSE striking conjugate system of extensional fractures recorded in the periclinal closure area. They are interpreted as Type III of Stearns (1968);

Furthermore, different meso-structures testify the strike-slip kinematics along the NNW-SSE oblique fault plane:

- NNW-SSE to N-S left-lateral faults and the associated WNW-ESE Riedel shears occurring in the periclinal closure area and in the backlimb of the anticline;
- NNW-SSE striking deformation bands recorded in the backlimb of the anticline;
- WNW-ESE striking deformation bands and shear fractures with a right-lateral kinematic occurring in the forelimb nose of the anticline;
- NW-SE generic fractures occurring in the backlimb and in the forelimb of the anticline may be also related to this event.

N-S trending fractures in the strata of the Guanaco Formation (Jujuy Subgroup) are compatible to the latest strike-slip motion along NNW-SSE lineaments and faults mapped in the area of the Hotel Termas.

A strike-slip kinematic is also recorded in the strata of Pirgua Subgroup, in the area of Ceibal and in correspondence to the Balboa anticline. In detail, in this latter area, NW-SE and N-S striking deformation bands and N-S, NNW-SSE and NNE-SSW generic fractures testify the occurrence of this kinematics. On the contrary, the left-lateral strike-slip fault trending NE-SW and off-setting the stratigraphic succession in the area of Ceibal, is better

recorded at the outcrop scale from fractures striking NNE-SSW and ENE-WSW. The map view analysis suggests that this fault occurred after fold development. Furthermore, the occurrence of the highest frequency of the fracture sets related to the NE-SW strike-slip fault in the strata of Pirgua Subgroup suggests that this fault was active after the deposition of the units of the Salta Group and before the deposition of Jesús María Formation in which they are not observed. At the same time, the ENE-WSW left-lateral shear fractures occurring along the limbs of Termas anticline are correlable to this deformative event.

Later on, in a mature stage of inversion, in the central and northern portion of the structure, E-W trending normal faults dipping both to the north and to the south dissect main compressive and transpressive deformation (Fig. 3.13d). These faults are interpreted to occur in the final stage of the regional fold growing on the base of cross-cut relationships probably related to the fold plunge. This latter event chronology differs from the reconstruction of Seggiaro et al. (1997) and Iaffa et al. (2013) that consider these faults as passively inherited Cretaceous normal faults. At the outcrop scale, the E-W extensional fractures and the ENE-WSW and E-W normal faults occurring in the strata of Anta Formation in correspondence to the backlimb nose of Termas anticline are interpreted to reflect this final stage of the folding process.

CHAPTER IV

3-D MODEL OF THE RESERVOIR AND FRACTURE MODELLING

4.1 Introduction

The aim of the chapter is to assess the quality of the geothermal reservoir of Rosario de La Frontera system. In order to achieve this goal a fracture modelling was performed inside a 3-D volume of the reservoir deposits. The modelling was based on fracture data collected at the outcrop scale and allowed to estimate the secondary permeability and porosity of the reservoir. Furthermore, an evaluation of its geothermal potential was performed by applying the volume method.

4.2 Methodology

The method followed for the assessment of the studied geothermal reservoir consists of different steps mainly focused on the elaboration of structural data collected at the outcrop scale and on fracture modelling (Fig. 4.1).

Firstly, fieldwork allowed to identify the deposits acting as the reservoir of the thermal fluids. Subsequently, a detailed analyses of structural data collected at the outcrop scale was performed.

Fractures were classified as longitudinal, transverse and oblique with respect to the fold axis trend (e.g. Stearns, 1968; Hancock, 1985; Cooper, 1992; Storti and Salvini, 1996; Hennings et al., 2000; Van Dijk et al., 2000; Tavani et al., 2008; Carminati et al., 2014) and so divided into different sets on the base of their orientation in order to perform the fracture modelling within the reservoir volume.

A frequency distribution of fracture data within the anticline was obtained by the acquisition of spacing data derived from scan-line surveys (Priest and Hudson, 1981; Rouleau & Gale 1985; Priest, 1993; Wu and Pollard, 1995). The method consists of counting the number of fractures per unit length along a sampling line. Spacing values of

fractures belonging to the same set were computed by applying the Terzaghi trigonometric correction, in order to reduce the measurements bias (Terzaghi, 1964). For each scan-line I also measured the attitude (dip-azimuth, dip angle), deformation mode and length of the different fractures in order to provide the main fracture systems parameters subsequently used for the fracture modelling. In addition, owing to the long time required for the acquisition of scan-lines, in several localities fast scan-lines were also performed. They were carried out perpendicularly to each fracture set measuring only the spacing value of fractures. Features of the 15 scan lines and 5 fast scan lines performed are reported in Table 4.1.

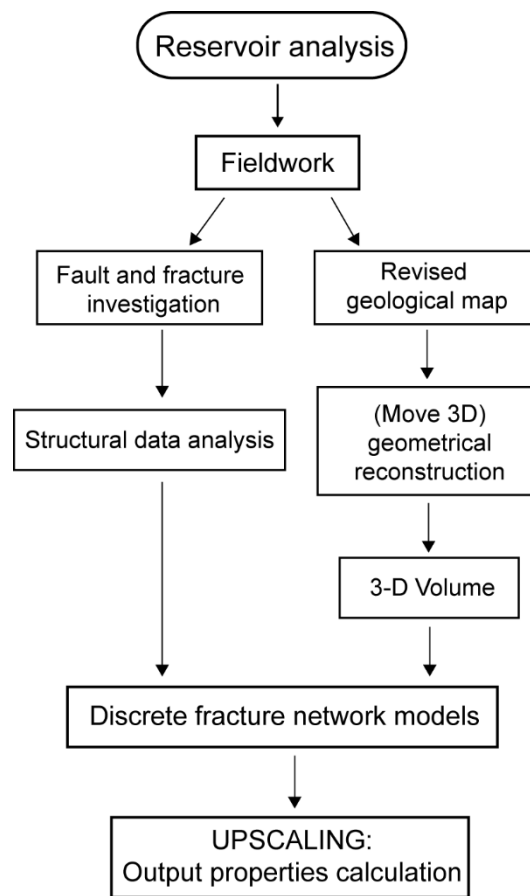


Fig. 4.1 - Flow diagram illustrating the sequential steps followed in order to perform the fracture modelling. Fieldwork and the 3-D software modelling are at the base of the work (see text for detailed explanation).

The next step concerned the construction of a 3-D reservoir geological model representing the tectonic structure. It was elaborated with the software MOVETM (Midland Valley Ltd.). The dataset used as input and constrain for the geometrical model was provided by

computerized data mainly derived from the digitalization of the revised geological map 1:250.000 scale, and control points from field survey (Fig. 4.2).

Table 4.1 - Summary of data for scan lines (SL) and fast scan lines (FSL) carried out on the outcropping reservoir (R) and cap (C) rocks of the geothermal system.

Survey type	Longitude	Latitude	Rock type	Dip direction/dip angle	Length (cm)	Number of data
SL 1	-25,83554	-64,93138	CR	255/15	1000	75
SL 2	-25,83833	-64,93341	CR	330/05	1000	26
SL 3	-25,83650	-64,93487	CR	10/0	750	61
SL 4	-25,83790	-64,93052	CR	30/10	527	17
SL 5	-25,83461	-64,93719	CR	20/0	903	49
SL 6	-25,83854	-64,93333	CR	220/10	500	39
SL 7	-25,99150	-64,91741	R	290/15	490	15
SL 8	-25,98974	-64,91750	R	110/05	600	20
SL 9	-25,99024	-64,91951	R	280/05	1000	30
SL 10	-25,98809	-64,91719	R	340/25	990	20
SL 11	-25,97931	-64,93237	CR	100/10	976	91
SL 12	-25,83884	-64,93100	CR	30/0	452	26
SL 13	-25,89127	-64,87830	R	280/03	770	20
SL 14	-25,88923	-64,87990	R	310/03	1000	35
SL 15	-26,14929	-64,95553	R	150/0	650	40
FSL 1	-25,83790	-64,93389	CR	310/60	200	9
FSL 2	-25,98981	-64,92008	R	170/0	200	14
FSL 3	-25,98804	-64,91776	R	210/50	97	10
FSL 4	-25,88990	-64,88186	R	74/0	96	16
FSL 5	-25,90636	-64,87943	R	100/0	63	11

2D geological data (stratigraphic boundaries, structural elements, attitudes) and a DEM (Digital Elevation Model) of the area provided a 3-D dataset as starting point for the 3-D elaboration. In order to reconstruct an accurate structural model of the deep reservoir, I built twenty-six geological cross-sections, across the Sierra de La Candelaria anticline, oriented normal (2500 m spaced) and parallel to the fold axes trend (Fig. 4.3).

The 3D reconstruction of the main geological surfaces (top and bottom of target reservoir, faults and thrust planes) allowed the built of the reservoir volume, subsequently converted into a GeoCellular volume. This latter consists of regular, defined size, grid-like cells that can be converted into equivalent properties (such as porosity and permeability) on the base of the fracture modelling performed through the upscaling process.

The fracture modelling process was based on the elaboration of field data in order to generate the DFN model in the 3-D volume of the geothermal reservoir.

Furthermore, an evaluation of the geothermal potential of the reservoir was performed by applying the volume method (Muffler and Cataldi, 1978).

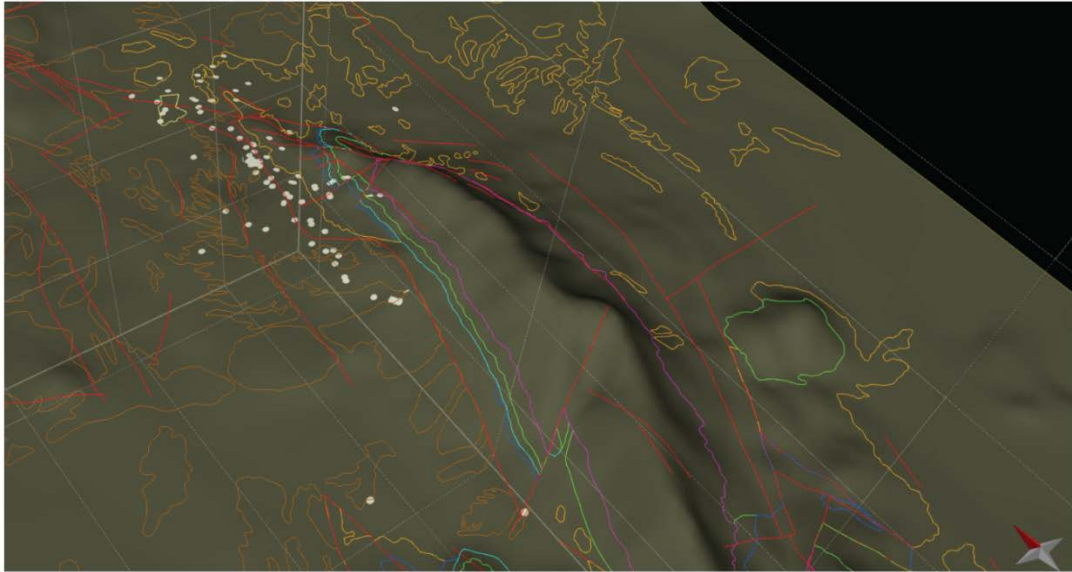


Fig. 4.2 – Dataset used as input for the 3D reservoir model. Color lines and white circles represent the digitized stratigraphic boundaries and the dip data, respectively.

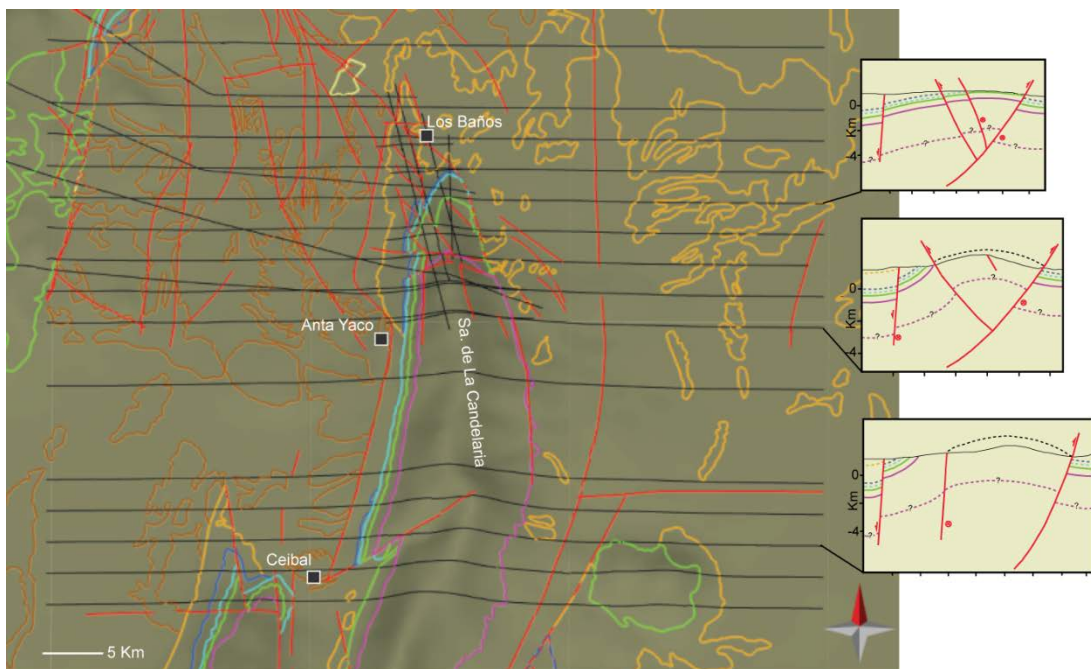


Fig. 4.3 – Traces of the geological cross sections (black lines) and map used to construct the three-dimensional structural model. In the grey panels some examples of geological cross sections. Continuous green and pink lines represent top and bottom of the Pirgua Subgroup deposits, respectively. They were used to build the reservoir volume.

4.3 Lithological components of the geothermal system

Fieldwork observations allowed to establish the role played by the main lithological groups in the geothermal system and so to identify the deposits acting as the reservoir and cap-rock of the studied geothermal system.

The main lithotypes of the Medina Formation (phyllites with low permeability) and the presence of healed fractures allowed to consider it as the impermeable basement of the geothermal system (Fig. 4.4a).



Fig. 4.4 – Outcrops of the studied rocks. (a) Precambrian laminated phyllites of the Medina Formation. (b) Cretaceous sandstones of the syn-rift Pirgua Subgroup. (c) Conglomeratic facies of the Pirgua Subgroup deposits. (d) Limestones outcrops belonging to the late Cretaceous-early Paleocene Yacoraite Formation. (e) Interbedded black shales in the Yacoraite Formation. (f) Miocene Anta beds characterized by very fine grained sandstones, siltstones, and mudstones.

On the contrary, the syn-rift deposits of the Pirgua Subgroup, mainly represented by sandstones and conglomerates, were considered to represent the main thermal fluid

reservoir of the geothermal system (Fig. 4.4b, c). These observations are in agreement with Seggiaro et al. (1995) and Moreno Espelta et al. (1975). Furthermore, laboratory test measures performed on sandstone hand sample collected from Arroyo Bonete Puca high valley by Invernizzi et al. (2014) provided a density value of 2.24 g/cc, a total porosity of 7.2%, and a mean permeability value of 81.2 mDarcy (min =24.1 mD, max =137.1 mD).

To the top, the Balbuena Subgroup is mainly represented by the high-energy limestones belonging to Yacoraite Formation (Fig. 4.4d). They consist of medium- to coarse-grained oolitic grainstone with spherical sparitic oolites and oolitic packstone. Interbedded black shales were also observed (Fig. 4.4e). The low value of frequency and aperture of the fracture system allowed me to consider it as a low permeability deposit probably acting as a cap-rock of the geothermal system. From a regional point of view, some of the units composing the Santa Barbara Subgroup and the Orán Group show a prevalence of marly and clay rich thick horizons; although fractured, they maintain low permeability since fractures often show clayey, gypsum and calcite filling. Thus, these units behave as the main cap-rock of the geothermal system (Fig. 4.4f).

4.4 3-D reservoir model

The accurate reconstruction in a 3-D view of the reservoir deposits allowed to highlight the shape and the trend of the Sierra de La Candelaria anticline (Fig. 4.5).

In detail, the anticline is characterized by a gently dipping forelimb (30°) and a steeply westward dipping backlimb (60°). Its general trend is N-S but further to the north it turns to a NNW-SSE orientation in the axial plunging of the Hotel Termas area.

In a 3-D reconstruction, I propose a possible confinement of the reservoir continuity at depth, in particular on the western side of the main anticline, calculating a minimum conservative volume of the reservoir's deposits. It is delimited to the east by the main high-angle thrust fault that borders the anticline on the eastern side. To the north, it is confined by the E-W normal fault plane dipping to the north, and to the west by a continuous lineament, almost N-S oriented, well visible on remote sensing images. To the south, the reservoir is confined by the outcrops of Pirgua subgroup and by the NE-SW strike-slip fault occurring in the Ceibal area.

In the present reconstruction, it can be assumed that the Cretaceous sandstones, that form the main geothermal reservoir, consist of a single and continuous hydrogeothermal body with an estimated volume of about 53km³ and a mean thickness of about 450m. The

maximum depths reached by the top and bottom surfaces of Pirgua subgroup are 2000m and 2500m, respectively. They are calculated in the northern sector of the anticline and along its western margin.

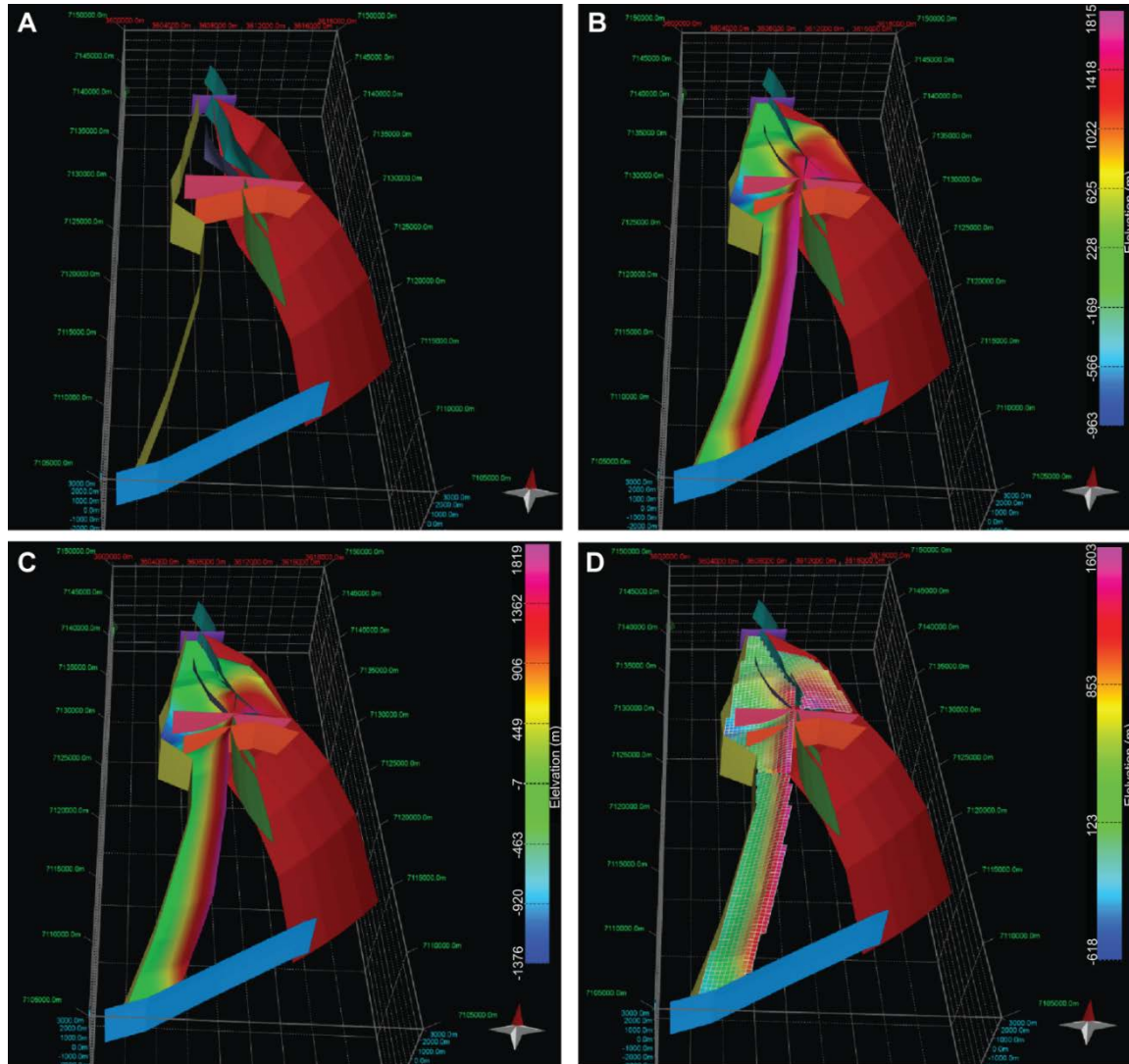


Fig. 4.5 – Three-dimensional displays showing (a) the main interpreted fault planes, the contoured surface representing the top (b) and the bottom (c) of the reservoir, and (d) the geocellular volume of the reservoir. The 3-D volume represents the buried portion of the *Pirgua* Subgroup, whereas no volume was considered for its outcropping portion.

4.5 Reservoir discrete fracture network model

The process of the DFN generation for the geothermal reservoir of the system of Rosario de La Frontera was performed by using the Fracture Modelling module within the commercial MOVE™ software package from Midland Valley Exploration Ltd.

The modelling consists of a multi-step process: first, fracture sets are identified, then fracture parameters (size and intensity) are calculated for each fracture sets on the base of

field observations. The discrete fracture network can thus be generated: fractures are firstly reproduced as planar surfaces that have the same geometrical parameters as the ones described in the field and then, throughout the upscaling process, they are converted into fractures properties such as porosity and permeability. Like many other commercial packages used to generate DFN models, MOVETM is designed for tight rocks (negligible matrix porosity/permeability), where porosity and permeability are provided only by the fractures. Therefore, the software assigns null values of porosity/permeability to those portions of the volume that are not crosscut by any structure (i.e. the host rock). It then computes the porosity/permeability of a given cell on the base of its fractured volume.

4.5.1 Fracture data elaboration

In the present modelling, fracture dataset was divided into six sets on the base of orientation data. They were grouped into longitudinal (set I), transverse (sets II) and oblique (IA, IB, IIA and IIB) with respect to the fold axis.

In order to perform the fracture modelling in the reconstructed reservoir volume, the used software requires some initial input parameters for each fracture set concerning the fracture intensity, the mean orientation, and the fracture-size with the corresponding statistical distribution (length, length over height and opening). The input parameters have been calculated for each fracture set from the scan-lines surveys carried out on the outcrops of the reservoir rocks. In the area of the Termas anticline, where the reservoir does not outcrop, I considered the fracture data collected from the strata of Anta Formation to model the fracture network in the buried portion of the reservoir.

Furthermore, in order to evaluate the frequency variability of each fracture set along the anticline, scan-line surveys were performed in four different portions of the studied anticline characterized by different deformation intensity: Balboa and Termas anticlines, Anta Yaco and Ceibal areas (see paragraph 3.2 for details). To represent this in the DFN model, I divided the entire volume in four different small volumes representing these areas of the anticline.

Figure 4.6 shows in detail the variation of the fracture frequency (number of fractures per meter) of each set across the anticline.

Therefore, the performed DFN model represents the merge of twenty-four stochastic DFN models generated for each fracture set recognized in the different portions of the anticline.

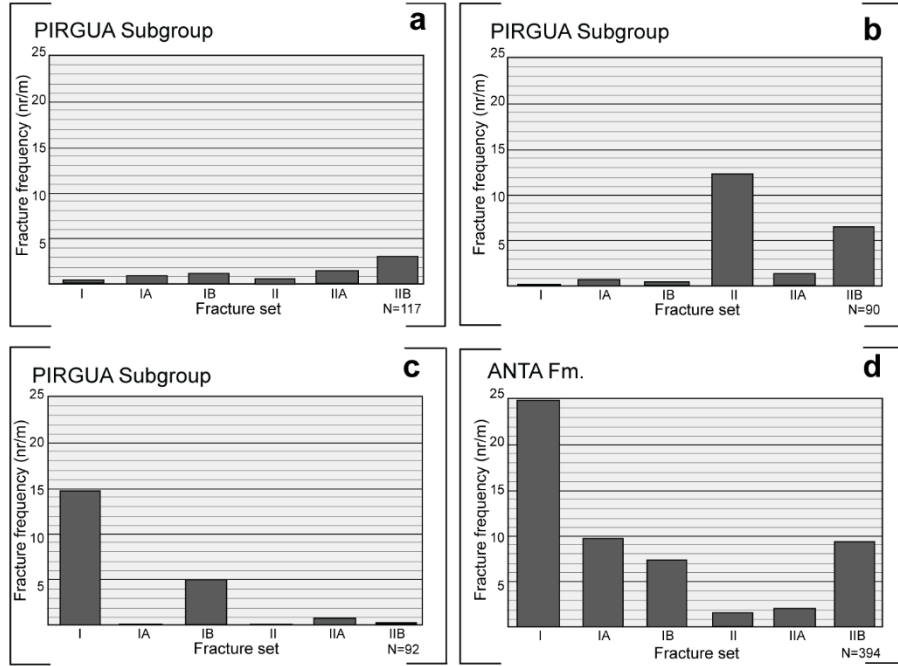


Fig. 4.6 - Histograms showing the fracture frequency values for each fracture set computed for the reservoir and cap-rock in the (a) Anta Yaco and (b) Ceibal areas, (c) Balboa and (d) Termas anticlines. Fracture frequency values are calculated from the number of fractures per unit length of scan-line measured during this specific survey for each fracture set and corrected by Terzaghi for removing sampling bias.

Table 4.2 shows the different parameters used to elaborate the fracture modelling. Input parameters and the methodologies to obtain them are described and detailed in the following sub-sections.

4.5.1.1 Type and orientation

The orientation of the fractures was analysed constructing rose diagrams for fractures azimuth for groups of scan-lines carried out in the same area. Six groups of fractures were compiled (Fig. 4.7).

In detail:

- Set I includes $N30^{\circ}W \pm 10^{\circ}$ fractures, striking sub-parallel to the fold axis;
- Set IA and Set IB include fractures striking $N60^{\circ}W \pm 10^{\circ}$ and $N-S \pm 10^{\circ}$, respectively;
- Set II includes fractures striking $N60^{\circ}E \pm 10^{\circ}$, transverse to the fold axis;
- Set IIA and Set IIB includes fractures striking $N30^{\circ}E \pm 10^{\circ}$ and $E-W \pm 10^{\circ}$, respectively.

The stereo plot tool integrated in MOVETM provided the mean orientation and the standard deviation of each fracture set and the Fisher K parameter used to define if a data cloud is clustered or not (Table 4.2) (Fisher et al., 1987).

Table 4.2 - Parameters calculated for the six fracture sets in the four measurement areas of the anticline. Length values were obtained from outcrop analyses, whereas the mean and standard deviation parameters by distribution analysis performed with EasyFit. All fractures sets show a normal distribution except for fracture set II in the area of Balboa anticline that show a constant distribution. An up-scale of the mean values was necessary in order to perform the fracture modelling. Mean Principal Plane includes the average values of dip and dip direction obtained with the Fisher method implemented in Move 2013 (Midland Valley).

<i>Anta Yaco area</i>						
	Set I	Set IA	Set IB	Set II	Set IIA	Set IIB
P 32	0.53	1.07	1.27	0.86	1.78	3.00
Aperture (mm)	0.50	0.65	0.77	0.59	0.50	0.53
Mean Lenght (m) - Std. dev. (m)	0.57-0.19	0.79-0.50	0.82-0.84	0.67-0.37	0.55-0.32	0.50-0.27
Mean Principal Plane (°)	65/61	67/27	88/94	72/329	72/296	75/172
Fisher Dispersion (K value)	18.25	18.00	17.83	33.54	27.36	37.51
<i>Ceibal area</i>						
	Set I	Set IA	Set IB	Set II	Set IIA	Set IIB
P 32	0.27	0.71	0.35	12.31	1.54	6.46
Aperture (mm)	0.50	0.80	0.10	1.00	0.79	0.55
Mean Lenght (m) - Std. dev. (m)	0.57-0.19	1.19-0.65	0.38-0.02	1.76-1.31	0.70-0.16	0.43-0.18
Mean Principal Plane (°)	79/240	72/205	77/280	80/150	88/309	78/179
Fisher Dispersion (K value)	83.29	158.58	109.30	51.43	81.45	26
<i>Balboa anticline</i>						
	Set I	Set IA	Set IB	Set II	Set IIA	Set IIB
P 32	14.96	0.27	5.16	0.06	1.00	0.22
Aperture (mm)	0.84	0.72	0.79	0.35	0.89	0.59
Mean Lenght (m) - Std. dev. (m)	1.22-0.85	0.82-0.47	1.17-0.67	0.33	1.08-0.91	0.79-0.34
Mean Principal Plane (°)	76/239	55/210	73/260	65/150	80/120	72/171
Fisher Dispersion (K value)	42.00	65.47	46.56	-	45.55	34.70
<i>Termas anticline</i>						
	Set I	Set IA	Set IB	Set II	Set IIA	Set IIB
P 32	24.99	9.79	7.11	1.83	2.03	9.19
Aperture (mm)	0.70	0.69	0.79	0.56	0.74	0.57
Mean Lenght (m) - Std. dev. (m)	0.80-0.45	0.85-0.55	0.94-0.67	0.55-0.22	0.72-0.31	0.61-0.28
Mean Principal Plane (°)	77/241	61/210	66/260	68/329	75/120	73/171
Fisher Dispersion (K value)	62.65	64.37	46.56	35.00	45.55	34.70

Table 4.3 shows the fractures types included in each set, the deformation event and the stage of the positive inversion related to their formation. The reconstruction of the deformation sequence of the anticline described in detail in paragraph 3.4 is at the base of this distinction.

In detail, in the different areas of the anticline (Anta Yaco and Ceibal areas, and Balboa anticline) where the reservoir crops out, a shear displacement was recognized only along fractures belonging to the set IIB. They are interpreted as syn-folding features since their trend and sense of motion is in accordance with the direction of regional shortening. The

other fracture sets are defined as generic fractures since no deformation mode was recognized along these fractures in the field. Anyway, their trend parallel to the main fault planes and lineaments mapped along the anticline allowed to consider them as post-folding features (Figs. 3.1, 3.12).

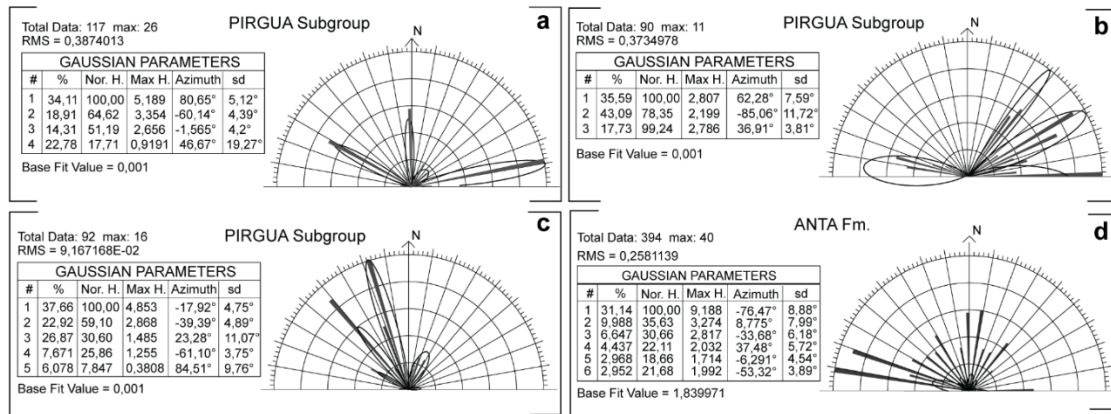


Fig. 4.7 - Cumulative polymodal Gaussian distribution statistics as obtained from the structural dataset collected in the (a) Anta Yaco and (b) Ceibal areas, (c) Balboa and (d) Termas anticlines. Fracture data are shown as rose diagram for azimuth, but they are not weighted by abundance because most data were acquired along scan-lines. Consequently the number of fractures per-set that cross-cuts the scan-line traces is controlled by the trend of the fractures with respect to the scan-line trace.

In the area of Termas anticline, a shear displacement was better recognized along fractures belonging to sets I, IA and IIB. The analyses of the fractures network allowed to highlight their relation with the folding process or the strike-slip event that took place during the late transpressive tectonic regime along the NNW-SSE fault plane that gave rise to the formation of the Termas anticline. The strike-slip event is better represented by fractures belonging to sets I and IA. Fractures belonging to the same sets together with fracture set IIB record the folding process. Differently, fracture sets IB, II and IIA are classified as generic fractures and interpreted to occur after the transpressive event.

In the different analysed areas of the regional anticline, veins and deformation bands were not included in the fracture modelling since they are interpreted to reduce the reservoir permeability acting as barriers to flow (reservoir type 4 of Nelson, 1992). Likewise, extensional fractures characterizing the outcrops of Anta Formation in correspondence of Termas anticline were not considered during modelling because extrados features.

4.5.1.2 Intensity

Fracture intensity represents the amount of fractures per measure unit. It can be expressed by the number of fractures per volume (parameter P30), the fracture length per volume

(P31), or the fracture area per volume (P32) (Dershowitz and Herda, 1992). In particular, the software used during this modelling generates DFN models using two of these intensity parameters, the P30 and P32 values.

Table 4.3 – The table shows the fractures types of each set. Fractures were defined as generic fractures when no deformation mode was recognized in the field. Intermediate and late stages of the positive inversion are based on the kinematic model of the anticline described in detail in the paragraph 3.4 and schematized in figure 3.13.

<i>Anta Yaco area</i>						
	Set I	Set IA	Set IB	Set II	Set IIA	Set IIB
<i>Fracture Type</i>	Generic fractures	Generic fractures	Generic fractures	Generic fractures	Generic fractures	Shear fractures
<i>Deformation event</i>	Post-folding	Post-folding	Post-folding	Post-folding	Post-folding	Folding
<i>Stage of the positive inversion</i>	Late	Late	Late	Late	Late	Intermediate
<i>Ceibal area</i>						
	Set I	Set IA	Set IB	Set II	Set IIA	Set IIB
<i>Fracture Type</i>	Generic fractures	Generic fractures	Generic fractures	Generic fractures	Generic fractures	Generic fractures
<i>Deformation event</i>	Post-folding	Post-folding	Post-folding	Post-folding	Post-folding	Folding
<i>Stage of the positive inversion</i>	Late	Late	Late	Late	Late	Intermediate
<i>Balboa anticline</i>						
	Set I	Set IA	Set IB	Set II	Set IIA	Set IIB
<i>Fracture Type</i>	Generic fractures	Generic fractures	Generic fractures	Generic fractures	Generic fractures	Generic fractures
<i>Deformation event</i>	Post-folding	Post-folding	Post-folding	Post-folding	Post-folding	Folding
<i>Stage of the positive inversion</i>	Late	Late	Late	Late	Late	Intermediate
<i>Termas anticline</i>						
	Set I	Set IA	Set IB	Set II	Set IIA	Set IIB
<i>Fracture Type</i>	Shear fractures	Shear fractures	Generic fractures	Generic fractures	Generic fractures	Shear fractures
<i>Deformation event</i>	Folding; Strike-slip	Folding; Strike-slip	Post-transpression	Post-transpression	Post-transpression	Folding
<i>Stage of the positive inversion</i>	Late	Late	Late	Late	Late	Late

In the present modelling, I have used the P32 intensity parameter calculated from the number of fractures per length of scan-line measured during the fieldwork for each fracture set (Table 4.2). Fracture frequency value, in fact, derived from scan-lines surveys (P10 parameter) and corrected by Terzaghi for removing sampling bias, can be used as roughly equivalent to the 3D fracture intensity (m^2/m^3) (Priest, 2004; Barthélémy et al. 2009; Zeeb et al., 2013).

Terzaghi's correction method was employed as a weighting function to evaluate the degree of underestimation of each orientation family per scan-line. This weighting function approximates the number of fractures that a scan-line carried out perpendicularly to the fracture set would have intersected elaborating an estimate of the true fracture density, as opposed to the observed one. Orientation bias, in fact, is caused by fractures that intersect the scan-line at oblique angles. Thus, an apparent distance, or spacing, is measured between two adjacent fractures, which cause an underestimation of fracture frequency. Accordingly, a typical correction method for this orientation bias is the Terzaghi correction (Terzaghi, 1964; Priest, 1993), where the apparent distance (S_A) is corrected by the cosine of the acute angle θ of the fracture normal and the scan-line to obtain the true spacing (S):

$$S = S_A \times \cos\theta \quad (1)$$

Linear fracture intensity (P10), which is also commonly referred to as fracture frequency, is equal to $1/S$.

In three dimensions, $\cos \theta$ is given by (Hudson and Priest, 1983):

$$\cos\theta_i = \cos(\alpha - \alpha_i)\cos\beta\cos\beta_i + \sin\beta\sin\beta_i \quad (2)$$

where α and β are the dip direction and dip of the scan-line, and α_i and β_i are the dip direction and dip of the i th fracture set normal (Fig. 4.8).

The scan-line sampling method estimates the linear fracture intensity P10. A relationship between linear (P10) and volumetric (P32) fracture intensities (Table 2) is provided by Barthélemy et al. (2009):

$$P10 = P32 \times e[\cos(\theta)] \quad (3)$$

where $e[\cos(\theta)]$ is the expected mean of the cosines of angles θ for the fractures of one set. For a

scan-line parallel to the normal of a fracture set, $e[\cos(\theta)]$ equals 1, thus the relationship between

linear (P10), areal (P21), and volumetric (P32) fracture intensities is given by:

$$P10 = P21 = P32 \quad (4)$$

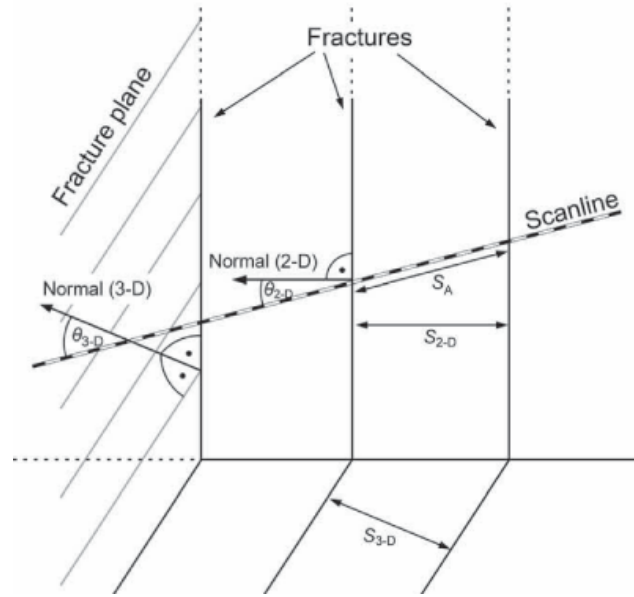


Fig. 4.8 - Sketch illustrating the variables required to calculate the Terzaghi correction (equation 1). S_A is the apparent spacing measured along a scanline, S_{2-D} is the true spacing between two fracture traces, and S_{3-D} is the true spacing between two fracture planes. θ_{2-D} and θ_{3-D} are the angles between the normal to a fracture trace or a fracture plane, respectively, and a scan-line (from Zeeb et al., 2013).

4.5.1.3 Size (height, length and aperture)

The parameters requested by the software concerning fracture size are the length distribution, the aspect ratio and the aperture.

The height values of the fractures were acquired in the field. The aspect ratio height/length was kept as recommended in the software tutorial 1:2, as bedding thickness commonly restricts fracture height, allowing fractures to have a longer length relative to their height.

Regarding fractures length, the stochastic distribution of length in the model requires a statistical function which describes the distribution of fracture length data. The latter were analysed by using the software *EasyFit*. The results show that the analysed data are explicated by a normal (or Gaussian) distribution expressed by:

$$F(x, \mu, \sigma) = \frac{1}{\sigma\sqrt{2\pi}} e^{-(x-\mu)^2/(2\sigma^2)} \quad (5)$$

where μ is the mean value and σ is the standard deviation (π is a constant = 3.14159, and e is a constant = 2.71828). These values are required by the software in order to apply the normal statistical distribution.

The last parameter requested by the software to complete the modelling phase is the aperture value of each fracture set. It represents an important parameter as it has a large influence on the calculated permeability of the model by the “cubic law” (Louis, 1969;

Kranz et al., 1979; Tsang and Witherspoon, 1981; Fetter, 1993). In fact, according to the so-called parallel plate model (Snow, 1965; Witherspoon et al., 1980) the flow rate along a fracture is related to the cube of the aperture and thus permeability K_j of a single fracture is given by:

$$K_j = \frac{(Ha)^2}{12} \quad (6)$$

where Ha represents the hydraulic aperture of the fracture.

Because the permeability of deformation bands can be one or more orders of magnitude less than the matrix permeability (e.g. Antonellini and Aydin, 1994; Aydin, 2000; Fisher and Knipe, 2001; Sternolf et al., 2004), and permeability of other structural discontinuities, depending on their aperture, can be several orders of magnitude greater than matrix permeability, the combined effect of these structures on subsurface flow can be complex and substantial. For this reason, I did not included in the fracture modelling the deformation bands recognized in the outcrops of Pírgua and Anta Formations in the area of Balboa and Termas anticline.

Unfortunately, no direct aperture data were available and so for the other fracture types I have considered the aperture value proportional to the trace length of fractures based on the non-linear, square root power-law distribution between aperture and length, proposed by Olson (2003):

$$D_{max} = \alpha L^{0.5} \quad (7)$$

where D_{max} is the maximum (shearing) displacement along the fault/fracture, L the length and α a proportionality coefficient:

$$\alpha = \frac{K_{Ic}(1-\nu)^2 \sqrt{8}}{E \sqrt{\pi}} \quad (8)$$

including the fracture toughness K_{Ic} , Poison's ratio ν , and Young's modulus E , all material specific constants of the host rock.

4.5.2 Problems in data modelling

In the present modelling particular attention has been devoted to the computation of the secondary permeability related to the fracture systems that affect the studied geothermal reservoir previously modelled in three-dimensions. Different problems have been encountered during modelling mainly related to the capacity of the used software to model the fracture systems into a large volume of reservoir combining outcrop and reservoir scales.

One of the critical issue in fracture modelling and in the description of the equivalent continuum medium of a fractured/faulted system is the choice of the cell size that is needed for the discretization of the numerical model (Antonellini et al., 2014). Obviously, a small cell size may allow describing with accuracy the geologic and structural characteristics of the reservoir but it will require a long computation time and some problems in terms of system memory limitations during generation of the fracture system and the subsequent conversion into hydraulic properties. On the other hand, a large cell size will keep down the computation time but it will limit the structural and lithologic detail that can be represented.

Also fracture data length and density highly affect the capacity of the modelling software to generate fractures (Bigi et al., 2014). In particular, the generation of fractures with low values of length (as values computed at the outcrop scale), requires a long computation time by the software and can create problems of system memory since the software may generate a high number of fractures. This problem occurs especially when fracture modelling may be performed in a large reservoir volume, due to the dimension of the model with respect to the scale of the outcrop observations.

With the aim to avoid these issues, during this work several attempts have been performed by modifying cell size and up-/down scaling length of fractures, in order to combine the size of the model and the software capability.

Regarding cells size, they were originated with a side of 300 m.

Unfortunately, MOVETM is not able to avoid the issues due to the use of data (fracture length) obtained at the outcrop scale. Therefore, I performed the present modelling by applying an up-scale of the mean value of fractures lengths of two orders of magnitude (from 1 to 100 m) for analysing them at the reservoir scale (10-1000 m) since it is demonstrated that the statistic distribution of this parameter is scale independent (Barton and Larsen, 1985; La Pointe, 1988; Barton and Hsieh, 1989; Babadagli et al., 2001; Van Dijk, 2000; Marchegiani et al., 2006). The statistic distribution was kept “normal” as indicated by the analyses of values collected at the outcrop scale. Published case histories have revealed that many faults and fractures trace length distribution covering several orders of magnitude, show Power-Law trends (Walsh & Watterson 1988; Gillespie et al. 1992; Crovelli and Barton, 1995; Barton, 1995; Schlische et al., 1996; Cello, 1997; Cowie 1998; Cowie & Roberts 2001; Tondi & Cello 2003; Van Dijk et al., 2000; Marchegiani et al., 2006). Nevertheless, the application of this type of distribution in the present modelling

have not been possible since it led to the generation of a high number of small fractures and so to a software memory problems.

From a general point of view, a critical issue in performing fracture modelling is the decrease in permeability with depth due to changing in the stress state and to the increase of temperature.

The depth dependence of permeability can be expressed by Black's equation (1987):

$$k = az^{-b} \quad (9)$$

where a and b are constant and z is the vertical depth below ground surface. These constant can be derived from experimental analyses.

A decrease in permeability with depth is generally observed (see Singhal & Gupta, 1999 for a review) since it leads to the reduction in fracture aperture, but there is not much justification of such a universal rule. Site specific studies are necessary in order to establish the stress in situ. Stress being a directional phenomenon, its state determines the relative permeability of different fracture sets in a rock mass. Fractures parallel to the maximum stress tend to be open, whereas those perpendicular to it tend to be closed. The effect of stress on permeability of jointed rocks also depends on the direction of stress in relation to joint orientation.

On the other hand, an increase in temperature can cause a volumetric expansion of the rock material leading to reduction in fracture aperture and an overall decrease in rock permeability. Temperature changes can also cause precipitation and dissolution of minerals thereby affecting rock permeabilities. Changes in temperature may also change the effective stress in the rock mass.

The modelling software cannot take into account these permeability variations with depth as both temperature and stress state are complex issues to be addressed. A quantitative approach to include them would request specific laboratory investigations on surface and subsurface samples and in bore holes to measure representative parameters for a more advanced evaluation of reservoir properties.

4.5.3 Results

The performed fracture modelling allowed to calculate the fractured volume affecting the reservoir.

It results of 0,012Km³ (Fig. 4.9; Table 4.4).

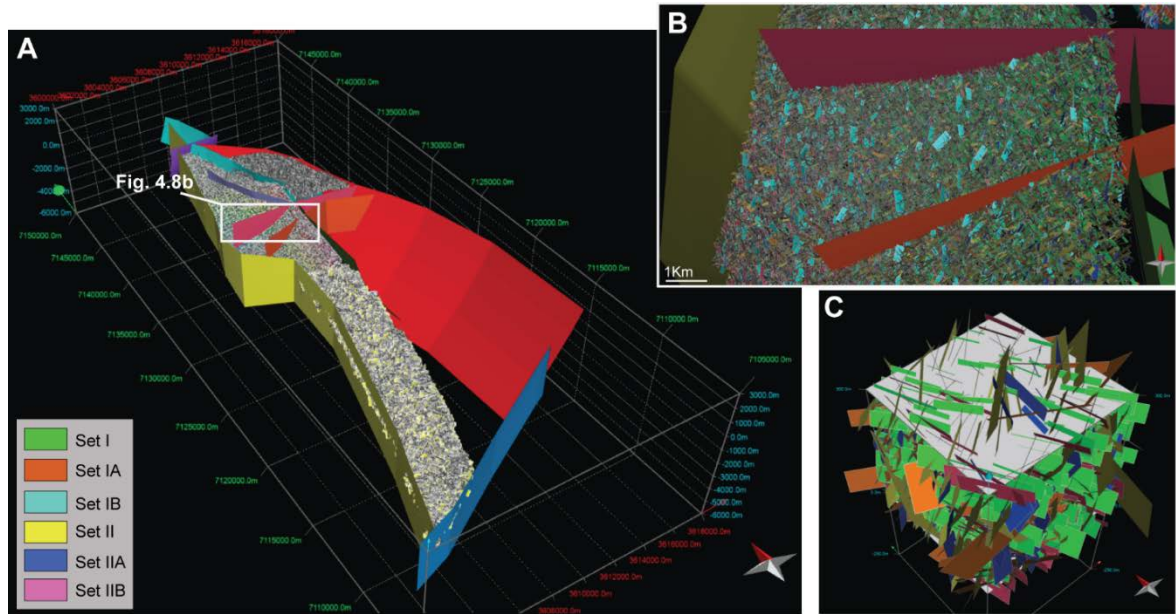


Fig. 4.9 - (a) Three-dimensional fracture model reconstructed inside the geocellular volume of the reservoir. (b) Detail of the 3-D fracture model shown in panel a. (c) Top view of the grid cell illustrating the trend of the six main sets of fractures.

In detail, the DFNs show that Termas anticline represents the most fractured area of Sierra de la Candelaria ridge (Table 4.4). There, the intensive brittle deformation testifies the folding process and the strike-slip kinematics due to the transpressive event along the NNW-SSE fault plane. Accordingly, fracture sets I (NNW-SSE), IA (WNW-ESE), IB (N-S) and IIB (E-W) very affect the fractured volume as they are the most frequent fracture sets.

The brittle deformation is less intensive in the other portions of the ridge. In particular, the Anta Yaco area represents the less fractured area where fracturing mainly records the folding process happened in the early stage of the positive inversion. Accordingly, fractures set IIB (E-W) represents the most frequent fracture set in this area. On the contrary, the fracture volume is mainly related to the fracture sets II (ENE-WSW) and IIB (E-W) in the Ceibal area and to the fracture sets I (NNW-SSE) and IB (N-S) in correspondence of the Balboa anticline. Their relation with the faults mapped in these areas suggest that the associate deformation took place after the folding process.

4.6 DFN upscaling

The upscaling process converts the Discrete Fracture Network model to equivalent continuum medium of the required properties formed by cubic cells distributed over a grid. For each grid cell, a permeability tensor based on the DFNs was computed using the

geometric methodology proposed by Oda (1985). The calculation of the permeability tensor that the fracture modelling module performs is therefore geometric, and done on the base of all fracture fragments that belong to each cell in the GeoCellular volume. Therefore, the contribution to the permeability of each fracture depends on the clipped fracture polygon area, the aperture dimension, and the orientation of the fracture. Furthermore, the software calculates the secondary porosity as the ratio of total fracture volume in a cell per cell volume.

Table 4.4 – The table shows the fracture volume in the different areas of the Sierra de La Candelaria anticline. For each area is also reported the range of secondary permeability value in the different directions (i.e. “xx”, “yy”, “xy”, “xz”, “yz”, “zz”) and the average fracture porosity.

Site	Secondary Permeability (mD)						Secondary Porosity	Fracture volume (Km ³)
	Kxx	Kyy	Kzz	Kxy	Kxz	Kyz		
<i>Anta Yaco</i>	0.58/1.0 0	0.62/1.19	0.87/1.49	0.03/0.17	0.06/0.2 8	0.02/0.0 9	4.8E-05	8.2E-04
<i>Ceibal</i>	5.51/9.0 5	4.81/8.56	11.44/19.3 5	6.77/11.99	1.23/2.3 4	0.72/1.6 0	1.9E-04	1.6E-03
<i>Balboa anticline</i>	1.54/4.0 9	3.96/10.16	4.61/12.09	1.30/4.05	0.91/2.4 5	0.49/1.4 0	1.7E-04	1.3E-03
<i>Termas anticline</i>	15.61/1 9.49	11.01/14.0 7	14.24/17.7 8	3.78/4.92	2.75/3.6 8	2.26/2.8 9	4.2E-04	8.5E-03

Table 4.4 shows the values of the secondary porosity and permeability computed by the software for the twenty-four DFNs performed in the four modelled areas of Sierra de La Candelaria anticline. The results obtained comparing the hydraulic behaviour of each zone show permeability and porosity variations among them; in the case of permeability, variations are also shown in the different directions (i.e. “xx”, “yy”, “xy”, “xz”, “yz”, “zz”).

In detail, the highest values of porosity and permeability occur in correspondence to the Termas and Balboa anticlines and in the area of Ceibal, where fractures are characterized by the highest values of frequency. In particular, permeability is highest in the direction parallel to the strike of the main fault planes (“yy”). These values are until 13 times higher (~14 mD) than the one of the Anta Yaco area (~1 mD). Highest values are also found along the “xx” direction in correspondence to the Termas anticline, probably related to the high frequency of fracture set IIB.

In the vertical direction “zz” parallel to the dip of the main fracture systems, all areas show the highest permeability values. Differently, the lowest permeability values occur along the horizontal and vertical oblique direction to the faults strike (“xy”, “xz” and “yz”).

4.7 Geothermal potential

The performed fracture modelling highlights the role played by the fracture network on the permeability of the geothermal reservoir of Rosario de La Frontera system. The results show that even though fracture network enhances the reservoir permeability, its primary one probably plays the most important role in the storage and circulation of fluids since secondary permeability values are very low. On this base, a more detailed evaluation of the potential of the studied reservoir was performed by applying the volume method (e.g. Cataldi et al., 1978). This method uses estimates of subsurface temperature, volume, specific heat and density to calculate the accessible resource base, multiplying the resultant value by a recovery factor to get the recoverable thermal energy.

Particular attention was devoted to the northern portion of the regional anticline. I considered this area as the most interesting one for a potential exploitation of the thermal fluids, since here temperatures at surface are higher than the ones occurring in the Ceibal area and reservoir reaches the maximum depths. Accordingly, a new calculation of the reservoir volume excluding the southern portion was necessary. It was computed on the base of the 3D model reconstructed with the aid of the software MoveTM (see paragraph 4.4). The reservoir is delimited by the outcrops of Pirgua subgroup in the area of the Balboa anticline, to the south, and by a NW-SE structural lineament to the south-west (Invernizzi et al., 2014). The computed volume is of 28 Km³ with a fracture volume of 0,001Km³ (see paragraph 4.5.3).

Furthermore, I considered the volume where fluid temperature exceeds 60°C as an interesting reservoir volume for geothermal purposes, at least for the direct use of heat (Bono, 1981).

Considering a 40°C/km geothermal gradient (as suggested by Seggiaro et al., 1995), and a surface temperature of 20°C (Invernizzi et al., 2014), the meteoric water can reach 60°C at 1000m depth and can exceed temperatures of 100°C at the base of the reservoir located deeper than 2000m. On the base of some geothermometers, Chiodi et al. (2015) suggested an average temperature of about 115°C within the system.

On this base, a reservoir volume below the depth of 1000m was considered for the evaluation of the geothermal potential. It was computed by the 3D model of the reservoir reconstructed with the aid of the software MoveTM (see paragraph 4.4). The boundary of the reservoir portion below the 1000m of depth allowed to estimate 4.35Km³ of interesting volume (Fig. 4.10).

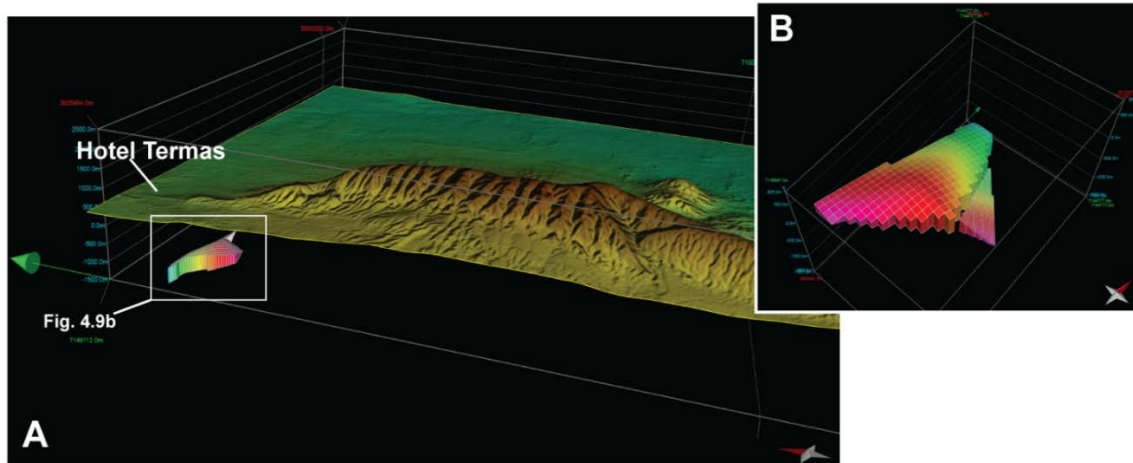


Fig. 4.10 - (a) The portion of the reservoir volume below the depth of 1000 m under the topographic surface. (b) Top view of the geo-cellular volume.

The application of the volume method (Muffler and Cataldi, 1978) for the calculation of the geothermal potential at Rosario de la Frontera allows to the following equation:

$$E = E_r + E_f = [(1 - \phi) \rho_r c_r V (T - T_o)] + [(\phi) \rho_f c_f V (T - T_o)], \quad (10)$$

where E_r is the heat stored in the solid rocks and E_f in the fluid phase.

Given a total volume for the reservoir of $4.350.000.000 \text{ m}^3$, a rock density of 2200 kg/m^3 for the Pirgua reservoir (ρ_r) with an average porosity of 0.07 (ϕ) (Invernizzi et al., 2014), 1000 J/kg K for the rock specific heat (c_r), 4200 J/kg K for water specific heat (c_f), an average T of $115 \text{ }^\circ\text{C}$ in the reservoir (Chiodi et al., 2015) and a T of $20 \text{ }^\circ\text{C}$ as air temperature (Invernizzi et al., 2014), I obtained the following results:

$$E_r = 3.3 \cdot 10^{18} \text{ J}$$

$$E_f = 4.7 \cdot 10^{17} \text{ J}$$

$$E = 3.8 \cdot 10^{18} \text{ J}$$

A recovery factor, R_f , defined as the ratio of the extractable geothermal heat, E_e , and the total geothermal heat stored in a given volume, E , allows to evaluate the extractable geothermal heat (Bono, 1981; Bodvarsson, 1974; Nathenson, 1975):

$$R_f = E_e/E \quad (11)$$

After a review of heat extraction from geothermal systems, Muffler and Cataldi (1978) proposed that in liquid-dominated geothermal systems, R_f may attain the maximum theoretical value of 0.5 , assuming that the reservoir has an effective porosity of 20% ; a

more realistic estimate, based on world-wide experience, is that R_f varies between 0.05 and 0.15 (e.g., Garg and Combs, 2010; Sanyal and Sarmiento, 2005).

Since the low value of primary porosity for the reservoir deposits measured by Invernizzi et al. (2014), I propose an R_f value of 0.05, obtaining an extractable geothermal heat value of:

$$E_e = 1.89 \cdot 10^{17} \text{ J}$$

CHAPTER V

EVALUATION OF THE CAP-ROCK EFFECTIVENESS

5.1 Introduction

In this chapter, the focus is on the assessment of the quality of the cap-rock of Rosario de La Frontera geothermal system by evaluating its degree of thermal alteration.

In order to accomplish this goal, cap rock was sampled in correspondence to:

- poorly fractured outcrops far away and close to the hot springs (respectively at distances higher and lower than one km from the Hotel Termas);
- intensely fractured outcrops close to the hot springs, affected by brittle deformation related to later stages of deformation (high angle faults dissecting the main fold).

X-ray diffraction of clay minerals, organic matter optical analysis and fluid inclusions microthermometry on vein fillings allowed unraveling the thermal evolution of the couple reservoir + cap rock of the geothermal system with the aid of 1D thermal modelling. The comparison between features and distribution of fractures and thermal indicators allowed to define the role played by hot fluids circulation onto thermal alteration of the cap-rock.

5.2 Methods and materials

Methods described in this section have been directly used to derive information about the thermal evolution of studied sedimentary succession.

Adopted analytical inorganic and organic thermal indicators are:

- stacking order and illite content in mixed layers illite-smectite observed in <2µm grain-size fraction of sediments, coupled with XRD patterns on whole rock to preliminary characterize the mineralogical assemblages;
- mean vitrinite reflectance of organic matter dispersed in sediments;
- homogenization temperatures (Th), melting temperatures (Tm) from fluid inclusions, coupled with petrographic characterisation.

In addition, preliminary thermal models performed by means of 1-D Basin-mod (Platte River, 1996) software were calibrated against the new dataset of organic and inorganic thermal indicators to devise scenarios of temperature distribution and evolution as a function of time and depth.

In this thesis, a suite of 22 samples was collected from Sierra de La Candelaria anticline (Fig. 5.1).

In detail, samples for XRD and organic matter investigations derive from the main cap-rocks of the geothermal system (6 samples from Balbuena and 16 from Metán Subgroup). They were collected along the anticline in correspondence to both poorly fractured outcrops recording mainly the folding process, and to the intensely fractured outcrops recording both the folding process and the strike-slip kinematics related to the late transpressive deformation that took place along the NNW-SSE fault plane (Table 5.1). One sample for XRD analyses was collected from the geothermal reservoir (Pirgua Subgroup). Samples for fluid inclusions analyses come from calcite and gypsum syn-tectonic veins developed at various stages during the tectonic evolution of the studied area since Miocene times.

5.2.1 Optical study of organic matter dispersed in sediments for thermal evolution of sedimentary basins

5.2.1.1 Generalities

The organic matter (OM) dispersed in sediments is composed of a mixture of organic compounds of various origin and composition. Aquatic organisms contribute mainly proteins, lipids and carbohydrates; higher plants contribute resins, waxes, lignins and carbohydrates in the form of cellulose (Barnes et al., 1990).

In the starting phases of sediment burial, the OM sustains irreversible physical and chemical variations that are extremely sensitive to temperature changes concerning the re-organization of carbon-hydrogen bonds. These transformations will produce an organic macromolecule called kerogen that progressively will convert into hydrocarbons with increasing burial and temperature.

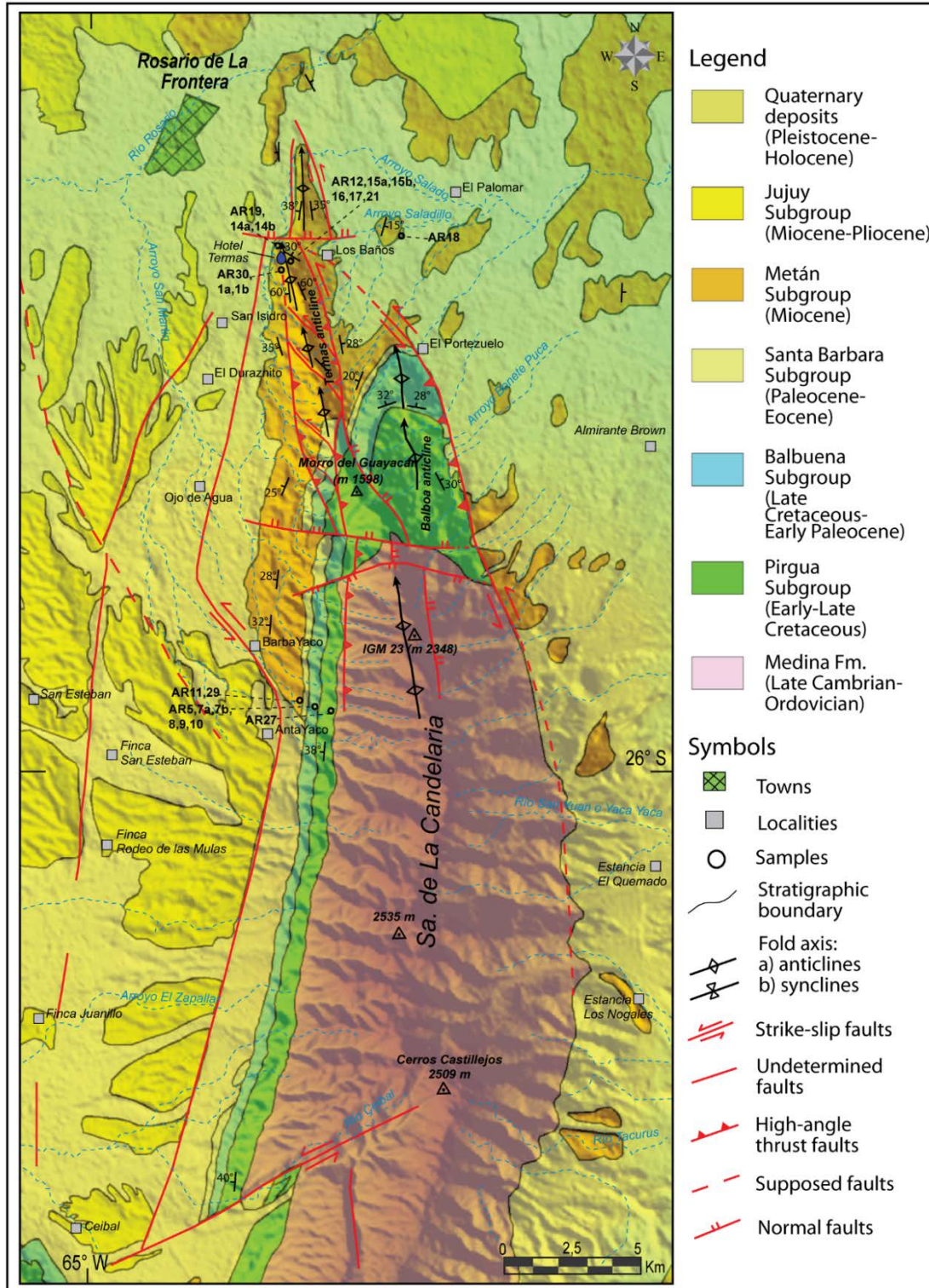


Fig. 5.1 – Geological map of Sierra de La Candelaria anticline. Black rounds indicate the sample sites.

Kerogens are commonly characterized by the use of bulk parameters, such as the H/C and O/C atomic ratios, obtained from elemental analyses (Fig. 5.2).

On the basis of these ratios, four types of kerogen have been defined which appear to follow distinct diagenetic pathways. This division of kerogen in four types has been

supported by another independent scheme of classification using transmitted-light microscopy, so that kerogen types are defined by the morphologies of the kerogen particles called macerals.

Type I kerogen has high initial H/C and low O/C ratios. The source material is mainly algal, or a combination of algal lipids and waxes from higher plants. It forms part of the liptinite macerals in coal (Fig. 5.3).

Type II kerogen has intermediate initial H/C and O/C ratios, and larger contributions by aromatic and carboxylic acid groups than the type I kerogens. Ester bonds are abundant, as are medium-length aliphatic hydrocarbon chains and naphthenic rings. Both algal and higher plant sources appear to contribute to type II kerogens (liptinite macerals).

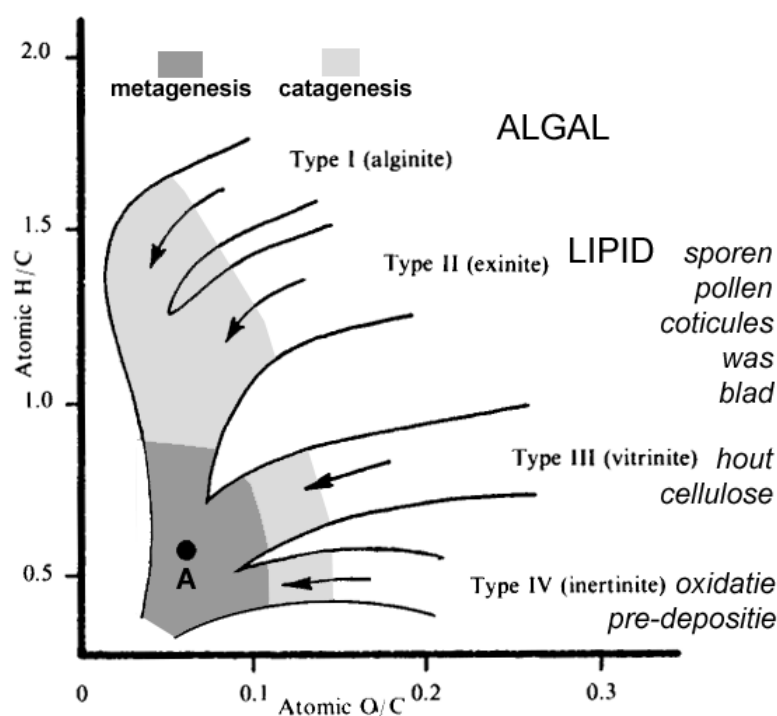


Fig. 5.2 - Van Krevelen diagram showing maturation pathways for Types I to IV kerogen as traced by changes in atomic H/C and O/C ratios. The progressively darker shaded areas approximately represent diagenesis, catagenesis, and metagenesis stages, respectively (from http://www.falw.vu/~rondeel/grondstof/oil/oil-total-web.html#_Toc531067567).

Type III kerogen has an initial H/C ratio less than 1, an initial O/C ratio of 0.2 to 0.3, and is derived dominantly from terrestrial plants. It consists mainly of aromatic groups formed from lignins and humic compounds, and represents the huminite/vitrinite fractions of coal petrography. Oxygen is present as carboxylic acids, ketones and ethers rather than in ester bonds.

Type IV kerogen has the H/C ratio less than 0.5 and contains mostly decomposed organic matter and highly oxidized material of various origins and represents the inertinite group.

With increasing maturity, kerogen loses first preferentially O to produce CO₂ and H₂O, then H to produce hydrocarbons. Changes in the molecular structure have effect in the petrographic appearance of the vitrinite macerals with a strong increase of their capacity to reflect light.

Reflectance of vitrinite is one of the most commonly used indicators of thermal maturity and is correlated to the stages of hydrocarbon generation and other thermal parameters in sedimentary environments (Hunt, 1986; Scotti, 2003; Fig. 5.4).

Thus, it is one of the most widely used parameter to calibrate basin modelling (Dow, 1977; Mukhopadhyay, 1994). The method relies on the presence of the huminite-vitrinite maceral group that is derived from cellulose, lignin and tannins in OM from terrestrial woody plants.

<i>Kerogen Type (according to IFF)</i>	<i>Principal biomass</i>	<i>Environment (general)</i>	<i>Original Hydrogen Index</i>	<i>Sulphur incorporation</i>	<i>Hydrocarbons generated and expelled (1)</i>
Type I	algae, bacteria	tectonic non-marine basin	> 700	low	oils
Type II	marine algae, bacteria	marine	400-700	moderate	oils
Type II S (sulphur rich)	marine algae, bacteria	marine, carbonatic environment	400-700	high	oils
Type III “H”	spores, pollens, cuticles, resin, lignin, bacteria	fluvial-lacustrine, coastal plains	300-600	low	waxy oils
Type III	lignin	coastal plains, deltaic, turbiditic	50-250	low	gas and light oils (gas traces when HI < 100)
Type IV	lignin	coastal plains, deltaic	< 50	low	none

(1) Also depending by kerogen maturity level.

Fig. 5.3 – The main kerogen types from Scotti (2003).

5.2.1.2 Thermal maturity parameters used in this Thesis

5.2.1.2.1 Vitrinite Reflectance

Mean vitrinite reflectance (VRO%) is measured as the percentage of the incident light intensity which is reflected from the polished surface of vitrinite macerals fragments relative to a standard substance (e.g glass, sapphire, etc.). This measurement uses

immersion oil and is related to the refractive index and absorptive index of immersion oil and standards which follows the Fresnel-Beer equation:

$$R_o = (\mu - \mu_o)^2 + \mu^2 k^2 / (\mu + \mu_o)^2 + \mu^2 k_o^2$$

where:

μ , μ_o = refractive index of vitrinite and immersion oil, respectively;

k , k_o = absorption index of vitrinite and immersion oil, respectively.

These indexes are wavelength dependent, thus a green monochromatic non-polarised light ($\lambda = 526 \text{ nm}$) is chosen for $R_o\%$ measurements.

Maturation rank		Paleo Temp. (1) (°C)	Microscopic parameters					Chemical parameters						
Kerogen	Coal		Vitrinite Reflectance (Ro %)	TAI (2)	SCI (2)	CAI	Fluorescence of alginite	T _{max}	Biomarker Isomerization Sterane Hopane		Hydrocarbon main product			
Immature	Peat	50	0.2	1 Yellow	1	1 Yellow	Blue-green	420		0,10	Bacterial gas			
	Lignite		0.3				Greenish-yellow							
	Sub-bituminous Coal		0.4				Golden yellow							
Mature	Bituminous Coal	100	0.5 – 0.55	2 Orange	3	2 Light brown	Dull yellow	430	0,10 0,50	0,50	Immature heavy oil (3)			
Very Mature			0.7											
High Maturity			0.8											
Overmature			1.0				3 Brown					6	3 Brown	Orange
			1.35											Red
Organic Methamorphisme	Semi Anthracite	150	1.5	4 Brown/Black	7	4 Dark brown	Nonfluorescent	465	None	None	Wet gas			
	Anthracite	2.0	200					2.5				9	5 Black	500
		3.0												
	Meta Anthracite	250	4.0	5 Black	10	5 Black		None			Dry gas			
			5.0											

(1) Depending by duration

(2) International standard is not available - a lot of correlation scales are present in literature.

(3) Depending also by kerogen type

(1) Depending by duration

(2) International standard is not available - a lot of correlation scales are present in literature

(3) Depending also by kerogen type

Fig. 5.4 - Correlation chart among the most important organic maturity parameters from Scotti (2003).

In diagenesis and in the first stages of catagenesis ($R_o\% < 1.5$), vitrinite is optically isotropic and the aromatic clusters present in the organic structure have no preferred orientations. In metagenesis instead, vitrinite behaves like an anisotropic material because of the orientation of aromatic clusters (Oberlin et al., 1980). When tectonic stress affects the thermal maturity of sediments, vitrinite macerals can turn out to be biaxial (Levine and Davis, 1989).

The indigenous vitrinite fragments are generally more abundant than altered or reworked woody material and show a gaussian distribution (see histogram of Fig. 5.4). In the example of figure 5.5, where reflectance step are 0.05%, mean vitrinite reflectance derives from the

arithmetic mean of the indigenous vitrinite population (in orange), and standard deviation is calculated on these fragments alone.

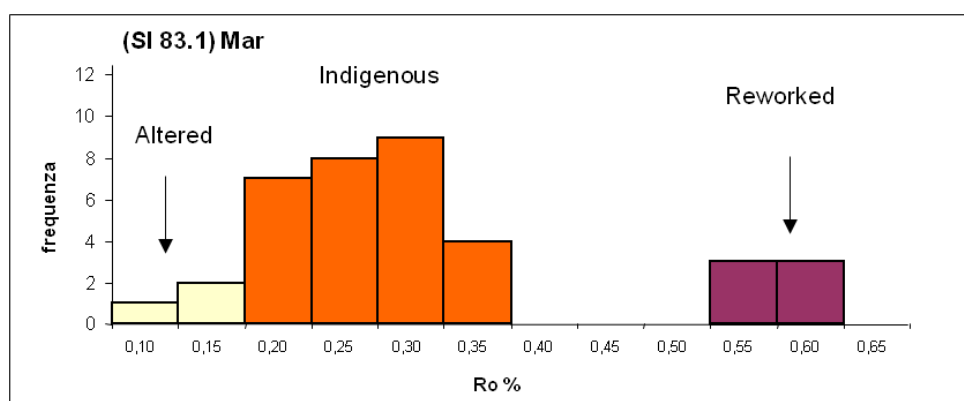


Fig. 5.5 – An example of histogram of vitrinite reflectance readings is shown.

Most of the methodological limitations are due to:

- the lack of information on macerals different from the vitrinite group;
- a lower reliability for $Ro\% < 0.3$;
- the presence of re-worked organic material;
- the whole-rock composition of the hosting rocks.

$Ro\%$ data, measured on subsurface samples and on outcropping sedimentary successions, usually allow to reconstruct the organic matter thermal maturity trend as a function of time and depth. These values used together with other geological pieces of information related to the sedimentary basin allow to deduce the thermal evolution of the sedimentary succession filling the basin. In particular, it is possible to use $Ro\%$ data for:

- reconstructing burial and thermal history calibrating the time-temperature models by the calculation of paleo-geothermal gradient, erosion and/or exhumation rates (Van Hinte, 1978);
- identifying the hydrocarbons generation stages reached by vitrinite-bearing rocks;
- correlating with other organic (e.g. thermal alteration index, conodont alteration index, biomarkers) and inorganic (e.g. %I in I-S, Kübler index, fluid inclusions) paleotemperature indicators in diagenesis and in very low-grade metamorphism environments (Fig. 5.3).

Sample preparation and analysis

The analysed samples for vitrinite reflectance were prepared according to standardized procedures described in Bustin et al. (1990). Grounded material and extracted kerogen

particles were englobe into an epoxy resin block. The samples were polished using and automated polishing system, 250, 500, 1000 carborundum papers and isopropanol as lubricant. After washing the sample in order to remove debris, three alumina powders of decreasing grain size (1, 0.3, 0.01 μm) were used to polish the samples.

Organic matter optical analysis were performed in Rome Tre laboratories using a Zeiss Axioplan microscope, under oil immersion ($n = 1.518$, 23°C) in reflected monochromatic non-polarised light ($\lambda = 546 \text{ nm}$). On each sample, minimum twenty measurements were performed on vitrinite fragments never smaller than 5 μm and only slightly fractured. Mean reflectance and standard deviation values were calculated from all measurements identifying the indigenous population.

Paleotemperature conversion is based on Barker and Pawlewicz's equation (1994).

5.2.2 XRD study of clay minerals

5.2.2.1 Generalities

The study of clay mineralogy has provided several useful tools for diagenesis and very low-grade metamorphism by furnishing information on the burial and thermal history of sedimentary sequences (Botti et al., 2004; Corrado et al., 2005)

Clay minerals in shales and sandstones undergo diagenetic and very low-grade metamorphic reactions in response to sedimentary and/or tectonic burial. Reactions in clay minerals are irreversible under normal diagenetic and anchizonal conditions, so that exhumed sequences generally retain indices and fabrics indicative of their maximum maturity and burial (Merriman and Frey, 1999).

An important reaction occurring in shales during burial diagenesis and in hydrothermal settings is the gradual conversion of smectite to illite through I-S mixed layers as intermediate phases. The progressive trend ranging from early diagenesis to the epizonal setting includes the following series: dioctahedral smectite - disordered mixed layers (R0) - ordered mixed layers (R1 and R3) - illite - dioctahedral white K-mica (muscovite). This prograde series is characterized by various crystal structural changes as the decrease of proportions of swelling phases and the increase of ordering in mixed layers. The layers are stacked along a direction parallel to the c-axis in random, partially regular, or regular sequences. The classical terminology for the stacking order is based on the term R (Jadgozinski, 1949) that expresses the probability, given a layer A, of finding the next layer

to be B. The R parameter may range from 0 to 3. R=0 means that there is no stacking order and illite and smectite layers are stacked randomly along the c-axis, R=1 indicates that a smectite layer is followed by an illite layer and a stacking order appears in the interstratification sequence, R=3 means that each smectite layer is surrounded by at least three illite layers on each side.

In this thesis, I-S structures will be described by means of the Reichweite nomenclature using R1 to mean R=1, R3 for R=3, etc. (Fig. 5.6).

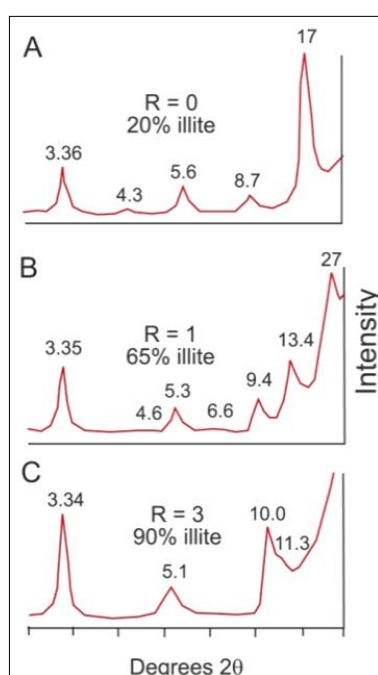


Fig. 5.6 – Calculated XRD patterns of illite-smectite mixed layers with different illite content and stacking order: A) random ordered I-S, B) short range ordered I-S, C) long range ordered I-S (after Pollastro, 1990).

The most common approaches utilizing I-S “geothermometer” in diagenetic studies are vertical profiles from wells and outcrops and thermal maturity mapping at local and regional scale. In the first case, illitization reaction profiles are generally produced. They are compared to the present geothermal gradient profile and organic matter maturity profiles in order to determine the temperature range in a particular point of the well correlating them to hydrocarbon generation phases (Pollastro, 1993; Merryman and Frey, 1999; Fig. 5.7).

In the second case, I-S mixed layers of a particular unit or a stratigraphic succession are studied to detect variations in the area distribution of the thermal evolution of sediments and to reconstruct the tectonic loading those units have experienced during the evolution of fold-and-thrust belts (Botti et al., 2004; Corrado et al., 2005).

Although the conversion to paleotemperatures depends on more than one factor (e.g., heating rate, protolith, fluid composition, permeability, fluid flow), Pollastro (1990; 1993) summarized the application of two simple time-temperature models for I-S geothermometry studies based primarily on the duration of heating (or residence time) at critical I-S reaction temperatures. The first model was developed by Hoffman and Hower (1979) for long-term, burial diagenetic settings that can be applied to most geologic and petroleum studies of sedimentary rocks and basins of Miocene age or older. In this model the major changes from R0 to R1 and from R1 to R3 occur in the temperature range of about 100-110 °C and of 170 °C-180 °C respectively and a minimum heating duration of 2 My is generally placed (Hoffman and Hower, 1979; Merriman and Frey, 1999).

The second model, which was developed for short-lived heating events, applies to young basins or areas characterized by relatively recent thermal activity with high geothermal gradients, or to recent hydrothermal environments. Such settings are those where relatively young rocks were subject to burial temperatures in excess of 100 °C for <2 My. In this model the conversion from R0 to R1 and from R1 to R3 ordering occurs at about 130-140°C and 170-180°C respectively (Jennings and Thompson, 1986).

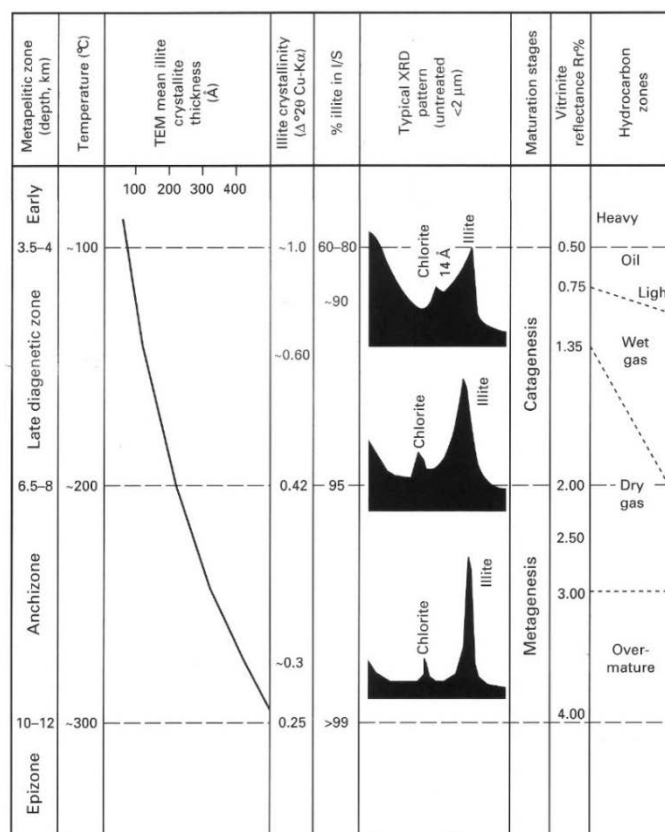


Fig. 5.7 – Correlation scheme among clay mineral geothermometers, vitrinite reflectance data, hydrocarbon zones, metapelitic zones and palaeotemperatures according to Merriman and Frey (1999).

Many authors have studied the use of illite-smectite reaction as a measurement of temperature. Bibliographic data of approximative temperatures for changes in mixed layer illite/smectite, relative to different geological settings, are reported in Table 5.1.

Sample preparation and analysis

Samples were analyzed at University “Sapienza” of Rome by XRD using a Scintag X1 system (CuK α radiation) at 40 kV and 45 mA. Randomly-oriented whole-rock powders were run in the 2-70 °2 θ interval with a step size of 0.05 °2 θ and a counting time of 3 s per step. Oriented air-dried and ethylene-glycol solvated samples were scanned from 1 to 48 °2 θ and from 1 to 30 °2 θ respectively with a step size of 0.05 °2 θ and a count time of 4 s per step. The <2 μ m grain-size fraction was separated by centrifuging, and oriented slides were prepared by the pipette-on-slide method, keeping the specimen thickness as constant as possible, within the range of 1 to 3 mg of clay per cm² of glass slide. The illite content in mixed layers I-S was determined according to Moore and Reynolds (1997) using the delta two-theta method after decomposing the composite peaks between 9 and 10 °2 θ and 16-17 °2 θ . Peaks in relative close position were selected for clay mineral quantitative analysis of the <2 μ m (equivalent spherical diameter) in order to minimize the angle-dependent intensity effect. Composite peaks were decomposed using Pearson VII functions and the DMSNT Scintag associated program. The I-S ordering type (Reichweite parameter, R; Jagodzinski, 1949) was determined by the position of the I 001-S 001 reflection between 5 and 8.5 °2 θ (Moore and Reynolds, 1997).

5.2.3. Fluid Inclusion Studies

5.2.3.1. Generalities

Fluid inclusions (FI) are fluid-filled vacuoles sealed within minerals. When trapped within diagenetic minerals, they provide the only direct mean of examining the fluids present in ancient diagenetic environment.

Fluid inclusions can be thought of as time capsules storing information about ancient temperatures, pressures and fluid compositions (Goldstein & Reynolds, 1994). They may provide the following valuable information with simple petrographic observations, microthermometric analysis, or geochemical analysis of inclusion contents.

Table 5.1 – Approximate temperatures for changes in mixed layer illite/smectite proposed by different authors from Corrado and Aldega (2008).

	% I in I-S (Reichweite parameter)	0-20% (Smectite to R0)	30-60% (R0)	60-80% (R0 to R1)	80-90% (R1 to R3)	90-95% (R3)	100% illite
Authors	Hoffman & Hower, 1979	50-60 °C		100-110 °C	170-180 °C		210 °C
	Jennings & Thompson, 1986			130-140 °C	170-180 °C		
	Weaver <i>et al.</i> , 1994		90-140 °C (only 40%)		200 °C	250-280 °C	
	Merriman & Frey, 1999	<100 °C		100 °C		200 °C	300 °C
	Jaboyedoff & Thelin, 1999	<100 °C		100-130 °C		200-250 °C	
	Uysal <i>et al.</i> , 2000			115-120 °C			

Fluid inclusions analysis is one of the tools that allows the reconstruction of the thermal history of a sedimentary succession. FI are micrometric cavities in minerals containing paleofluids remains (Fig. 5.8).



Fig. 5.8 – Euhedral quartz crystal containing CH₄, water and vapour inclusions (courtesy of Dr. Paolo Scotti, ENI).

Based on the time of trapping with respect to the crystal growth, different types of fluid inclusions (primary, secondary, pseudosecondary) may occur in rock crystals (Roedder, 1984). From their analysis, it is possible to obtain information on P-T conditions during fluids trapping and, consequently, on the rock's evolution history. In the recent past, FI have been widely used as geothermo-barometers in studies of igneous and metamorphic rocks, mainly for mineral and geothermic exploration and, in basin analysis, for petroleum exploration (e.g., Ceriani *et al.*, 2002; Ceriani, 2003). More recently, they have been used to solve structural geology issues, in particular on environmental changes during

progressive deformation, i.e. prograde and retrograde P-T path reconstruction (Crispini & Frezzotti, 1998; Invernizzi et al., 1998; Corrado et al., 2010), and changes in fluid circulation and composition in active fault zones (Cello et al., 2001). FI may be studied by microthermometry. This technique allows to measure: homogenization temperatures (T_h), which are indicative of the minimum trapping temperatures (Goldstein & Reynolds, 1994), and melting temperatures (T_m), which give information on fluid composition. By doing so, it is possible to choose a characteristic phase diagram for the examined fluid and to draw a P-T diagram by integrating FI data with information obtained by other techniques such as structural analysis, organic matter and clay mineralogy analyses.

Limitations of this technique, in sedimentary rocks, can derive from: the small size of the inclusions (usually between 2 and 10 μm), and the possibility that the system was not closed (isoplethic) and/or isochoric (i.e. constant volume inclusions) since the time of entrapment. In the latter instance, fluid inclusions would record thermal reequilibration at some stage of the tectonic evolution. This represents a common limitation for the study of carbonate rocks where non-isoplethic and non-isochoric conditions can develop more frequently for the presence of a 'soft' mineral such as calcite.

5.2.3.1.1 Phase changes in Fluid Inclusions

Most fluids in the diagenetic realm are incredibly complex in composition. One of the best examples of this is seawater, a highly concentrated fluid (about 3.5 wt.%) that has major amounts of, Na^+ , Mg^{2+} , Ca^{2+} , K^+ , Sr^{2+} , Cl^- , SO_4^{2-} , HCO_3^- , Br^- , F^- , and B and minor amounts of many other elements. Working with phase equilibria and microthermometry requires that the fluid inclusionist either carefully characterizes the composition of the fluid or make some assumptions about what a good model might be for the composition of the fluid (Goldstein, 2001). Therefore, the equilibrium phase relations provide the link between the laboratory measurements of temperatures at which phase transitions occur within inclusions when heated and cooled and the interpretations of the measurements. Some of the most common model compositions and examples of the phase equilibria that would apply to their interpretation are summarized in: i) single component system H_2O and pure CH_4 ; ii) two component system H_2O - NaCl ; iii) two component system H_2O - CH_4 and iv) multicomponent systems.

Single component system H₂O

A system of variable state is determined by the four quantities of Pressure (P), temperature (T), composition (X) and volume (V). For a unary system, the transitions between the three basic physical states (solid, liquid, gas) may be affected by changing one or more of the parameters P, V and T (Goldstein & Reynolds, 1994). In figure 5.9, the intersections of planes of constant volume with the surface representing stable single-phase equilibria are shown as dashed lines.

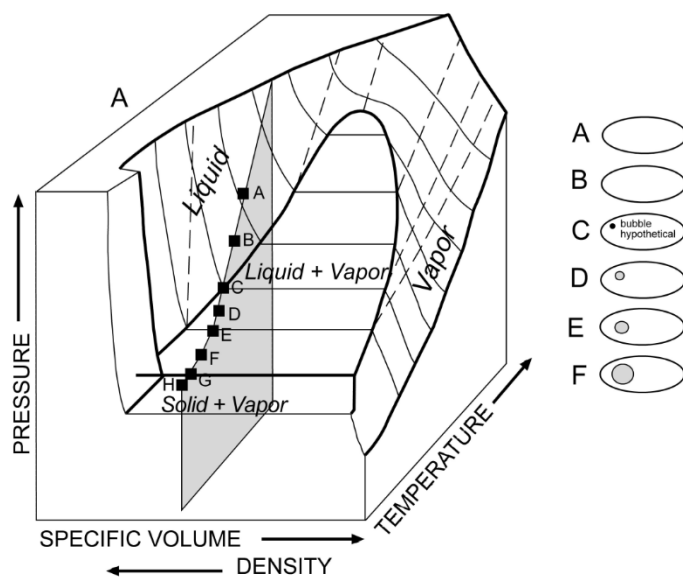


Fig. 5.9 – Generalized and schematic P-V-T diagram for the unary system H₂O modified from Roedder (1984).

The intersections of planes of constant temperature with the surface representing stable single-phase equilibria are shown as curved, light solid lines. The surface representing stable two-phase (liquidvapor) equilibria delimited by heavy solid lines. The intersection of these surfaces of stable equilibria with a plane of constant specific volume defines a curve known as an isocore. If an inclusion traps a fluid of specific volume (of that shown by shaded plane) at the P-T conditions of point A, the inclusion will be constrained to the locus of points in P-V-T space described by the intersection of the surface of the shaded (constant volume) plane with the surfaces of stable equilibria (for cooling, A-B-C-D-E-F-G-H is shown).

Relatively pure H₂O is common in sedimentary systems, especially near the surface and in shallow parts of basins. The fresh-water system is best identified by its behaviour during microthermometric cooling of fluid inclusions. The melting temperature of ice for these fluid inclusions is 0°C.

Two component system H_2O - $NaCl$

Aqueous solutions dominated by $NaCl$ are common in many natural systems of the sedimentary realm. Compositions of fluid inclusions represented by the H_2O - $NaCl$ system are easily determined from temperatures of phase changes during microthermometric analysis. Figure 5.10 is a T-X projection of the H_2O - $NaCl$ system showing the phases that are stable at various temperature-composition conditions. Note that vapor is present and in equilibrium everywhere on the diagram.

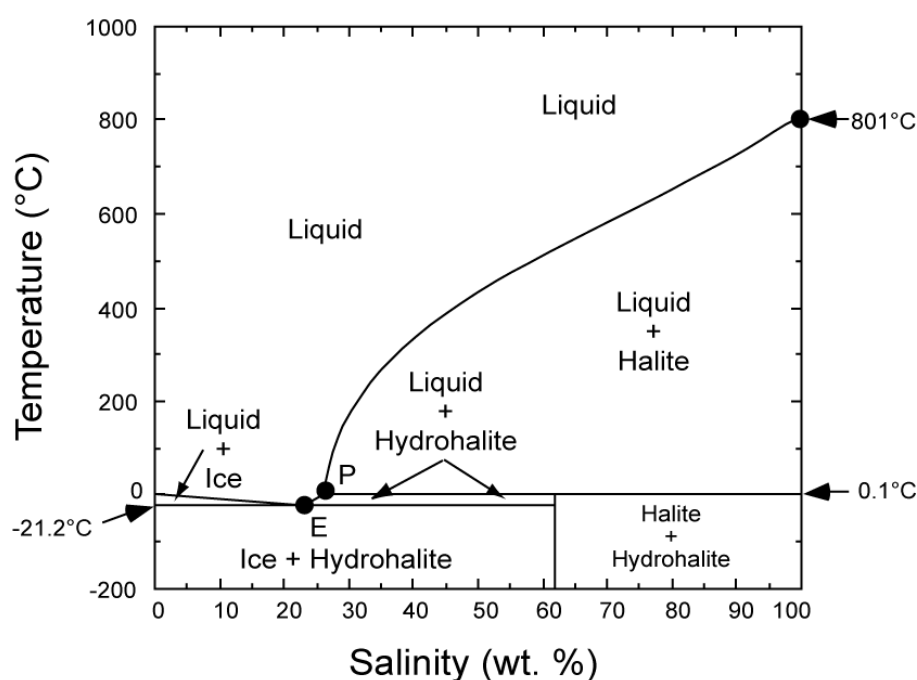


Fig. 5.10 – T-X plot for the lower temperature, lower salinity portions of the system H_2O - $NaCl$. Each point on this diagram is at equilibrium vapor pressure. Produced from Crawford (1981), Roedder (1984) and Hall et al. (1988).

For salinities <23.2 wt.% $NaCl$, the composition is determined from the ice-melting temperature. When an H_2O - $NaCl$ fluid inclusion with salinity between 0-23.2 wt.% is cooled to low temperatures, the inclusion will freeze to form a mixture of ice and hydrohalite ($NaCl \cdot 2H_2O$) in proportions consistent with the bulk inclusion salinity. When heated, the hydrohalite will decompose at the eutectic temperature (-21.2°C) to produce ice and a liquid with the eutectic composition (23.2 wt.%) (Fig. 5.11). As the inclusion is heated beyond the eutectic temperature, ice continues to melt, diluting the salinity of the liquid phase.

The temperature at which the last of the ice melts defines the freezing point of the inclusion, and this value is used to determine the salinity. For example, the last ice crystal

in the inclusion shown on figure 5.11 melts at -6.6°C , corresponding to a salinity of 10.0 wt.% NaCl (Table 5.2).

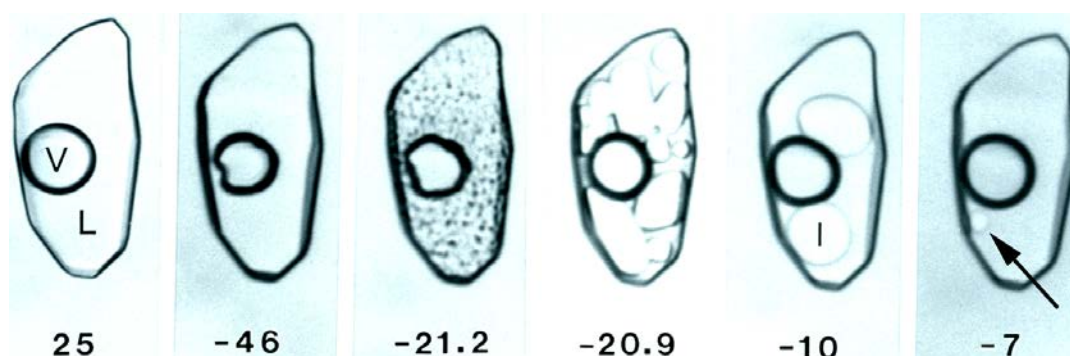


Fig. 5.11 – Phase behavior of an H_2O -NaCl fluid inclusion with a salinity of 10 wt.% during heating from low temperature. At -46°C the inclusion contains a glassy solid that devitrifies at the eutectic temperature (-21.2°C) to produce a fine-grained mixture of hydrohalite and ice. With slight heating above the eutectic temperature the hydrohalite disappears and the ice re-crystallizes to form several large crystals. With continued heating, the ice crystals gradually dissolve, leaving a single small crystal at -7°C , which dissolves completely at -6.6°C .

5.2.3.1.2 Fluid Inclusions petrography

There are many ways to classify fluid inclusions (Roedder, 1984; Goldstein, 2003), but one of the most useful classification schemes relates to the timing of formation of the inclusion relative to that of the host mineral (Fig. 5.12).

Table 5.2 – Salinities (wt.%) corresponding to measured freezing point depressions (degrees Celsius) calculated according to Bodnar (1993).

FPD	.0	.1	.2	.3	.4	.5	.6	.7	.8	.9
0.	0.0	0.2	0.4	0.5	0.7	0.9	1.1	1.2	1.4	1.6
1.	1.7	1.9	2.1	2.2	2.4	2.6	2.7	2.9	3.1	3.2
2.	3.4	3.6	3.7	3.9	4.0	4.2	4.3	4.5	4.7	4.8
3.	5.0	5.1	5.3	5.4	5.6	5.7	5.9	6.0	6.2	6.3
4.	6.5	6.6	6.7	6.9	7.0	7.2	7.3	7.5	7.6	7.7
5.	7.9	8.0	8.1	8.3	8.4	8.6	8.7	8.8	9.0	9.1
6.	9.2	9.3	9.5	9.6	9.7	9.9	10.0	10.1	10.2	10.4
7.	10.5	10.6	10.7	10.9	11.0	11.1	11.2	11.3	11.5	11.6
8.	11.7	11.8	11.9	12.0	12.2	12.3	12.4	12.5	12.6	12.7
9.	12.9	13.0	13.1	13.2	13.3	13.4	13.5	13.6	13.7	13.8
10.	13.9	14.0	14.2	14.3	14.4	14.5	14.6	14.7	14.8	14.9
11.	15.0	15.1	15.2	15.3	15.4	15.5	15.6	15.7	15.8	15.9
12.	16.0	16.1	16.2	16.2	16.3	16.4	16.5	16.6	16.7	16.8
13.	16.9	17.0	17.1	17.2	17.3	17.3	17.4	17.5	17.6	17.7
14.	17.8	17.9	18.0	18.0	18.1	18.2	18.3	18.4	18.5	18.6
15.	18.6	18.7	18.8	18.9	19.0	19.1	19.1	19.2	19.3	19.4
16.	19.5	19.5	19.6	19.7	19.8	19.8	19.9	20.0	20.1	20.2
17.	20.2	20.3	20.4	20.5	20.5	20.6	20.7	20.8	20.8	20.9
18.	21.0	21.0	21.1	21.2	21.3	21.3	21.4	21.5	21.5	21.6
19.	21.7	21.8	21.8	21.9	22.0	22.0	22.1	22.2	22.2	22.3
20.	22.4	22.4	22.5	22.6	22.7	22.7	22.8	22.9	22.9	23.0
21.	23.1	23.1	23.2							

Accordingly, primary fluid inclusions are formed during, and as a direct result of growth of the surrounding host crystal. If a crystal fractures after it has been formatted, some fluid may enter the fracture and become trapped as secondary fluid inclusions as the fracture heals. Thus, secondary inclusions are trapped after the crystal growth is complete. If fracturing occurs during growth of the crystal, pseudosecondary fluid inclusions may be trapped during continued crystal growth.

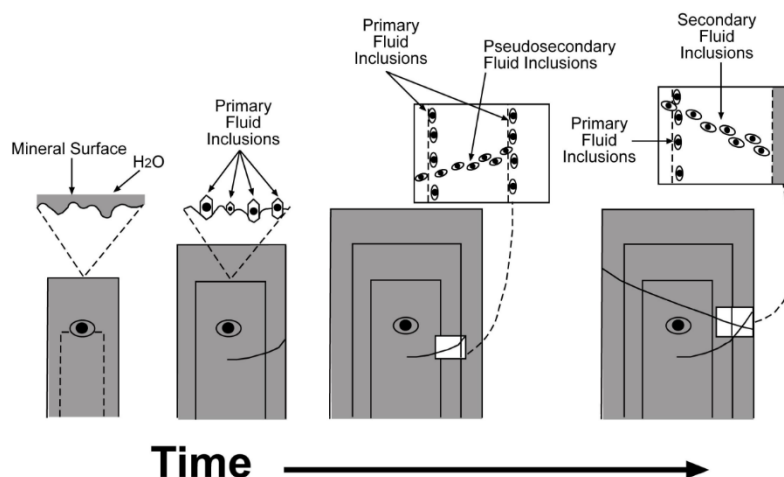


Fig. 5.12 – Schematic representation showing the formation of primary, secondary and pseudosecondary fluid inclusions during crystal growth (Roedder, 1984; Goldstein, 2003).

Petrographically, sometimes the origin of the inclusions relative to formation of the crystal cannot be determined with confidence and the inclusion origin is said to be indeterminable (Goldstein, 2003). Therefore, determining the temporal classification of any given fluid inclusion is to interpret the origin and evolution of the host mineral, yet this determination is often difficult.

To minimize the emphasis on the primary, secondary and pseudosecondary classification of inclusions, Goldstein & Reynolds (1994) introduced the concept of the Fluid Inclusion Assemblage (FIA, Fig. 5.13) to describe a group of fluid inclusions that were all trapped at the same time. An FIA thus defines the most finely discriminated fluid inclusion trapping event that can be identified based on petrography (Goldstein, 2003).

Normally, petrography is regarded as the most important part of any fluid inclusion study to determine the timing of entrapment of fluid inclusions. Fluid inclusion petrography and the identification of fluid inclusions assemblages is also the most important approach for evaluating if fluid inclusions have been altered significantly after their entrapment, through

necking down after a phase change (Bodnar, 2003a) or through thermal re-equilibration (Bodnar, 2003b).

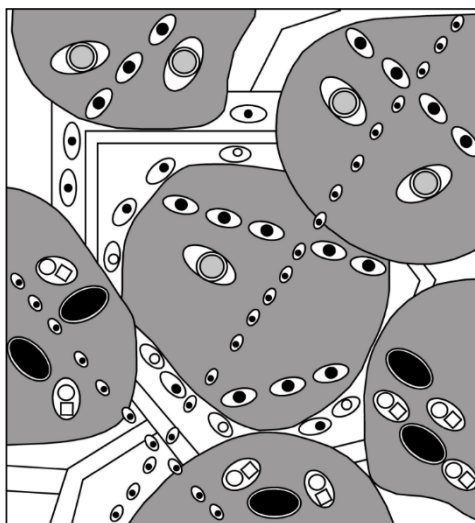


Fig. 5.13 - Schematic representation of the various FIAs that might be observed in a well-cemented sandstone from a hydrocarbon basin. The original detrital grains are shaded (from Bodnar, 1994).

5.2.3.1.3 Fluid Inclusions microthermometry

The determination of temperatures of phase changes within fluid inclusions during heating and cooling of samples is termed microthermometry. The technique is invaluable for discovering the temperatures at which minerals form, the thermal history a rock has experienced, and the compositions of the fluids that traversed a rock in its history. The fundamental principles upon which microthermometry is based are the principles of phase equilibria and the characterization the fluid inclusion petrography introduced before (Goldstein & Reynolds, 1994). The only way to be able to interpret fluid inclusion microthermometric data is if data from many inclusions within a single FIA, the most finely discriminated, petrographically associated, group of inclusions, are collected and recorded together as a group. The ability to collect microthermometric data with the greatest possible efficiency and under the best possible optical conditions requires appropriately prepared doubly polished plates, where thickness are 100 μm or more, and a good heating/cooling stage on a appropriately set up and adjusted microscope. This technique allows to measure homogenization temperatures (T_h), which are indicative of the minimum trapping temperatures, and melting temperatures (T_m), which give information on fluid composition (Goldstein & Reynolds, 1994).

Sample preparation and analysis

Samples analyses were performed at School of Science and Technology of Camerino.

Fluid inclusions microthermometry in 200 μm thick, resin-impregnated, doubly-polished wafers were measured using a USGS heating-freezing stage calibrated at 0 °C, -56.6 °C and 374 °C with synthetic standards. Temperatures of phase changes at $T \geq 0^\circ\text{C}$ are accurate to $\pm 0.1^\circ\text{C}$; temperatures above 50°C are accurate to $\pm 1.0^\circ\text{C}$.

Microthermometric analyses were carried out on small (4-6 mm) fragments of the polished wafers. For two-phase inclusions, temperature of the following phase transitions, when observed, were recorded: (i) ice melting temperature (T_m), indicative of fluid composition; (ii) homogenization temperature (T_h), indicative of fluid density. All the measurements were repeated two/three times to confirm the datum.

5.2.4 - Thermo-structural modelling

Thermo-structural modelling was performed by using Basin Mod-1D software (1996). This software allows reconstructing the burial and thermal history of sedimentary sequences in deformed and undeformed conditions from geological data (e.g., age of sedimentary sequences and depositional/erosional events, pure and mixed lithologies, thicknesses, age and thermal conductivity of sedimentary sequences).

Input data used in this work derive from the integration between the database of physical features provided by the libraries available of the modelling software and the geological information coming from the regional literature and the stratigraphic and structural data collected in the field (Moreno Espelta et al., 1975; Seggiaro et al., 1995; Reynolds et al., 2000; Marquillas et al., 2004; Hain et al., 2011; Barcelona et al., 2014; Invernizzi et al., 2014).

The main assumption for the modelling are: (1) correction for decompaction of the burial curves according to Sclater and Christie's method (1980); (2) sea level changes, are neglected, as the thermal evolution is influenced more by sediment thickness than water depth (Butler, 1992); (3) thrusting is considered instantaneous when compared with the duration of sedimentation, as generally suggested in theoretical models (Endignoux and Wolf, 1990).

Thermal modelling was performed through LLNL Easy %Ro method (Sweeney and Burnham, 1990) adopting different geothermal gradients for the syn-rift and, post-rift and syn-orogenic sedimentation, using a surface temperature of 20°C and a present geothermal gradient of 40°C/Km as reported by literature (Seggiaro et al., 1995; Invernizzi et al., 2014).

Burial curves were generally calibrated with Ro% and I% in I-S, according to the geothermometer's correlation proposed by Pollastro (1993).

Regarding the study area, thermal models were performed for two areas along the anticline where the samples were collected: along the southwestern limb of the regional anticline far away from the hot springs (Anta Yaco area) and in the northern portion, close to the hot springs (Hotel Termas area) (Figs. 5.1, 5.14).

Constraints to modelling will be presented in the Results paragraph.

5.3 Results

5.3.1 Structural data

Structural surveys performed at the outcrop scale allowed to highlight the intensity and type of deformation affecting the outcropping sedimentary succession in different area of the studied anticline and to reconstruct its kinematic evolution (see also chapter 3 for further details). The new interpretation takes into account a multi-stage model of positive inversion that explains the formation of the regional anticline, the later flower-like structure and the normal faults that dissect it. Accordingly, the N-S high-angle fault plane, bordering the anticline along its eastern margin, is considered the main responsible of the uplift of the Sierra de La Candelaria anticline (Moreno Espelta et al., 1975; Seggiaro et al., 1995, 1997) (Fig. 5.1). The thickness lateral variation of the syn-rift deposits (Pirgua Subgroup) moving from the area of Balboa anticline to the area of Anta Yaco allowed to consider it as a former Cretaceous normal fault inverted during the Cenozoic tectonic phase, in agreement with Iaffa et al., 2013.

In the Anta Yaco area, along the western limb of the anticline, far away the hot springs of the Hotel Termas area, N-S trending stylolites in the strata of Yacoraite Formation are in accordance with the direction of regional compression (Marrett et al., 1994) (Fig. 3.4d).

Later on, the growing of the regional anticline was accompanied by a series of related syn-folding features. Far away the Hotel Termas area, along the western limb of the Sierra de La Candelaria anticline, they are represented by NNW-SSE and E-W conjugate strike-slip fractures occurring in the strata of Anta Formation (Fig. 3.4b), and by E-W shear fractures with a right-lateral kinematic, mainly occurring in the strata of Pirgua Subgroup (Fig. 3.4c).

In the late stage of inversion, the development of a NNW-SSE oblique fault plane, dissecting the regional anticline in the northern portion, enhanced the growth of Balboa and

Termas minor anticlines (Barcelona et al., 2014). The occurrence of this fault characterized by reverse dip-slip and left-lateral strike-slip components led to a positive flower-like structure with associated NW-SE riedel shears characterized by a left-lateral strike-slip transtensional kinematics. At the meso-scale, close to the hot springs area, in correspondence to the outcrops of Anta Formation, small NNW-SSE left-lateral faults with the associated Riedel shears and WNW-ESE calcite-filled veins testify the strike-slip kinematic related to this late transpressive event. At the same time, different meso-structures testify the folding process. Gypsum extensional veins striking NNE-SSW, steeply dipping and at low angle to bedding in the pelitic strata of Anta Formation, indicate the initial stage of folding under overpressure condition (Shearman et al., 1972; Gustavson et al., 1994; Sibson and Scott, 1998) (Fig. 3.9). Syn-folding features are mainly represented by NNW-SSE and E-W conjugate shear fractures, NNW-SSE conjugate system of extensional fractures, N-S-trending joint (Fig. 3.7). Shear veins in gypsum bearing pelites and N-S calcite filled veins also testify the folding process recording the flexural slip on the limbs of the anticline, in the first case, and an extension sub-parallel to the fold axis trend in the second one. E-W conjugate system of extensional fractures, and the ENE-WSW and W-E normal faults are interpreted to reflect the final stage of the folding process (Fig. 3.7c).

With the aim to evaluate the thermal alteration of the cap rocks of the studied geothermal system, samples for paleo-thermal analyses were collected both far away and close to the hot springs area (Figs. 5.1, 5.14).

In the first case, they come from the Anta Yaco area, along the western limb of the Sierra de La Candelaria anticline, characterized by a minor intensive brittle deformation recording mainly the folding process. In this area, 7 samples for x-ray diffraction of clay minerals analyses were collected from the outcropping Yacoraite, Pirgua and Anta Formations in order to evaluate changes in clay minerals structures and compositions to constrain the maximum temperatures experienced by rocks far from the influence of the hot fluids. In the same area, 3 samples from the organic rich beds of Yacoraite Formation were analysed by means of organic matter maturity (Fig. 4.3e). They were collected both from deeper and shallower stratigraphic units in order to reconstruct the thermal history of the studied structure.

Close to the hot springs, the brittle deformation is more intensive and records both the folding process and the strike-slip kinematic related to the late transpressive event that took place along the NNW-SSE fault plane. In this area, 10 samples were collected from Anta

Formation both from poorly fractured outcrops, where the affecting fracture system is mainly related to the folding process, and from the intensely fractured outcrops mainly affected by the deformation related to the strike-slip kinematic. In addition, 2 samples (AR12 and 15) coming from the NNW-SSE and WNW-ESE calcite-filled veins, related to transtensional kinematics, were analysed for fluid inclusions in order to obtain information on minimum trapping temperatures during crystallization. Differently, 2 samples (AR17 and 19) come from the N-S calcite-filled veins and NNE-SSW gypsum-filled veins mainly related to the folding process (Fig. 3.9). One sample was collected from the Jesús Maria Formation.

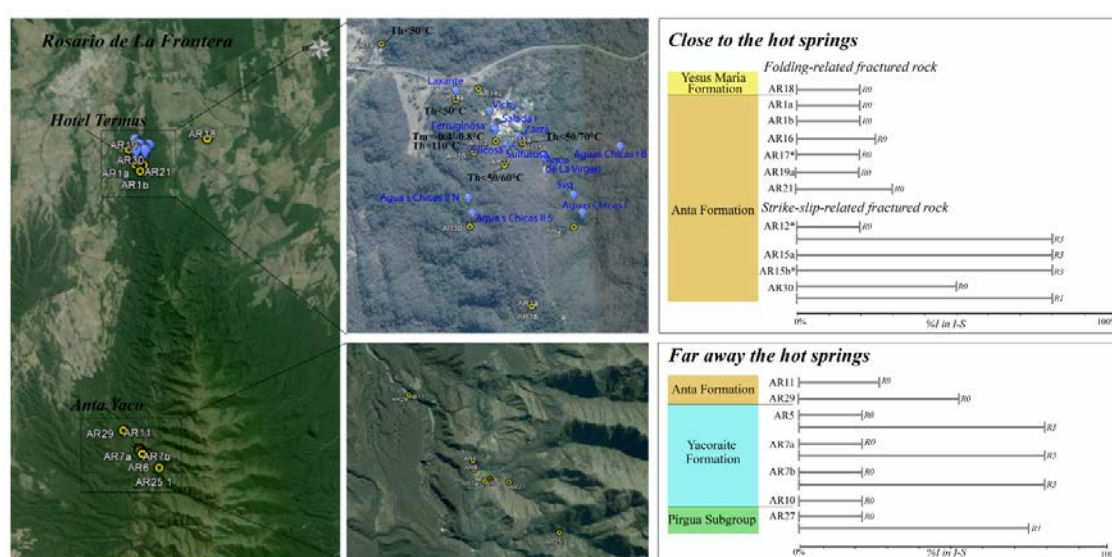


Fig. 5.14 – The map shows the two different sampled areas along the regional anticline: close and far away the hot springs of the Hotel Termas area. For each sample are indicated the related paleo-thermal data derived from clay mineralogy analyses. Samples with star (*) indicate that fluid inclusion analyses were also performed.

5.3.2 X-ray diffraction of clay minerals

XRD data on whole rock samples indicate a predominance of phyllosilicates (from 68% to 87%, Table 5.3) on other mineralogical phases in the three sampled formations (Jesús Maria, Anta and Yacoraite) (Table 5.3).

Amounts of quartz (3-18%), k-feldspar (1-2%), plagioclase (2-20%) are also present, whereas analcime with percentage between 1 and 7%, is frequent but not ubiquitous (absent in Jesús María Fm) as well as hematite and pyrite. Laumontite is present in small amounts only in Yacoraite Fm (2%). Calcite and gypsum predominate either in veins filling (AR19) or in deeply altered host rocks close to one of the hot springs (AR 14).

Table 5.3 – Organic matter maturity and clay mineralogy data used as input for the burial and thermal history reconstruction.

Subgroup	Formation	Age	Coordinates (Lat.; Long.)	Sample	XRD analysis		%I in I-S	R parameter	VRo% ± s.d. (n. measures)	FI	
					<2µm	Whole-rock				Th (°C)	Tm (°C)
Metán	Jesús María	Miocene	25,8263; 64,8916	AR18	I ₇ I- S ₉₁ Ch ₁	Qtz ₁₂ Cal ₄ Plg ₁₀ Hem ₂ Ph ₇₂	20	R0			
	Anta		25,8344; 64,9372	AR19b	I ₉₁ I- S ₅ Ch ₁	Qtz ₄ Cal ₁ Kfs ₁ Plg ₄ Anl ₁ Ph ₇₀ Ank ₁₉	20	R0			
			25,8344; 64,9372	AR19a	ND	Cal ₁₆ Gyp ₈₄				<50°*	
			25,8386; 64,9316	AR12	I ₃₆ I-S ₆₄	Qtz ₁₀ Dlme ₁ Plg ₁₀ Ph ₇₉	20; 80	R0; R3		115° -0,4°/ -0,8°	
			25,8369; 64,93361	AR14a	I ₁₉ C-S ₈₁	Qtz ₅ Cal ₁₃ Kfs ₁ Plg ₇ Anl ₃ Ph ₇₁	ND	ND		<50°*	
			25,8364; 64,93255	AR14b	I ₂₇ C- S ₇₂ Ch ₁	Qtz ₁₈ Cal ₂ Dlme ₃ Kfs ₂ Pl g ₂₀ Anl ₇ Ph ₄₈	ND	ND			
			25,8387; 64,93042	AR15a	ND	Qtz ₇ Kfs ₁ Plg ₂ Hem ₃ Ph ₈₇	80	R3			
			25,8387; 64,93043	AR15b	I ₄₂ I-S ₅₇	Qtz ₁₄ Plg ₄ Anl ₁ Ph ₈₁	80	R3		<50°/ 70°*	
			25,8391; 64,93268	AR16	I ₂₉ I- S ₇₀ Ch ₁	Qtz ₇ Kfs ₁ Plg ₅ Hem ₂ Ph ₈₅	25	R0			
			25,8396; 64,93123	AR17	I ₂₀ I-S ₈₀	Qtz ₁₆ Kfs ₁ Plg ₅ Anl ₃ Hem ₂ Ph ₇₅	20	R0		<50°/ 60°*	
			25,8422; 64,92803	AR21	ND	ND	30	R0			
			25,8422; 64,93282	AR30	ND	ND	50; 80	R0; R1			
			25,84535; 64,92992	AR1a	I ₁₇ I-S ₈₃	Qtz ₁₆ Kfs ₂ Plg ₃ Anl ₄ Ph ₇₅	20	R0			
			25,84535; 64,92993	AR1b	I ₂₅ I-S ₇₅	Qtz ₂ Cal ₁ Kfs ₂ Plg ₆ Anl ₇ Py ₃ Ph ₇₉	20	R0			
			25,97931; 64,93237	AR 29	ND	ND	50	R0	Barren		
			25,979; 64,93317	AR11	I ₃₂ I- S ₆₇ Ch ₁	Qtz ₇ Kfs ₂ Plg ₂₃ Ph ₆₈	25	R0			
Balbuena	Yacoraite	Cretaceous	25,9903; 64,92046	AR5	I ₂₁ I-S ₇₉	Qtz ₈ Kfs ₂ Plg ₁₂ Hem ₅ Ph ₇₃	20; 83	R0; R3	Barren		
			25,9906; 64,9212	AR7a	I ₁₄ I-S ₈₆	Qtz ₄ Kfs ₁ Plg ₉ Anl ₃ Ph ₈₃	20; 83	R0; R3	0.65±0.11 (13)		
			25,9906; 64,9213	AR7b	I ₁₆ I-S ₈₄	Qtz ₃ Kfs ₁ Plg ₅ Lm ₂ Ph ₈₉	20; 83	R0; R3	Barren		
			25,989040; 64,22885	AR8	ND	ND			0.67±0.11 (19)		
			25,987858; 64,923046	AR9	ND	ND			0.59±0.08 (15)		
			25,987858; 64,923046	AR10	I ₆₉ I-S ₃₁	Qtz ₅ Cal ₁ Kfs ₁ Plg ₇ Anl ₁ Py ₁ Ph ₈₄	20	R0			
Pirgua	Los Blanquitos		25,98804; 64,91776	AR 27	ND	ND	20; 75	R0; R1			
<i>Note:</i> Ank-Ankerite; Anl-analcime; Cal-calcite; Ch-chlorite; C-S-mixed-layer chlorite-smectite; Dlme-dolomite; Gyp-Gypsum; Hem-hematite; I-illite; I-S-mixed-layer illite-smectite; Lm-laumontite; Kfs-K-feldspar; Ph-phyllsilicates; Plg- Plagioclase; Py-Pyrite; Qtz-quartz. S.O.= stacking order; F.I. = fluid inclusions; Th= homogenization temperature; Tm= ice melting temperature; * estimated from petrographic analyses; Subscript numbers correspond to mineral weight percentage.											

Less than 2 μm fraction indicate a prevalence of illite-smectite (I-S) mixed-layers (about 60 to 90%), subordinate amounts of illite (about 10-40%) in the four formations with the exception of AR14 samples in highly altered Anta Fm where illite-chlorite mixed layers prevail (70-80%) and in samples AR10 and 19b, of Yacoraite and Anta Fms respectively, where illite (about 70-90%) prevails on mixed layers. Minor amounts of chlorite are present only in the Metán Subgroup.

In poorly fractured fold related outcrops far from the Hotel Termas area, in the syn-rift deposits, two populations of I-S mixed layers coexist with 75% and R1 ordering, and 20% I in I-S and R0, whereas in post-rift Yacoraite Fm, occur two populations with 83% and R3 ordering, and 20% I in I-S and R0 ordering.

In syn-orogenic Metán subgroup, I-S mixed layers, when present, show mostly R0 structures with low amounts of illite (20-25%) in poorly fractured outcrops deformed during folding, indicating low thermal maturity both far from and close to hot springs.

On the contrary, R3 structures prevail in samples from damage zones of both left lateral 250° dipping faults (AR12) and transtensive 210° dipping faults (AR15).

5.3.3 Vitrinite reflectance data

Organic rich beds in poorly fractured outcrops of Yacoraite Formation were sampled for vitrinite reflectance studies in the Anta Yaco area, far away the hot springs (samples AR 7a, 8, 9; Figs. 5.1, 5.14). Reflected light optical analyses allowed recognizing a prevalence of fragments of the huminite-vitrinite group macerals with one indigenous population and a less abundant, reworked one. The indigenous population provided mean vitrinite reflectance of about 0.6-0.7% indicating the early-mid mature stage of hydrocarbon generation (Fig. 5.15; Table 5.3).

5.3.4 Fluid inclusions microthermometry and petrography

Few mineralized veins are present in the sampled outcropping sedimentary succession along the anticline. Reliable results derive from centimetric calcite- and gypsum-filled extensional veins deforming Metán Subgroup and related to syn-orogenic fracture systems.

AR12 and AR15 samples derive from veins associated to the strike-slip kinematic, whereas AR17 and AR19 come from poorly fractured outcrops whose deformation is mainly related to the folding process.

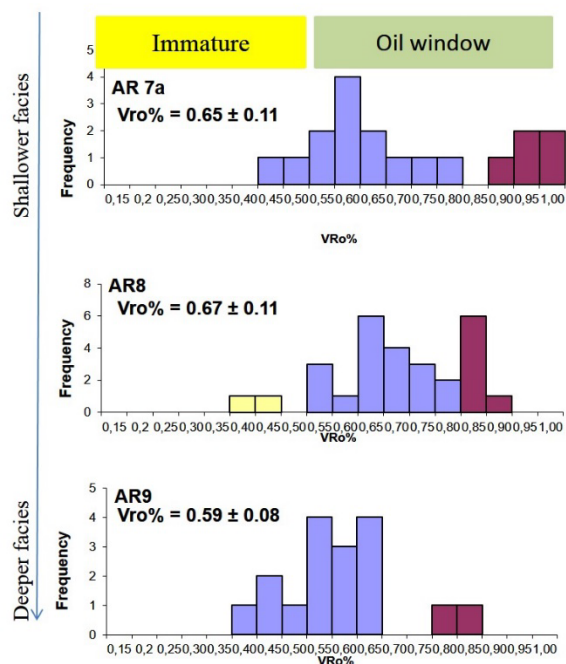


Fig. 5.15 - Histograms of vitrinite reflectance for samples of Yacoraite Formation.

Petrographic analyses on double polished wafers mainly reveal in all samples the prevalence of mono-phase primary inclusions and scarcely healed microfractures with secondary inclusions. This, together with an inhomogeneous distribution of vapour phase in the less abundant two-phase inclusions, suggests an entrapment temperature below 50-60°C (immiscible liquid and vapour). Nevertheless, sporadic two-phase fluid inclusion assemblages with homogeneous vapour distribution characterize AR12 sample (Fig. 5.16, Table 5.3).

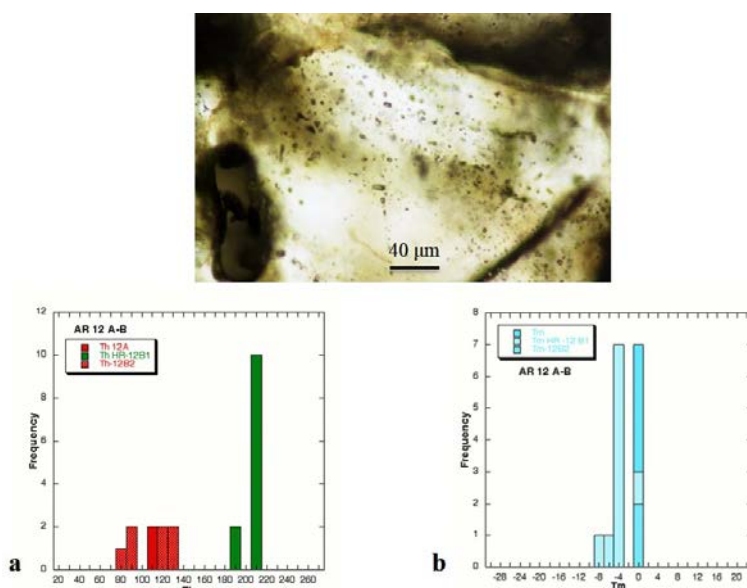


Fig. 5.16 - Fluid inclusion data. Microphotograph showing groups of secondary two-phases inclusions in sample AR12; (a,b) histograms showing Th and Tm data of sample AR12.

Homogenization temperatures (T_h) of 115°C and ice melting temperatures (T_m) of -0.4-0.8°C within calcite crystals provide constraints on trapping temperature and fluid salinity respectively.

Tens of primary and secondary all-liquid inclusions were observed in sample AR19 within gypsum and calcite crystals confirming an entrapment temperature <50°C (Fig. 5.17).

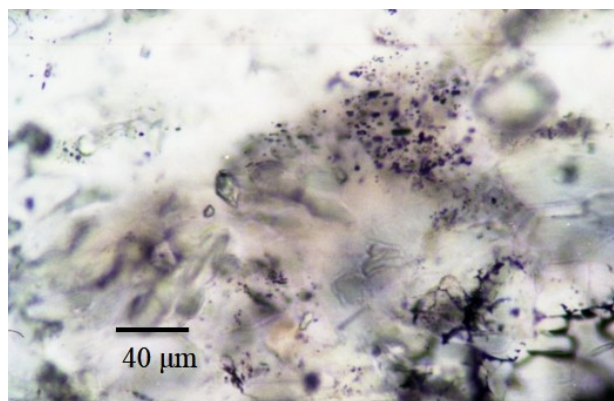


Fig. 5.17 - Fluid inclusion data. Microphotograph showing groups of small primary mono-phase inclusions in sample AR19.

5.3.5 Burial and thermal modelling

Results of the burial and thermal modelling of the two different areas of the regional anticline are reported in figure 5.18.

The reconstructed burial history began in Barremian times with the deposition of the syn-rift deposits of the Pirgua Subgroup and continued since Eocene with a post-rift basinal succession. During the Cretaceous period, sedimentation took place in the basin at low sedimentation rates increasing in the Upper Cretaceous and stopped in Eocene times (Marquillas et al., 2005).

Deposition started again during Miocene times with the syn-orogenic sedimentation of the Metán and Jujuy Subgroups and continued at high rates until Zanclean times (Reynolds et al., 2011). Uplift and erosion started in Upper Miocene times (orogenic Quechua phase), ruled by a high angle inverted-fault that led to the formation of the Balboa anticline (González, 2000; Mon, 2001; Sobel and Strecker, 2003; Salfity and Monaldi, 2006; Mon and Gutierrez, 2007; Iaffa et al., 2013; Barcelona et al., 2014). Later on, the deformation migrated northward in the area of the Hotel Termas developing the Termas anticline.

The maximum recorded paleo-temperatures, corresponding to the different depths of burial, are about 110°C for the syn-rift deposits, about 90-100°C for the post-rift and 80-

90°C for the syn-orogenic deposits (Fig. 5.18). Therefore, the rift succession experienced a thermal evolution compatible with late diagenetic conditions in the early stages of hydrocarbon generation during Miocene times.

The calculated load of sedimentary origin, currently eroded, is characterized by variations showing a decrease moving from north to south in correspondence of the southwestern limb of the anticline since this sector of the anticline was the first to be exhumated (Barcelona et al., 2014). In detail, in this latter area a load of about 900 m deposited onto the syn-rift deposits increasing up to about 1600 m close to the Hotel Termas area.

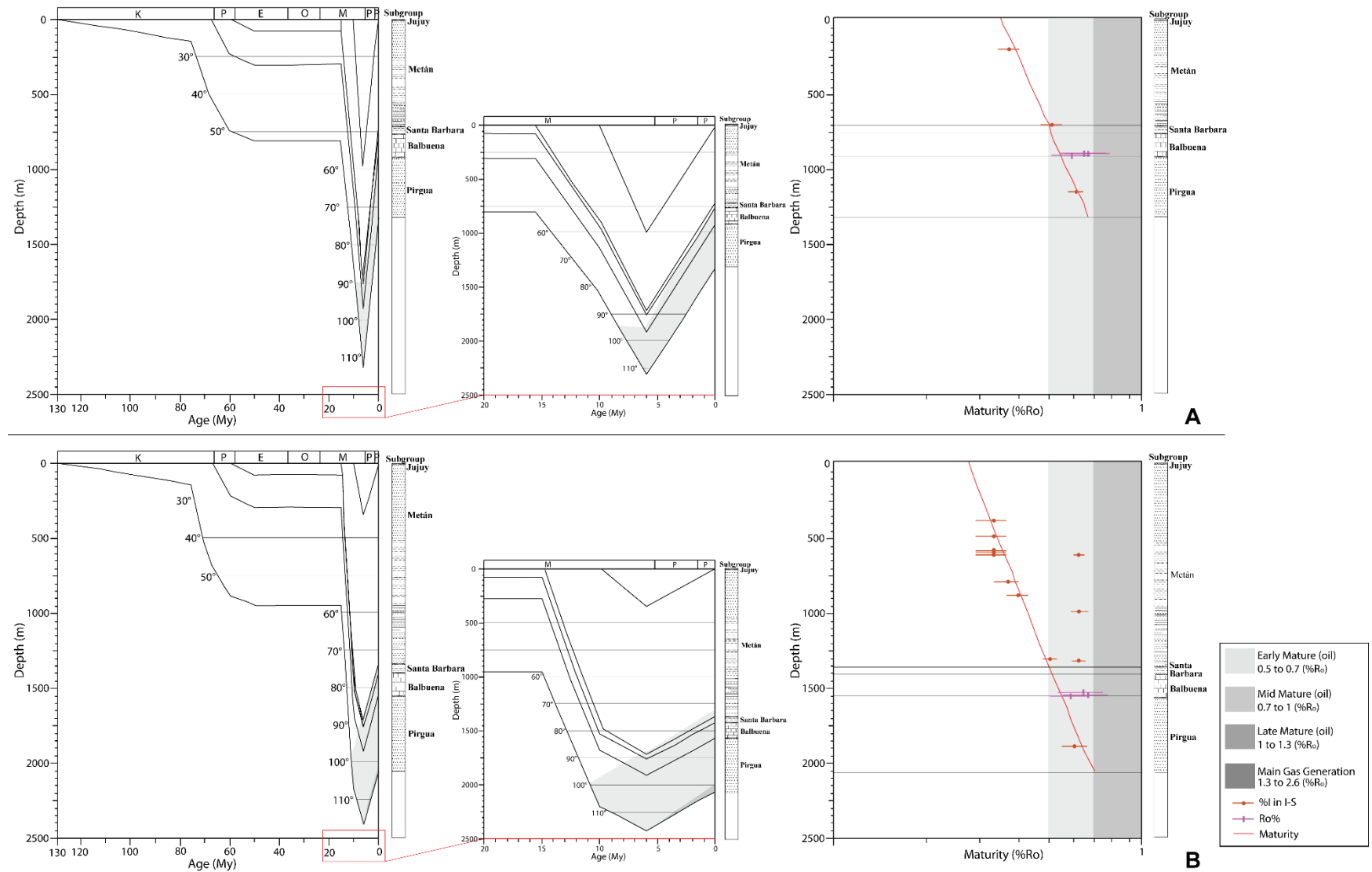


Fig. 5.18 - Representative one-dimensional burial and conductive thermal models of the Sierra de La Candelaria succession in the Anta Yaco (a) and Hotel Termas (b) areas and related present-day thermal maturity distribution in the sedimentary succession.

5.4 Discussion

Thermal calibration data were necessary to reconstruct the thermal evolution of the stratigraphic succession of the Sierra de La Candelaria anticline. The reconstruction was elaborated with the modelling software BasinMod 1D, commonly used in oil exploration studies where heat is transferred by conduction. Accordingly, it uses as input parameters indicators of thermal maturity of the organic matter dispersed in sediments and the stacking order of clays minerals whose transformations are mainly related to the increasing of temperature with depth (Muffler and White, 1969; Hoagland and Elders, 1978; Battaglia et al., 2007). However, when the heat transfer takes place through convection, such as in the case of a geothermal reservoir, the geothermal gradient becomes negligible within the permeable rocks and increases in the overlay lithologies with respect to a pure conductive model (Della Vedova et al., 2001) (Fig. 5.19).

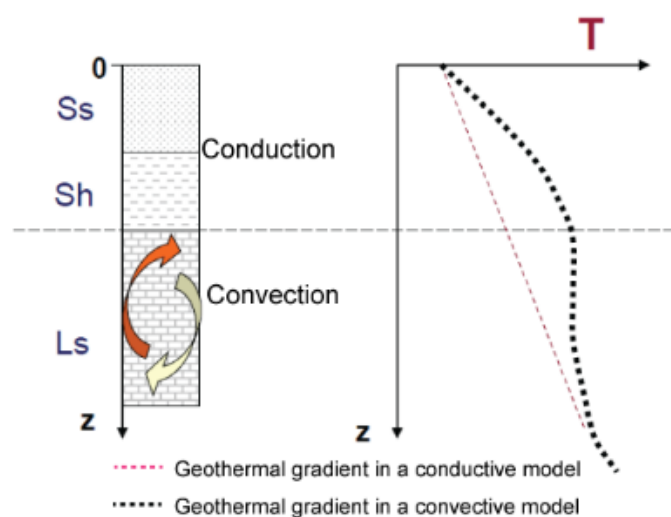


Fig. 5.19 – Difference of the geothermal gradient between a conduction and convective models (from Della Vedova et al., 2001).

In this work, performed conductive models were satisfactory calibrated against thermal indicators in the area of Anta Yaco, far away from the hot springs, where the heat transfer is evidently dominated by conduction. Differently, in the area of the Hotel Termas, close to the hot springs, the modelling does not take into account the heat transfer due to the convection, active after the establishment of the geothermal fluid circulation. Anyway, the obtained results allow to detect the degree of the thermal alteration of the cap-rock of the studied geothermal system and its origin.

5.4.1 Geothermal gradient

Different geothermal gradients were tested for the presented modelling.

The best modelling provided a variable geothermal gradient for the syn-rift (45 °C/km) and, post-rift and syn-orogenic deposits (40 °C/km) (Fig. 5.20).

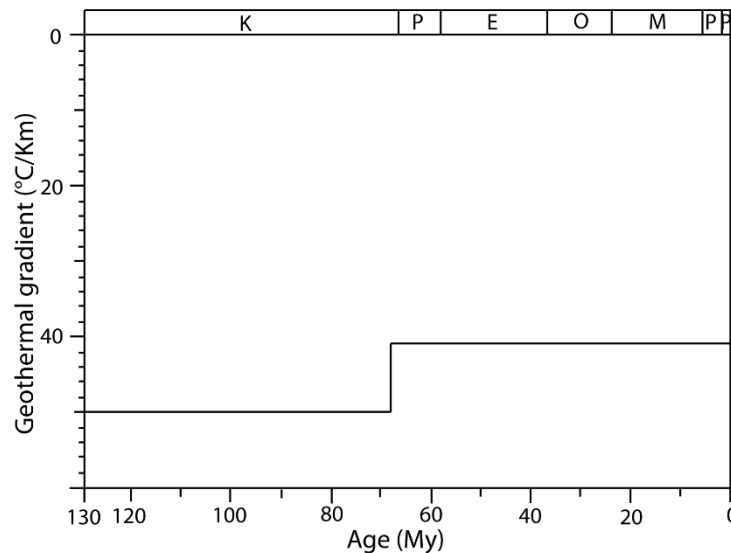


Fig. 5.20 – Geothermal gradients applied for the burial/thermal modelling of the sedimentary succession of Sierra de La Candelaria anticline.

A present-day geothermal gradient of 40°C/Km is reported by Seggiaro et al. (1995) and Invernizzi et al. (2014) on the base of the reconstruction of the geothermal fluids circulation of Rosario de La Frontera system.

Seismologic, gravimetric and magnetotelluric studies in this sector of Andes highlighted the occurrence of a thin mantle lithosphere and a low flexural rigidity in this segment of the Andean foreland (Withman et al., 1992, 1994; Krüger, 1994; Kress et al., 1995). Since this geometry is considered inherited from a thermal anomaly established during mantle-activated Cretaceous rifting (e.g. Kley and Monaldi, 2002), the geothermal gradient of 40°C/Km is supposed to establish from Upper Cretaceous times after the rift event and to be constant up to present time.

5.4.2 Thermal interpretation of the tectono-stratigraphic units

5.4.2.1 Pirgua Subgroup

A sample (AR27) was collected from these deposits in the area of Anta Yaco, far away from the hot springs (Table 5.3; Fig. 5.14).

The results of clay mineralogy analyses indicate the coexistence of two populations of I-S mixed layers with 75% and R1 ordering, and 20% I in I-S and R0.

In this formation, carbonate nodules were observed in poorly developed paleo-soils, probably related to a semiarid to arid climate (Gile et al., 1966; Milnes, 1992) that must have prevailed during the deposition. Several researchers have demonstrated experimentally the strong inhibiting effect of Ca^{2+} ions on the smectite to illite reaction progress (Blank & Seifert, 1976; Roberson & Lahann, 1981; Howard & Roy, 1985; Corrado et al., 2010). The occurrence of Ca^{2+} ions related to the caliche within this formation could explain the occurrence of an R0 ordering. Accordingly, the R1 ordering value was considered as the most representative of the degree of thermal alteration of these deposits. This parameter has been used and fits the performed conductive thermal modelling suggesting its relation with the temperatures experienced by these deposits (Fig. 5.18).

5.4.2.2 Balbuena and Santa Barbara Subgroups

Samples for both thermal maturity and clay mineralogy analyses were collected from the post-rift Yacoraite Fm. along the southwestern limb of the Sierra de La Candelaria anticline, far away the area of the hot springs. Vitrinite reflectance results of 0.6-0.7% whereas XRD on clay minerals indicate the coexistence of both R0 and R3 ordering with a illite% in I-S mixed layers of 20% and 80%, respectively.

The lack of R1 ordering allows excluding diagenetic reactions of clay minerals in response to the burial experienced by these deposits. Accordingly, a detritic origin for the R3 ordering could be possible. R0 values could be used for the burial/thermal modelling. Nevertheless, this value indicates in the same strata slightly lower temperatures than vitrinite reflectance. On this base, I privileged the use of vitrinite reflectance to calibrate models that is by far a more robust thermal parameter for reconstructing sedimentary succession thermal evolution, suggesting a retarded response of clay minerals to temperature increase when compared to organic matter indicators. This is particularly frequent in cases of fast burial (Aldega et al. 2011).

5.4.2.3 Metán Subgroup

Thermal maturity detected on the syn-orogenic succession shows two main clusters of data: samples with low illite content in mixed layers I-S (20 and 25%) and R0 stacking order, and samples with two populations of illite percentage (20-50 and 80%) and, R0 and R3 stacking orders, respectively. The low maturity level is ubiquitous in the structure in correspondence to the poorly fractured outcrops where the deformation is mainly related to

the folding process. Fluid inclusions analyses performed in veins related to the same deformative process record a temperature of entrapment below 50-60°C.

On the contrary, a high maturity level suggested by an R3 stacking order is mainly concentrated along the damage zones of the strike-slip faults close to the hot springs. Figure 5.18 shows as these parameters do not fit the conductive 1D thermal model suggesting the occurrence of a restricted thermal alteration area in these deposits, probably due to the circulation of the geothermal fluids. Fluid inclusions analyses performed on calcite veins associated to the strike-slip faults, confirms this hypothesis indicating a temperature of entrapment of 115°C (sample AR12). Accordingly, convection related to the geothermal fluids played a key role in the thermal alteration of the cap rock only in correspondence of its strike-slip-related fractured areas.

CHAPTER VI

DISCUSSION

The geothermal system of Rosario de La Frontera belongs to the Sierra de La Candelaria anticline, located in the Subandean foreland of the Santa Barbara System (NW Argentina) (Fig.1.1). Surface evidence of the existence of this geothermal system are represented by several hot springs that occur near the town of Rosario de La Frontera, at the northern edge of the anticline, with temperatures ranging between 24° and 90°C. One further hot spring occurs along the south-western limb of the anticline, in the Ceibal area, with surface temperature of about 38°C (Fig. 3.1). Fieldwork observations conducted during this PhD project, suggested that the main geothermal reservoir is represented by the fractured sandstones of the Cretaceous syn-rift deposits (Pirgua Subgroup). The low permeable post-rift and the syn-orogenic deposits (respectively, Balbuena and Santa Bárbara subgroup, and Metán subgroup) were considered to act as the cap-rock of the system (in agreement with Moreno Espelta et al., 1975; Seggiaro et al., 1995; Invernizzi et al., 2014). These deposits are deformed in a N-S trending anticline (Sierra de La Candelaria) developed in the hanging wall of an inverted normal fault and dissected by subsequent strike-slip and normal fault planes. The anticline and the associated structures (faults and fractures) represent the structural context of the geothermal system.

The current study focuses on the quality assessment of the reservoir and cap-rock of the geothermal system and, in particular, on the evaluation of the possibility of exploitation of its thermal fluids, by means of the integration of different methodologies: structural analyses at the outcrop scale, reservoir fracture modelling and paleo-thermal analyses.

Structural investigations were performed in different areas along the studied anticline (Ceibal, Anta Yaco, Balboa and Termas localities) in order to obtain information on the deformation events that affected the regional anticline and to highlight the influence of the structural discontinuities on fluids migration. Moreover, the collected structural data were used to model the fracture network in a 3-D volume of the geothermal reservoir to compute its secondary permeability and porosity.

Paleo-thermal analyses were performed by means of analyses on fluid inclusions on veins filling, clay mineralogy (%I in I-S mixed layers) and vitrinite reflectance on the cap-rock and reservoir, performed on a total of twenty-two samples collected far and close to the area of the hot springs. The aim was to assess the quality of the cap-rock as a function of thermal vs fracturing state. Mono-dimensional thermal and burial models were also built to reconstruct the thermal history and the origin of the thermal anomaly of the studied geothermal system.

Furthermore, the integration with hydrogeological, geochemical and geophysical studies available on this geothermal system (Barcelona et al., 2014; Invernizzi et al., 2014; Chiodi et al., 2015) allowed to evaluate the sustainability of the geothermal resource through the elaboration of a conceptual model of the reservoir fluid.

Results obtained from the integrated analysis and modelling have been illustrated in chapters 3, 4 and 5 and they will be synthetically discussed and integrated all together in this chapter (CHAPTER 6).

The best starting point in order to assess the reservoir quality for exploration programs consists in the elaboration of a reliable tectonic model of the studied geothermal field. It helps making predictions about lithology, faulting, and fluid flow in and out of the reservoir. Moreover, the formation and evolution of natural fractures is closely related to the deformation history of the host rock. As a whole, it provides a robust data set for the location of wells.

The kinematic evolution and timing of the Sierra de La Candelaria anticline was deciphered by analysing (1) the structural relationships with the faults mapped in the area, (2) the geometry of the different stratigraphic units, and (3) the structural data collected at the outcrop scale (CHAPTER 3). The results show that the Sierra de La Candelaria regional anticline developed according to a kinematic model of transpressional inversion compatible with the latest Andean regional WNW-ESE shortening, acting on a pre-orogenic N-S normal fault (see Figs. 3.1, 3.13). In the late stage of inversion, the development of a NNW-SSE oblique fault plane, dissecting the regional anticline in the northern portion, defined a push-up geometry controlling the development of the minor Termas and Balboa anticlines.

Many examples derived from seismic interpretation and analogue modelling have demonstrated that in a positive inversion, push-up geometries are related to the transpressional reactivation of pre-existing normal faults (Harding 1985; Vejbaek and

Andersen, 1987; McClay, 1989; Deeks and Thomas, 1995; de Jager, 2003; Krzywiec et al., 2003; Cooper and Warren, 2010; Pace et al., 2012; Pace and Calamita, 2013).

In this reconstruction, the Balboa anticline might represent the early developed northern closure of the Sierra de la Candelaria anticline, in agreement with Barcelona et al. (2014).

Brittle deformation recognized at the outcrop scale is robustly consistent with the transpression event recognized at regional scale, recording both the related folding process and the strike-slip kinematics.

In detail, the first stage of the deformation is better recorded at the outcrop scale in the Ceibal and Anta Yaco areas, along the western limb of the regional anticline. Syn-folding features are represented by E-W generic and shear fractures mainly occurring in the strata of Pirgua Subgroup, and by NNW-SSE and E-W striking conjugate strike-slip fractures occurring in the strata of Anta Formation (see Figs. 3.3, 3.4). Differently, NNE-SSW and ENE-WSW generic fractures, occurring in the Ceibal area, and N-S, NNW-SSE and NNE-SSW trending ones, occurring in the Anta Yaco area, are mainly related to the subsequent deformative events testified by the faults mapped in these areas (see Fig. 3.2).

In the northern Termas anticline, close to the hot springs area, where Anta Formation extensively crops out, the brittle deformation is more intense and records both the folding process and the strike-slip kinematics related to the late transpressive event that took place along the NNW-SSE oblique fault plane that dissect the early formed anticline in its central portion. At the outcrop scale, NNW-SSE left-lateral faults, with the associated Riedel shears, and WNW-ESE calcite-filled veins testify mainly the strike-slip kinematics. At the same time, different meso-structures record the folding process: NNE-SSW gypsum extensional and shear veins, NNW-SSE and E-W conjugate shear fractures, NNW-SSE conjugate system of extensional fractures, N-S-trending joint and calcite filled veins. Moreover, E-W conjugate system of extensional fractures, and ENE-WSW and W-E normal faults are interpreted to reflect the final stage of the folding process (see Figs. 3.7, 3.8, 3.9, 3.10, 3.11).

Differently, in the area of the Balboa anticline, the structural data collected in correspondence of the outcrops of Pirgua Subgroup mainly testify the strike-slip kinematics: NW-SE and N-S deformation bands and N-S, NNW-SSE and NNE-SSW generic fractures (see Fig. 3.5).

Fracture frequency analysis was performed in the four investigated areas by means of scan-line surveys (CHAPTER 4). The results show that fractures characterized by the

highest values of frequency are related to the transpression event along the NNW-SSE oblique fault plane that dissect the anticline in its central portion. Furthermore, the analyses of the fracture frequency distribution shows that Termas anticline represents the most fractured area of the Sierra de La Candelaria ridge (see Fig. 4.6). On the contrary, the area of Anta Yaco represents the less fractured area where fracturing mainly records the folding process occurred in the early stage of positive inversion. Accordingly, the secondary porosity and permeability of the reservoir deposits, computed by means of fracture network modelling, show the highest values ($4.2\text{E-}04$ and until $\sim 20\text{mD}$, respectively) in correspondence to the Termas and Balboa anticlines and in the area of Ceibal (see Table 4.4).

In terms of fluid circulation, the results of the qualitative and quantitative structural analysis together with the performed DFN models, show that fault and fracture network can affect fluid circulation. NE-SW and NNW-SSE fault planes, with the associated WNW-ESE riedel planes, in the latter case, associated with the intermediate and late stages of the positive inversion, can be considered the main structures controlling the migration paths of hot fluids at depth and their upwelling from the reservoir to the surface. This evidence derives from the calcite-filled fractures that develop along those fault systems that are well exposed in the area of Ceibal and of Balboa and Termas anticlines. The DFNs show that permeability is highest in the direction parallel to the strike of the fault planes. These results, with special regard to the variation of the permeability values among the different sectors of the analysed structure, suggest that the NNW-SSE fault plane may act as a barrier to fluid flow across its strike, producing a reservoir compartmentalization and its confinement at depth.

As a whole, the DFN models performed in the reservoir volume indicate that fracture network enhances its permeability and its fractured portion represents the 0.03% of the total volume corresponding to 53Km^3 on the base of the elaboration of the 3D reservoir model (see Figs 4.5, 4.9).

Since the analysed reservoir is mainly represented by sandstone, also its primary porosity and permeability may play an important role in the circulation and storage of fluids at depth. Nevertheless, a full characterization of the reservoir deposits is beyond the aim of this thesis. The only available data on its primary porosity and permeability, measured on a sample collected from the Arroyo Bonete Puca high valley (see Fig. 3.1), correspond to low values of 7.2% and $\sim 81.2\text{mD}$, respectively (Invernizzi et al., 2014).

Furthermore, in a foreseeable exploitation of the thermal fluids of the studied geothermal system, particular attention was devoted to the northern portion of the regional anticline. I considered this area as the most interesting one, since here the reservoir reaches the maximum depths (~2,100m and ~2,400m at the northern edge of Termas and Balboa anticlines, respectively) ensuring to the fluids to achieve the highest temperatures (see Figs. 3.1 and 4.5).

The 3-D reservoir model allowed to compute the volume belonging to this northern portion. It results of 28Km³ with a fracture volume of 0.001Km³ (see Fig. 4.10)

Furthermore, considering the portion where temperature exceeds 60°C, at least for direct heat uses, a high value of extractable geothermal heat from this reservoir corresponding to $1.89 \cdot 10^{17}$ J was computed.

In the northern area of the Sierra de La Candelaria anticline, where the cap-rock extensively crops out, its quality was investigated by evaluating the degree of thermal alteration vs. fracturing state (CHAPTER 5). In general, the results show that the cap-rock act as a good insulator since the thermal alteration is limited to its fractured zones where the deformation mainly testifies the strike-slip kinematics related to the NNW-SSE oblique fault planes.

In detail, the analyses of clay mineralogy indicate a low thermal maturity of these deposits (Fig. 5.14, Table 5.3). The identified I-S mixed layers show mostly R0 structures with low amounts of illite (20-25%). On the contrary, a high degree of thermal alteration, mainly indicated by R3 structures, occur in correspondence of the area of the hot springs (Hotel Termas area). These R3 structures do not fit the performed purely conductive 1D thermal models suggesting that hot fluids circulation may have played a key role in the thermal alteration of the cap-rock only in correspondence of its most fractured portions (Fig. 5.18). Furthermore, fracturing features and distribution, derived from field mapping and structural investigations at the meso-scale, suggest that deformation due to the strike-slip kinematics rather than to folding may have focused hot fluids and driven localized thermal alteration of the cap-rock.

As demonstrated by the thermal models reconstructed in the two investigated areas (Termas anticline and Anta Yaco area), the thermal maturity characterizing the cap-rock deposits is mainly a function of its experienced burial history under a geothermal gradient of about 40 °C/Km established after the Cretaceous rifting event (in agreement with Seggiaro et al., 1995 and Invernizzi et al., 2014). In this scenario, the rift succession

experienced a thermal evolution compatible with late diagenetic conditions in the early stages of hydrocarbon generation during Upper Miocene times. At that time, the reservoir deposits reached a maximum temperature of about 110 °C. The differential exhumation between the two areas have led these rocks at different depths at present (~2,100m and ~1,300m in the Hotel Termas and Anta Yaco area, respectively). In particular, in the area of the Hotel Termas, where the rocks were less exhumed, the cap-rock is thickest (1570m).

The results of the structural investigations and modelling, together with the available geochemical data, allow to integrate the previously reconstructed conceptual model of the fluid circulation belonging to the Rosario de La Frontera geothermal system (Invernizzi et al., 2014; Chiodi et al., 2015) (Fig. 6.1).

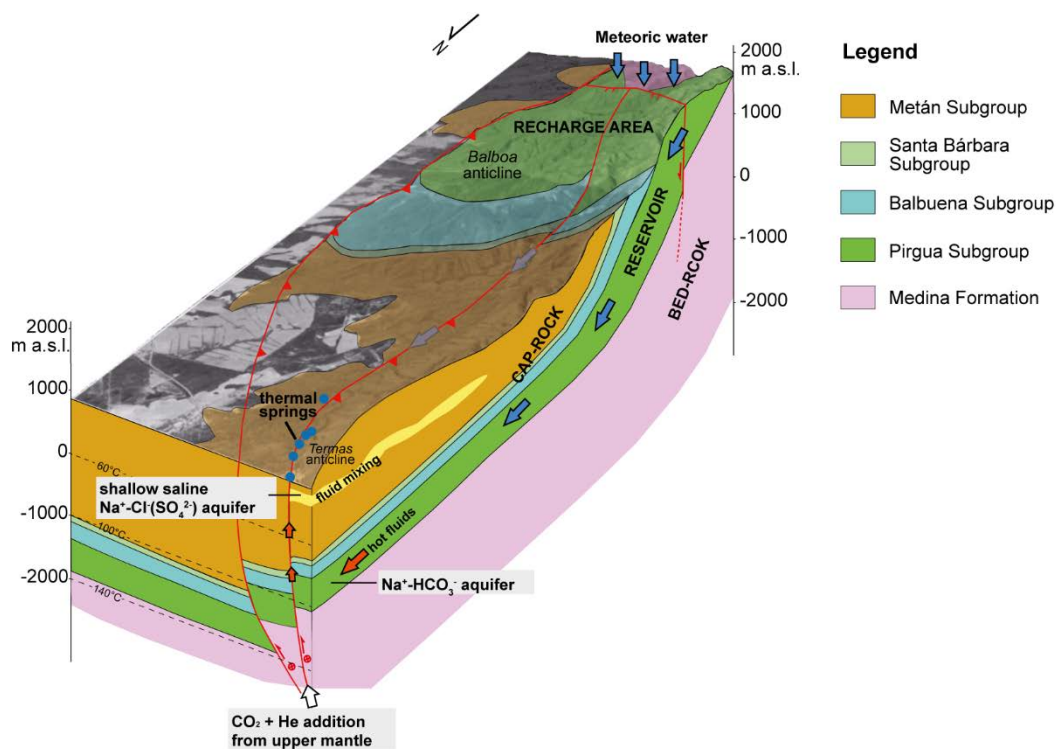


Fig. 6.1 - Conceptual cartoon illustrating the path of the fluid flow based on the integrated results of this study. Meteoric water infiltrates to depth in the southern sector of the Sierra de La Candelaria anticline in correspondence of the permeable Pirgua Subgroup fractured and porous rocks and through the E-W trending normal fault. At depth, heating due the geothermal gradient of 40°C/Km originates the hydrothermal fluids. The NNW-SSE oblique fault plane enhances the motion of the thermal fluids at depth and their upflow toward the surface (modified from Chiodi et al., 2015).

In this reconstruction, I consider that the fault plane trending NNW-SSE, responsible of the growing and exhumation of the Termas anticline, could represent a preferential path along which fluids move at depth from the recharge area to the north and toward the surface.

Isotopic data ($\delta^{18}\text{O}$ and δD) suggest that the deep hydrothermal reservoir, represented by the syn-rift deposits, is mainly recharged by meteoric water that could infiltrate from an area close to the thermal baths, located in the northern sector of Sierra de la Candelaria ridge in correspondence of the outcrops of the Pirgua Subgroup deposits (Invernizzi et al., 2014). This water shows a Na– HCO_3 composition produced by water–rock interactions involving sedimentary formations mostly consisting of conglomerates and sandstones, which are interbedded with alkaline volcanic rocks, shales and limestones (Chiodi et al., 2015). A relatively long residence time (>50 years; Smedley et al., 2002) of water at depth was computed by means of analyses of tritium content (Invernizzi et al., 2014).

In this framework, the E-W trending normal fault, dipping to the north and occurring in the central sector of the regional anticline, could enhance the infiltration of meteoric water at depth (Seggiaro et al., 1997). Moreover, the two faults that confine the reservoir in the three-dimensional reconstruction (the inverted Cretaceous normal fault that borders the anticline to the east and N-S lineament to the west) may act as barriers for the motion of the fluid at depth.

The aquifer also receives significant contributions of crustal CO_2 and He from mantle degassing, the latter probably favoured by the regional tectonics characterized by a deep detachment (at about 10 km depth) in the basement of the Santa Bárbara thick-skinned thrust system and a thinned lithosphere (Chiodi et al., 2015).

The uprising thermal fluids mix with a relatively high salinity Na–Cl dominated shallow aquifer (~150 m) produced by the interaction of meteoric water with evaporitic deposits of the Anta Formation (Bercheñi et al., 2003; Barcelona et al., 2014; Chiodi et al., 2015).

At depth, water moves inside the reservoir assisted by its primary and secondary permeability. Considering a present geothermal gradient of 40 °C/km, reported by bibliography (Seggiaro et al., 1995; Invernizzi et al., 2014; Chiodi et al., 2015) and confirmed by the performed conductive 1D thermal models, and a surface temperature of 20 °C (Invernizzi et al., 2014), the meteoric water can reach 60 °C at 1,000 m of depth and can exceed temperatures of 100°C at the base of the reservoir located deeper than 2,000 m at the northern edge of Termas and Balboa anticlines. A temperature ranging between 100–130°C for the reservoir fluids is also suggested by various geothermometers (Seggiaro et al., 1995; Invernizzi et al., 2014; Chiodi et al., 2015). As a consequence, a convective circulation can be triggered at depth within the system. Fluid inclusions analyses on veins filling indicate an entrapment temperature of 115°C suggesting that no important changes may have occurred in fluid circulation from its establishment.

As a whole, the water ascent can be enhanced by the fracture systems well developed in correspondence of the northern end of the plunging structure, occurring at surface with the alignment of the thermal springs.

These results confirm that the Rosario de La Frontera geothermal system represents an important site to improve the sustainable development of the cities of the Salta province. The heat stored at depth in the large volume of the geothermal aquifer can be utilized for different purposes.

Firstly, economical benefits can be derived by increasing the thermal tourism and balneology with the construction of new thermal centres or by implementing the already existing structure of the Hotel Termas. Furthermore, the undersaturation in calcite and other salts of waters may render the geothermal aquifer suitable for district heating (tele-heating) and cooling by installing appropriate heat exchangers (Chiodi et al., 2015).

Other applications for direct or indirect uses, e.g. green-housing, agro-industrial activities and electric power generation in general, could be also feasible considering the high temperatures reached by the thermal fluids at depth. With this perspective, the northern edge of Termas and Balboa anticlines represent the best suited areas for location of productive deep-drillings since the reservoir reaches the maximum depths allowing the fluid to achieve temperatures over 100°C. Electricity generation from fluids with these temperatures could come from a binary cycle power plant.

Furthermore, considering the reservoir compartmentalization ruled by the NNW-SSE fault plane, occurring in the central area of the regional anticline, I suggest that the area located in the northern buried plunge of the Balboa anticline could represent the best site for a potential exploitation of the thermal fluids in order to preserve the geothermal resource exploited at present for thermal and bathing purposes by the Hotel Termas structure. This hypothesis is further supported by the presence of a low resistivity anomaly, recently detected by means of AMT investigations (Barcelona et al., 2013), that indicates the occurrence of fluids preserved at depths in the Pirgua Subgroup coarse deposits at the core of the Balboa anticline (Figs. 6.2, 6.3).

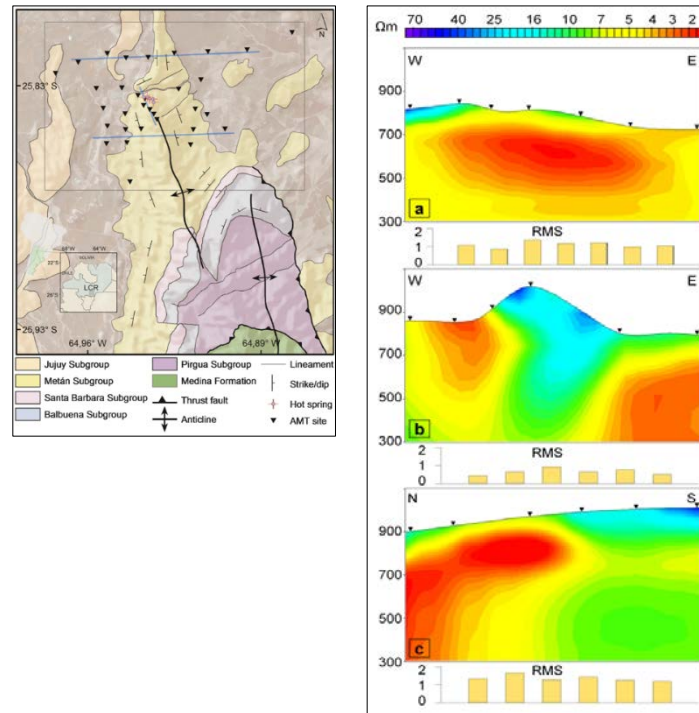


Fig. 6.2 - 2D inversion models along E-W (a, b) and N-S profiles (c) representing the resistivity distribution in the northern sector of the Sierra de La Candelaria anticline. Histograms shows the misfit for each site included in the profile. Location of the surveys area and AMT sites are indicate on the left in the geological map with black rectangle and black triangles, respectively. Solid blue lines corresponds to the profiles where 2D inversion of AMT data has been carried out.

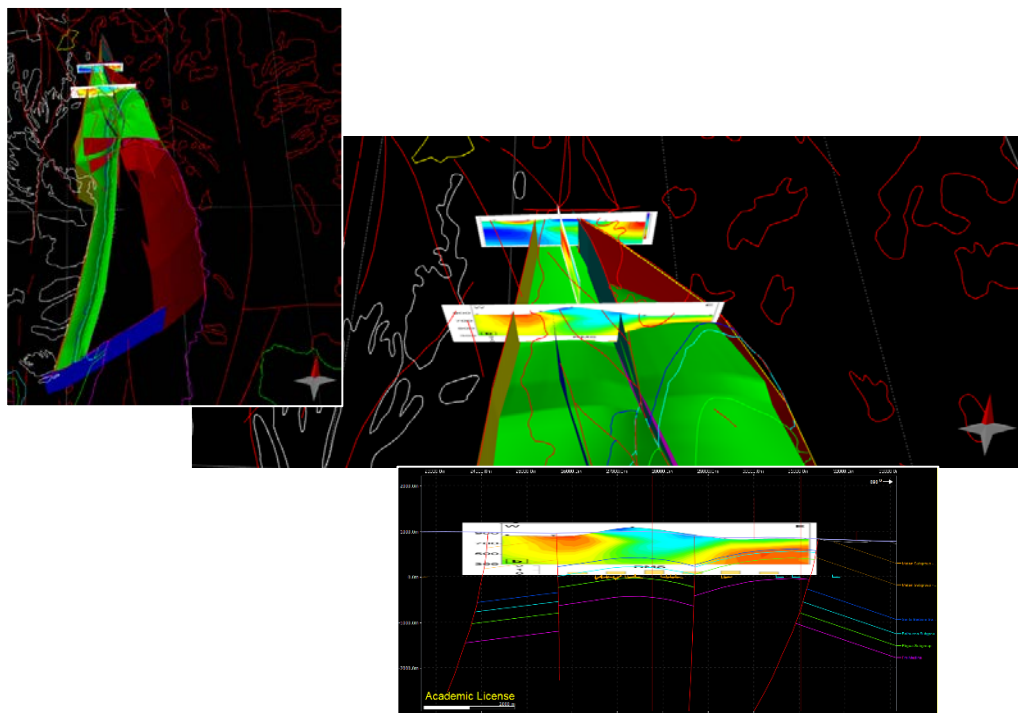


Fig. 6.3 Three-dimensional reservoir model integrated with the AMT profiles. Green surface indicates the top of the reservoir. The deep conductive anomaly detected at the eastern margin of the southern E-W profiles (b in figure 6.2), indicating the presence of hot fluids, intercept the reservoir deposits.

In order to confirm the rule played by the NNW-SSE fault plane in the reservoir compartmentalization, different hydrogeological scenarios of the geothermal system were simulated during a graduate thesis, whose I was a co-tutor (Palucci, 2014). The simulations were performed with the aid of the software Groundwater Vistas, by changing the permeability of this fault plane along the three directions (e.g. K_x, K_y and K_z) (Balsamo and Storti, 2010) (Table 6.1).

Table 6.1 – Hydrogeological models performed by varying the permeability of the NNW-SSE fault plane along the three directions (K_x, K_y, K_z). The models RdF_impermeable, RdF_permeable and RdF_nofault were simulated considering the analysed fault impermeable and permeable along the three directions, and with the same permeability of the host rock.

Models	K _x	K _y	K _z	Mass balance error	target vs mean residual (springs)
RdF_impermeable	0.000001	0.000001	0.000001	-0.00894	-76 / -74.27
RdF_X1	0.00001	0.000001	0.000001	-0.00894	-76 / -74.27
RdF_X2	0.001	0.000001	0.000001	-0.00163	-76 / -73.75
RdF_X3	0.1	0.000001	0.000001	-0.03143	-76 / -73.44
RdF_Y1	0.000001	0.00001	0.000001	-0.00349	-76 / -74.26
RdF_Y2	0.000001	0.001	0.000001	-0.00770	-76 / -74.07
RdF_Y3	0.000001	0.1	0.000001	-0.02393	-76 / -73.26
RdF_Z1	0.000001	0.000001	0.00001	-0.01213	-76 / -74.27
RdF_Z2	0.000001	0.000001	0.001	-0.01155	-76 / -74.27
RdF_Z3	0.000001	0.000001	0.1	-0.00339	-76 / -74.27
RdF_YZ1	0.000001	0.00001	0.00001	-0.00807	-76 / -74.26
RdF_YZ2	0.000001	0.001	0.001	-0.00522	-76 / -74.09
RdF_YZ3	0.000001	0.1	0.1	-0.04067	-76 / -73.87
RdF_permeable	K res	K res	K res	-0.00116	-76 / -75.32
RdF_nofault	K host rock	K host rock	K host rock	-0.03663	-76 / -73.52

The hydrogeological scenario obtained by considering the fault plane impermeable across its strike and permeable along its strike and plunge (RdF_YZ3), best fit the hydrogeologic water balance computed by Invernizzi et al. (2014) (Fig. 6.4).

These simulations confirm the reservoir compartmentalization produced by the NNW-SSE fault plane, suggesting that the northern plunge of the Balboa anticline represents the best suited areas for a potential exploitation of the thermal fluids of the Rosario de La Frontera geothermal system.

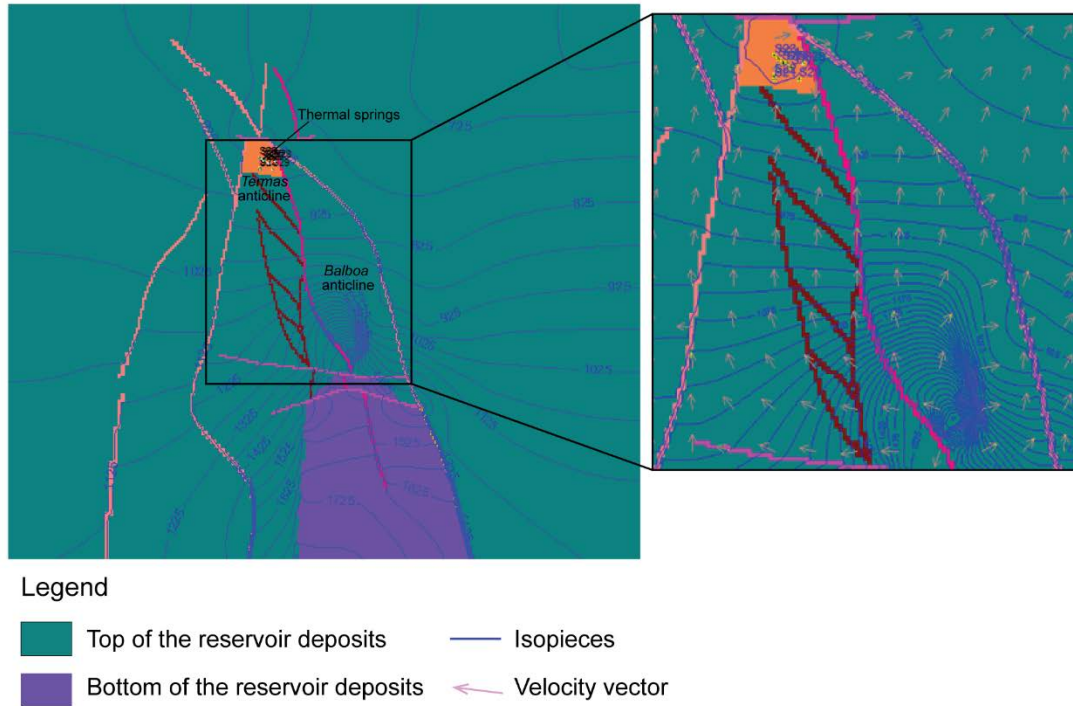


Fig. 6.4 – RdF_YZ3 hydrogeological model performed considering the NNW-SSE fault plane permeable along its strike and plunge, and impermeable across its strike. In the model, the N-S fault plane, bordering to the east the Sierra de La Candelaria anticline and the western N-S lineament (pink lines) are considered impermeable, acting as barrier to fluid flow. Differently, the E-W trending normal fault planes, occurring in the central portion, are considered permeable since they could enhance the infiltration of meteoric water at depth. Faults planes indicated with red lines are not considered in the simulations.

It is visible a shifting of the isopieces between the two area to the east and to the west of the central NNW-SSE fault plane (a). Velocity vectors (b) show as this fault plane acts as a conduit along its strike.

References cited

- Aceñolaza, F.G., Miller, H., Toselli, A.J., 2002. Proterozoic-Early Paleozoic evolution in western South America. A discussion. *Tectonophysics* 354, 121-137.
- Aceñolaza, G. F. 2005. The Cambrian System in Northwestern Argentina: stratigraphical and palaeontological framework. Reply. *Geologica Acta*, 3, 73-77. Barcelona.
- Allmendinger, R.W., Ramos, V.A., Jordan, T.E., Palma, M., Isacks, B.L., 1983. Paleogeography and Andean structural geometry, northwest Argentina. *Tectonics* 2 (1), 1-16.
- Allmendinger, R.W., Gubbels, T., 1996. Pure and simple shear plateau uplift, Altiplano-Puna, Argentina and Bolivia. *Tectonophysics* 259, 1-13.
- Allmendinger, R., Jordan, T., Kay, S., and Isacks, B., 1997. The evolution of the Altiplano-Puna plateau: *Annual Review of Earth and Planetary Sciences*, 25, 139-174, doi: 10.1146/annurev.earth.25.1.139.
- Antonellini, M., Aydin, A., 1994. Effect of faulting on fluid flow in porous sandstones: petrophysical properties. *AAPG Bulletin* 78, 355-377.
- Antonellini, M.A., Aydin, A., Pollard, D.D., 1994. Microstructure of deformation bands in porous sandstones at Arches National Park, Utah. *Journal of Structural Geology* 16, 941-959.
- Antonellini, M., Cilona, A., Tondi, E., Zambrano, M., Agosta, F., 2014. Fluid-flow numerical experiments of faulted porous carbonates, Northwest Sicily (Italy). *Marine and Petroleum Geology*, 55, 186-201.
- Aramayo Flores, R. F., 1989. El cinturón plegado y sobrecorrido del Norte Argentino, *Bol. Inf. Pet.*, 17, 2-16.
- Aydin, A., Johnson, A.M., 1978. Development of faults as zones of deformation bands and as slip surfaces in sandstone. *Pure and Applied Geophysics* 116, 931-942.
- Aydin, A., and A. M. Johnson, 1983. Analyses of faulting in porous sandstones. *Journal of Structural Geology*, 5, 19-31.
- Aydin, A. 2000. Fractures, faults, and hydrocarbon entrapment, migration, and flow. *Marine and Petroleum Geology* 17, 797-814.
- Babadagli, T. 2001. Scaling of Cocurrent and Countercurrent Capillary Imbibition for Surfactant and Polymer Injection in Naturally Fractured Reservoirs, *SPEJ*, Dec., 465-478.

- Babeyko, A.Y., and Sobolev, S.V., 2005. Quantifying different modes of the late Cenozoic shortening in the central Andes: *Geology*, 33, 621-624, doi: 10.1130/G21126.1
- Baby, P., G. Herail, J. M. Lopez, J. Oller, J. Pareja, T. Sempere, and D. Tufiño, 1989. Structure de la Zone subandine de Bolivie: Influence de la géométrie des séries sédimentaires antéorogéniques sur la propagation de chevauchements., *C.R. Acad. Sci. Paris, Sér. II*, 309, 1717–1722.
- Baby, P., G. Herail, R. Salinas, and T. Sempere, 1992. Geometry and kinematic evolution of passive roof duplexes deduced from cross section balancing: Example from the foreland thrust system of the southern Bolivian Subandean zone, *Tectonics*, 11, 523-536.
- Balsamo, F., Storti, F., 2010. Grain size and permeability evolution of soft-sediment extensional sub-seismic and seismic fault zones in high-porosity sediments from the Croton basin, southern Apennines, Italy. *Mar. Pet. Geol.* 27, 822837. <http://dx.doi.org/10.1016/j.marpetgeo.2009.10.016>.
- Barazangi, M., and Isacks, B.L., 1976. Spatial distribution of earthquakes and subduction of the Nazca plate beneath South America: *Geology*, 4, 686-692.
- Barberi, F., Carapezza, M.L., Cioni, R., Lelli, M., Menichini, M., Ranaldi, M., Ricci T., Tarchini L., 2013. New geochemical investigations in Platanares and Azacualpa geothermal sites (Honduras). *J. Volcanol. Geotherm. Res.*, 237, 113-134.
- Barcelona, H., Favetto, A., Peri, V., Pomposiello, C., Ungarelli, C., 2013. The potential of audiomagnetotellurics in the study of geothermal fields: a case study from the northern segment of the La Candelaria Range, northwestern Argentina. *J. Appl. Geophys.* 88, 83-93.
- Barcelona, H., Peri, G., Tobal, J., Sagripanti, L., Favetto, A., 2014. Tectonic activity revealed by morphostructural analysis: Development of the Sierra de la Candelaria range, northwestern Argentina. *Journal of South American Earth Sciences* 56, 376-395.
- Barchi, M., Lavecchia, G., Menichetti, M., Minelli, G., Piali, G., Nardon, S., 1991. Analisi della fratturazione del Calcere Massiccio in una struttura anticlinalica dell'Appennino Umbro-marchigiano. *Boll. Soc. Geol. Ital.* 110, 101–124.
- Barchi, M., Cardellini C., Checcucci R., Frondini F., Fulignati P., Pauselli C., Pazzaglia F., Sbrana A., Viterbo A., 2013. Integrated Multidisciplinary Approach for the Study of the Geothermal Potential of Umbria (Central Italy). *Proceedings of the European Geothermal Congress*. Pisa, 3-7 June, 2013.

- Barker, C.E., and Pawlewicz, M.J., 1994. Calculation of vitrinite reflectance from thermal histories and peak temperatures, A comparison of methods, in Mukhopadhyay, P.K., and Dow, W.G., eds., *Vitrinite Reflectance as a Maturity Parameter: Applications and Limitations: American Chemical Society Symposium Series*, 570, 216–229.
- Barthélémy, J.-F., M. L. E. Guiton, and J.-M. Daniel, 2009. Estimates of fracture density and uncertainties from well data: *International Journal of Rock Mechanics and Mining Sciences*, 46, 590-603, doi:10.1016/j.ijrmms.2008.08.003.
- Barton, C. C. 1995. Fractal analysis of the scaling and spatial clustering of fractures in rock. In: Barton, C.C. & La Pointe, P. R. (eds). *Fractals in the Earth Sciences*. Plenum Press, New York 141-177.
- Barton, C.C, and Larsen, E., 1985. Fractal geometry of two-dimensional fracture networks at Yucca Mountain, southwest Nevada, in Stephansson, Ove, ed., *Fundamentals of rock joints: International Symposium on Fundamentals of Rock Joints*, Bjorkliden, Lapland, Sweden, September 1985, Centek Publishers, Lulea, Sweden, Proceedings, p. 77-84.
- Barton, C.C., and Hsieh, P.A., 1989, Physical and hydrologic-flow properties of fractures: *American Geophysical Union, Field Guide Book*, T385, 28th International Geological Congress, July 1989, 36.
- Basin Mod® 1-D for Windows™, version 5.4 Software, 1996, A Basin Analysis Modelling System by Platte River Associates, Denver.
- Battaglia, S., Gherardi, F., Gianelli, G., Leoni, L., Origlia, F., 2007. Clay mineral reactions in an active geothermal area (Mt. Amiata, southern Tuscany, Italy). *Clay Minerals* 42, 353–372.
- Beck, S.L., and Zandt, G., 2002. The nature of orogenic crust in the central Andes: *Journal of Geophysical Research*, 107, doi: 10.1029/2000JB000124.
- Bertani R., Cappetti G., 1995. Numerical simulation of the Monteverdi zone western border of the Larderello geothermal Field. *World Geothermal Congress Proceedings*, Florence, 1735–1740
- Bianucci, H., Acevedo, O., Cerdán, J., 1981. Evolución tectosedimentaria del Grupo Salta en la Subcuenca Lomas de Olmedo (provincias de Salta y Formosa). In: *Actas 8th Congr. Geol. Arg.*, vol. 3, 159-172.
- Bigi, S., Marchese, M., Meda, M., Nardon, S., Franceschi, M., Preto N., 2014. Discrete fracture network of the Latemar carbonate platform. *Italian Journal of Geosciences*, DOI:10.3301/IJG.2014.34

- Blank, P. & Seifert, W. 1976. Zur Untersuchung diagenetischer Tonmineralbildungen und deren experimentelle Modellierung. *Zeitschrift für Angewandte Geologie*, 22, 560–564.
- Bodnar, R.J., 1993. Revised equation and table for determining the freezing point depression of H₂O–NaCl solutions. *Geochim. Cosmochim. Acta*, 57, 683-684.
- Bodnar, R.J., 1994. Philosophy of fluid inclusion analysis. In *Fluid Inclusions in Minerals, Methods and Applications* (B. De Vivo & M. L. Frezzotti, eds.) Virginia Tech, Blacksburg, VA, 1-6.
- Bodnar, R.J., 2003a. Introduction to fluid inclusions. In *Fluid Inclusions: Analysis and Interpretation* (I. Samson, A. Anderson & D. Marshall, eds.). Mineral. Assoc. Can. Short Course, 32, 1-8.
- Bodnar, R.J., 2003b. Interpretation of data from aqueous-electrolyte fluid inclusions. In I. Samson, A. Anderson, & D. Marshall, eds. *Fluid Inclusions: Analysis and Interpretation*. Mineral. Assoc. Can., Short Course Ser. 32, 213-232.
- Bodvarsson, G., 1974. Geothermal resource energetics. *Geothermics* 3, 83–92.
- Bono, P., 1981. Valutazione preliminare del potenziale geotermico della regione Lazio. *Geol. Romana*, 20, 69-78.
- Botti, F., Aldega L. and Corrado, S., 2004. Sedimentary and tectonic burial evolution of the Northern Apennines in the Modena-Bologna area: constraints from combined stratigraphic, structural, organic matter and clay mineral data of Neogene thrust-top basins: *Geodinamica Acta*, 17, 185-203.
- Brogi A., Lazzarotto A., Liotta D. & Ranalli G., 2003. Extensional shear zones as imaged by reflection seismic lines: the Larderello geothermal field (central Italy). *Tectonophysics* 363, 127-139.
- Brogi A., Lazzarotto A., Liotta D. & Ranalli G., 2005a. Crustal structures in the geothermal areas of Southern Tuscany (Italy): insights from the CROP 18 deep seismic reflection lines. *J. Volcan. Geotherm. Res.*, 148, 60-80.
- Brogi A., Lazzarotto A. & Liotta D., 2005b. Results of the CROP 18 Project. *Boll. Soc. Geol. It.*, 3, 239 pp.
- Brogi, A., Liotta, D., Ruggieri G., Capezzuoli E., Meccheri M., Dini A., 2015. An overview on the characteristics of geothermal carbonate reservoirs in southern Tuscany. *Italian Journal of Geosciences*, DOI:10.3301/IJG.2014.41.
- Bustin, R.M., Barnes, M.A., and Barnes, W.C., 1990. Determining levels of organic diagenesis in sediments and fossil fuels, in McIlreath, I.A., and Morrow, D.W., eds., *Diagenesis: Geoscience Canada Reprint*, 4th series, 205-226.

- Butler, R.W.H., 1982. The terminology of structures in thrust belts. *Journal of Structural Geology* 4, 239-245.
- Butler, R. W. H., 1992, Hydrocarbon maturation, migration and tectonic loading in the Western Alps, in England, W. A., and Fleet, A.J., eds., *Petroleum migration: Geological Society of London Special Publication*, 59, 227-244.
- Cantón, E., 1896. *Estudios de las aguas minerales del norte de la República Argentina*, 283.
- Cahill, T.B., Isacks, L., 1992. Seismicity and shape of the subducted Nazca plate. *J. Geophys. Res.* 97, 17.503-17.529.
- Cardoso, R.R., Hamza, V.M., and Alfaro, C., 2010. Geothermal resource base for South America: A continental perspective. *Proceedings World Geothermal Congress 2010, Bali, Indonesia*, 25-29 April 2010, 6 pp. Website: <http://www.geothermal-energy.org/pdf/IGAstandard/WGC/2010/1618.pdf>
- Carapezza, M.L., Ranaldi, M., Gattuso, A., Pagliuca, N.M., Tarchini, L., 2015. The sealing capacity of the cap rock above the Torre Alfina geothermal reservoir (Central Italy) revealed by soil CO₂ flux investigations. *Journal of Volcanology and Geothermal Research* 291, 25-34.
- Carminati, E., Aldega, L., Trippetta, F., Shaban, A., Narimani, H., Sherkati, S., 2014. Control of folding and faulting on fracturing in the Zagros (Iran): The Kuh-e-Sarbalesh anticline. *Journal of Asian Earth Sciences*, 79, 400-414.
- Carrapa, B., Adelmann, D., Hilley, G.E., Mortimer, E., Sobel, E.R., Strecker, M.R., 2005. Oligocene range uplift and development of plateau morphology in the southern Central Andes. *Tectonics* 24. <http://dx.doi.org/10.1029/2004TC001762>
- Carrera, N., Muñoz, J.A., Sábat, F., Mon, R., Roca, E., 2006. The role of inversion tectonics in the structure of the Cordillera Oriental (NW Argentinean Andes). *Journal of Structural Geology* 28(11), 1921-1932, doi:10.1016/j.jsg.2006.07.006.
- Carrera, N., Muñoz, J.A., 2008. Thrusting evolution in the southern Cordillera Oriental (northern Argentine Andes): Constraints from growth strata. *Tectonophysics* 459, 107-122.
- Cataldi, R., Squarci, P., 1978. Valutazione del potenziale geotermico in Italia con particolare riguardo alla Toscana centrale meridionale. *Ass. Elettrotecnica Italiana* I 32, 1-8.
- Cello, G. 1997. Fractal analysis of a Quaternary fault array in the central Apennines, (Italy). *Journal of Structural Geology*, 19, 945-953.
- Cello, G., Invernizzi, C., Mazzoli, S. & Tondi, E., 2001. Fault properties and fluid flow pattern from quaternary faults in the apennines, Italy. *Tectonophysics*, 336, 63-78.

- Ceriani, A., Di Giulio, A., Goldstein, R.H. & Rossi, C., 2002. Diagenesis associated with cooling during burial: an example from lower cretaceous reservoir sandstones (sirt basin, Libya). *Aapg bulletin*, 86, 1573-1591.
- Ceriani, A., 2003. Thermal constraints from fluid inclusions and applications to petroleum exploration. *Atti Ticinensi di Scienze della Terra*, 9, serie speciale, 43-54.
- Chiodi, A., Tassi, F., Baez, W., Maffucci, R., Di Paolo, L., Viramonte, J.G., 2012a. Características geoquímicas e isotópicas de los fluidos hidrotermales del sistema geotérmico de Rosario de la Frontera, Sierra de la Candelaria, Salta, Argentina. In: Congreso Latinoamericano de Hidrogeología y IV Congreso Colombiano de Hidrogeología. Colombia.
- Chiodi, A., Tassi, F., Baez, W., Maffucci, R., Di Paolo, L., Viramonte, J.G., 2012b. Chemical and isotope characteristics of the Rosario de la Frontera geothermal fluids, La Candelaria Range (Salta, Argentina). 86° Convegno SGI, Arcavacata di Rende-Cosenza, 18-20 Settembre. *Rend. Online Soc. Geol. It.* ISSN: 2035-800821, 800-801.
- Chiodi A., Tassi, F., Báez, W., Maffucci, R., Invernizzi, C., Giordano, G., Corrado, S., Bicocchi, G., Vaselli, O., Viramonte, J.G., Pierantoni, P.P., 2015. New geochemical and isotopic insights to evaluate the geothermal resource of the hydrothermal system of Rosario de la Frontera (Salta, northern Argentina). *Journal of Volcanology and Geothermal Research*, 295, 16-25.
- Chiodini, G., Granieri, D., Avino, R., Caliro, S., Costa, A., Werner, C., 2005. Carbon dioxide diffuse degassing and estimation of heat release from volcanic and hydrothermal systems. *Journal of Geophysical Research – Solid Earth* 110, B082041.
- Comnínquez, A.H., Ramos, V.A., 1995. Geometry and seismic expression of the Cretaceous Salt Rift System, northwestern Argentina, in Tankard, A.J. et al, *Petroleum basins of South America: American Association of Petroleum Geologists, Memoir* 62, 325-340.
- Cooper, M., 1992. The analysis of fracture systems in subsurface thrust structures from the foothills of the Canadian Rockies. In: *Thrust Tectonics*, McClay, K.R. (Ed.), 391-405, Chapman and Hall, London.
- Corrado S., Aldega L., Di Leo P., Giampaolo C., Invernizzi C., Mazzoli S., and Zattin M., 2005. Thermal maturity of the axial zone of the Southern Apennines fold-and thrust-belt (Italy) from multiple organic and inorganic indicators: *Terra Nova*, 17 (1), 56-65.
- Corrado, S., Aldega, L., 2008. Correlation of organic and inorganic parameters for thermal maturity reconstructions in the Apennine-Maghrebian fold-and-thrust belt (Italy).

- International Geological Congress OSLO 2008. Symposium: GEP-09 Linking petroleum systems and plays to sedimentary basin evolution; Oslo (Norvegia), 6-14 Agosto 2008.
- Corrado, S., Zattin, M. & Aldega, L., 2010. Sedimentary vs. tectonic burial and exhumation along the Apennines (Italy). In: The Geology of Italy (Ed. by M. Beltrando, A. Peccerillo, M. Mattei, S. Conticelli, and C. Doglioni), Journal of the Virtual Explorer, Electronic Edition, ISSN 1441-8142, 36, paper 100 (in dynamic review).
- Corrado, S., Aldega, L., Celano, A.S., De Benedetti, A. A., Giordano, G., 2014. Cap rock efficiency and fluid circulation of natural hydrothermal systems by means of XRD on clay minerals (Sutri, Northern Latium, Italy). *Geothermics*, 50, 180-188.
- Coutand, I., Cobbold, P.R., de Urreiztieta, M., Gautier, P., Chauvin, A., 2001. Style and history of Andean deformation, Puna plateau, northwestern Argentina. *Tectonics*, 20, 210-234.
- Cowie, P. A. 1998. A healing–reloading feedback control on the growth rate of seismogenic faults. *Journal of Structural Geology*, 20, 1075–1087.
- Cowie, P.A. & Roberts, G., 2001. Constraining slip rates and spacings for active normal faults. *Journal of Structural Geology*, 23, 1901-1925.
- Cox, M.E., Browne, P., 1998. Hydrothermal alteration mineralogy as an indicator of hydrology at the Ngawha geothermal field, New Zealand. *Geothermics* 27 (3), 259-270.
- Crane, R.C., 1987. Geologic interpretation of thrust belts. *Alaskan North Slope Geology* 2, 621-630.
- Crawford, M.L., 1981. Phase equilibria in aqueous fluid inclusions. In: (Hollister, L.S. & Crawford, M.L. eds.), *Fluid Inclusions: Applications to Petrology*. Mineralogical Association of Canada, 6, 75-97.
- Crispini, L. & Frezzotti, M.L., 1998. Fluid inclusion evidences for progressive folding in metasediments of the voltri group (western alps, italy). *Journal of Structural Geology*, 20, 1733-1746.
- Cristallini, E., Cominguez, A.H., Ramos, V.A., 1997. Deep structure of the Metán-Guachipas region: tectonic inversion in Northwestern Argentina. *J. S. Am. Earth Sci.* 10, 403-421.
- Crovelli, R.A., and Barton, C.C., 1995. Fractals and the Pareto distribution applied to petroleum field-size distributions, in Barton, C.C. and La Pointe, P.R., eds., *Fractals in Petroleum Geology and Earth Processes*: Plenum Press, New York, 59-72.
- D'Amore F., Bolognesi L., 1994. Isotopic evidences for a magmatic contribution to fluids of the geothermal systems of Larderello, Italy and Geysers, California. *Geothermics* 23:21–32. doi:10. 1016/0375-6505(94)90043-4.

- DeCelles, P. G., Carrapa, B., Horton B. K. and G. E. Gehrels, 2011. Cenozoic foreland basin system in the central Andes of northwestern Argentina: Implications for Andean geodynamics and modes of deformation. *Tectonics*, 30, TC6013, doi:10.1029/2011TC002948.
- De Benedetti, A.A., Caprilli, E., Rossetti, F., Giordano, G., 2010. Metamorphic, metasomatic and intrusive xenoliths of the Colli Albani volcano and their significance for the reconstruction of the volcano plumbing system. In: Funiciello, R., Giordano, G. (Eds.), *The Colli Albani Volcano*, Special Publication of IAVCEI, vol. 3. The Geological Society, London, 153–176.
- De Filippis, L., Faccenna, C., Billi, A., Anzalone, E., Brilli, M., Özkul, M., Soligo, M., Tuccimei, P., Villa, I.M., 2012. Growth of fissure ridge travertines from geothermal springs of Denizli Basin, western Turkey. *Geological Society of America Bulletin* 124 (9-10), 1629-1645.
- Della Vedova, B., Bellani, S., Pellis, G., Squarci P., 2001. Deep temperatures and surface heat flow distribution. *Anatomy of an Orogen: the Apennines and Adjacent Mediterranean Basins* 2001, pp 65-76.
- Dershowitz, W.S., Herda, H.H., 1992. Interpretation of fracture spacing and intensity. *Proceedings of the 33rd U.S. Symposium on Rock Mechanics*, eds. Tillerson, J. R., and Wawersik, W. R., Rotterdam, Balkema. 757-766.
- Dewey, J.F., Bird, J.M., 1970. Mountain belts and the new global tectonics. *Journal of Geophysical Research* 75 (14), 2625-2647
- Di Paolo, L., Aldega, L., Corrado, S., Giordano, G., Invernizzi, C., 2012. Modelling of organic and inorganic paleo-thermal indicators to constrain the evolution of the geothermal system of Rosario de La Frontera (La Candelaria Ridge, NW Argentina): a new tool for geothermal exploration. *Rend. Online Soc. Geol. Ital.* 21, 807–808.
- Dickson, M. H., Fanelli, M., 1994. Small Geothermal Resources: A Review. *Energy Sources*, 16, 3, 349-376.
- Dow, W.G., 1977. Kerogen studies and geological interpretation: *Journal of Geochemical Exploration*, 7, 79-99.
- Dunn, F., K. G. Hartshorn, P. W. Hartshorn, 1995. Structural styles and hydrocarbon potential of the sub-Andean thrust belt of southern Bolivia, in *Petroleum Basins of South America*, edited by A. J. Tankard, R. Suárez Soruco, and H. J. Welsink, AAPG Mem., 62, 523-543.

- Endignoux, L., and Wolf, S., 1990. Thermal and kinematic evolution of thrust basins: a 2D numerical model: in Letouzey, J., ed., *Petroleum Tectonics in mobile belts*: Paris, Edit. Technip, 181-192.
- Erkan, K., Holdmann, G., Benoit, W., Blackwell, D., 2008. Understanding the Chena Hot Springs, Alaska, geothermal system using temperature and pressure data from exploration boreholes. *Geothermics* 37 (6), 565–585.
- Fetter, C. W., 1993. *Contaminant Hydrogeology*, Macmillan, New York, 458.
- Finetti I., 2006. Basic regional crustal setting and superimposed local pluton-intrusion-related tectonics in the Larderello-M Amiata geothermal province, from integrated CROP seismic data. *Boll Soc Geol Italy* 125, 117-146.
- Fisher, N. I., Lewis T. & Embleton B. J. J., 1987. *Statistical Analysis of Spherical Data*. Cambridge University Press.
- Fisher, Q.J., Knipe, R.J., 2001. The permeability of faults within siliciclastic petroleum reservoirs of the North Sea and Norwegian Continental Shelf, *Marine and Petroleum Geology*, 18, 1063-1081. doi: 10.1016/S0264-8172(01)00042-3
- Fossen, H., Hesthammer, J., 1997. Geometric analysis and scaling relations of deformation bands in porous sandstone. *Journal of Structural Geology* 19, 1479-1493.
- Galliski, M.A., Viramonte, J.G., 1988. The Cretaceous Paleorift in North-western Argentina: a petrological approach. *S. Am. Earth Sci. Bull.* 1 (4), 329-342.
- Ganguly, S., Kumar, M.S.M., 2012. Geothermal reservoirs – a brief review. *Journal of the Geological Society of India* 79 (6), 589-602.
- Garg, S.K., Combs, J., 2010. Appropriate use of USGS volumetric “heat in place” method and Monte Carlo calculations. In: *Proceedings 34th Stanford Geothermal Reservoir Engineering Workshop*, Stanford University, Stanford, California, USA, 7 pp.
- Gebhard, J. A., Giudici, A. R. y Oliver Gascón, J. 1974. Geología de la comarca entre el río Juramento y arroyo Las Tortugas, provincias de Salta y Jujuy, República Argentina. *Revista de la Asociación Geológica Argentina* 29(3), 359-375.
- Gile, L.H., Peterson, F.F., Grossman, R.B., 1966. Morphological and genetic sequences of carbonate accumulation in desert soils. *Soil Sci* 101, 347-360.
- Gillespie, P. A., Walsh, J.J. & Watterson, J., 1992. Limitations of dimension and displacement data from single faults and the consequences for data analysis and interpretation. *Journal of Structural Geology*, 14, 1157-1172.
- Giordano, G., Pinton, A., Cianfarra, P., Baez, W., Chiodi, A., Viramonte, J., Norini, G., Gropelli, G., 2013. Structural control on geothermal circulation in the Cerro Tuzgle–

- Tocomar geothermal volcanic area (Puna plateau, Argentina). *Journal of Volcanology and Geothermal Research*, 249, 77-94.
- Goldstein, R.H. & Reynolds, T.J., 1994. Systematics of fluid inclusions in diagenetic minerals: Society for Sedimentary Geology Short Course 31, 199.
- Goldstein, R.H., 2001. Fluid inclusions in sedimentary and diagenetic systems. *Lithos*, 55, 159-193.
- Goldstein, R.H., 2003. Petrographic analysis of fluid inclusions. In I. Samson, A. Anderson, & D. Marshall, eds. *Fluid Inclusions: Analysis and Interpretation*. Mineral. Assoc. Can., Short Course Ser. 32, 9-53. Goldstein & Reynolds, 1994.
- Gómez Omil, R. y Albariño, L.M. 1996. Análisis geológico petrolero del bloque Olleros, sistema de Santa Bárbara, provincia de Salta. 13° Congreso Geológico Argentino, Actas 1, 27-44.
- González Bonorino, F., 1950. Geologic cross-section of the cordillera de los Andes at about Parallel 33 S.L. (Argentina y Chile). *Geological Society of America Bulletin* 61, 17-86.
- González, O., and R. Mon, Tectónica del extremo norte de las Sierras Pampeanas y su transición a la Cordillera Oriental y a las Sierras Subandinas, paper presented at XIII Congreso Geológico Argentino y III Congreso de Exploración de Hidrocarburos, Asoc. Geol. Argent., Buenos Aires, 1996.
- González, O., Viruel, M., Mon, R., Tchilinguirian, P., Barber, E., 2000. Hoja Geológica 2766-II. San Miguel de Tucumán. Boletín 245. Programa Nacional de Cartas Geológicas, 1:250.000. SEGEMAR.
- Grier, M. E., J. A. Salfity, and R. W. Allmendinger, 1991. Andean reactivation of the Cretaceous Salta rift, northwestern Argentina, *J. S. Am. Earth Sci.*, 4, 351-372.
- Gustavson, T.C., Hovorka, S.D., Dutton, A.R., 1994. Origin of satin spar veins in evaporate basins. *Journal of Sedimentary Research* A64, 88-94.
- Gutscher, M. A., Spakman, W., Bijwaard, H. & Engdahl, E. R. 2000. Geodynamics of flat subduction: seismicity and tomographic constraints from the Andean margin. *Tectonics*, 19, 814-833.
- Hall, D.L., Sterner, S.M. & Bodnar, R.J., 1988. Freezing point depression of NaCl-KCl-H₂O solutions. *Economic Geology*, 83, 197-202.
- Hancock, P.L., 1985. Brittle microtectonics: principles and practice. *Journal of Structural Geology* 7, 437-457.
- Hamza, V.M. and Muñoz, M., 1996. Heat Flow Map of South America. *Geothermics*, 25, 599-646. [http://dx.doi.org/10.1016/S0375-6505\(96\)00025-9](http://dx.doi.org/10.1016/S0375-6505(96)00025-9)

- Hamza, V.M., Silva Dias, F.J.S., Gomes, A.J.L. and Delgadillo Terceros, Z.G. (2005) Numerical and Functional Representations of Regional Heat Flow in South America. *Physics of the Earth and Planetary Interiors*, 152, 223-256. <http://dx.doi.org/10.1016/j.pepi.2005.04.009>
- Hain, M.P., Strecker, M.R., Bookhagen, B., Alonso, R.N., Pingel, H., Schmitt, A.K., 2011. Neogene to Quaternary broken foreland formation and sedimentation dynamics in the Andes of NW Argentina (25°S). *Tectonics* 30, 1-27.
- Hennings, P.H., Olson, J.E., Thompson, L.B., 2000. Combining Outcrop Data and Three Dimensional Structural Models to Characterize Fractured Reservoirs: An Example from Wyoming. *AAPG Bulletin* 84(6), 830-849.
- Hoffman, J., and Hower, J., 1979. Clay mineral assemblages as low grade metamorphic geothermometers - application to the thrust faulted disturbed belt of Montana, USA, in Scholle, P.A., and Schluger, P.S., eds., *Aspects of Diagenesis: SEMP Special Publication*, 2, 55-79.
- Hongn, F., C. del Papa, J. Powell, I. Petrinovic, R. Mon, and V. Deraco, 2007. Middle Eocene deformation and sedimentation in the Puna–Eastern Cordillera transition (23°–26°S): Control by preexisting heterogeneities on the pattern of initial Andean shortening, *Geology*, 35(3), 271-274, doi:10.1130/G23189A.1.
- Howard, J.J. & Roy, D.M. 1985. Development of layer charge and kinetics of experimental smectite alteration. *Clays and Clay Minerals*, 33, 81-88.
- Hunt, J.M., 1986. *Petroleum*. McGraw-hill yearbook of science and technology, 362-365.
- Iaffa, D.N., Sàbat, F., Muñoz, J.A., Mon, R., Gutierrez, A.A, 2011. The role of inherited structures in a foreland basin evolution. The Metán Basin in NW Argentina. *Journal of Structural Geology* 33, 1816-1828.
- Iaffa, D.N., Sabat, F., Munoz, J.A., Carrera N., 2013. Basin fragmentation controlled by tectonic inversion and basement uplift in Sierras Pampeanas and Santa Bárbara System, northwest Argentina. *Geological Society, London, Special Publications*, 377.
- Invernizzi, C., Vitik, M. Cello, G. & Bodnar, R., 1998. Fluid inclusions in high pressure-low temperature rocks from the calabrian arc (southern Italy): the burial and uplift history of the subduction-related diamante-terranova unit. *Journal of Metamorphic Geology*, 16, 247-258.
- Invernizzi, C., Pierantoni, P., Chiodi A., Maffucci, R., Corrado, S., Baez, W., Tassi, F., Giordano G., Viramonte, J., 2014. Preliminary assessment of the geothermal potential of Rosario de la Frontera area (Salta, NW Argentina): insight from hydro-geological, hydro-

- geochemical and structural investigations. *Journal of South American Earth Science*, 54, 20-36.
- Isacks, B. L. 1988. Uplift of the Central Andean Plateau and Bending of the Bolivian Orocline. *Journal of Geophysical Research*, 93, 3211-3231.
- Jagodzinski, H., 1949. Eindimensionale Fehlordnung in Kristallen und ihr Einfluss auf die Röntgen Interferenzen. *Acta Crystallographica*, 2, 201-207.
- James, D. E., 1971. Plate-tectonic model for the evolution of the central Andes, *Geol. Soc. Am. Bull.*, 82, 3325-3346, doi:10.1130/0016-7606(1971)82[3325:PTMFTE]2.0.CO;2.
- Jamison, W.R., and D.W. Steams, 1982. Tectonic deformation of Wingate Sandstone, Colorado National Monument, *AAPG Bull.*, 66, 2584-2608.
- Jennings, S., and Thompson, G.R., 1986. Diagenesis of Plio-Pleistocene sediments of the Colorado River delta, southern California: *Journal of Sedimentary Petrology*, 56, 89-98.
- Jordan, T.E., Isacks, B., Allmendinger, R.W., Brewer, J.A., Ramos, V.A., Ando, C.J., 1983. Andean tectonics related to geometry of subducted Nazca plate. *Bulletin of the Geological Society of America* 94, 341-361.
- Jordan, T.E., Allmendinger, R.W., 1986. The Sierras Pampeanas of Argentina: a modern analogue of Rocky Mountain foreland deformation. *Am. J. Sci.* 286, 737-764.
- Jordan, T. E. & Alonso, R. N. 1987. Cenozoic stratigraphy and basin Tectonics of the Andes Mountains, 208–288 South Latitude. *The American Association of Petroleum Geologists Bulletin*, 71, 49-64.
- Kley, J., and Monaldi, R., 1998, Tectonic shortening and crustal thickening in the Central Andes: How good is the correlation? *Geology*, 26, 723-726.
- Kley, J. y Monaldi, C. R. 1999. Estructura de las Sierras Subandinas y del Sistema de Santa Bárbara. En González Bonorino, G., Omarini, R. y Viramonte, J. (eds.) *Geología del Noroeste Argentino*, 14° Congreso Geológico Argentino, Relatorio 1, 415-425, Salta.
- Kley, J., Monaldi, C.R., 2002. Tectonic inversion in the Santa Barbara System of the central Andean foreland thrust belt, northwestern Argentina. *Tectonics* 21 (6), 1061.
- Kloditz O., Clauser C., 1998. Numerical simulation of flow and heat transfer in fractured crystalline rocks: application to the hot dry rock site in Rosemanowes (U.K.). *Geothermics* 27:1–23. doi: 10.1016/S0375-6505(97)00021-7
- Kranz, R.L., Frankel, A.D., Engelder, T., Scholz, C.H., 1979. The permeability of whole and jointed Barre granite, *International Journal of Rock Mechanics and Mining Science and Geomechanics Abstract*, 16, 225-234.

- Kress, P., 1995. Tectonic inversion of the subandean foreland: A combined geophysical and geological approach, Berlin. Geowiss. Abh. Reihe B, 23,1-120, 1995.
- Krüger, D., 1994. Modellierungen zur Struktur elektrisch leitfähiger Zonen in den südlichen zentralen Anden, Berlin. Geowiss. Abh., 21, 91.
- Lacombe, O., Mouthereau, F., 2002. Basement-involved shortening and deep detachment tectonics in forelands of orogens: Insights from recent collision belts (Taiwan, Western Alps, Pyrenees). *Tectonics* 21, 1030, <http://dx.doi.org/10.1029/2001TC901018>.
- La Pointe, P.R., 1988. A Method to Characterize Fracture Density and Connectivity Through Fractal Geometry. *International Journal of Rock Mechanics and Mining Science & Geomechanics Abstracts*, 25, 421-429.
- La Vigna, F., Mazza, R., Capelli, G., 2012. Detecting the flow relationships between deep and shallow aquifers in an exploited groundwater system, using long-term monitoring data and quantitative hydrogeology: the Acque Albule basin case (Rome, Italy). *Hydrological Processes*, Published online in Wiley Online Library. Available on <http://onlinelibrary>
- Levine, J.R., and Davis, A., 1989. The relationship of coal optical fabrics to Alleghanian tectonic deformation in the Central Appalachian fold-and-thrust belt, Pennsylvania: *Geol. Soc. Am. Bull.*, 101, 1333-1347.
- Liotta D., Ruggieri, G., Brogi, A., Fulignati, P., Dini, A., Nardini, I., 2010. Migration of geothermal fluids in extensional terrains: the ore deposits of the Boccheggiano-Montieri area (southern Tuscany, Italy). *Int. J. Earth Sci.*, 99, 623-644.
- Louis, C., 1969. A study of groundwater flow in jointed rock and its influence on the stability of rock masses. *Rock Mech. Res. Rep.* 10, Imperial College, London.
- Lucassen, F., S. Lewerenz, G. Franz, J. Viramonte, and K. Mezger, 1999. Metamorphism, isotopic ages and composition of lower crustal granulite xenoliths from the Cretaceous Salta Rift Argentina, *Contrib. Mineral. Petrol.*, 134, 325-341.
- Lüschen E., 2005. Relationship between recent heat flow and seismic properties: some notes from crustal research in Germany. *J Volcan Geotherm Res* 148, 31-45. doi:10.1016/j.jvolgeores.2005.04.012
- Maffucci, R., Bigi, S., Corrado, S., Di Paolo, L., Chiodi, A., 2012a. Fracture modelling applied to the geothermal system potential reservoir of Rosario de La Frontera (La Candelaria Ridge, NW Argentina). *Rendiconti Online della Soc. Geol. Ital.* ISSN: 2035-8008 21, 829-831.
- Maffucci, R., Caffè, P., Corrado, S., Invernizzi, C., Giordano, G., Pierantoni, P., Viramonte, J., 2012b. La Candelaria Ridge (NW Argentina) as a natural lab for the exploration of the

- geothermal system of Rosario de la Frontera: methods and preliminary results. *Rendiconti Online della Soc. Geol. Ital.* ISSN: 2035-8008 21, 826-828.
- Maffucci, R., Bigi, S., Chiodi, A., Corrado, S., Giordano, G., Di Paolo, L., 2013. Reconstruction of a “Discrete Fracture Network” in the geothermal reservoir of Rosario de La Frontera (La Candelaria Ridge, Salta province, NW Argentina). In: *Proceedings of the European Geothermal Congress 2013; Pisa, Italy, 3-7 June*, ISBN 978-2-8052-0226-1.
- Maffucci, R., Bigi, S., Corrado, S., Chiodi, A., Di Paolo, L., Giordano, G., Invernizzi, C., 2013. Quality assessment of reservoirs by means of outcrop data and "discrete fracture network" models: the case history of Rosario de La Frontera (NW Argentina) geothermal system. *Tectonophysics*, 647-648, 112-131.
- Magro G., Ruggieri G., Gianelli G., Bellani S., Scandiffio G., 2003. Helium isotopes in paleofluids and presentday fluids in the Larderello geothermal field: constraints on the heat source. *J Geophys Res* 108:1–12. doi:10.1029/2001JB001590.
- Magri F., Akar T., Gemici U. and Pekdeger A., 2010. Deep geothermal groundwater flow in the Seferihisar–Balcova area, Turkey: results from transient numerical simulations of coupled fluid flow and heat transport processes. *Geofluids* 10, 388-405.
- Mair, K., Main, I., Elphick, S., 2000. Sequential growth of deformation bands in the laboratory. *Journal of Structural Geology* 22, 25-42.
- Majumdar, R.K., Majumdar N., Mukherjeem A.L., 2000. Geoelectric investigations in Bakreswar geothermal area, West Bengal, India. *Journal of Applied Geophysics*, 45, 187-202.
- Marchegiani, L., Van Dijk, J.P., Gillespie P.A., Tondi E., Cello G., 2006. Scaling properties of the dimensional and spatial characteristics of fault and fracture systems in the Majella Mountain, central Italy. *Geological Society, London, Special Publications*, 261, 113-131.
- Marquillas, R., Del Papa, C., Sabino, I.F., 2005. Sedimentary aspects and paleoenvironmental evolution of a rift basin: Salta Group (Cretaceous-Paleogene), northwestern Argentina. *International Journal of Earth Sciences* 94, 94-113.
- Marrett, R.A., Allmendinger, R.W., Alonso, R.N., Drake, R.E., 1994. Late Cenozoic tectonic evolution of the Puna Plateau and adjacent foreland, northwestern Argentine Andes. *Journal of South American Earth Sciences* 7, 179-207.
- Mazza, R., Taviani, S., Capelli, G., De Benedetti, A.A., Giordano, G., 2013. Quantitative hydrogeology of volcanic lakes with management, volcanological and geothermal

- implications. In: Tassi, F., Christenson, B., Vandemeulebrouck, J., Rouwet, D. (Eds.), *Volcanic Lakes, Advances in Volcanology IAVCEI Book Series*. Springer, Heidelberg.
- Merriman, R.J., and Frey, M., 1999. Patterns of very low-grade metamorphism in metapelitic rocks, in Frey, M., and Robinson, D., eds., *Low grade metamorphism*: Oxford, Blackwell, 61-107.
- McClay, K.R., 1989. Analogue models of inversion tectonics. In: Cooper, M.A. & Williams, G.D. (eds) *Inversion Tectonics*. Geological Society, London, Special Publications 44, 41-59.
- McQuarrie, N., 2002. The kinematic history of the central Andean foldthrust belt, Bolivia: Implications for building a high plateau, *Geol. Soc. Am. Bull.*, 114, 950-963, doi:10.1130/0016-7606(2002)114<0950:TKHOTC>2.0.CO;2.
- McQuarrie, N., Horton, B.K., Zandt, G., Beck, S., and DeCelles, P.G., 2005, Lithospheric evolution of the Andean fold-thrust belt, Bolivia, and the origin of the central Andean plateau: *Tectonophysics*, 399, 15-37, doi: 10.1016/j.tecto.2004.12.013
- Mingramm, A., Russo, A., Pozzo, A. y Cazau, L. 1969. Sierras Subandinas. En Turner, J.C.M. (ed.) *Segundo Simposio de Geología Regional Argentina*, Academia Nacional de Ciencias 1: 95-137, Córdoba.
- Mingramm, A., A Russo, A. Pozzo, and L. Cazau, 1979. Sierras Subandinas, in *Segundo Simposio Geología Regional Argentino*, 1, 95-138, Acad. Nac. de Cienc., Cordoba, Argentina.
- Minissale A., Magro G., Martinelli G., Vaselli O., Tassi G.F., 2000. Fluid geochemical transect in the Northern Apennines (central-northern Italy): fluid genesis and migration and tectonic implications. *Tectonophysics* 319:199–222. doi:10.1016/S0040-1951(00)00031-7.
- Minissale, A., 2004. Origin, transport and discharge of CO₂ in central Italy. *Earth-Science Reviews*, 66(1-2), 89-141.
- Moeck, I., Hinz, N., Faulds, J., Bell, J., Kell-Hills, A., and Louie, J., 2010. 3D geological modeling as a new method in geothermal exploration: A case study from central Nevada. *Geothermal Resources Council Transactions*, 34, 807-811.
- Mon, R., 1971. Estructura geológica del extremo austral de las Sierras Subandinas, Prov. de Salta y Tucumán Republica Argentina, *Rev. Asoc. Geol. Argent.*, 26, 209-220.
- Mon, R., 1972. Esquema estructural de la Provincia de Tucumán Republica Argentina, *Rev. Asoc. Geol. Argent.*, 27, 223-228.

- Mon, R., and J. C. Dinkel, 1974. Geología de la comarca del Cerro Remate (Provincias de Salta, Tucumán y Santiago del Estero) y nuevos datos sobre la distribución del Paleozóico inferior en el Noroeste Argentino, *Rev. Asoc. Geol. Argent.*, 29, 61–71.
- Mon, R., 1976. The structure of the eastern border of the Andes in north western, Argentina. *Geologische Rundschau* 65, 211-222.
- Mon, R., and J. A. Salfity, 1995. Tectonic evolution of the Andes of northern Argentina, in *Petroleum Basins of South America*, edited by A. J. Tankard, R. Suárez Soruco, and H. J. Welsink, pp. 269– 283, Am. Assoc. Petrol. Geol., Tulsa, Okla.
- Mon, R., Gutierrez, A., 2007. Estructura del extremo sur del sistema subandino (provincias de Salta, Santiago del Estero y Tucumán). *Rev. Asoc. Geol. Argent.* 62, 62-68.
- Monaldi, C. R., Salfity, J.A.& Kley, J. 2008. Preserved extensional structures in an inverted Cretaceous rift basin, northwestern Argentina. Outcrop examples and implications for fault reactivation. *Tectonics*, 27, TC1011.
- Moore, D.M., and Reynolds, R.C., Jr., 1997. X-Ray diffraction and the identification and analysis of clay minerals: Oxford, Oxford University Press, 1-378.
- Moreno Espelta, C., Viramonte, J.G., Arias, J.E., 1975. Geología del área termal de Rosario de la Frontera y sus posibilidades geotérmicas. *Actas del II Congreso Ibero-Americano de Geología Económica*, IV, 543-548.
- Mpodozis, C., and V. A. Ramos, 1989. The Andes of Chile and Argentina, in *Geology of the Andes and its Relation to Hydrocarbon and Mineral Resources*, *Earth Sci. Ser.*, vol. 11, edited by G. E. Ericksen, M. T. Cañas Pinochet and J. A. Reinemund, pp. 59-90, Circumpac. Counc. for Energy and Miner. Resour., Houston, Tex.
- Muffler, L.P.J., White, D.E., 1969. Active metamorphism of Upper Cenozoic sediments in the Salton Sea geothermal field and the Salton Trough, Southeastern California. *Geol Soc Am Bull* 80, 157-182.
- Muffler, P., Cataldi, R., 1978. Methods for regional assessment of geothermal resources. *Geothermics* 7, 53-89.
- Mukhopadhyay, P.K., 1994. Vitrinite reflectance as maturity parameter: petrographic and molecular characterization and its applications to basin modeling: in Mukhopadhyay, P.K., and Dow, W.G., eds., *Vitrinite reflectance as a maturity parameter: applications and limitations: American Chemical Society Symposium Series*, 570, 1-24.
- Müller, C., Siegesmund, S., and Blum, P., 2010. Evaluation of the representative elementary volume (REV) of a fractured geothermal sandstone reservoir. *Environmental Earth Sciences*. DOI:10.1007/s12665-010-0485-7

- Mwangi, S. M., 2013. Application of Geochemical Methods in Geothermal Exploration in Kenya. *Procedia Earth and Planetary Science*, 7, 602-606.
- Nathenson, M., Muffler, L.J.P., 1975. Geothermal resources in hydrothermal convection systems and conduction-dominated areas. In: White, D.E., Williams, D.L. (Eds.), *Assessment of Geothermal Resources of the United States – 1975*. U.S. Geol. Survey Circular 726, Arlington, VA, USA, pp. 104-121.
- Nelson, R.A., 1992. An approach to evaluating fractured reservoirs. Society of Petroleum Engineers, Annual Technical Conference & Exhibition, San Antonio, October, 198, 2167-2170.
- Nuti, S., 1992. Isotope techniques in geothermal studies. In: D'Amore, F. (Ed.), *Applications of Geochemistry in Geothermal Reservoir Development*. UNITAR/UNDP publication, Rome, Italy, pp. 215-252.
- Oberlin, A., Boulmier, J.L., and Villey, M., 1980. Electron microscopic study of kerogen microtexture. Selected criteria for determining the evolution path and evolution stage of kerogen. In: (Durand B., ed.), *Kerogen*, Editions Technip, Paris, 191-242.
- Oda, M., 1985. Permeability Tensor for Discontinuous Rock Masses. *Geotechnique* 35, 483-495.
- Olson, J.E., 2003. Sublinear scaling of fracture aperture versus length: an exception or the rule? *Journal of Geophysical Research* 108(B9), 2413. doi:10.1029/2001JB000419
- Omarini, R. H., Sureda, R. J., Götze, H. J., Seilacher, A. & Pflüger, f. 1999. Puncoviscana folded belt in northwestern Argentina: testimony of Late Proterozoic Rodinia fragmentation and pre- Gondwana collisional episodes. *International Journal of Earth Sciences (Geologische Rundschau)*, 88, 76-97.
- Oncken, O., Hindle, D., Kley, J., Elger, K., Victor, P. & Schemmann, K. 2006. Deformation of the central Andean Upper plate system – facts, fiction, and constraints for plateau models. In: Oncken, O., Chong, G., Franz, G., Giese, P., Götze, H.-J., Ramos, V., Strecker, M. & Wigger, P. (eds) *The Andes - Active Subduction Orogeny*. Springer, Berlin, 3–27.
- Palucci, C., 2014. Hydrogeological modeling of Rosario de la Frontera geothermal system by using Groundwater Vistas software: implications for geothermal exploitation. Master's degree thesis in “Geothermal Energy”, University “Roma Tre” of Rome. Tutor: Prof. S.Corrado; Co-tutor: G.Giordano, R.Maffucci, S.Taviani.
- Pankhurst, R. J. & Rapela, C. W. 1998. The proto-Andean margin of Gondwana: an introduction. In: Pankhurst, R. J. & Rapela, C. W. (eds) *The proto-Andean Margin of Gondwana*. Geological Society, London, Special Publications, 142, 1-9.

- Palucci, C., a.a. 2013-2014. Hydrogeological modeling of Rosario de la Frontera geothermal system by using Groundwater Vistas software: implications for geothermal exploitation. Master's degree in "Geothermal Energy", University "Roma Tre" of Rome.
- Pesce, A., 2000. Boundaries of geothermal basins in northeastern Argentina. In: 31° Congreso Geológico Internacional. Río de Janeiro. Brasil.
- Pesce, A., Miranda, F., 2003. Catálogo De manifestaciones termales de la República Argentina. In: Región Noroeste, Volumen I. SEGEMAR, Buenos Aires, Argentina, 165.
- Phillip, S. L., 2015. Fault zones and associated fracture systems in geothermal reservoir rocks. AAPG Europe Conference, Catania, Sicily, 16-17th April, 2015.
- Pierantoni, P.P., Invernizzi, C., Giordano, C., Corrado, S., Maffucci, R., Chiodi, A., Tassi, F., Viramonte, J., 2012. The geothermal System of Rosario de la Frontera (Salta, Argentina): preliminary geochemical and hydrogeological results. Rendiconti Online della Soc. Geol. Ital. ISSN: 2035-8008 22, 186-189.
- Pilger, R. H. 1981. Plate reconstructions, aseismic ridges, and low angle subduction beneath the Andes. Geological Society of America, Bulletin, 92, 448.
- Pollastro, R.M., 1990. The illite/smectite geothermometer - concepts, methodology and application to basin history and hydrocarbon generation, in Nuccio, F., and Barker, C.E., eds., Application of thermal maturity studies to energy exploration: SEPM Rocky Mountains section, 1-18.
- Pollastro, R.M., 1993. Consideration and applications of the illite/smectite geothermometer in hydrocarbon-bearing rocks of Miocene to Mississippian age: Clays and Clay Minerals, 41, 119-133.
- Priest, S.D., Hudson, J.A., 1981. Estimation of discontinuity spacing and trace length using scanline surveys. International Journal of Rock Mechanics and Mining Sciences & Geomechanics Abstracts 18, 183-197.
- Priest, S.D., 1993. Discontinuity analysis of rock engineering. Chapman and Hall, London.
- Priest, S.D., 2004. Determination of discontinuity size distributions from scanline data. Rock Mechanics and Rock Engineering 37, 347-368, <http://dx.doi.org/10.1007/s00603-004-0035-2>.
- Ramos, V.A., Cristallini, E.O., Perez, D., 2002. The Pampean flat-slab of the Central Andes. J. S. Am. Earth Sci. 15, 59-78.
- Reynolds, J.H., Galli, C.I., Hernández, R.M., Idleman, B.D., Kotila, J.M., Hilliard, R.V., Naeser, C.W., 2000. Middle Miocene tectonic development of the Transition Zone Salta

- Province, northwest Argentina: magnetic stratigraphy from the Metán Subgroup, Sierra de González. *GSA Bulletin* 112 (11).
- Naeser, C.W. Rivas, J.C., 2012. *Historias del Rosario de la Frontera*. Gráfica e Imprenta Pons, Salta, p. 190.
- Roberson, H.E. & Lahann, R.W., 1981. Smectite to illite conversion rates: effects of solution chemistry. *Clays and Clay Minerals*, 29, 129-135.
- Roedder, E., 1984. Fluid Inclusions, *Min. Soc. Am. Rev. in Min.* 12, 644 pp. Rosell & Puigdefàbregas, 1975.
- Rossetti, F., Aldega, L., Tecce, F., Balsamo, F., Billi, A., Brilli, M., 2011. Fluid flow within the damage zone of the Boccheggiano extensional fault (Larderello–Travale geothermal field, central Italy): structures, alteration and implications for hydro- thermal mineralization in extensional settings. *Geological Magazine* 148 (4), 558–579.
- Rouleau, A., Gale, J.E., 1985. Statistical characterization of the fracture system in the Stripa granite, Sweden. *International Journal of Rock Mechanics and Mining Sciences & Geomechanics* 22, 353-367.
- Ruiz Huidobro, O. J. 1968. Descripción geológica de la hoja 7e, Salta, provincias de Salta y Jujuy. Instituto Nacional de Geología y Minería, Boletín 109, 48 p., Buenos Aires.
- Salfity, J.A. & Marquillas, R. A. 1981. Las unidades estratigráficas cretácicas del Norte de la Argentina. In: Volkheimer, W. & Musacchio, E. (eds) *Cuencas Sedimentarias del Jurásico y Cretácico de América del Sur*, 1. Comité Sudamericano del Jurásico y Cretácico, Buenos Aires, Argentina, 303–317.
- Salfity, J.A., 1982. Evolución paleogeográfica del Grupo Salta (Cretácico-Eogénico), Argentina. V Congreso Latinoamericano de Geología, Actas 1, 11-26.
- Salfity, J.A., Monaldi, C.R., Marquillas, R.A. and Gonzáles, R.E., 1993. La inversión tectónica del Umbral de los Gallos en la cuenca del Grupo Salta durante la Fase Incaica, XII Congreso Geológico Argentino and II Congreso de Exploración de Hidrocarburos, Asociación Geológica Argentina, Mendoza, Argentina.
- Salfity, J.A. and Marquillas, R.A., 1994. Tectonic and sedimentary evolution of the Cretaceous-Eocene Salta Group, Argentina, in: *Cretaceous tectonics of the Andes*, J. A. Salfity, ed., Earth Evolution Sciences, Brunswick, Germany, Friedrich Vieweg and Sohn, 266-315.
- Salfity, J.A., Monaldi, C., 2006. Hoja Geológica 2566 - IV Metán. Boletín 319. Programa Nacional de Cartas Geológicas, 1:250.000. SEGEMAR.

- Sanyal, S.K., Sarmiento, Z.F., 2005. Booking geothermal energy reserves. *Geothermal Resources Council Transactions* 29, 467–474.
- Schlische, R. W., Young, S. S., Ackermann, R. V. & Gupta, A., 1996. Geometry and scaling relations of a population of very small rift-related normal faults. *Geology*, 24, 683–686.
- Sclater, J.G., and Christie, P.A.F., 1980. Continental stretching: an explanation of post-Mid Cretaceous subsidence on the Central North Sea Basin: *Journal of Geophysical Research*, 85, 3711-3739.
- Scotti, P., 2003. Thermal constraints from the organic matter: *Atti Ticinensi di Scienze della Terra*, 9, Serie Speciale, 23-32.
- Seggiaro, R., Aguilera, N., Gallardo, E., Ferreti, J., 1995. Structure and geothermal potential of the Rosario de la Frontera termal área. In: Salta. Argentina. World Geothermal Congress. Florence. Italy, vol. 2, pp. 764-767.
- Seggiaro, R., Aguilera, N., Ferretti, J., Gallardo, E., 1997. Estructura del area geotermica de Rosario de la Frontera, Salta, Argentina VIII Congreso Geologico Chileno. *Actas* 1(2), 390-394. Antofagasta.
- Serpen, U., 2004. Hydrogeological investigations on Balcova geothermal system in Turkey. *Geothermics* 33 (3), 309–335.
- Shaik, A.R., Rahman, S.S., Tran, N.H., Tran T., 2011. Numerical simulation of fluid-rock coupling heat transfer in naturally fractured geothermal system. *Applied Thermal Engineering*, 31, 1600-1606.
- Shearman, D.J., Mossop, G., Dunsmore, H., Martin, M., 1972. Origin of gypsum veins by hydraulic fracture. *Institution of Mining and Metallurgy Transaction, Section B: Applied Earth Science* 81, 149-155.
- Shipton, Z.K., Cowie, P.A., 2001. Damage zone and slip-surface evolution over mm to km scales in high-porosity Navajo sandstone, Utah. *Journal of Structural Geology* 23, 1825-1844.
- Sibson, R.H., Scott, J., 1998. Stress/fault controls on the containment and release of overpressured fluids: examples from gold–quartz vein systems in Juneau, Alaska, Victoria, Australia and Otago, New Zealand. *Ore Geology Reviews* 13, 293-306.
- Snow, D.T., 1965. A parallel plate model of fractured permeable media. PhD Thesis Univ. of Calif., Berkeley, USA.

- Sobel, E. & Strecker, M. R., 2003. Uplift, exhumation and precipitation: tectonic and climatic control of late Cenozoic landscape evolution in the northern Sierras Pampeanas, Argentina. *Basin Research*, 15, 431-451.
- Stearns, D.W., 1968. Certain aspect of fracture in naturally deformed rocks, in: National Science Foundation Advanced Science Seminar in Rock Mechanics, Special report, Rieker, R.E. (Ed.), 97-118, Air Force Cambridge Research Laboratories, Bedford, MA.
- Sternlof, K. R., Chapin, J.R., Pollard, D.D., Durlofsky, L.J., 2004. Permeability effects of deformation band arrays in sandstone. *AAPG Bulletin* 88, 1315-1329.
- Storti, F., Salvini, F., 1996. Progressive rollover fault-propagation folding: a possible kinematic mechanism to generate regional-scale recumbent folds in shallow foreland belts. *American Association of Petroleum Geologist Bulletin* 80, 174-193.
- Strecker, M.R., Alonso, R.N., Bookhagen, B., Carrapa, B., Hilley, G.E., Sobel, E.R., Trauth, M.H., 2007. Tectonics and climate of the southern central Andes. *Annual Review Earth Planet Sciences* 35, 747-787.
- Sweeney, J.J., and Burnham, A.K., 1990. Evaluation of a simple model of vitrinite reflectance based on chemical kinetics: *American Association of Petroleum Geologists Bulletin*, 74, 1559-1570.
- Tavani, S., Storti, F., Salvini, F., Toscano, C., 2008. Stratigraphic versus structural control on the deformation pattern associated with the evolution of the Mt. Catria anticline. *Journal of Structural Geology* 30(5), 664–681.
- Terzaghi, R.D., 1964. Source of error in joint surveys. *Geotechnique* 15, 287-304.
- Timlin, M., 2009. Effects of stratigraphy on geothermal reservoir performance. In: *AAPG Annual Convention and Exhibition*, Denver, CO, USA, 7-10.06.2009.
- Todaka, N., Akasaka, C., 2004. Reactive geothermal transport simulations to study the formation mechanism of an impermeable barrier between acidic and neutral fluid zones in the Onikobe Geothermal Field, Japan. *Journal of Geophysical Research – Solid Earth* 109, B05209.
- Todesco, M., Giordano, G., 2010. Modelling of CO₂ circulation in the Colli Albani area. In: Funiciello, R., Giordano, G. (Eds.). *The Colli Albani Volcano*, Special Publication of IAVCEI, vol.3. The Geological Society, London, 311-330.
- Tondi, E. & Cello, G. 2003. Spatiotemporal evolution of the Central Apennines fault system (Italy). *Journal of Geodynamics*, 36, 113–128.
- Truesdell, A.H., Hulston, J.R., 1980. Isotopic evidence on environments of geothermal systems. In: Fritz, P., Fontes, J.C. (Eds.), *Handbook of Environmental Isotope*

- Geochemistry, The Terrestrial Environment, vol. 1. Elsevier, Amsterdam, the Netherlands, pp. 179-226.
- Tsang, Y.W., Witherspoon, P.A., 1981. Hydromechanical behavior of a deformable rock fracture subject to normal stress. *Journal of Geophysical Research* 86, 9287-9298.
- Turner, J.C.M., 1959. Estratigrafía del cordón de Escaya y de la sierra de Rinconada (Jujuy). *Rev Asoc Geol Arg* 13, 15-39.
- Underhill, J. R., and Woodcock, N. H., 1987. Faulting mechanisms in high-porosity sandstones; New Red Sandstone, Arran, Scotland, in Jones, M. E., and Preston, R.M.F., eds., *Deformation of sediments and sedimentary rocks*, Geological Society Special Publication No. 29: Oxford, England, Blackwell Scientific Publications, 91-105.
- Van Dijk, J. P., 2000. Analysis and modelling of fractured reservoirs: SPE International Society of Petroleum Engineering 50570, 1-43.
- Van Hinte, J.E., 1978. Geohistory analysis - Application of micropaleontology in exploration geology: *AAPG Bull.*, 62, 201-222.
- Vieira, F. P. and Hamza, V. M., 2014. Advances in Assessment of Geothermal Resources of South America. *Natural Resources*, 5, 897-913.
- Viramonte, J.G., Kay, S.M., Becchio, R., Escayola, M., Novitski, I., 1999. Cretaceous rift related magmatism in Central-western South America. *J. South Am. Earth Sci.* 12, 109-121.
- Walsh, J.J. and Watterson, J., 1993. Fractal analysis of fracture patterns using the standard box-counting technique. Valid and invalid methodologies. *Journal of Structural Geology*, 15, 1509-1512.
- Wang, X., Ghassemi, A., 2011. A three-dimensional stochastic fracture network model for geothermal reservoir stimulation. *Proceedings, Thirty-Sixth Workshop on Geothermal Reservoir Engineering* Stanford University, Stanford, California, January 31 – February 2, 2011.
- Whitman, D., Isacks, B.L., Chatelain, J.-L., Chiu, J.-M. and Perez, A., 1992. Attenuation of high-frequency seismic waves beneath the central Andean plateau. *J. Geophys. Res.*, 97-19, 929-19, 947.
- Whitman, D., 1994. Moho geometry beneath the eastern margin of the Andes, northwest Argentina, and its implications to the effective elastic thickness of the Andean foreland, *J. Geophys. Res.*, 99, 15, 277-15, 289.

- Whitman, D., Isacks, B.L., Kay, S.M., 1996. Lithospheric structure and along-strike segmentation of the Central Andean Plateau: seismic, magmatism, flexure, topography and tectonics. *Tectonophysics* 259, 29-40.
- Witherspoon, P.A., Wang, J.S.Y., Iwai, K., Gale, J.E., 1980. Validity of cubic law for fluid flow in a deformable rock fracture. *Water Resources Research* 16, 1016-1024.
- Woodcock N.H. & Rickards B., 2003. Transpressive duplex and flower structure: Dent Fault System, NW England. *Journal of Structural Geology*, 25, 12, 1981–1992.
- Wu, H., Pollard D.D., 1995. An experimental study of the relationship between joint spacing and layer thickness. *Journal of Structural Geology* 17, 887-905.
- Yang, K., Browne, P.R.L., Huntington, J.F., Walshea, J.L., 2001. Characterising the hydrothermal alteration of the Broadlands-Ohaaki geothermal system, New Zealand, using short wave infrared spectroscopy. *Journal of Volcanology and Geothermal Research* 106, 53–65.
- Zeeb, C., Rivas, E. G., Bons, P. D. and Blum P., 2013. Evaluation of sampling methods for fracture network characterization using outcrops. *AAPG Bulletin*, 97, 9, 1545-1566.
- Zhang X., Sanderson D.J., 1996. Numerical modelling of the effects of fault slip on fluid flow around extensional faults. *J Struct Geol* 95, 109–119. doi:10.1016/0191-8141(95)00086-S

APPENDIX

LEGEND	131
SCAN-LINE SURVEYS	133
<i>Cap-rock deposits</i>	
SL1	134
SL2	136
SL3	137
SL4	139
SL5	140
SL6	142
SL11	143
SL12	146
<i>Reservoir deposits</i>	
SL7	147
SL8	148
SL9	149
SL10	150
SL13	151
SL14	152
SL15	153
FAST SCAN-LINE SURVEYS	155
<i>Cap-rock deposits</i>	
FSL1	156
<i>Reservoir deposits</i>	
FSL2	157
FSL3	158
FSL4	159
FSL5	160
CUMULATIVE FREQUENCY DISTRIBUTIONS FOR LENGHT	161
<i>Anta Yaco volume</i>	
Set 1	162
Set 1A	162
Set 1B	162
Set 2	163
Set 2A	163
Set 2B	163
<i>Ceibal volume</i>	
Set 1	164
Set 1A	164
Set 1B	164
Set 2	165
Set 2A	165

Set 2B	165
<i>Balboa anticline volume</i>	
Set 1	166
Set 1A	166
Set 1B	166
Set 2A	167
Set 2B	167
<i>Termas anticline volume</i>	
Set 1	168
Set 1A	168
Set 1B	168
Set 2	169
Set 2A	169
Set 2B	169
SECONDARY PERMEABILITY AND POROSITY MODELS	170
<i>Anta Yaco volume</i>	
Kxx	171
Kxy	171
Kxz	172
Kyy	172
Kyz	173
Kzz	173
Porosity	174
<i>Ceibal volume</i>	
Kxx	175
Kxy	175
Kxz	176
Kyy	176
Kyz	177
Kzz	177
Porosity	178
<i>Balboa anticline volume</i>	
Kxx	179
Kxy	179
Kxz	180
Kyy	180
Kyz	181
Kzz	181
Porosity	182
<i>Termas anticline volume</i>	
Kxx	183
Kxy	183
Kxz	184
Kyy	184
Kyz	185
Kzz	185
Porosity	186

X-RAY DIFFRACTION PATTERN	187
<i>Whole rock composition</i>	
AR1a	188
AR1b	188
AR5	188
AR7a	188
AR7b	189
AR10	189
AR11	189
AR12	189
AR14a	190
AR14b	190
AR15b	190
AR16	190
AR17	191
AR18	191
AR19a	191
AR19b	191
<i><2μm grain-size fraction</i>	
AR1a	192
AR1b	192
AR5	192
AR7a	193
AR7b	193
AR10	193
AR11	193
AR12	194
AR14a	194
AR14b	194
AR15b	194
AR16	195
AR17	195
AR18	195
AR19b	195
AR21	196
AR27	196
AR29	196
AR30.1	196
AR30.2	197

Legend

SCAN-LINE

Scan-line survey number

Field tab

Number of the scan-line			Date of acquisition		Dip and dip direction of the scan-line			Lenght	
Coordinates				Lithology			Bedding		
Latitude		Longitude							
FRACTURE PARAMETERS*									
Number	Distance	Dip-azimuth	Dip	Lenght up	Termination up	Lenght down	Termination down	Aperture	
*Note: Distance: distance of the fracture fromm the starting point of the scan-line; Length: fracture length above and below the trace of the scan-line; Termination: S= fracture persist in others strata, R= fracture ends in the rock, F= fracture terminates in another fracture I= the termination type is invisible, n.d.: not determined									

FAST SCAN-LINE

Fast scan-line survey number

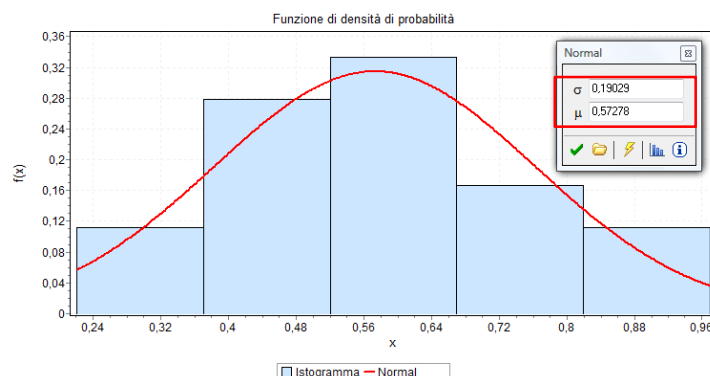
Field tab

Number of the fast scan-line		Date of acquisition		Lenght	
Coordinates				Lithology	
Latitude		Longitude			
FRACTURE PARAMETERS*					
Number	Distance	Spacing	Dip-azimuth	Dip	
*Note: Distance: distance of the fracture from the starting point of the scan-line; Spacing: distance from the previous fracture					

CUMULATIVE FREQUENCY DISTRIBUTION FOR LENGHT

Fracture Set

Distribution type and parameters



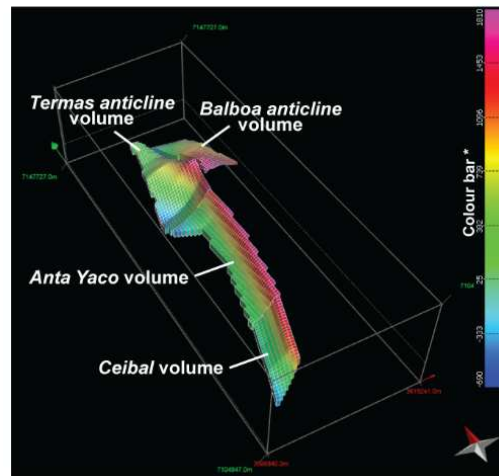
SECONDARY PERMEABILITY AND POROSITY MODELS

Name of the modelled volume

Output Property

Colour map showing the secondary permeability and porosity distributions in the four modelled volumes of the Sierra de La Candelaria anticline.

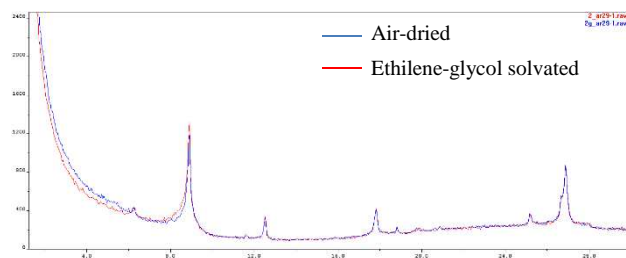
**Permeability values are in milliDarcy*



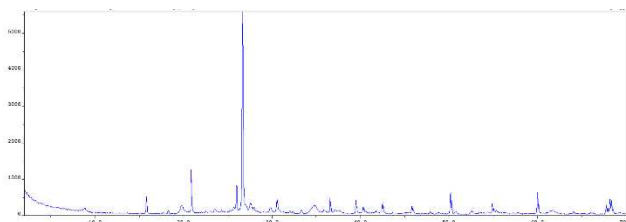
X-RAY DIFFRACTION PATTERN

Sample name

Diffraction patterns in the <2- μ m grain-size fraction.



Whole rock diffraction pattern.



SCAN-LINE SURVEYS

SCAN LINE 1

1			22/04/2012		255/15			10m
25.83554°		64.93138°		ANTA Fm – METÁN SUBGROUP			320-20	
FRACTURE PARAMETERS								
N°	Distance (cm)	Dip-azimuth	Dip	Lenght Up (cm)	Termination Up	Lenght Down (cm)	Termination Down	Aperture (mm)
1	0	50	88	55	P - R	30	P- I	2
2	16	80	88	50	P - R	5	R	1
3	22	252	88	4	R	23	P- I	1
4	29	250	88	21	P - R	5	R	1
5	42	300	86	10	R	4	F	1
6	47	120	65	6	R	3	R	1
7	51	80	88	1	R	2	R	1
8	58	240	65	70	P-I	35	P- R	1
9	66	120	65	1	R	5	R	1
10	72	90	88	13	R	18	R	1
11	77	250	88	16	R	11	R	1
12	84	150	65	6	R	22	P - R	1
13	85	100	80	5	R	21	P - R	1
14	87	200	88	5	R	6	R	1
15	94	100	80	6	R	3	R	1
16	104	130	55	15	I	21	R	1
17	105	214	70	7	R	2	R	2
18	113	200	75	7	R	35	P- I	1
19	125	240	88	80	P - R	32	P- I	1
20	144	280	88	10	R	12	R	1
21	158	230	88	93	P - R	35	P- I	1
22	168	210	88	3	R	8	R	1
23	171	60	88	12	R	10	R	1
24	180	230	88	5	R	19	R	2
25	187	250	88	30	P - R	43	P- I	1
26	196	70	76	85	P-I	45	P- I	1
27	220	120	70	60	P - R	47	P- I	2
28	240	140	65	5	R	30	R	2
29	250	270	88	56	P - R	25	R	2
30	262	100	80	3	F	4	R	1
31	263	300	35	4	R	1	F	1
32	273	60	72	80	P- I	41	P- I	1
33	274	60	72	61	P - R	37	P- I	1
34	284	60	72	77	P - R	32	P- I	2
35	320	230	50	35	P - R	35	P- I	2
36	320	90	88	41	P - R	45	P- I	2

37	327	280	88	25	P - R	48	P- I	1
38	358	260	30	44	P - R	10	F	1
39	367	80	65	17	F	20	F	1
40	373	270	70	11	R	30	P- I	2
41	377	300	88	45	P - R	35	P- I	1
42	381	300	88	5	F	5	F	2
43	432	70	66	3	I	30	P- I	1
44	447	70	66	50	P-I	30	P- I	1
45	458	70	70	55	P - R	42	P- I	1
46	465	180	55	60	P-I	30	P- I	1
47	526	230	85	41	P - R	23	F	1
48	532	140	70	10	F	60	P- I	1
49	540	280	70	5	F	15	F	2
50	545	265	78	35	F	60	P- I	1
51	550	290	65	25	F	60	P- I	1
52	586	120	74	48	P - R	5	R	1
53	620	100	80	6	R	80	I	1
54	632	190	60	10	R	2	R	2
55	634	300	85	30	P - R	80	P- I	2
56	664	190	74	35	P-I	80	P- I	2
57	668	120	70	32	P - R	80	P- I	2
58	678	120	70	1	R	5	R	2
59	694	270	85	12	R	22	R	2
60	704	110	85	17	R	62	P- I	2
61	732	90	80	31	P - R	35	R	2
62	742	110	80	32	P - R	67	R	2
63	764	70	85	30	P - R	70	R	2
64	780	110	75	55	P-I	68	P- I	3
65	820	50	85	10	F	10	F	3
66	824	100	70	3	R	13	R	2
67	850	270	88	5	R	65	P- I	2
68	868	250	80	4	R	36	P - R	2
69	904	240	70	51	P - R	80	P- I	1
70	910	90	70	15	R	30	F	2
71	940	230	65	70	P - R	90	P- I	3
72	952	90	60	37	P - R	3	R	1
73	954	230	30	39	F	25	R	1
74	980	240	80	48	P-I	84	P- I	1
75	998	80	70	30	F	80	P- I	1

SCAN-LINE 2

2			22/04/2012		330/05			10m
25.83833°		64.93341°		ANTA Fm – METÁN SUBGROUP			280-55	
FRACTURE PARAMETERS								
N°	Distance (cm)	Dip-azimuth	Dip	Lenght Up (cm)	Termination Up	Lenght Down (cm)	Termination Down	Aperture (mm)
1	0	20	52	12	F	16	I	2
2	12	210	84	1	I	74	I	2
3	46	180	45	28	F	3	I	2
4	62	20	82	1	I	120	I	2
5	118	280	55	n.d.	n.d.	n.d.	n.d.	2
6	127	20	85	9	I	80	F	2
7	180	40	15	n.d.	n.d.	n.d.	n.d.	n.d.
8	206	330	70	25	F	40	F	2
9	252	50	80	n.d.	I	7	R	2
10	265	160	65	5	F	25	F	2
11	283	350	88	40	F	26	F	2
12	290	3	84	120	F	32	F	2
13	297	90	65	28	R	15	F	2
14	330	140	50	n.d.	n.d.	n.d.	n.d.	2
15	363	80	35	2	I	5	I	2
16	377	160	60	100	I	27	I	2
17	390	200	75	75	F	30	F	2
18	400	60	40	2	I	5	I	2
19	455	200	70	n.d.	n.d.	n.d.	n.d.	n.d.
20	570	340	65	100	I	100	I	2
21	667	30	74	20	I	40	I	n.d.
22	686	180	75	300	I	100	I	2
23	770	190	60	300	I	100	I	n.d.
24	860	359	85	30	R	100	I	2
25	980	240	20	15	R	2	I	2
26	1000	120	65	20	F	100	I	2

SCAN-LINE 3

3			23/04/2012		10/0			7.5m
25.83650°		64.93487°		ANTA Fm – METÁN SUBGROUP			310-60	
FRACTURE PARAMETERS								
N°	Distance (cm)	Dip-azimuth	Dip	Lenght Up (cm)	Termination Up	Lenght Down (cm)	Termination Down	Aperture (mm)
1	0	30	70	40	I	35	I	1
2	8	30	70	40	I	35	I	1
3	10	20	70	15	F	2	F	1
4	16	10	80	20	F	20	I	1
5	59	290	10	2	F	6	R	1
6	65	20	78	14	I	1	F	1
7	70	30	65	19	F	2	F	1
8	73	30	65	50	I	2	R	1
9	74	30	65	23	I	21	F	1
10	84	20	55	50	I	10	F	1
11	86	34	85	5	F	1	F	1
12	90	60	75	12	F	1	F	1
13	100	270	8	2	F		I	1
14	107	80	75	50	I	25	F	1
15	130	130	50	15	F	5	F	1
16	146	40	85	50	I	15	I	1
17	155	210	88	35	F	5	F	1
18	163	290	20	10	F	1	F	1
19	170	40	85	50	I	10	I	1
20	186	30	80	50	R	15	I	1
21	193	30	80	80	I	1	I	1
22	197	50	82	80	I	1	I	1
23	200	50	82	80	I	1	I	1
24	206	30	68	60	I	5	I	1
25	240	35	80	80	I	15	I	1
26	250	35	80	80	I	1	I	1
27	258	250	25	45	F	10	I	1
28	270	280	20	40	F	2	I	1
29	272	20	70	54	I	1	I	1
30	323	60	85	50	I	1	I	1
31	333	30	85	40	I	5	I	1
32	355	70	50	30	I	10	I	1
33	370	210	88	25	F	10	I	1
34	420	23	80	40	F	36	I	1
35	467	23	70	43	I	35	I	1
36	476	310	80	8	I	32	I	1

37	520	18	80	26	I	27	I	1
38	533	20	80	24	I	28	I	1
39	543	18	70	36	R	27	I	1
40	553	305	80	21	I	29	I	1
41	563	20	80	44	I	36	I	1
42	570	305	80	30	R	15	I	1
43	570	120	85	20	I	15	R	1
44	592	195	80	31	I	21	I	1
45	600	195	80	6	F	46	I	1
46	603	300	80	12	I	21	I	1
47	603	358	60	29	R	17	I	1
48	611	220	25	13	I	1	I	1
49	613	190	50	15	F	19	R	1
50	629	190	70	21	F	40	I	1
51	638	190	70	27	R	30	F	1
52	672	10	40	41	I	40	I	1
53	682	10	80	36	I	17	I	1
54	691	30	75	34	I	26	I	1
55	702	35	80	40	I	31	I	1
56	710	308	50	40	I	34	I	1
57	713	10	80	20	F	40	I	1
58	717	20	75	15	F	35	I	1
59	727	284	35	10	R	5	I	1
60	730	10	88	16	F	33	I	1
61	750	360	65	12	R	20	R	1

SCAN-LINE 4

4			24/04/2012		30/10			5.3m
25.83790°		64.93052°		ANTA Fm – METÁN SUBGROUP			320-25	
FRACTURE PARAMETERS								
N°	Distance (cm)	Dip-azimuth	Dip	Lenght Up (cm)	Termination Up	Lenght Down (cm)	Termination Down	Aperture (mm)
1	0	230	88	4	R	20	R	1
2	10	130	88	1	I	14	I	1
3	43	240	65	26	F	1	I	1
4	50	320	25	n.d.	n.d.	n.d.	n.d.	n.d.
5	85	240	88	2	R	5	R	1
6	93	30	85	25	P-R	23	P- R	1
7	108	190	35	8	R	12	R	1
8	142	60	65	6	F	10	R	1
9	224	240	75	35	F	6	F	1
10	248	200	88	50	F	30	F	1
11	268	140	60	14	I	50	I	1
12	396	220	65	80	I	10	I	2
13	450	320	25	n.d.	n.d.	n.d.	n.d.	n.d.
14	390	30	80	80	F	6	F	2
15	393	50	50	50	F	5	R	2
16	525	180	35	35	F	40	F	1
17	527	180	35	35	F	40	F	2

SCAN-LINE 5

5			24/04/2012		20/0			9m
25.83461°		64.93719°		ANTA Fm – METÁN SUBGROUP			270-88	
FRACTURE PARAMETERS								
N°	Distance (cm)	Dip-azimuth	Dip	Lenght Up (cm)	Termination Up	Lenght Down (cm)	Termination Down	Aperture (mm)
1	0	28	80	15	I	6	I	1
2	0	250	30	10	F	1	I	2
3	6	28	80	11	I	6	I	1
4	21	20	86	36	I	80	I	1
5	28	190	70	10	F	6	I	1
6	32	190	70	2	I	6	F	1
7	82	310	60	5	F	25	F	2
8	148	360	74	80	I	30	R	10
9	162	280	15	6	I	15	I	3
10	176	360	70	9	I	18	I	1
11	181	360	70	1	I	27	R	1
12	208	360	75	1	I	23	F	1
13	230	190	75	80	F	60	F	1
14	332	260	10	2	I	1	I	2
15	352	200	88	36	F	7	I	1
16	374	30	75	9	F	2	F	1
17	392	180	88	10	F	7	F	1
18	413	10	88	10	F	8	F	2
19	426	200	85	30	F	38	F	2
20	447	10	88	8	F	10	I	1
21	465	170	88	20	F	3	F	1
22	472	40	75	10	F	5	F	1
23	485	202	88	23	F	67	I	1
24	492	25	75	11	F	5	I	1
25	501	20	80	19	I	29	F	1
26	518	200	89	20	F	5	F	1
27	559	20	83	13	F	62	R	1
28	567	18	89	12	F	6	F	1
29	575	18	85	29	F	17	F	1
30	597	20	88	9	F	3	F	1
31	603	20	65	9	F	4	F	1
32	616	22	83	4	F	35	F	1
33	622	28	18	5	F	10	F	5
34	625	326	80	13	F	14	F	3
35	636	178	85	20	F	21	F	3
36	640	360	85	18	F	20	F	3

37	662	308	88	100	I	38	I	3
38	662	190	60	100	R	100	I	5
39	672	304	29	25	F	5	F	5
40	682	305	10	10	F	9	F	5
41	707	188	75	50	F	50	I	1
42	720	180	75	80	F	68	I	1
43	800	185	88	28	F	51	I	1
44	807	195	88	30	F	20	F	1
45	818	190	75	40	F	18	I	1
46	844	230	75	14	F	18	F	1
47	852	110	25	7	I	1	I	3
48	879	202	88	6	I	48	I	0
49	903	200	85	60	F	57	I	1

SCAN-LINE 6

6			25/04/2012		220/10			5m
25.83854°		64.93333°		ANTA Fm – METÁN SUBGROUP			280-60	
FRACTURE PARAMETERS								
N°	Distance (cm)	Dip-azimuth	Dip	Lenght Up (cm)	Termination Up	Lenght Down (cm)	Termination Down	Aperture (mm)
1	0	90	35	5	I	41	F	2
2	10	280	85	4	F	5	I	1
3	20	285	75	5	F	8	I	2
4	40	80	45	5	R	100	I	2
5	42	208	88	80	R	10	I	2
6	62	244	45	4	R	10	I	2
8	72	30	68	2	R	40	F	1
10	110	290	65	1	R	80	I	2
11	112	70	45	21	F	25	F	1
13	127	52	30	5	F	30	F	1
14	152	186	70	37	F	64	F	2
15	160	65	38	2	F	30	F	1
18	230	90	45	4	I	65	I	1
19	230	190	85	40	R	30	I	1
21	260	190	70	5	F	10	I	1
22	260	58	60	20	F	2	I	1
23	271	230	50	26	F	31	I	2
24	280	270	55	10	R	5	I	2
27	340	210	55	150	I	40	I	2
28	354	320	70	80	F	30	I	2
29	370	170	80	80	F	39	I	2
30	383	268	65	58	F	28	I	1
31	386	128	85	10	I	20	I	1
32	425	80	65	27	I	18	I	2
33	430	100	65	2	I	10	I	2
35	465	200	40	5	I	20	F	2
38	498	110	30	15	I	2	F	2
39	500	208	40	27	R	5	I	2

SCAN-LINE 11

11			27/04/2012		100/10			9.8m	
25.97931°		64.93237°		ANTA Fm – METÁN SUBGROUP			310-30		
FRACTURE PARAMETERS									
N°	Distance (cm)	Dip- azimuth	Dip	Lenght Up (cm)	Termination Up	Lenght Down (cm)	Termination Down	Aperture (mm)	
1	0	105	80	200	I	100	I	1	
2	23	105	80	35	I	100	I	1	
3	32	105	80	20	I	100	I	1	
4	45	120	85	10	F	100	I	1	
5	47	105	80	10	F	100	I	1	
6	67	80	70	10	I	100	I	1	
7	112	330	88	54	I	40	F	1	
8	126	70	70	10	I	80	I	1	
9	133	330	88	5	I	100	I	1	
10	140	70	70	10	I	80	I	1	
11	142	10	75	10	I	60	I	1	
12	144	70	70	10	I	80	I	1	
13	152	70	70	10	I	80	I	1	
14	152	359	75	5	I	10	R	1	
15	155	10	75	10	I	60	I	1	
16	162	10	75	10	I	60	I	1	
17	172	186	85	5	I	43	I	1	
18	185	80	75	2	R	42	I	1	
19	190	80	75	2	R	42	I	1	
20	226	80	75	6	R	20	I	1	
21	231	168	88	14	R	27	I	1	
22	232	10	70	3	R	5	I	1	
23	238	358	75	5	R	5	I	1	
24	249	358	75	5	R	5	I	1	
25	253	106	75	10	R	5	I	1	
26	262	106	75	10	R	5	I	1	
27	274	100	70	2	R	2	I	1	
28	275	100	70	2	R	2	I	1	
29	278	14	70	2	R	2	I	1	
30	283	14	70	2	R	2	I	1	
31	296	12	80	2	R	2	I	1	
32	317	110	80	8	I	18	I	1	
33	356	34	70	5	R	13	I	1	
34	380	100	80	5	I	40	I	1	
35	392	100	80	15	I	48	I	3	
36	412	100	80	12	I	40	I	3	

37	433	10	75	20	F	52	F	1
38	438	20	85	3	I	18	F	1
39	445	104	70	10	F	21	F	1
40	452	10	80	25	I	5	I	1
41	456	104	70	10	F	3	I	1
42	456	10	80	23	I	8	F	1
43	462	104	70	18	F	10	I	1
44	469	104	70	10	I	3	I	3
45	486	10	85	15	I	60	I	1
46	488	86	80	21	I	80	I	1
47	488	10	80	15	F	18	I	1
48	496	154	88	25	I	70	I	1
49	510	90	80	2	R	24	R	1
50	518	90	80	5	R	64	I	1
51	526	86	75	20	I	60	I	1
52	540	86	75	30	I	21	F	1
53	541	86	75	18	F	9	I	1
54	554	78	80	35	I	7	I	1
55	568	200	88	41	F	1	I	1
56	571	78	80	19	F	1	I	1
57	589	235	85	6	I	1	I	1
58	595	78	80	36	I	53	I	1
59	606	166	75	14	F	14	I	1
60	618	78	80	45	I	58	I	1
61	628	166	75	14	F	14	I	1
62	640	78	80	8	F	50	I	1
63	642	166	74	8	I	15	I	1
64	666	340	80	16	I	80	F	1
65	708	356	88	41	I	21	I	1
66	720	85	70	40	I	2	F	1
67	727	85	70	37	I	45	I	1
68	733	174	85	19	I	1	I	1
69	767	70	80	43	I	30	I	1
70	771	355	88	8	I	14	F	1
71	777	75	85	60	I	12	I	1
72	800	350	80	80	I	24	I	1
73	811	355	88	12	F	22	I	1
74	823	348	75	14	F	10	I	1
75	837	190	88	22	I	1	I	1
76	841	90	65	20	F	26	I	1
77	860	356	85	38	F	2	I	1
78	864	90	75	26	I	18	I	1
79	886	100	80	38	I	23	I	1
80	893	176	89	70	I	25	I	1
81	910	200	88	7	I	1	I	1

82	912	76	85	60	I	30	I	1
83	936	82	70	34	F	1	R	1
84	943	90	70	10	F	10	F	1
85	949	90	70	50	I	13	F	1
86	966	72	80	35	I	7	I	1
87	966	346	76	52	I	30	I	1
88	969	346	76	34	F	23	I	1
89	972	346	76	56	I	23	I	1
90	975	72	80	20	F	70	I	1
91	976	346	76	25	F	52	I	1

SCAN-LINE 12

12		28/04/2012			30/0			4.5m
25.83884°		64.93100°		ANTA Fm – METÁN SUBGROUP			60-60	
FRACTURE PARAMETERS								
N°	Distance (cm)	Dip- azimuth	Dip	Lenght Up (cm)	Termination Up	Lenght Down (cm)	Termination Down	Aperture (mm)
1	0	202	55	5	I	20	F	2
2	20	208	55	7	I	7	F	2
3	40	82	40	5	F	8	F	2
4	50	82	40	5	I	14	F	2
5	54	100	80	20	F	40	I	1
6	74	66	50	100	F	20	I	1
7	94	78	65	60	I	30	I	1
8	204	250	70	10	F	40	F	1
9	231	200	85	10	F	60	I	2
10	233	120	60	2	I	15	R	1
11	269	160	35	13	I	2	I	1
12	274	178	70	21	F	10	R	1
13	275	60	55	27	I	28	F	1
14	280	160	35	15	I	2	I	1
15	284	140	65	14	F	3	I	1
16	284	122	65	2	I	21	R	2
17	300	178	70	10	F	8	F	2
18	303	90	75	10	R	15	F	2
19	323	234	80	100	I	15	I	2
20	324	150	35	15	F	10	I	2
21	354	170	55	27	I	20	I	2
22	362	240	20	20	F	15	I	2
23	412	240	20	5	F	5	I	1
24	422	230	80	57	F	5	I	2
25	426	220	85	30	F	40	F	1
26	452	230	80	5	I	5	I	1

SCAN-LINE 7

7			26/04/2012		290/15			4.9m
25.99150°		64.91741°		PIRGUA SUBGROUP			290-55	
FRACTURE PARAMETERS								
N°	Distance (cm)	Dip-azimuth	Dip	Lenght Up (cm)	Termination Up	Lenght Down (cm)	Termination Down	Aperture (mm)
1	0	260	55	50	F	40	F	2
2	80	160	70	40	F	80	I	2
3	92	100	45	40	I	13	I	2
4	142	20	80	150	F	40	I	2
5	201	40	65	20	F	30	I	2
6	270	350	80	54	F	7	I	2
7	287	360	75	61	R	10	I	2
9	335	64	70	25	R	13	R	5
10	345	50	85	39	R	8	R	5
11	377	170	70	38	R	18	R	2
12	410	170	85	5	I	20	R	2
13	460	340	65	80	F	2	F	2
14	485	70	55	20	F	2	I	2
15	490	160	75	70	I	2	I	5

SCAN-LINE 8

8			26/04/2012		110/05			6m
25.98974°		64.91750°		PIRGUA SUBGROUP			242-38	
FRACTURE PARAMETERS								
N°	Distance (cm)	Dip- azimuth	Dip	Lenght Up (cm)	Termination Up	Lenght Down (cm)	Termination Down	Aperture (mm)
1	0	60	70	73	I	24	I	n.d.
2	60	70	50	10	I	19	F	n.d.
3	79	220	80	80	I	25	I	n.d.
4	80	170	75	20	F	4	F	n.d.
5	175	190	70	20	F	36	I	n.d.
6	225	165	60	80	I	45	I	n.d.
7	282	320	80	50	F	47	I	n.d.
8	330	125	40	10	R	1	F	n.d.
9	372	120	80	40	I	38	I	n.d.
10	400	90	85	55	F	60	I	n.d.
11	410	60	85	35	F	35	F	n.d.
12	434	110	75	34	I	60	I	n.d.
13	450	235	70	20	F	54	I	n.d.
14	470	5	25	25	F	30	F	n.d.
15	483	245	75	35	F	55	I	n.d.
16	510	310	80	15	F	40	I	n.d.
17	540	100	85	10	F	18	F	n.d.
18	560	100	55	20	F	20	F	n.d.
19	583	170	88	8	F	50	I	n.d.
20	600	130	70	35	I	3	F	n.d.

SCAN-LINE 9

9			26/04/2012		280/05			10m
25.99024°		64.91951°		PIRGUA SUBGROUP			290-65	
FRACTURE PARAMETERS								
N°	Distance (cm)	Dip-azimuth	Dip	Lenght Up (cm)	Termination Up	Lenght Down (cm)	Termination Down	Aperture (mm)
1	0	335	85	8	I	10	F	2
2	48	325	75	19	R	10	I	2
3	60	320	80	7	I	15	I	2
4	120	320	80	35	F	21	I	2
5	170	145	50	40	I	24	I	2
6	170	164	60	60	I	23	I	2
7	190	340	85	45	I	60	I	2
8	284	90	55	12	I	60	I	2
9	342	360	88	30	F	55	I	2
10	400	215	80	21	F	32	I	2
11	430	354	80	10	F	27	F	2
12	435	5	70	10	F	45	I	2
13	458	358	80	30	F	35	I	2
14	485	358	88	23	F	10	I	2
15	510	40	85	40	F	5	I	2
16	578	160	74	80	I	60	F	3
17	586	330	60	22	F	5	F	3
18	615	136	65	26	I	43	F	4
19	678	360	66	19	I	45	F	2
20	679	74	42	18	I	43	F	2
21	734	250	80	40	F	28	F	2
22	804	294	88	40	I	1	F	2
23	837	300	88	24	I	8	F	2
24	844	112	64	13	I	2	F	2
25	900	278	80	11	I	15	F	2
26	918	340	50	38	I	7	F	2
27	937	160	88	35	R	17	F	2
28	973	20	66	15	F	33	F	2
29	978	300	65	5	I	26	F	2
30	1000	300	60	43	R	15	F	2

SCAN-LINE 10

10			27/04/2012		340/25			10m
25.98809°		64.91719°		PIRGUA SUBGROUP			260-30	
FRACTURE PARAMETERS								
N°	Distance (cm)	Dip-azimuth	Dip	Lenght Up (cm)	Termination Up	Lenght Down (cm)	Termination Down	Aperture (mm)
1	0	290	60	100	I	17	F	2
2	6	100	55	5	I	25	I	2
3	22	140	50	10	I	35	I	2
4	50	280	65	10	F	80	I	2
5	70	280	65	5	F	80	I	2
6	94	288	55	15	R	80	I	2
7	220	20	70	80	R	5	I	2
8	257	10	50	10	R	10	I	2
9	378	285	80	10	F	20	I	2
10	464	280	55	120	F	31	I	2
11	470	280	40	120	F	30	I	2
12	490	150	80	80	F	10	F	2
13	495	190	40	5	F	5	F	2
14	520	255	30	200	I	150	I	2
15	786	10	70	22	F	21	F	2
16	832	4	30	17	F	2	I	2
17	870	168	86	23	F	2	I	2
18	933	20	38	44	F	1	I	2
19	940	172	88	19	F	14	F	2
20	990	52	38	21	F	22	I	2

SCAN-LINE 13

13			29/04/2012		280/03			7.70m
25.891267°		64.87830°		PIRGUA SUBGROUP			70-45	
FRACTURE PARAMETERS								
N°	Distance (cm)	Dip-azimuth	Dip	Lenght Up (cm)	Termination Up	Lenght Down (cm)	Termination Down	Aperture (mm)
1	0	170	65	20	I	8	I	1
2	0	30	65	48	I	15	I	1
3	60	150	65	18	F	15	F	1
4	118	260	80	7	F	15	R	0
5	120	230	88	25	F	57	R	1
6	120	250	75	2	R	15	R	1
7	123	250	75	2	R	15	R	1
8	170	230	88	25	R	95	I	10
9	206	238	85	40	F	70	F	1
10	218	76	88	35	F	90	I	1
11	228	250	88	30	I	67	R	0
12	243	40	55	15	F	15	I	1
13	250	50	85	10	I	5	I	1
14	260	250	88	15	F	10	I	0
15	354	240	60	2	I	30	I	n.d.
16	435	270	70	25	I	27	I	n.d.
17	520	106	60	30	R	20	F	1
18	690	26	80	10	I	28	F	n.d.
19	744	304	85	15	F	8	F	n.d.
20	770	66	60	23	I	27	I	n.d.

SCAN-LINE 14

14			29/04/2012		310/03			10m
25.88923°		64.87990°		PIRGUA SUBGROUP			70-25	
FRACTURE PARAMETERS								
N°	Distance (cm)	Dip-azimuth	Dip	Lenght Up (cm)	Termination Up	Lenght Down (cm)	Termination Down	Aperture (mm)
1	0	260	60	60	R	100	I	1
2	80	210	50	30	I	20	I	n.d.
3	120	210	50	60	F	18	I	1
4	150	210	50	80	F	100	I	10
5	173	130	75	80	F	80	R	3
6	175	285	30	30	F	20	F	5
7	250	212	70	60	I	100	I	n.d.
8	265	118	75	20	F	70	R	1
9	270	358	70	50	I	40	F	n.d.
10	273	118	75	200	F	20	R	1
11	283	130	75	25	R	20	I	n.d.
12	384	246	70	5	F	100	I	15
13	430	230	70	80	F	100	I	15
14	450	230	70	80	F	100	I	1
15	462	250	60	10	F	40	F	1
16	464	250	60	20	R	40	I	1
17	471	100	55	100	F	100	I	3
18	472	250	60	60	R	95	I	2
19	478	252	80	41	F	100	I	1
20	478	165	50	100	F	12	R	0
21	497	238	80	200	I	100	I	3
22	550	115	85	80	F	10	I	1
23	560	238	80	200	I	100	I	1
24	614	230	75	33	I	10	R	0
25	639	120	88	300	I	60	F	1
26	675	230	80	30	R	100	I	0
27	708	230	80	100	I	100	I	0
28	710	230	80	200	I	100	I	10
29	760	180	40	38	F	80	I	0
30	810	10	75	50	F	15	I	0
31	822	230	80	60	R	100	I	2
32	850	230	80	60	R	100	I	2
33	873	230	80	60	R	100	I	2
34	880	60	50	50	F	100	I	0
35	940	234	75	80	I	28	I	2

SCAN-LINE 15

15			22/04/2013		150/0			6.5m	
26.14929°		64.95553°		PIRGUA SUBGROUP			15-50		
FRACTURE PARAMETERS									
N°	Distance (cm)	Dip-azimuth	Dip	Lenght Up (cm)	Termination Up	Lenght Down (cm)	Termination Down	Aperture (mm)	
1	0	20	88	13	F	60	R	2	
2	19	180	85	30	F	41	F	2	
3	23	180	80	2	F	70	R	2	
4	30	200	70	20	R	7	R	2	
5	36	205	70	20	F	7	R	2	
6	40	195	75	23	R	0	I	2	
7	47	190	70	35	I	28	R	2	
8	30	315	89	37	F	0	I	2	
9	32	310	85	37	F	0	I	2	
10	36	311	85	40	R	0	I	2	
11	54	190	65	10	F	20	F	2	
12	70	165	70	15	F	30	R	2	
13	80	15	85	60	I	200	I	2	
14	110	35	70	40	R	50	R	2	
15	190	25	50	200	I	50	R	n.d.	
16	215	355	80	0	I	40	F	2	
17	253	350	75	15	R	50	F	2	
18	295	325	75	17	F	10	F	2	
19	317	155	70	10	R	6	F	2	
20	342	125	70	13	R	30	F	2	
21	360	350	70	20	R	20	F	2	
22	370	275	75	10	R	25	F	n.d.	
23	286	285	80	0	I	40	F	n.d.	
24	410	345	85	5	R	30	F	n.d.	
25	415	330	80	10	R	30	F	n.d.	
26	418	175	80	10	R	8	F	n.d.	
27	427	195	80	10	R	12	F	n.d.	
28	433	160	85	10	F	200	I	n.d.	
29	444	335	85	200	I	200	I	n.d.	
30	469	165	89	0	I	20	R	n.d.	
31	500	305	75	200	I	50	F	n.d.	
32	530	180	80	0	I	50	R	n.d.	
33	555	175	85	0	I	50	R	n.d.	
34	576	165	89	200	I	50	R	n.d.	
35	594	140	80	30	I	7	I	n.d.	
36	620	165	89	60	R	200	I	n.d.	

37	620	155	85	80	R	5	R	n.d.
38	621	15	80	50	R	200	I	n.d.
39	652	195	35	10	F	10	F	n.d.
40	660	140	85	200	F	200	F	n.d.

FAST SCAN-LINE SURVEYS

FAST SCAN-LINE 1

FSL1		22/04/2012		2m
25.83790°	64.93389°	ANTA Fm – METÁN SUBGROUP		
FRACTURE PARAMETERS				
N°	Distance (cm)	Spacing (cm)	Dip-azimuth	Dip
1	0		130	15
2	20	20	130	15
3	37	17	130	15
4	54	17	130	15
5	87	33	130	15
6	113	26	130	15
7	147	34	130	15
8	167	20	130	15
9	200	33	130	15

FAST SCAN-LINE 2

FSL2		26/04/2012		2m
25.98981°	64.92008°	PIRGUA SUBGROUP		
FRACTURE PARAMETERS				
N°	Distance (cm)	Spacing (cm)	Dip-azimuth	Dip
1	0		170	70
2	7	7	170	70
3	23	16	170	70
4	34	11	170	70
5	54	20	170	70
6	72	18	170	70
7	95	23	170	70
8	110	15	170	70
9	123	13	170	70
10	140	17	170	70
11	154	14	170	70
12	169	15	170	70
13	181	12	170	70
14	200	19	170	70

FAST SCAN-LINE 3

FSL3		27/04/2012		97cm
25.98804°	64.91776°	PIRGUA SUBGROUP		
FRACTURE PARAMETERS				
N°	Distance (cm)	Spacing (cm)	Dip-azimuth	Dip
1	0		30	20
2	15	15	30	20
3	25	10	30	20
4	57	32	30	20
5	97	40	30	20

FAST SCAN-LINE 4

FSL4		29/04/2012		96cm
25.88990°	64.88186°	PIRGUA SUBGROUP		
FRACTURE PARAMETERS				
N°	Distance (cm)	Spacing (cm)	Dip-azimuth	Dip
1	0		254	85
2	12	12	254	85
3	17	5	254	85
4	21	4	254	85
5	23	2	254	85
6	30	7	254	85
7	34	4	254	85
8	40	6	254	85
9	44	4	254	85
10	61	17	254	85
11	63	2	254	85
12	78	15	254	85
13	82	4	254	85
14	83	1	254	85
15	94	11	254	85
16	96	2	254	85

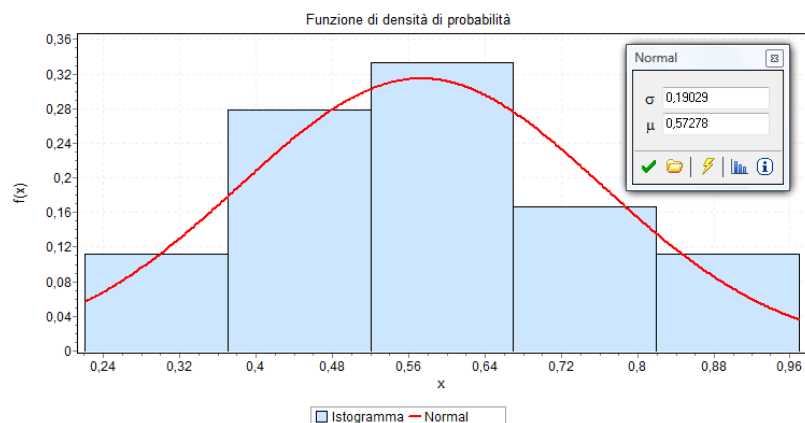
FAST SCAN-LINE 5

FSL5		20/04/2012		63cm
25.90636°	64.87943°	PIRGUA SUBGROUP		
FRACTURE PARAMETERS				
N°	Distance (cm)	Spacing (cm)	Dip-azimuth	Dip
1	0		120	85
2	12	12	125	80
3	17	5	90	70
4	21	4	80	80
5	23	2	78	75
6	30	7	110	80
7	34	4	100	80
8	40	6	105	85
9	44	4	110	85
10	61	17	100	85
11	63	2	290	75

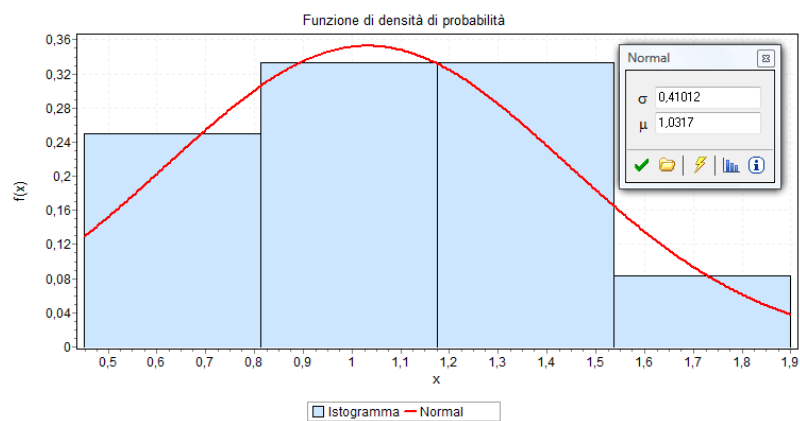
**CUMULATIVE FREQUENCY
DISTRIBUTIONS FOR LENGHT**

Anta Yaco volume

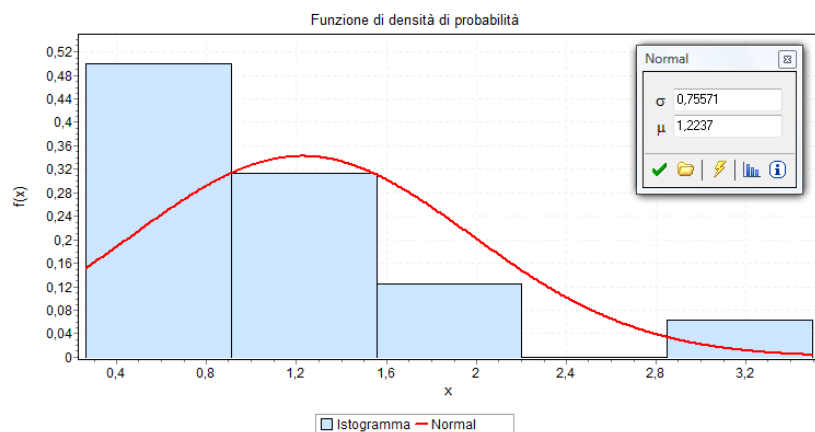
SET 1



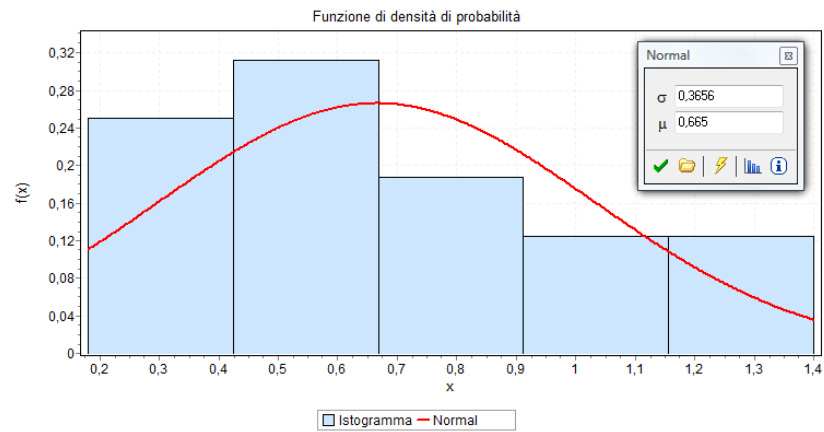
SET 1A



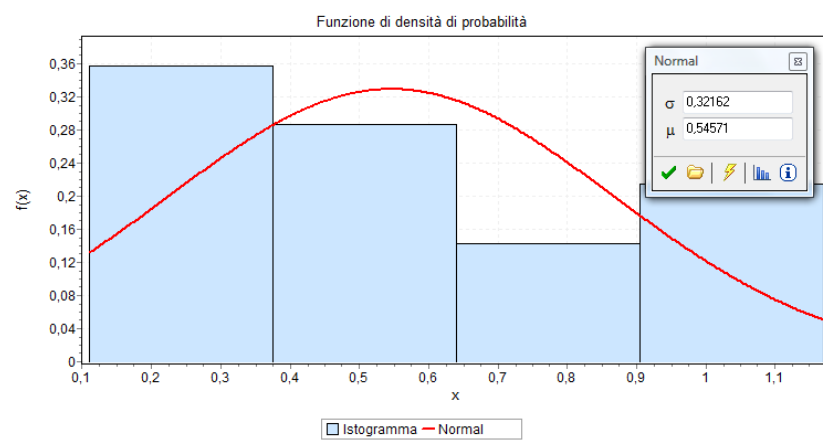
SET 1B



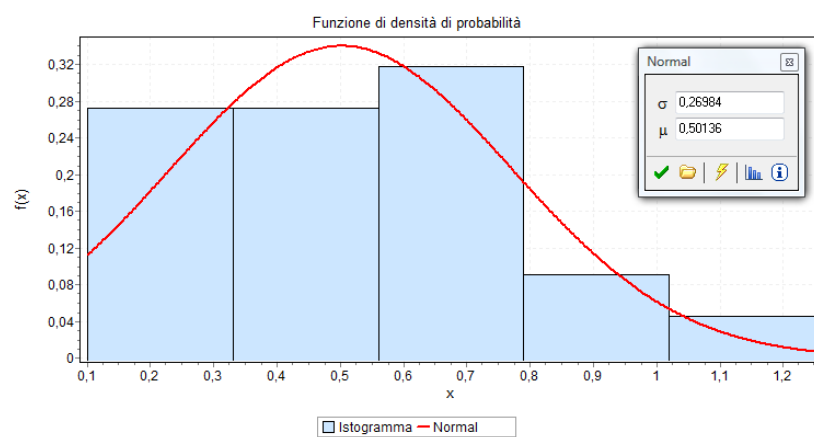
SET 2



SET 2A

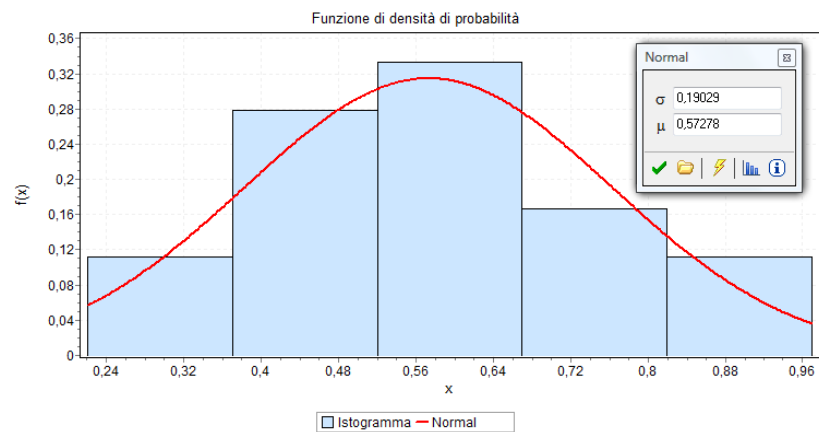


SET 2B

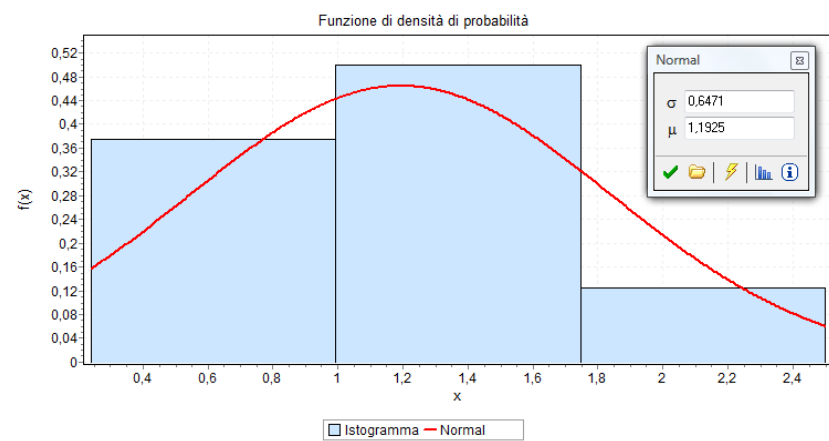


Ceibal volume

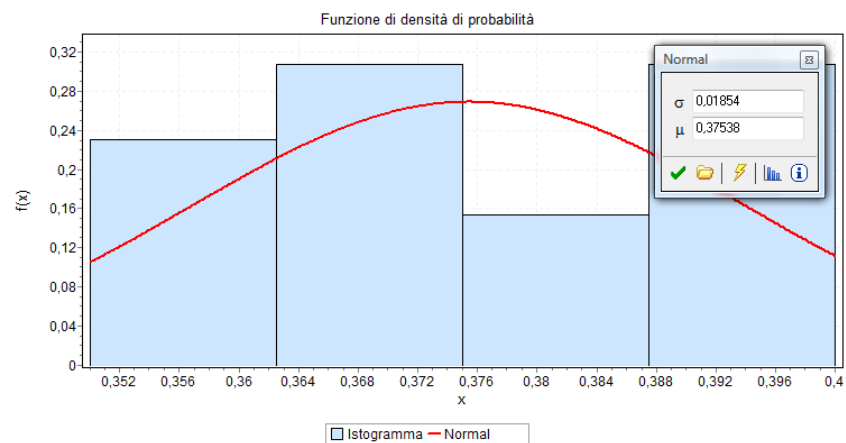
SET 1



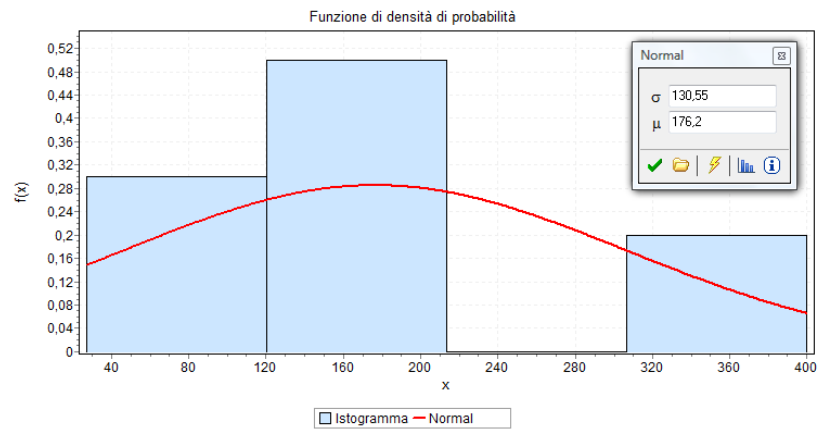
SET 1A



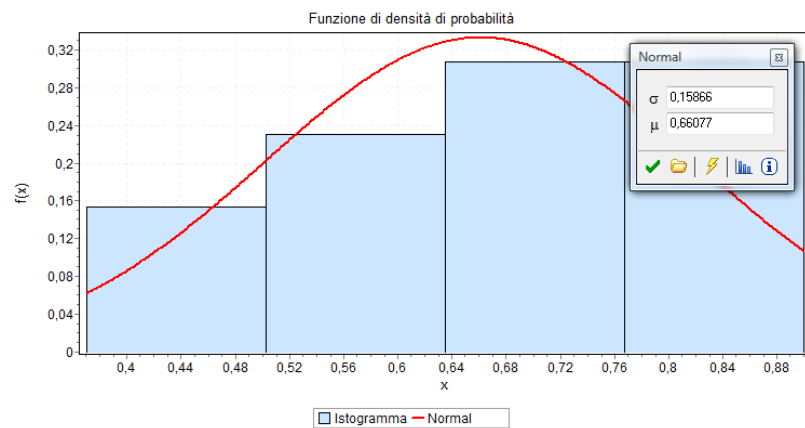
SET 1B



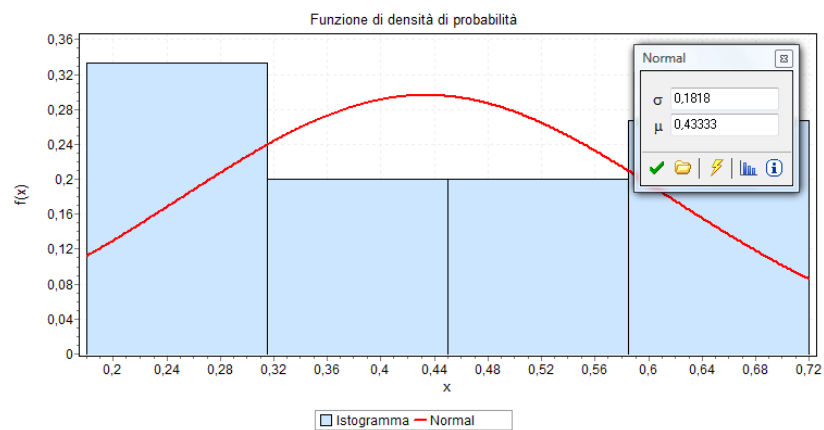
SET 2



SET 2A

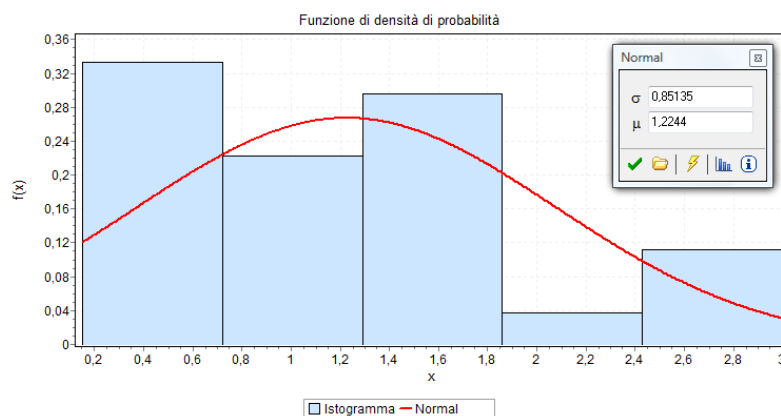


SET 2B

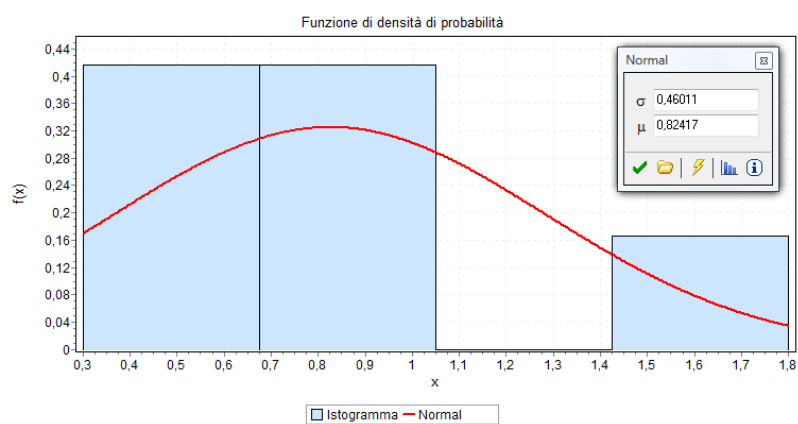


Balboa anticline volume

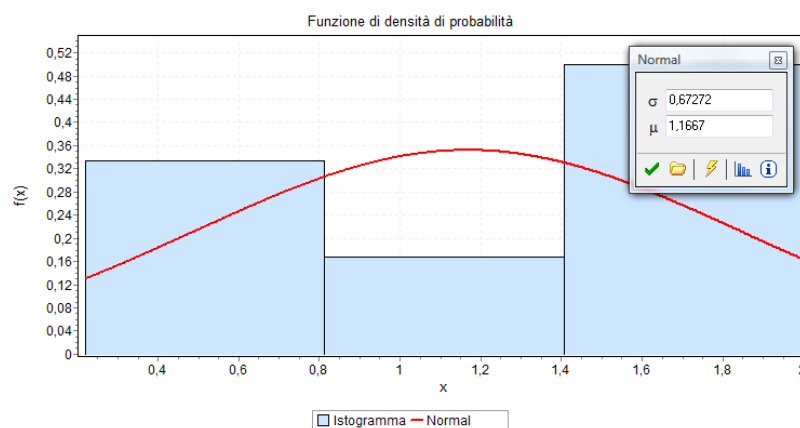
SET 1



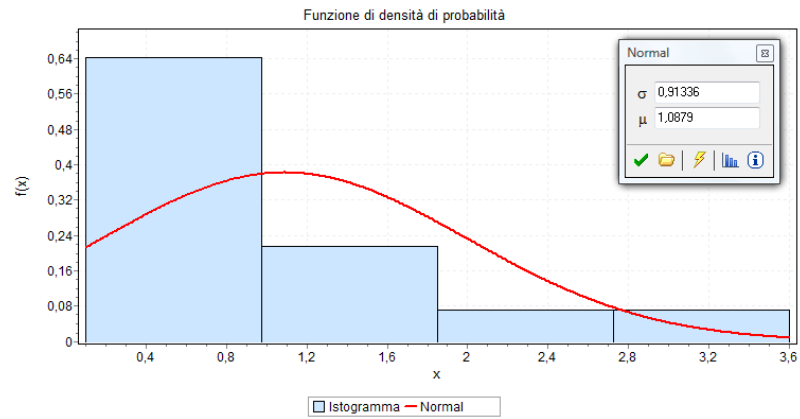
SET 1A



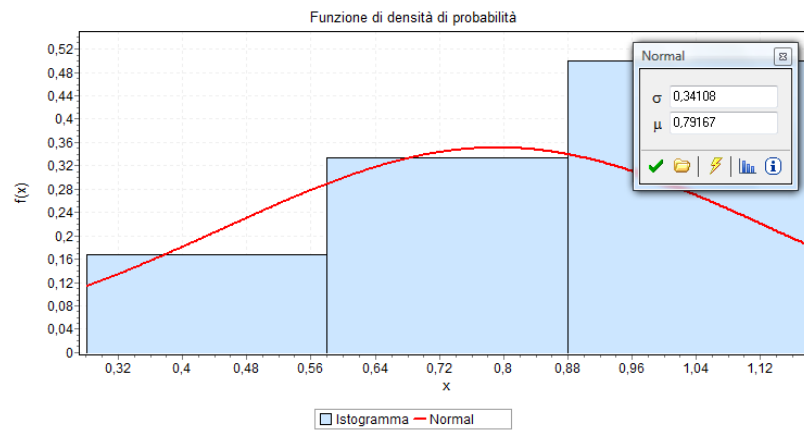
SET 1B



SET 2A

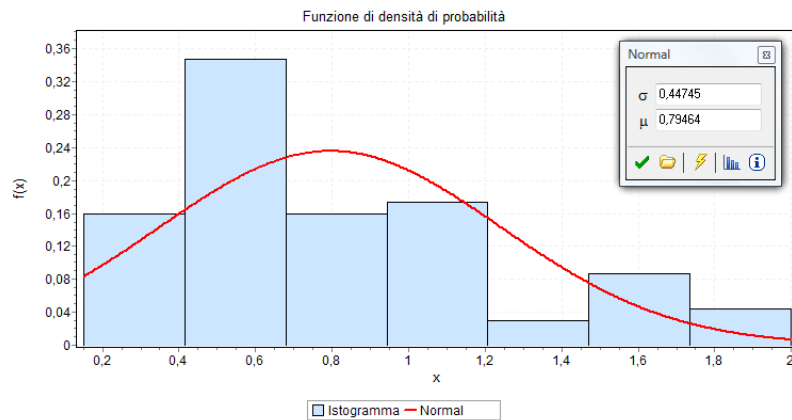


SET 2B

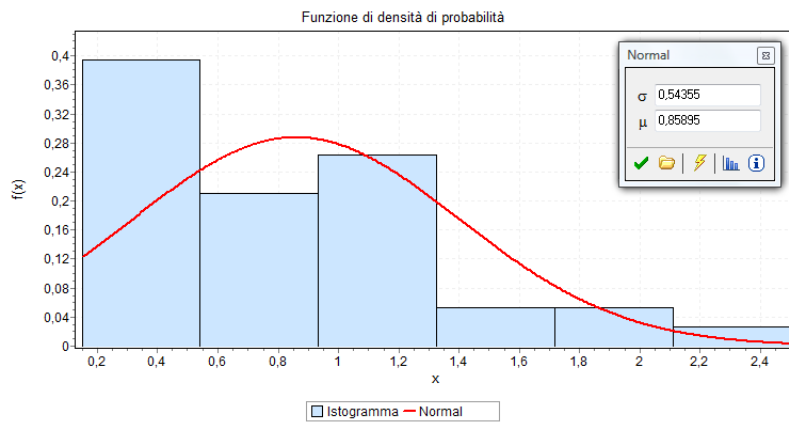


Termas anticline volume

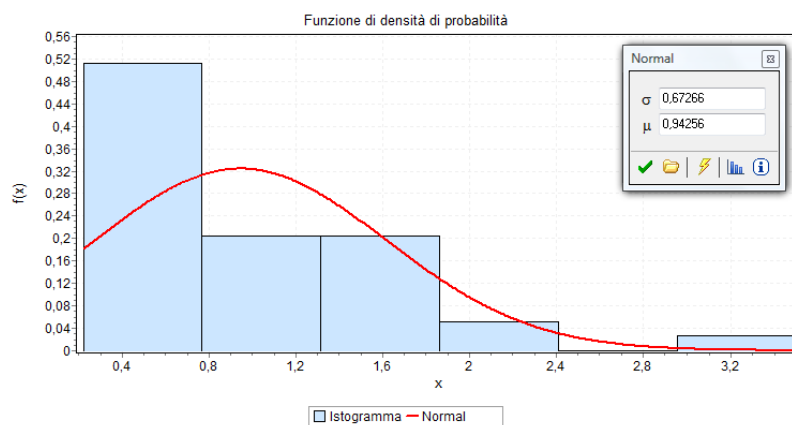
SET 1



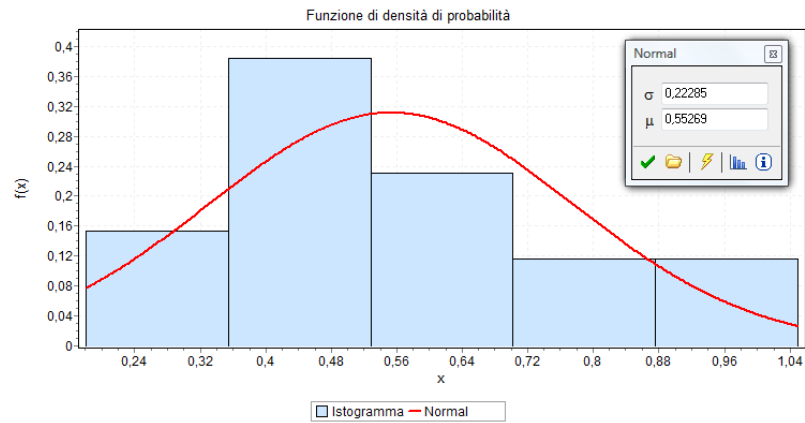
SET 1A



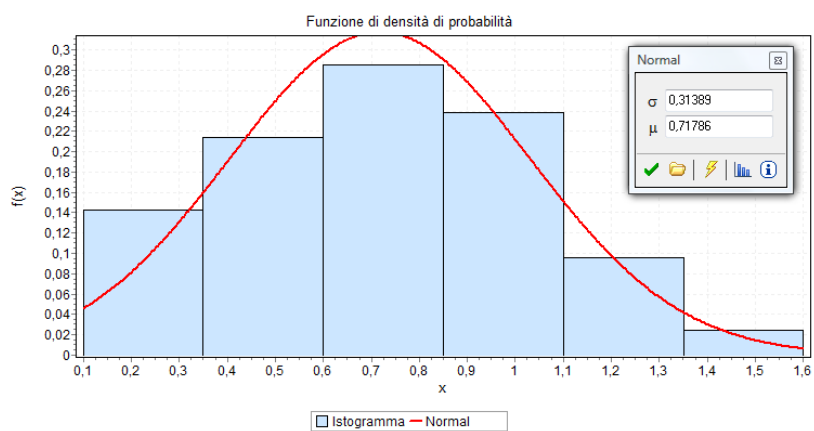
SET 1B



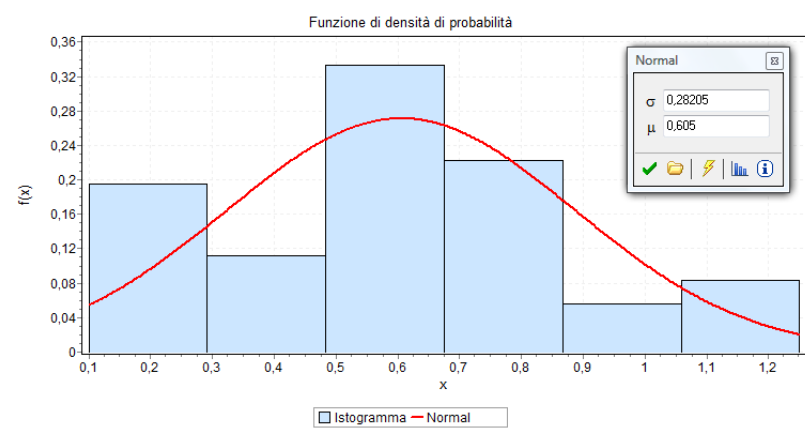
SET 2



SET 2A



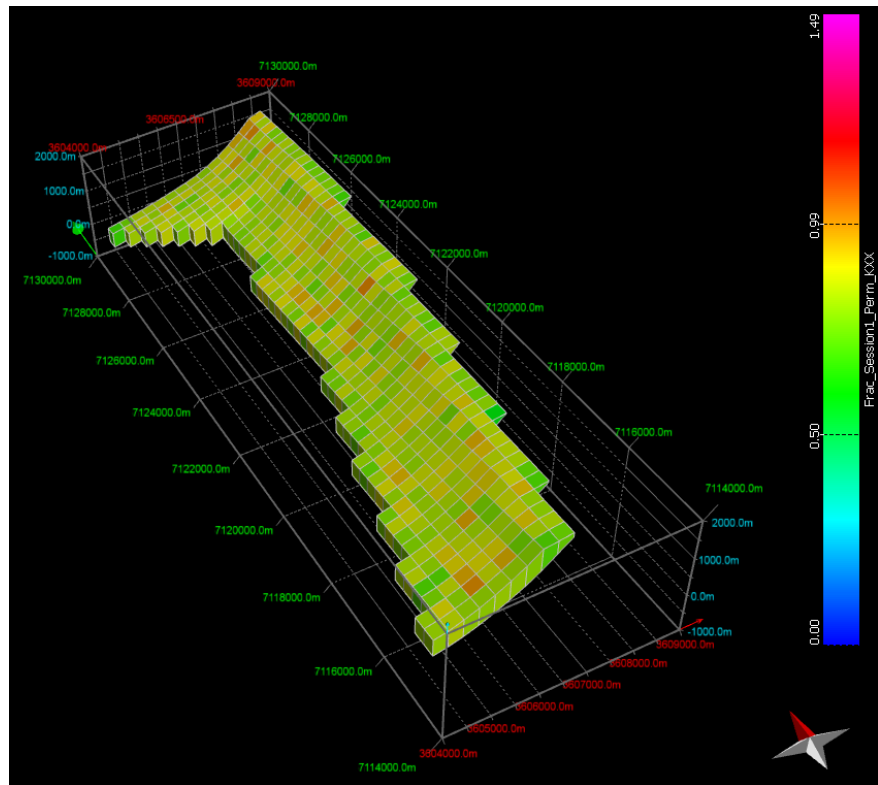
SET 2B



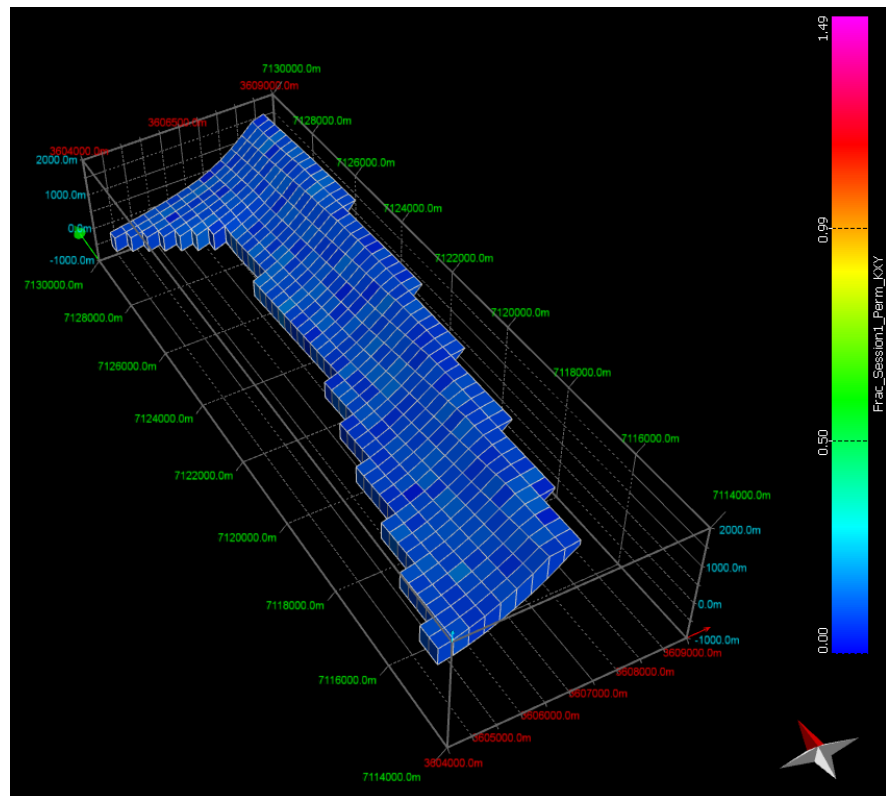
SECONDARY PERMEABILITY AND POROSITY MODELS

Anta Yaco volume

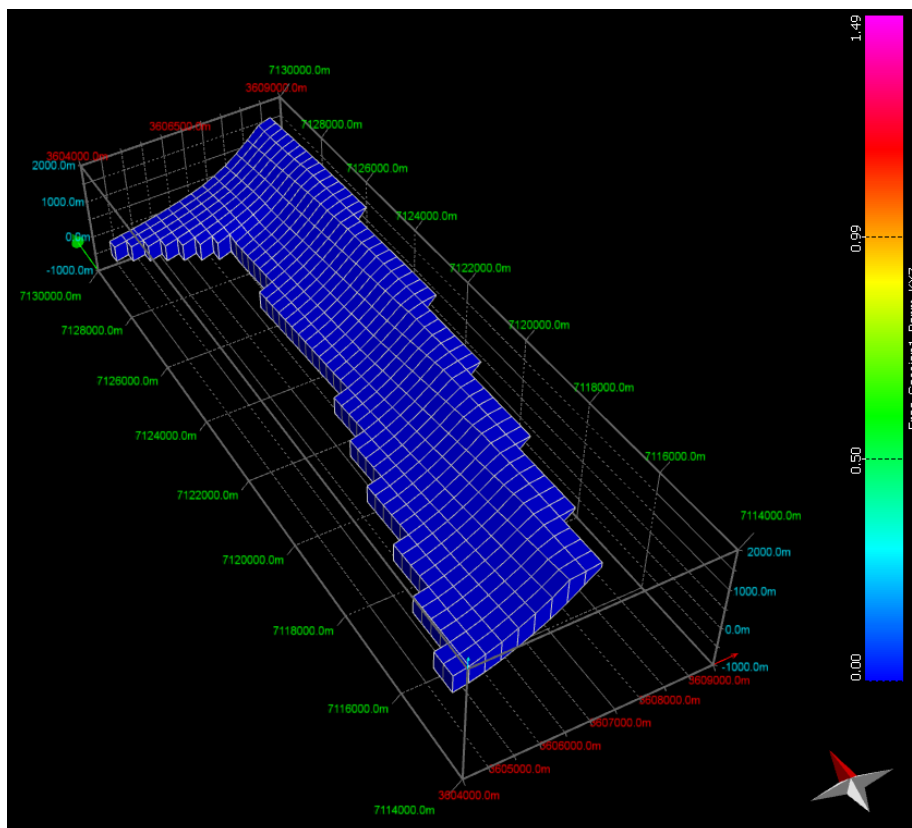
K_{xx}



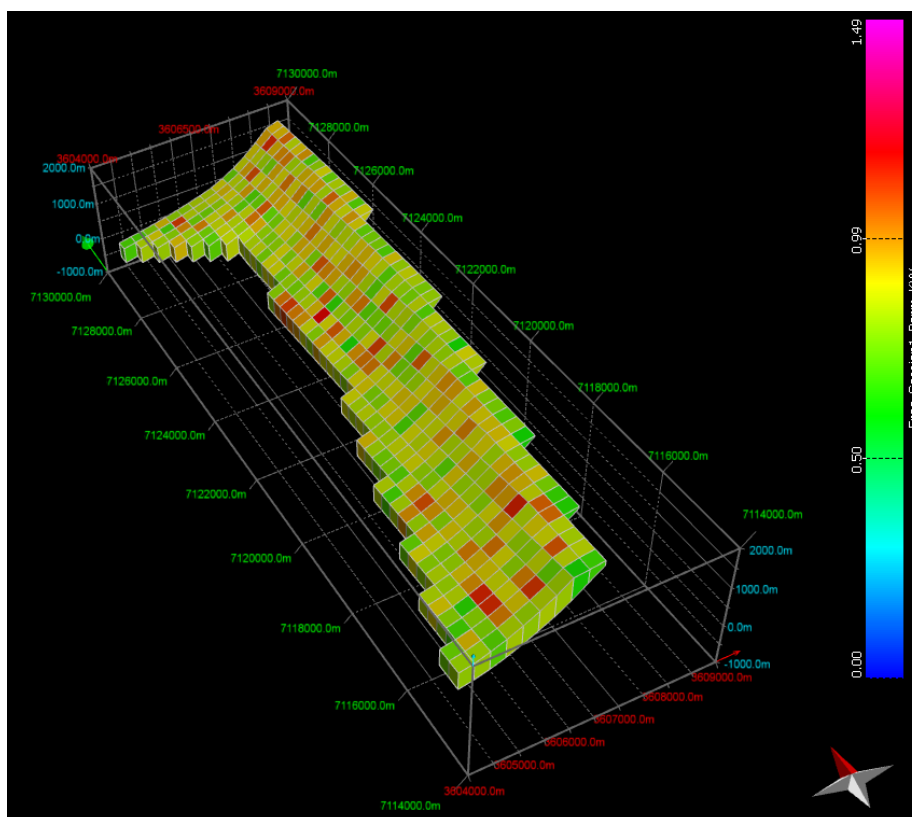
K_{xy}



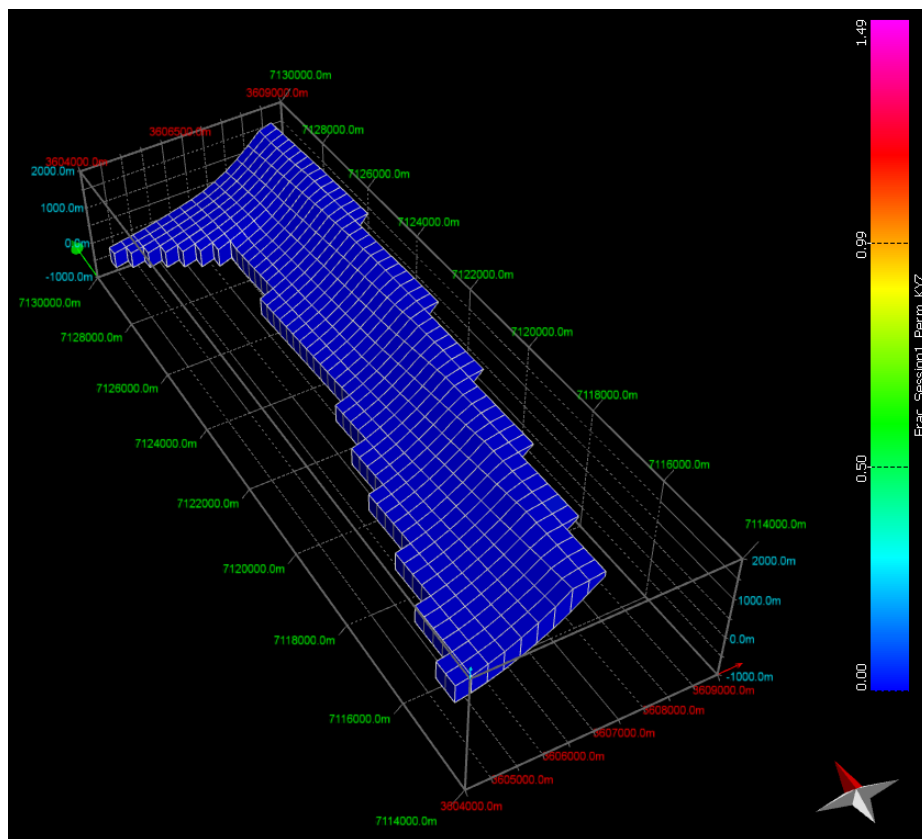
K_{xz}



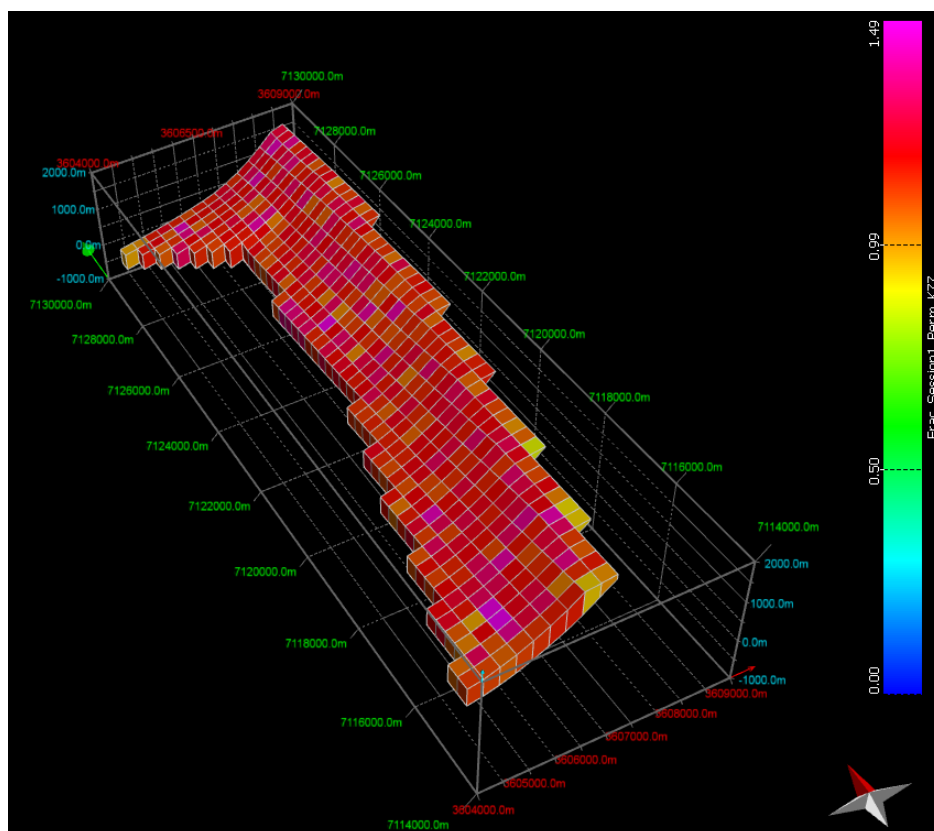
K_{yy}



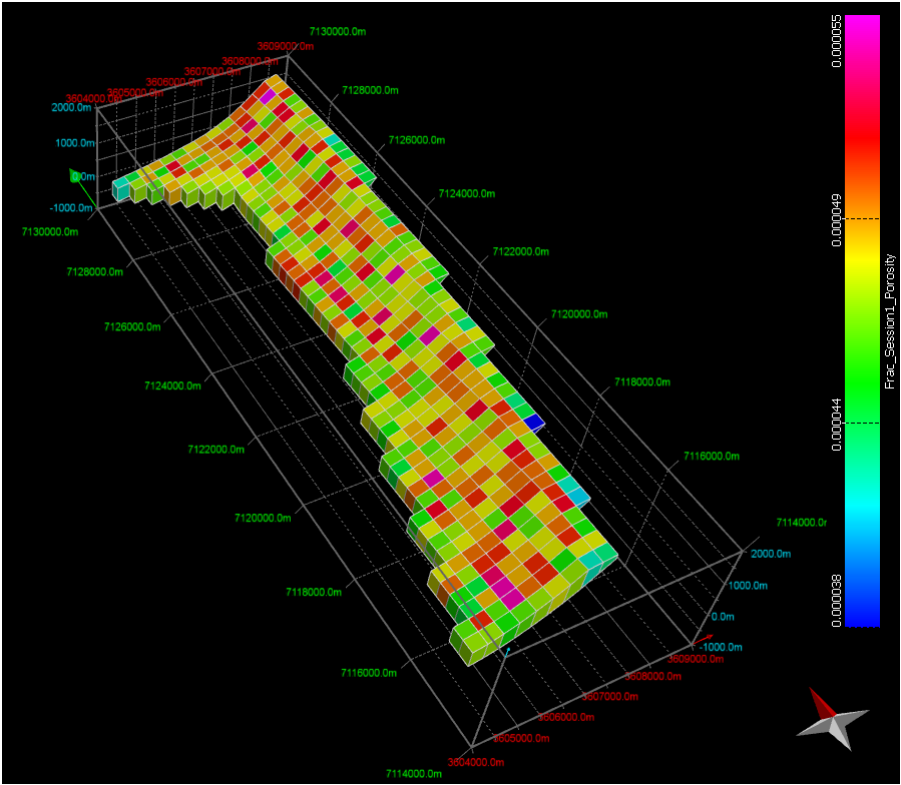
K_{yz}



K_{zz}

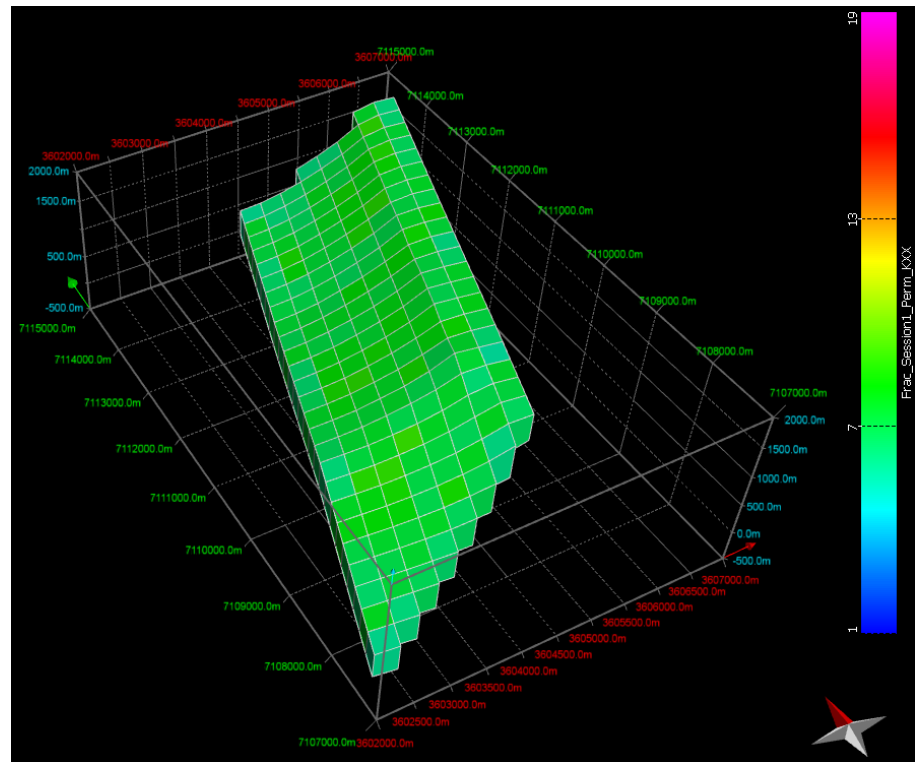


Porosity

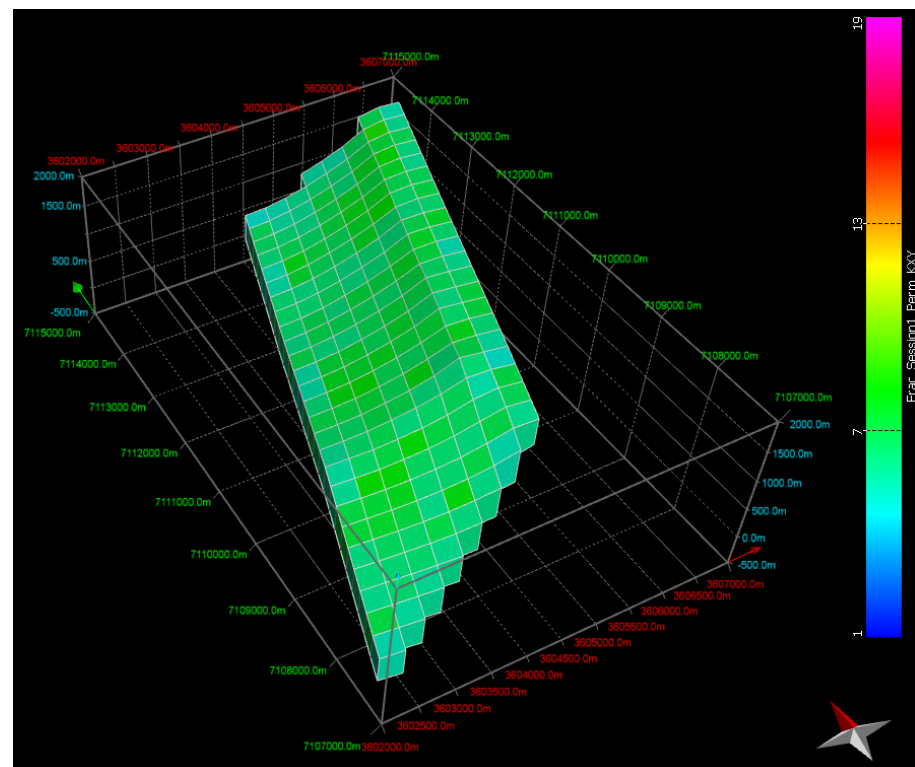


Ceibal volume

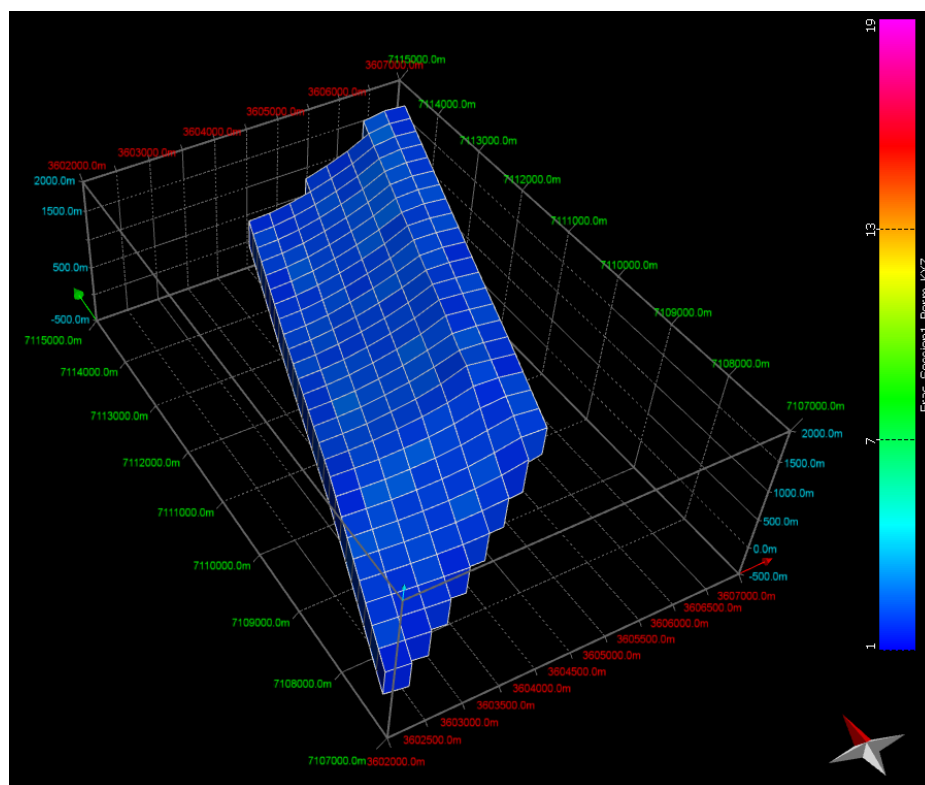
K_{xx}



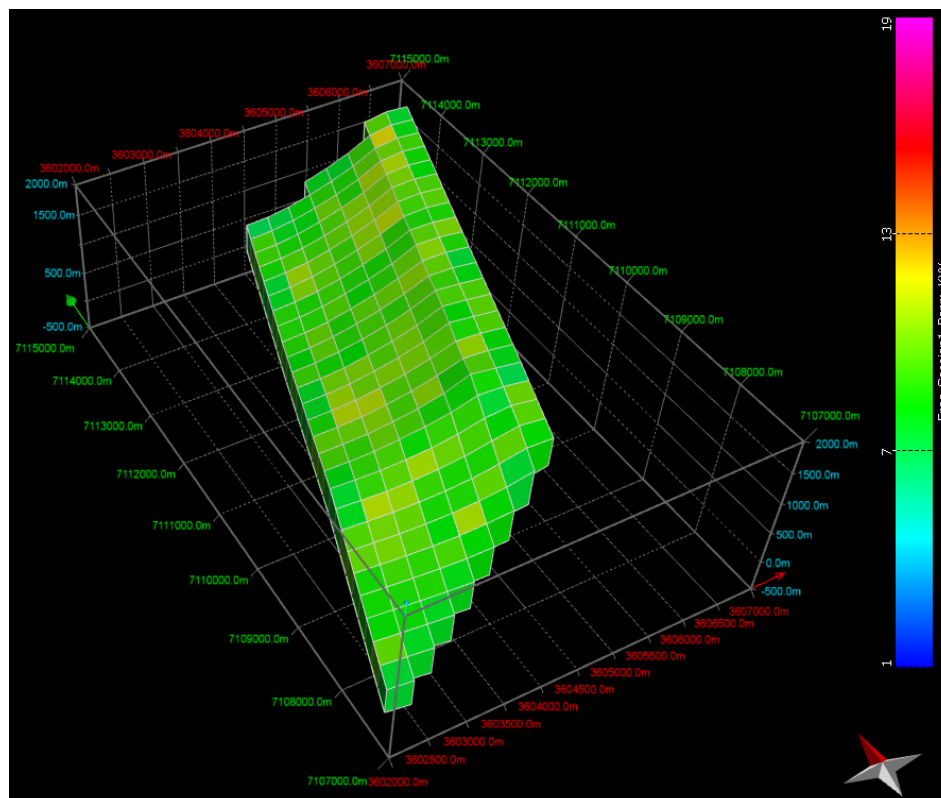
K_{xy}



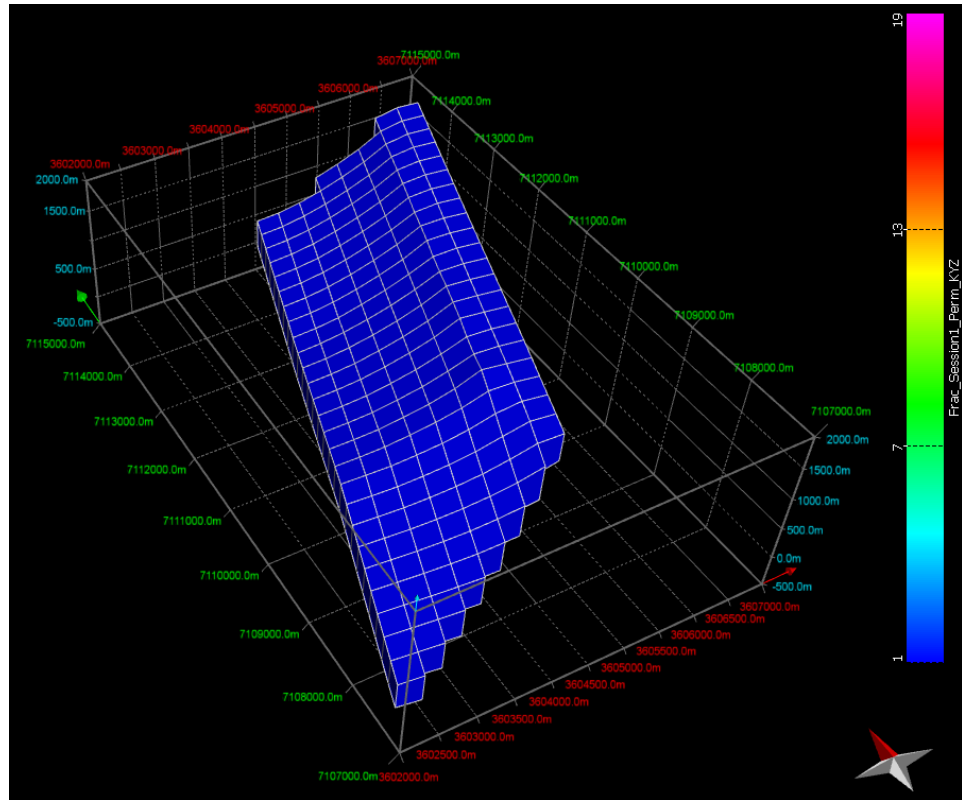
K_{xz}



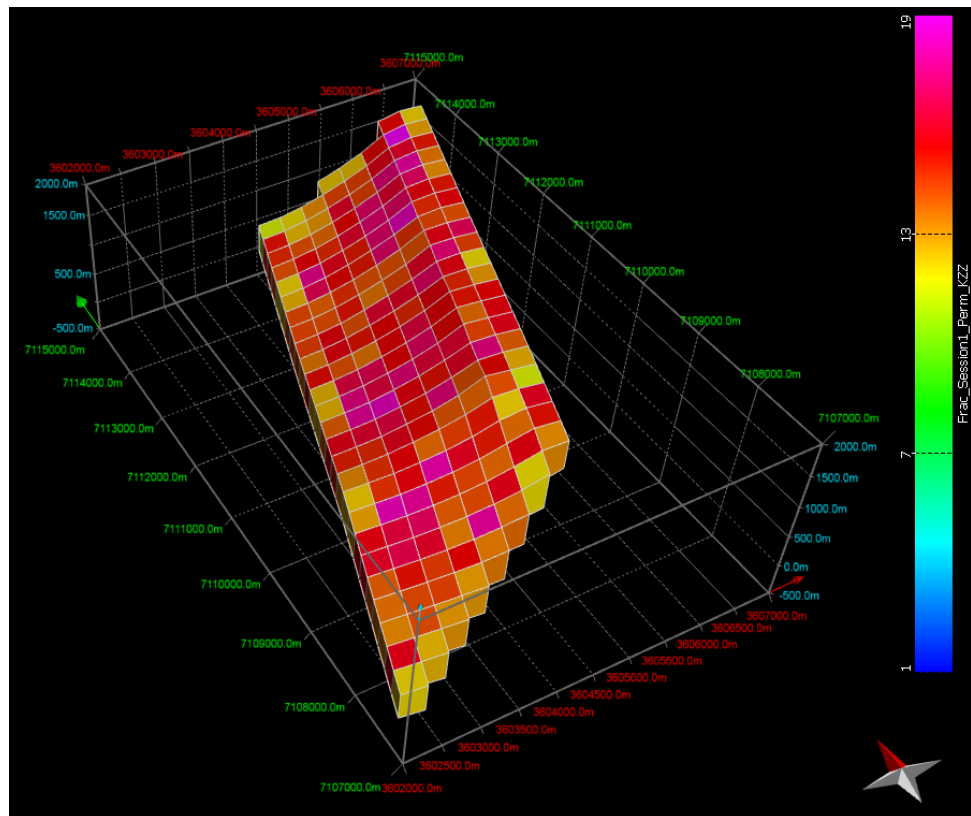
K_{yy}



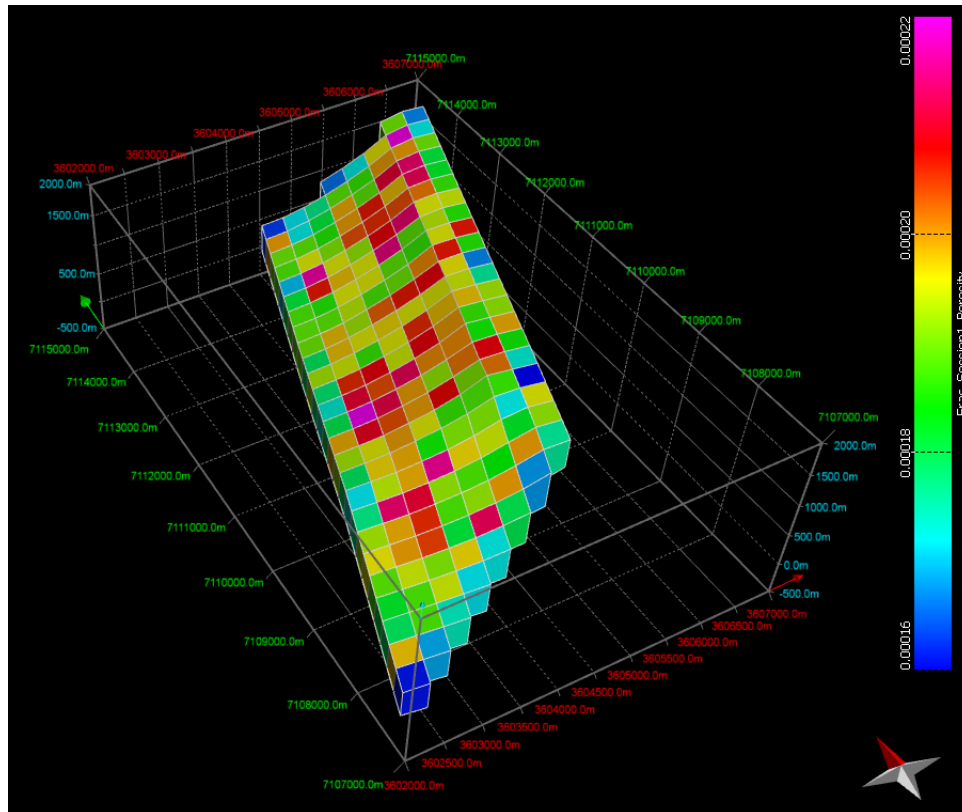
K_{yz}



K_{zz}

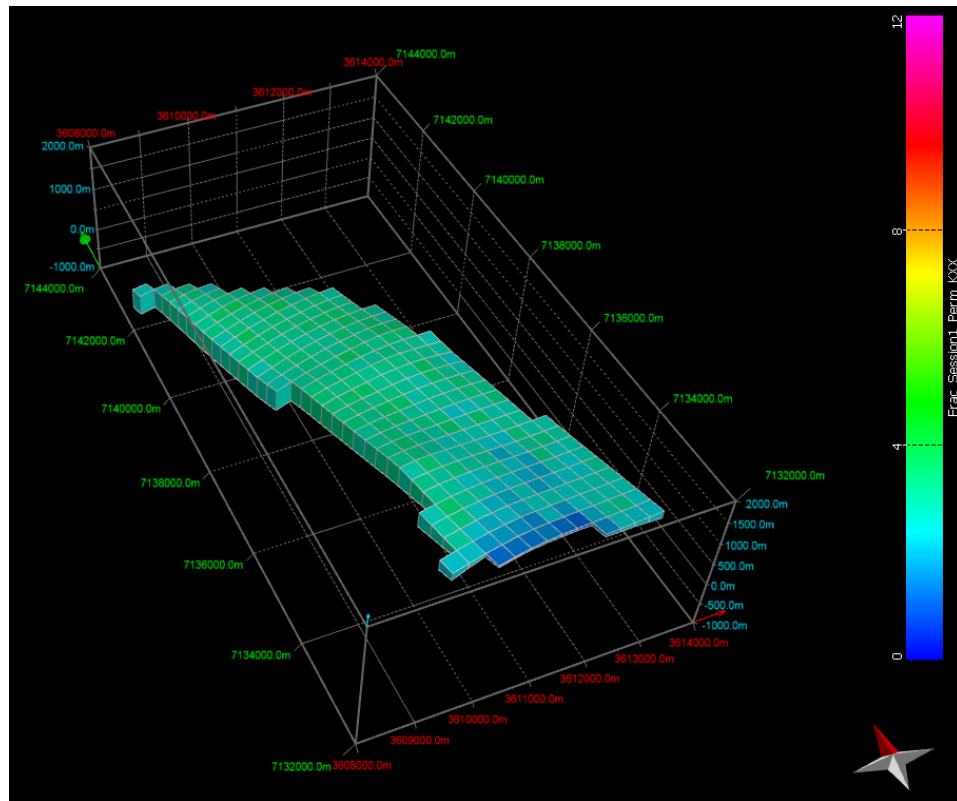


Porosity

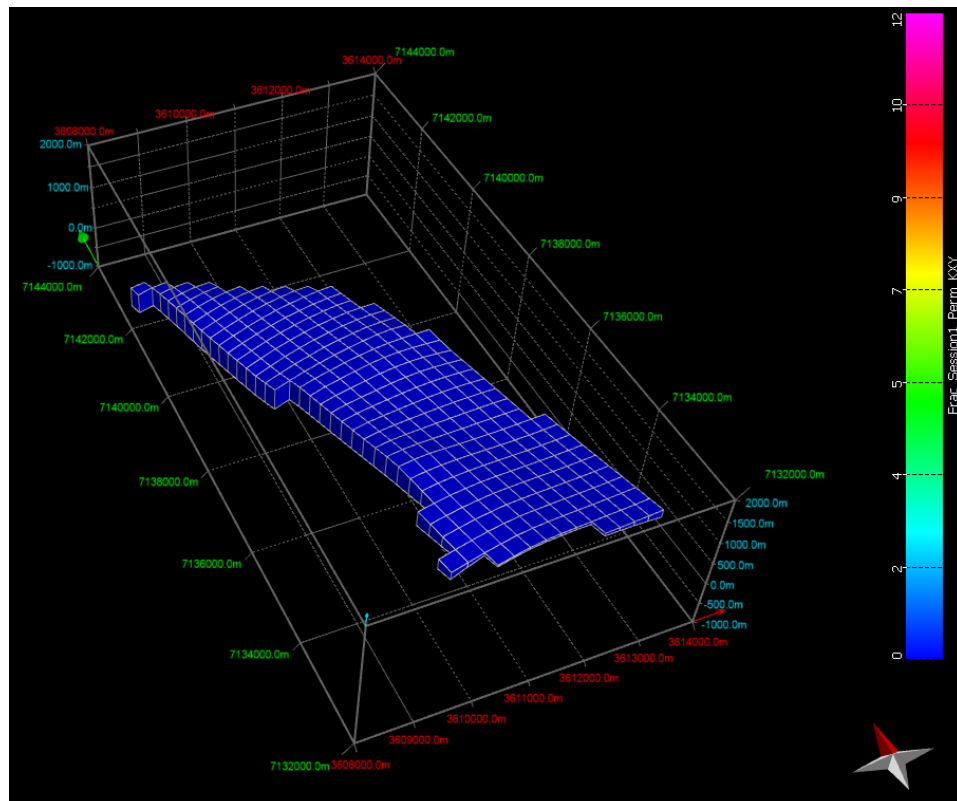


Balboa anticline volume

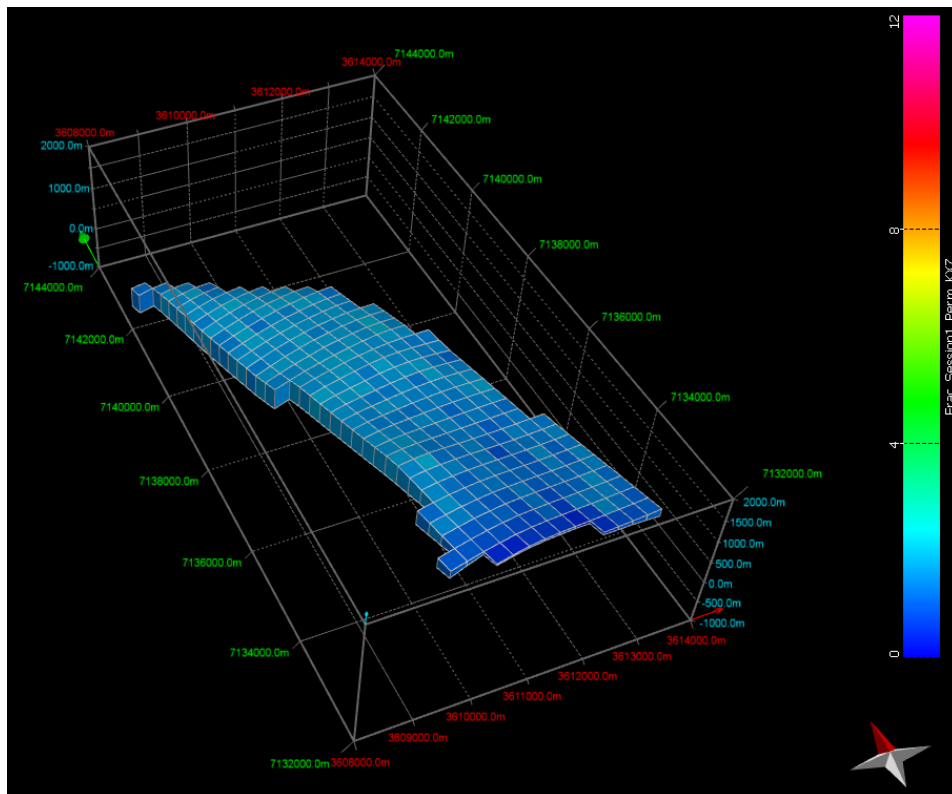
K_{xx}



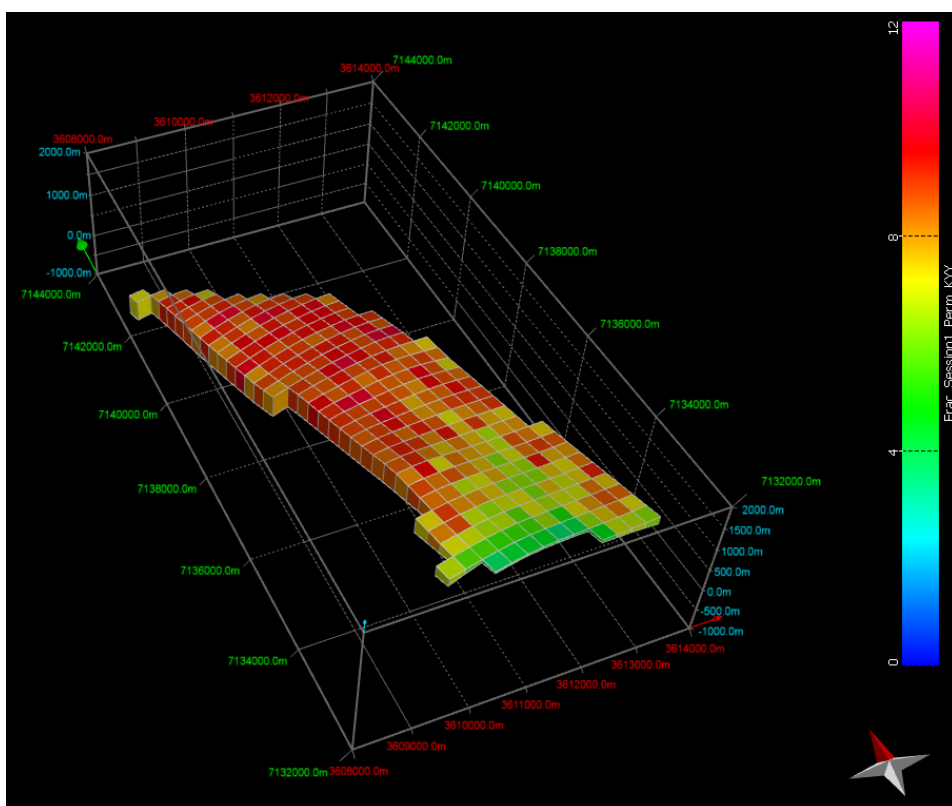
K_{xy}



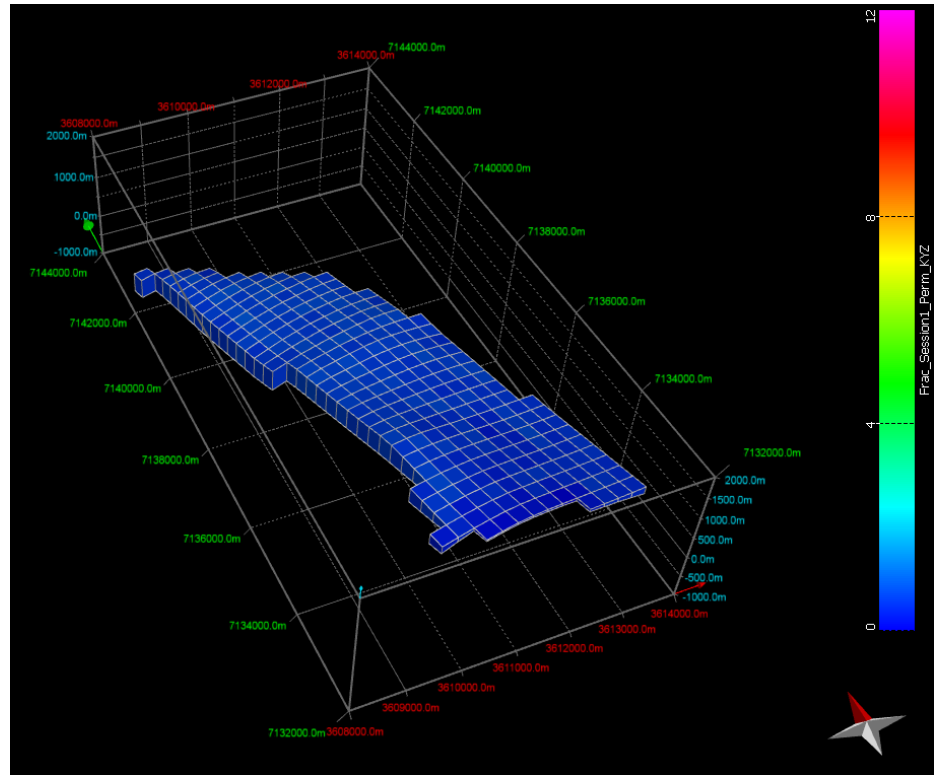
K_{xz}



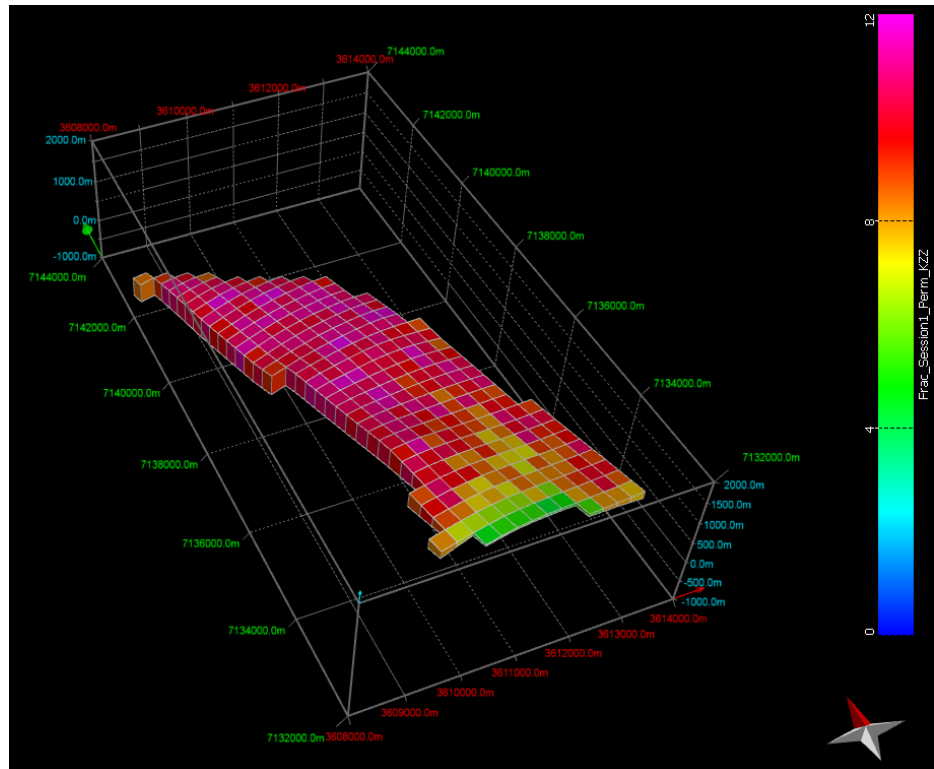
K_{yy}



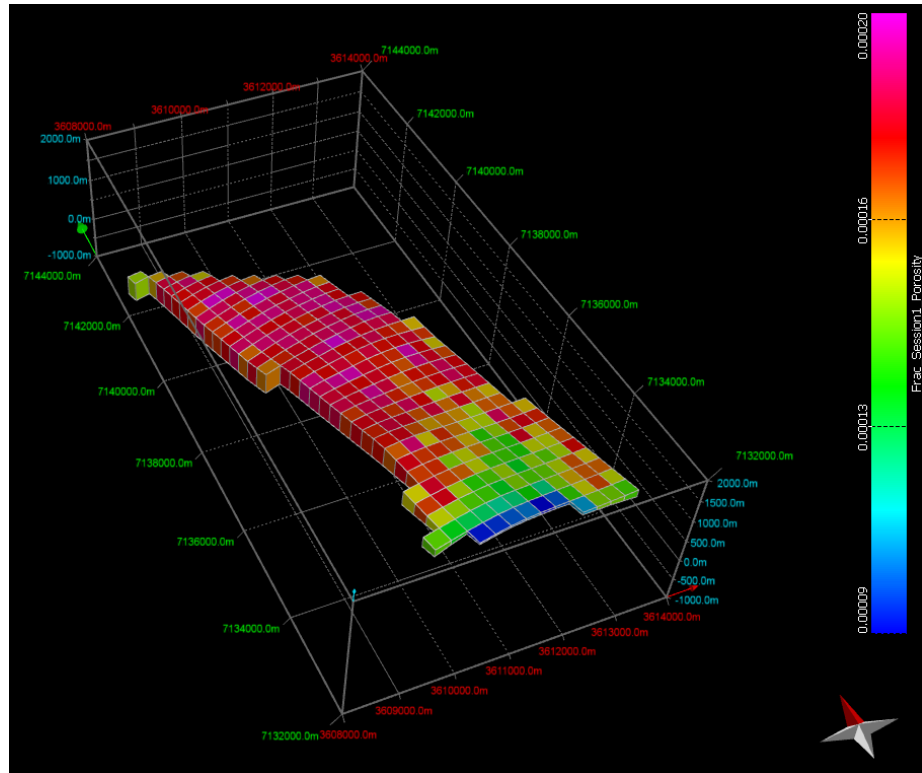
K_{yz}



K_{zz}

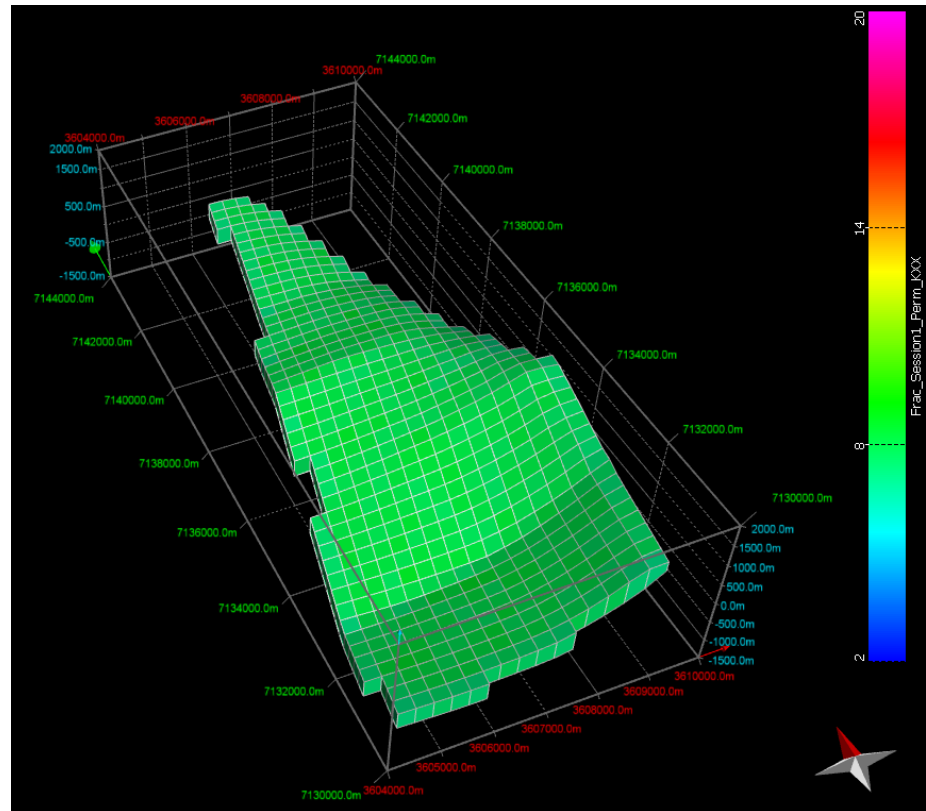


Porosity

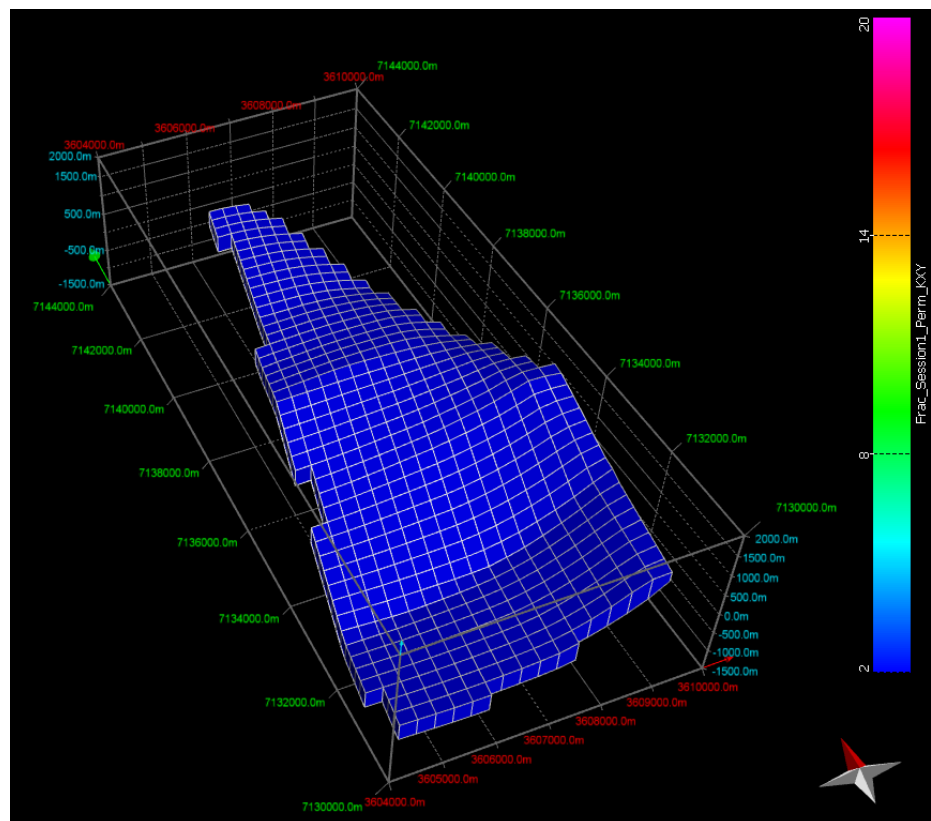


Termas anticline volume

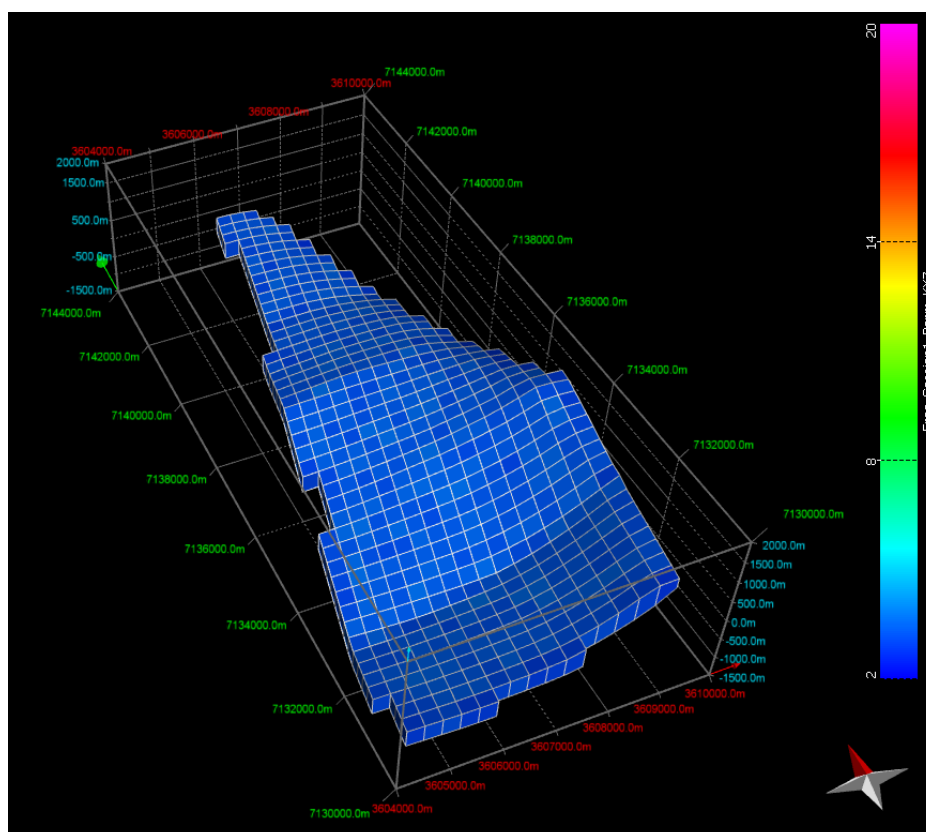
K_{xx}



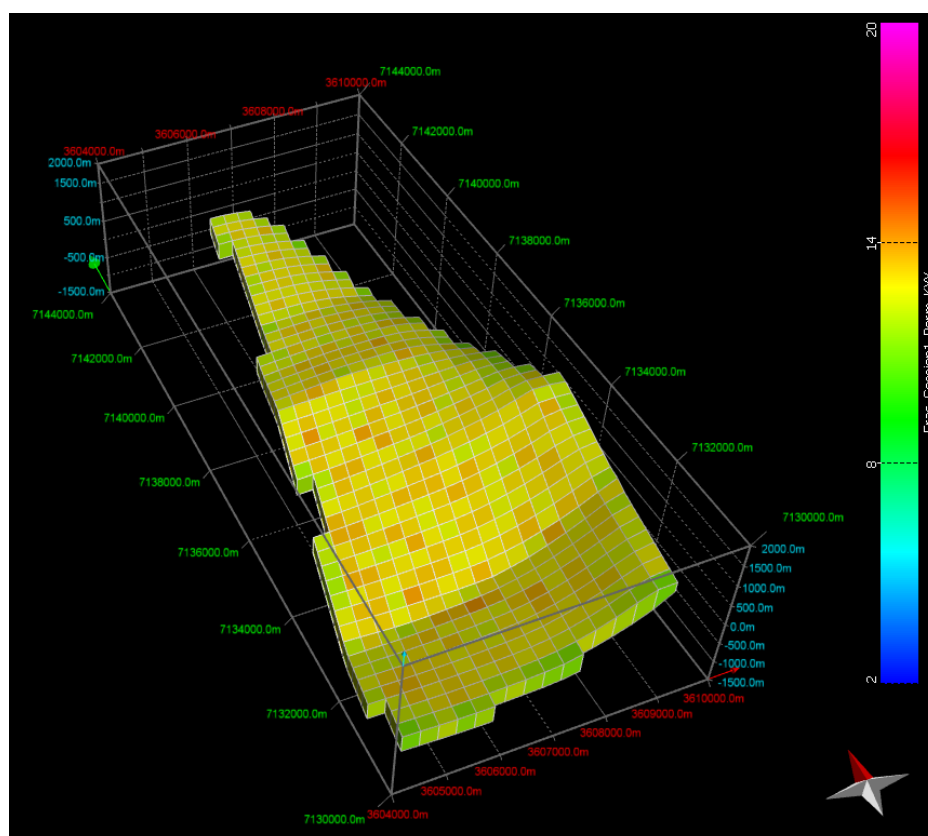
K_{xy}



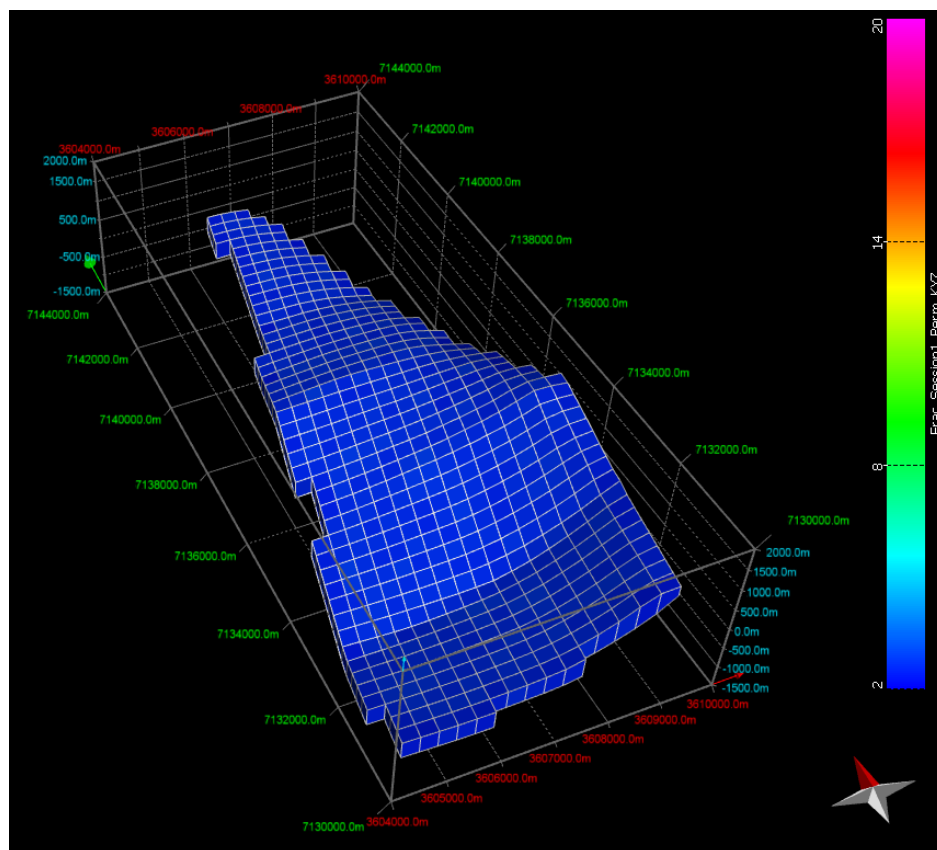
K_{xz}



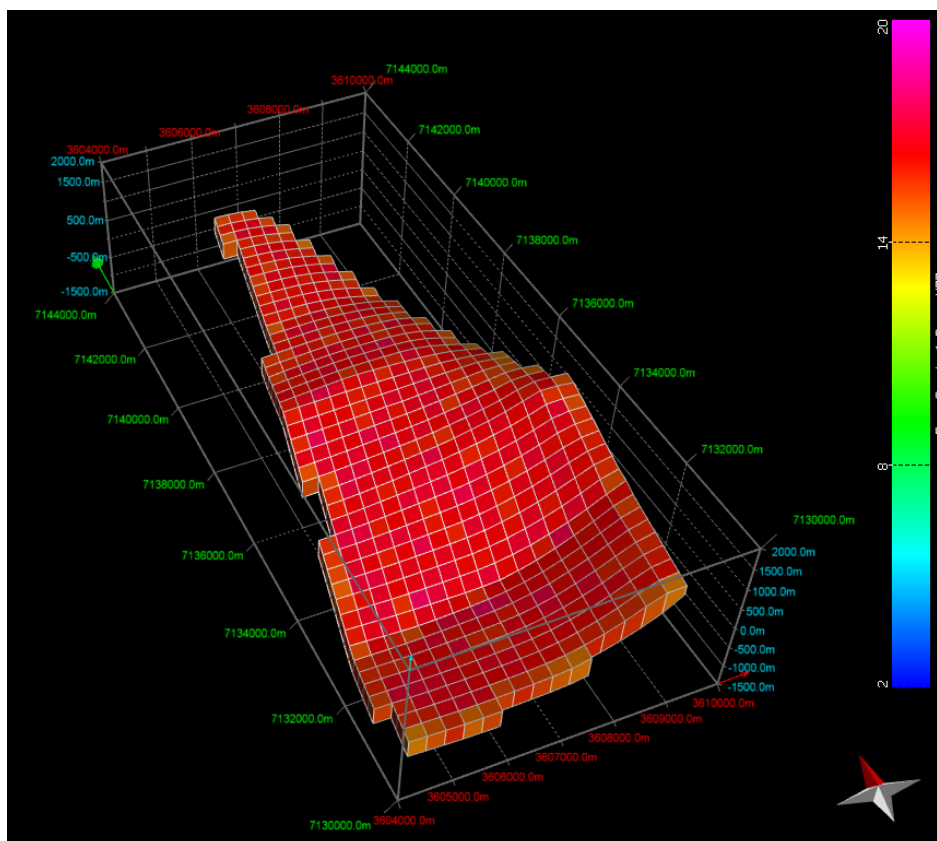
K_{yy}



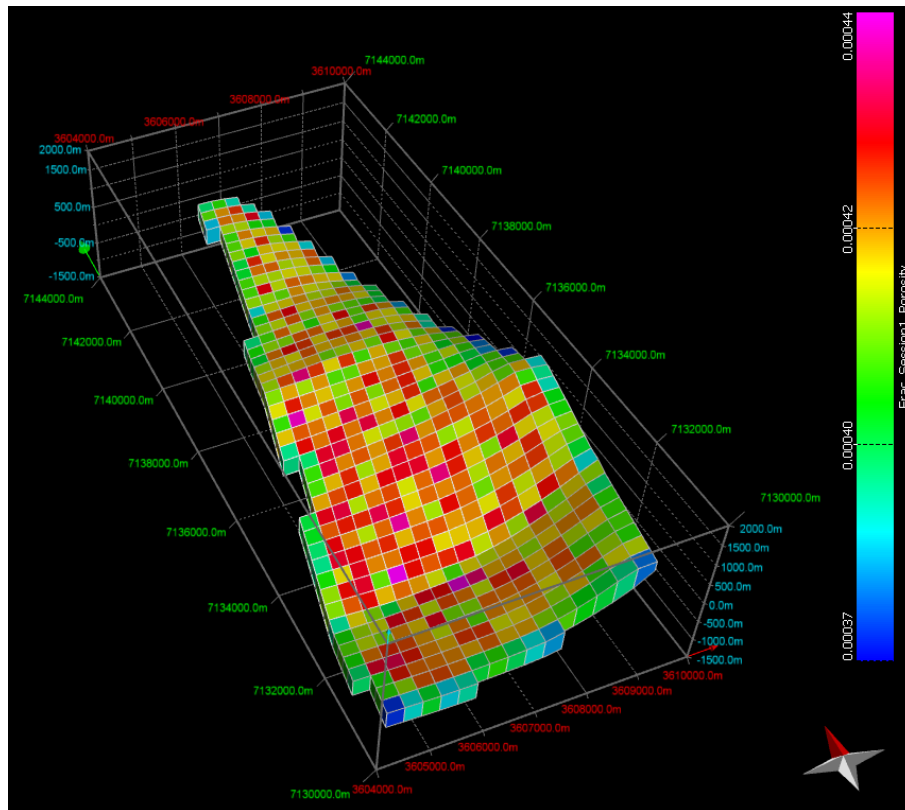
K_{yz}



K_{zz}



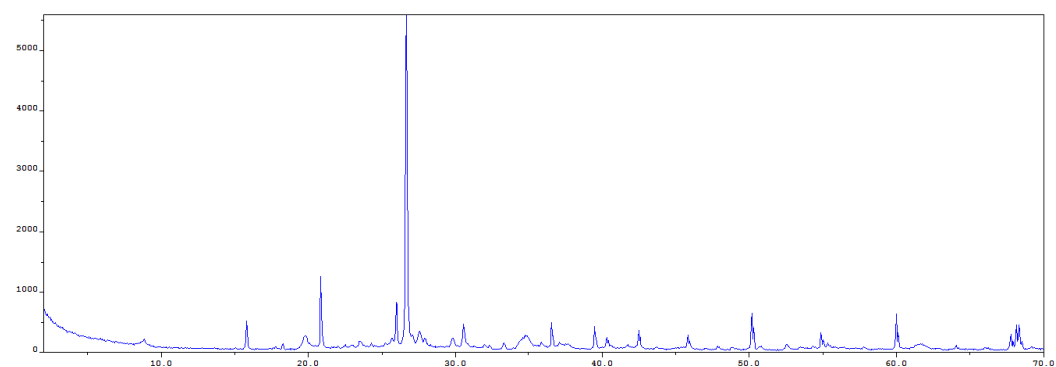
Porosity



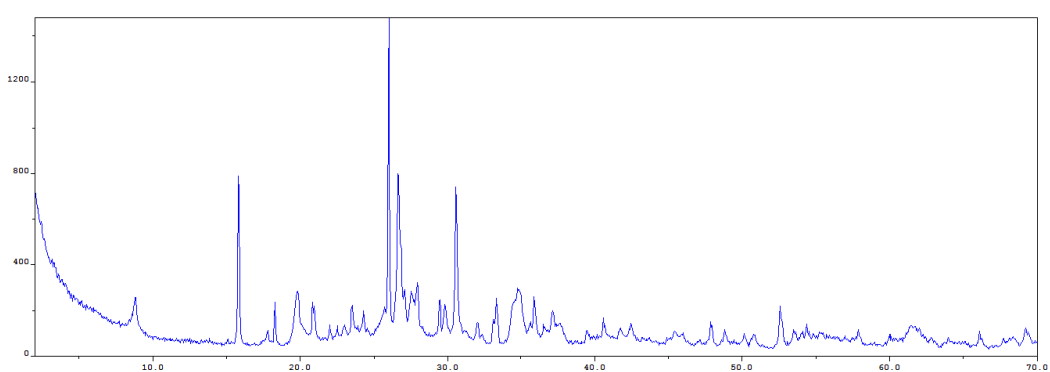
X-RAY DIFFRACTION PATTERN

Whole rock composition

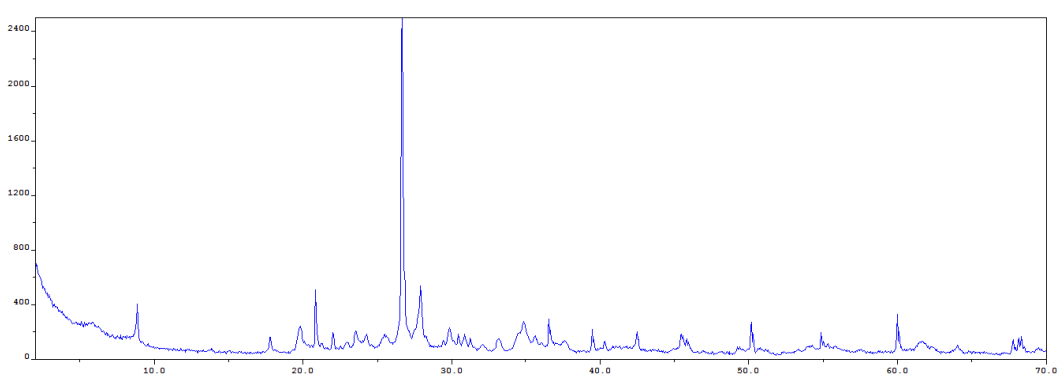
AR1a



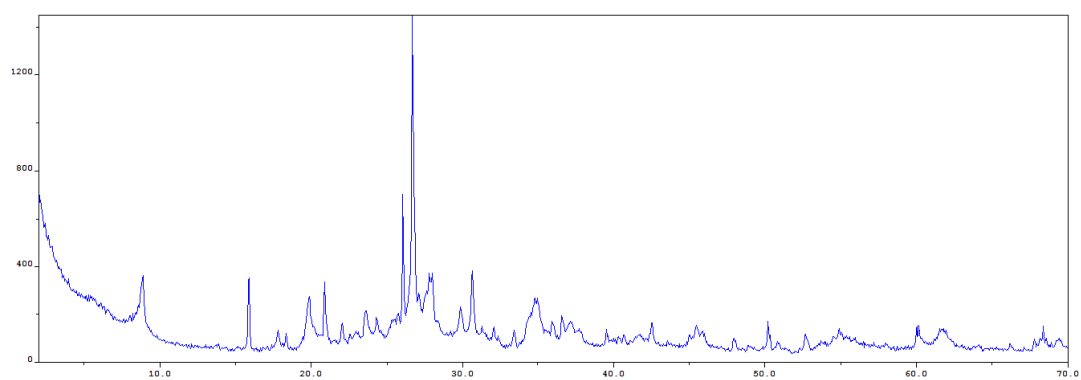
AR1b



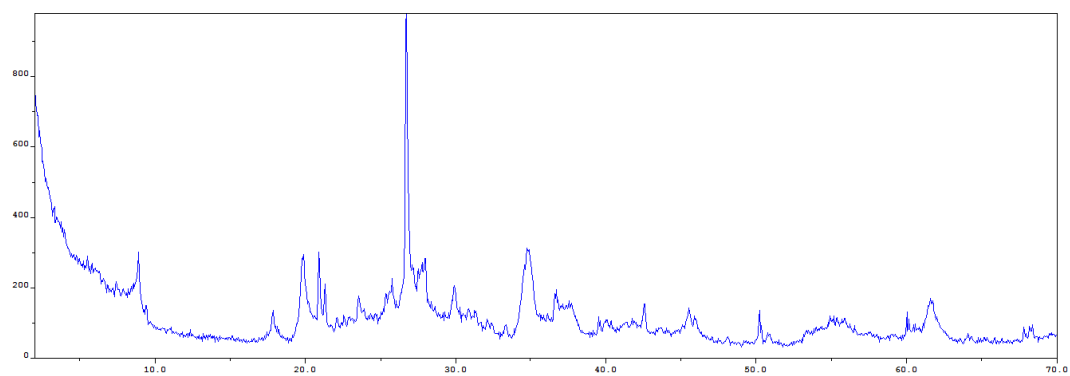
AR5



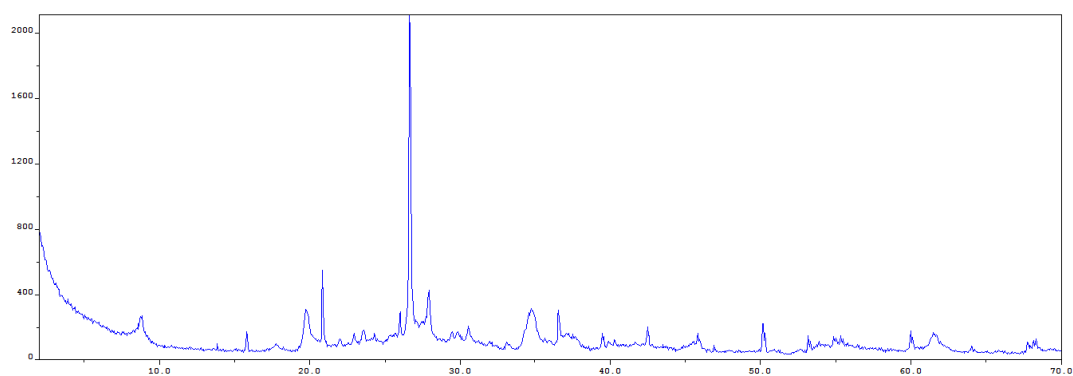
AR7a



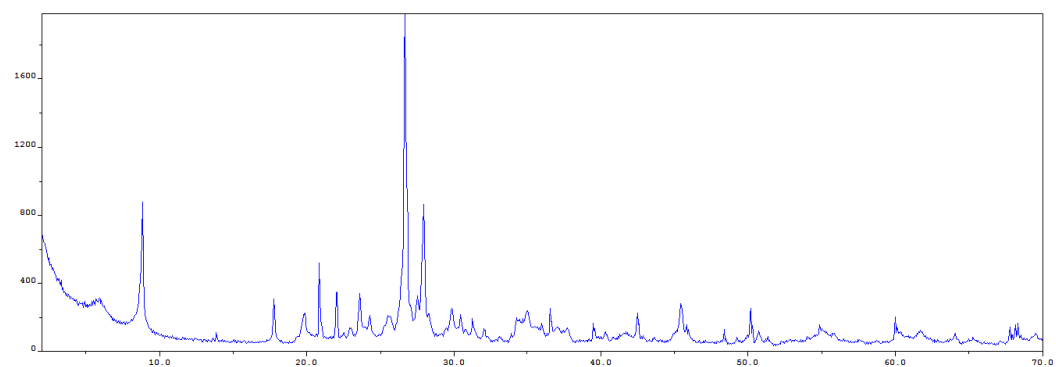
AR7b



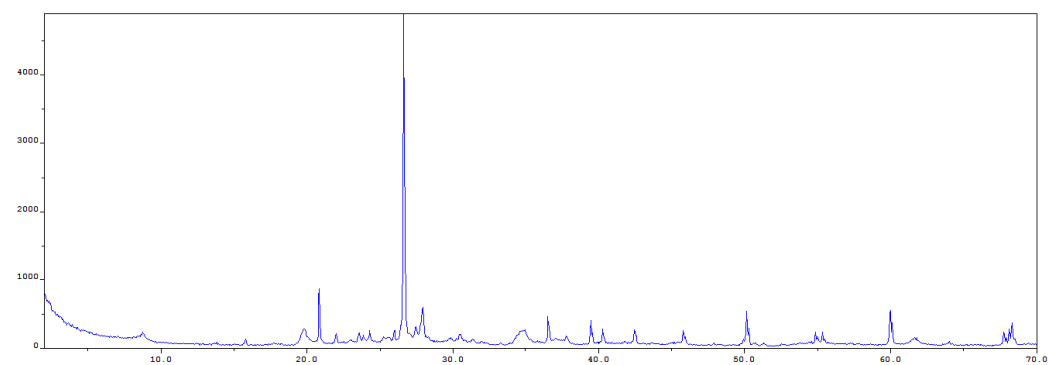
AR10



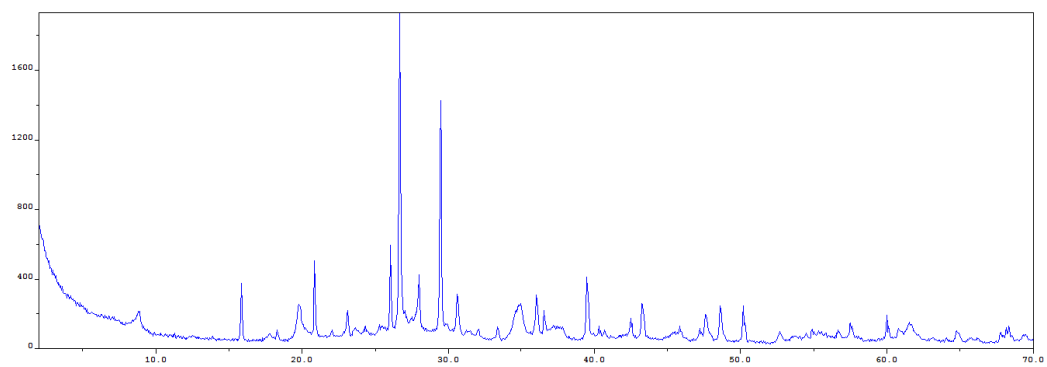
AR11



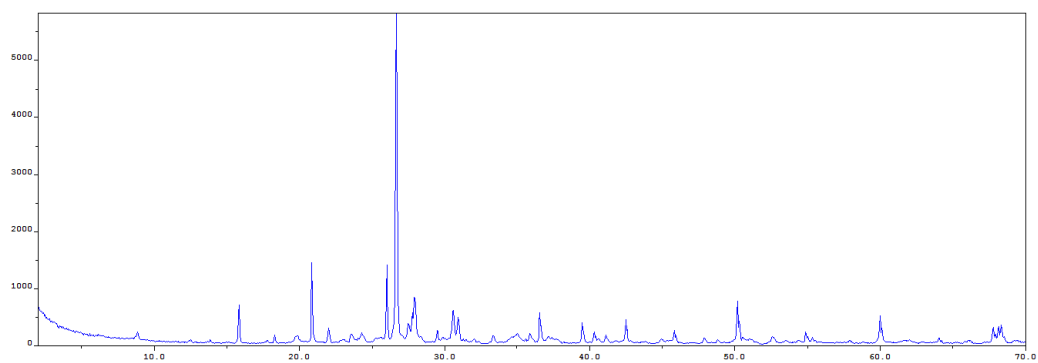
AR12



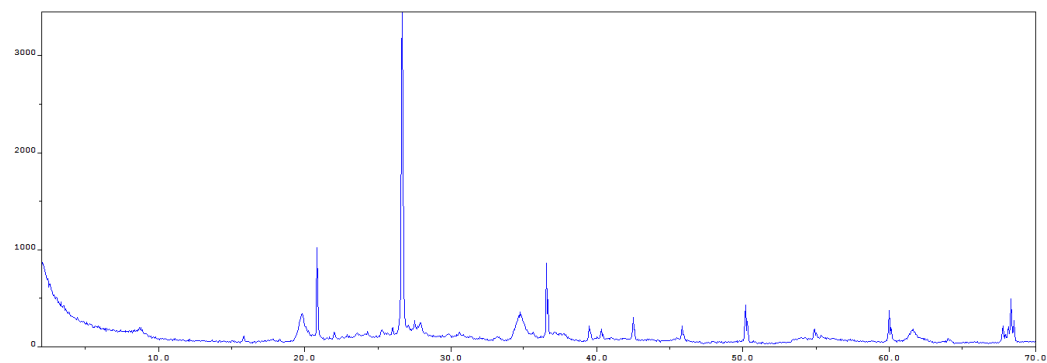
AR14a



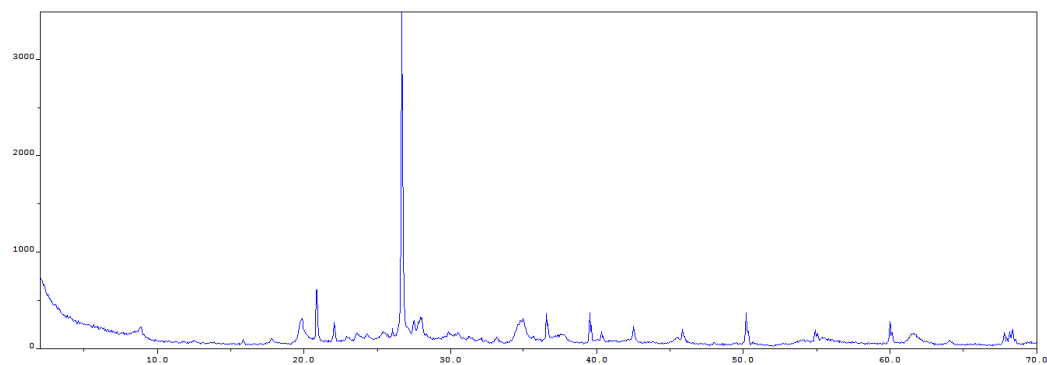
AR14b



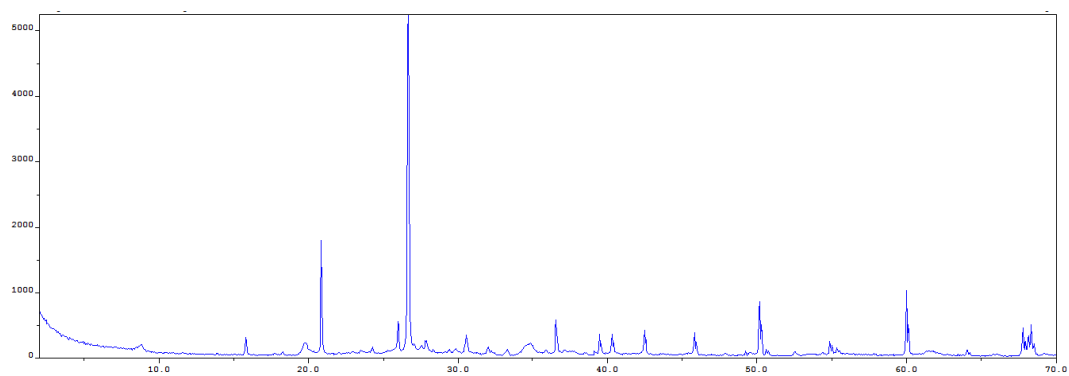
AR15b



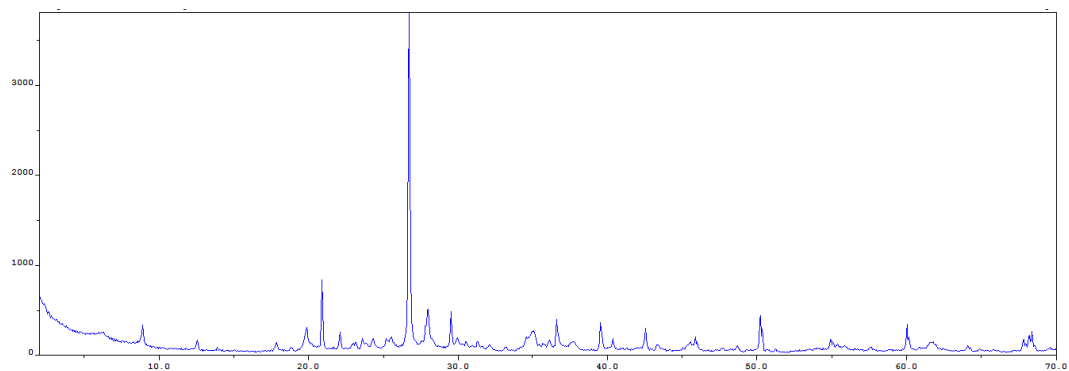
AR16



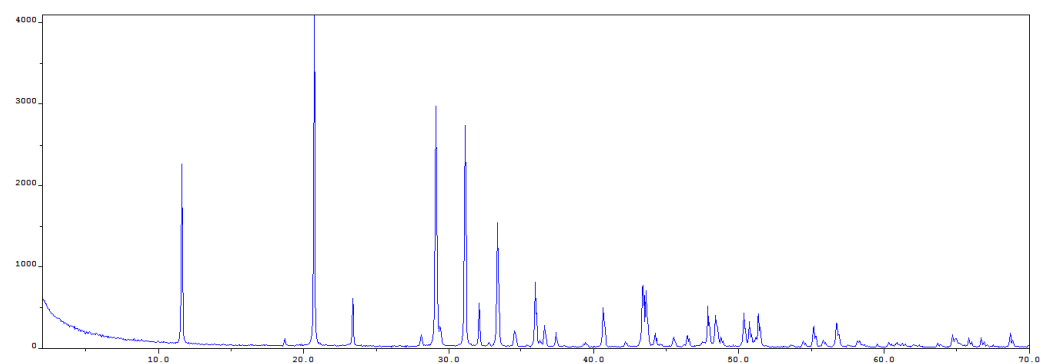
AR17



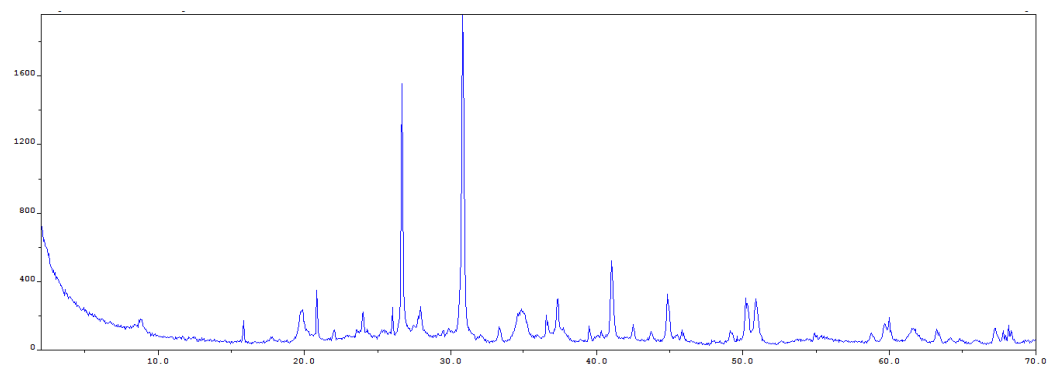
AR18



AR19a

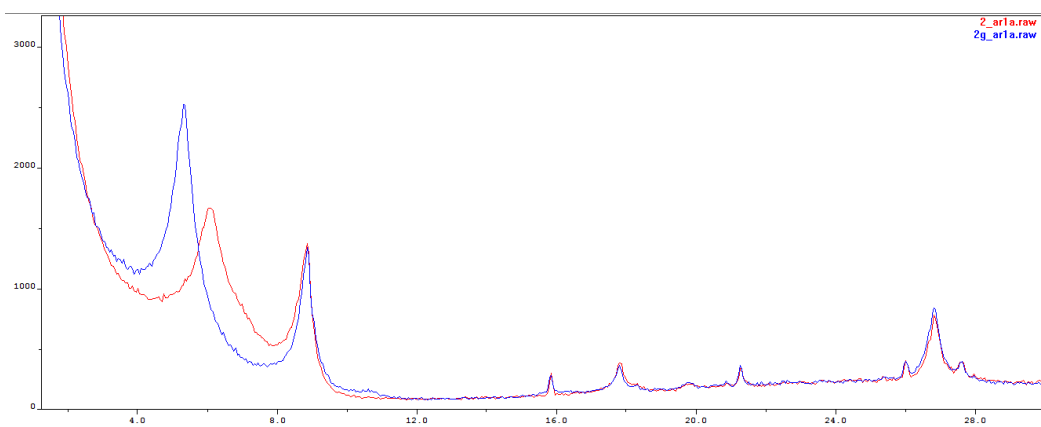


AR19b

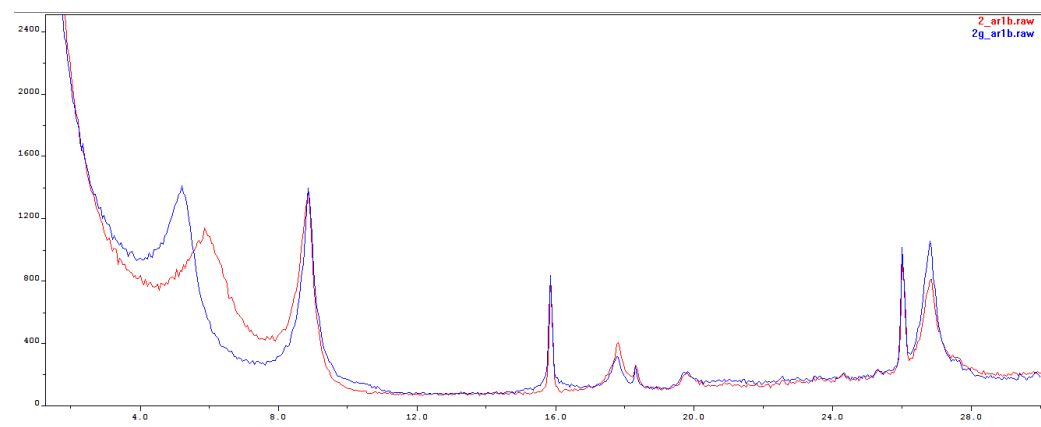


<2 μ m grain-size fraction

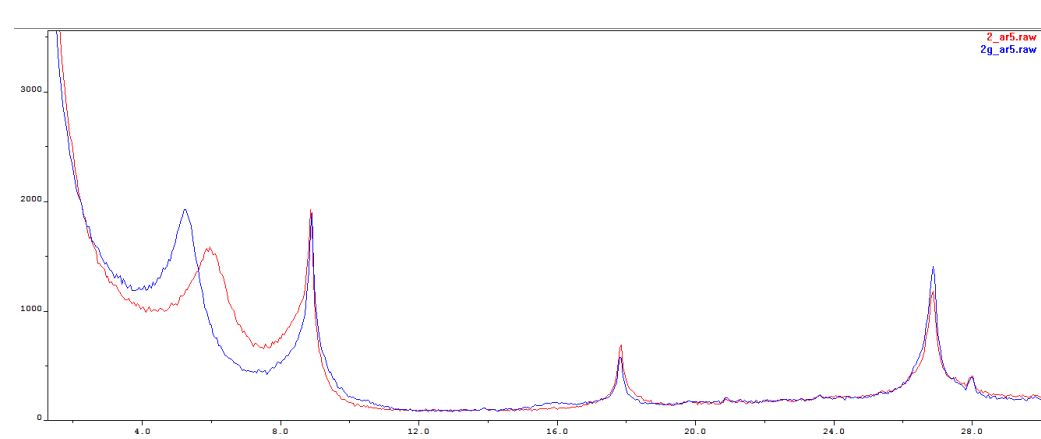
AR1a



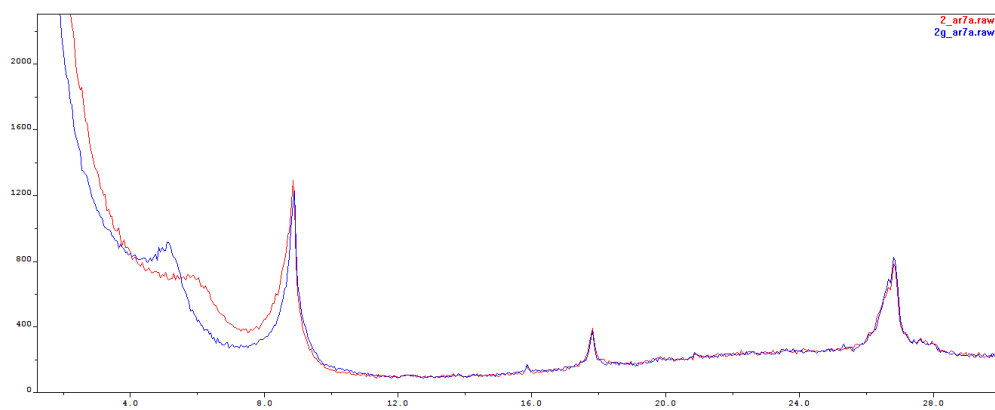
AR1b



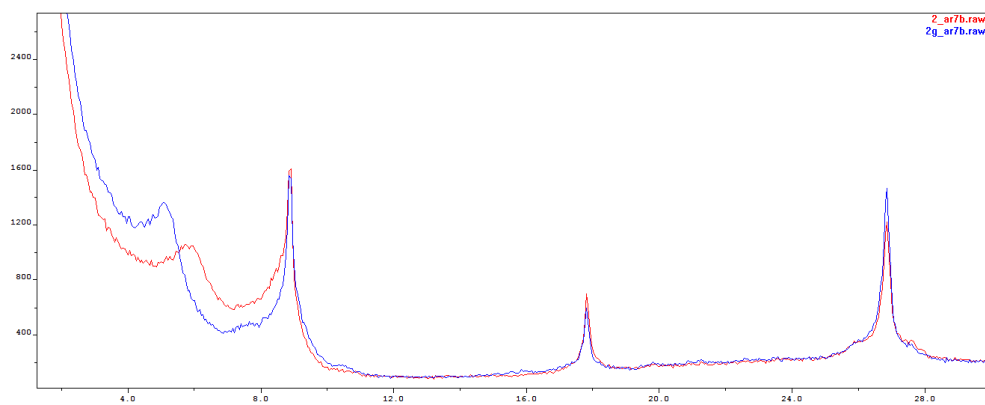
AR5



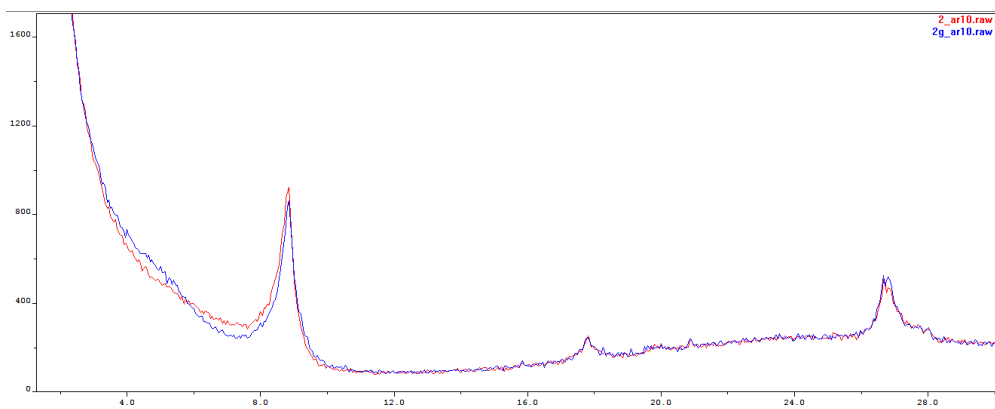
AR7a



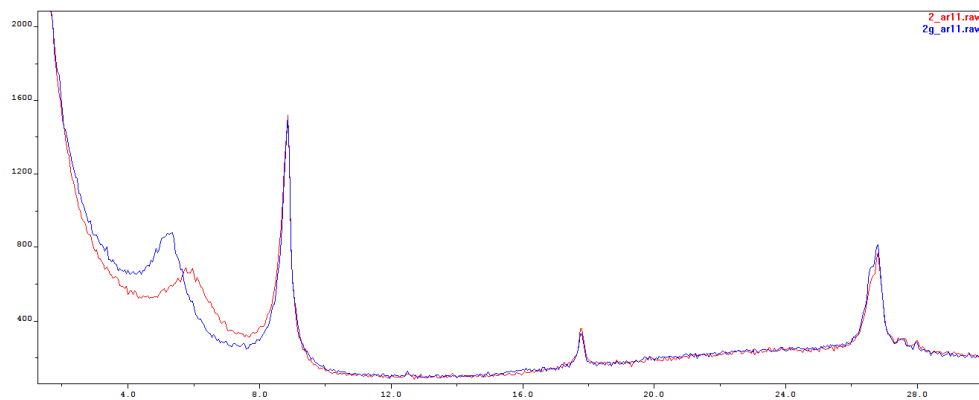
AR7b



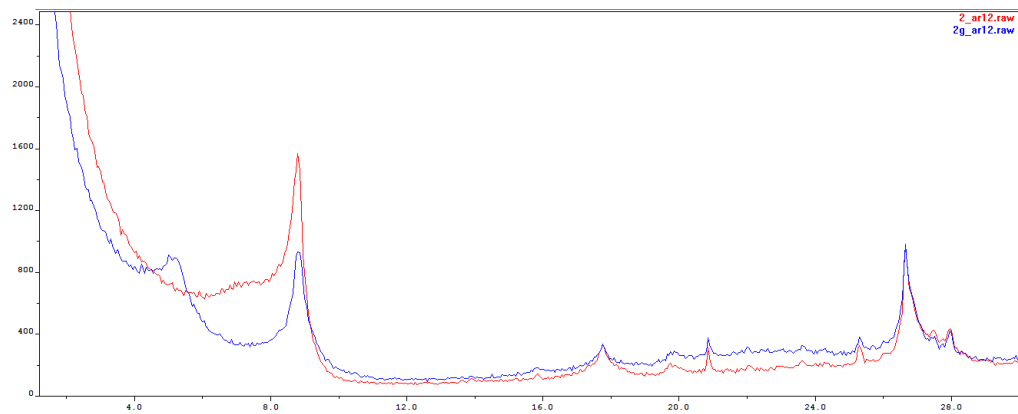
AR10



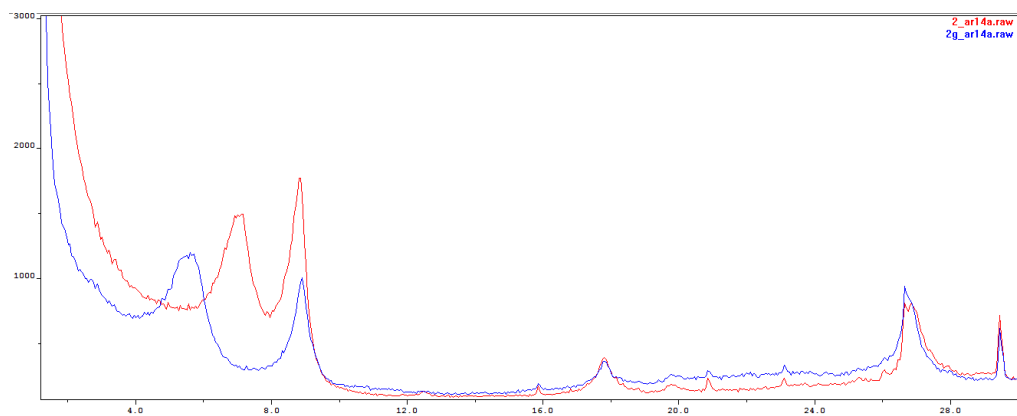
AR11



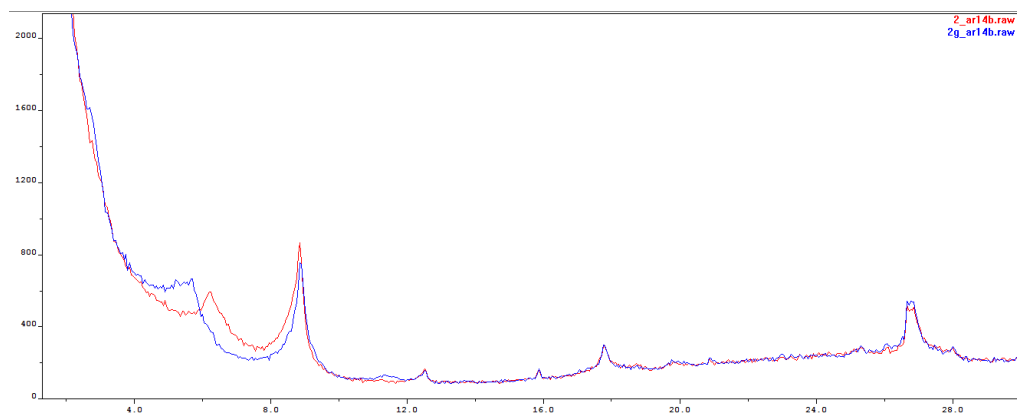
AR12



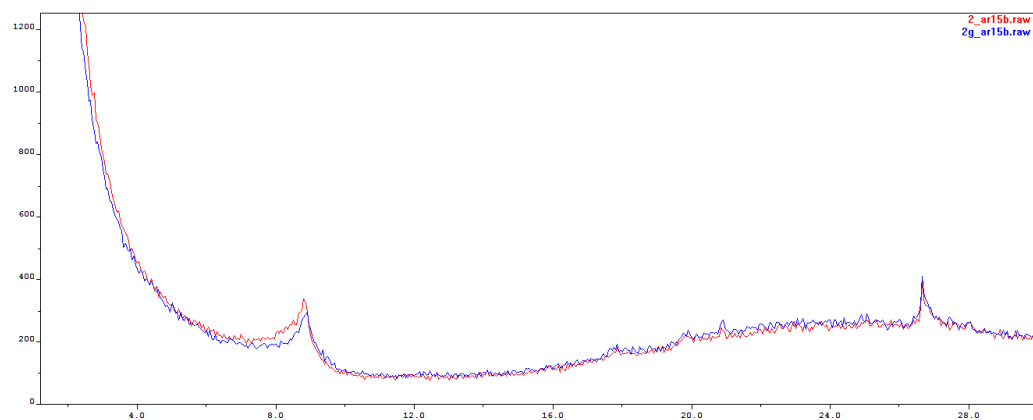
AR14a



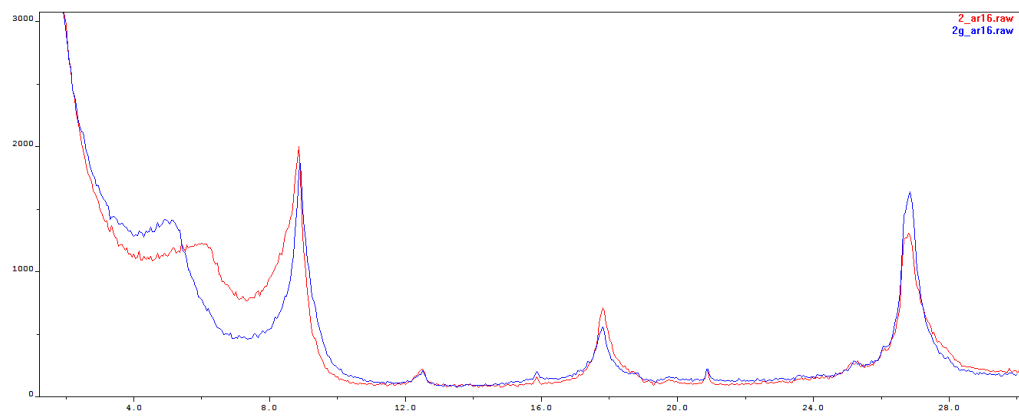
AR14b



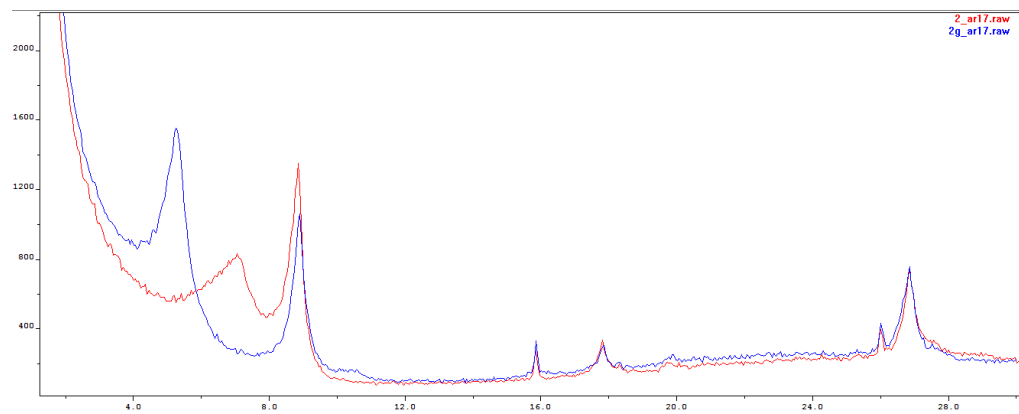
AR15b



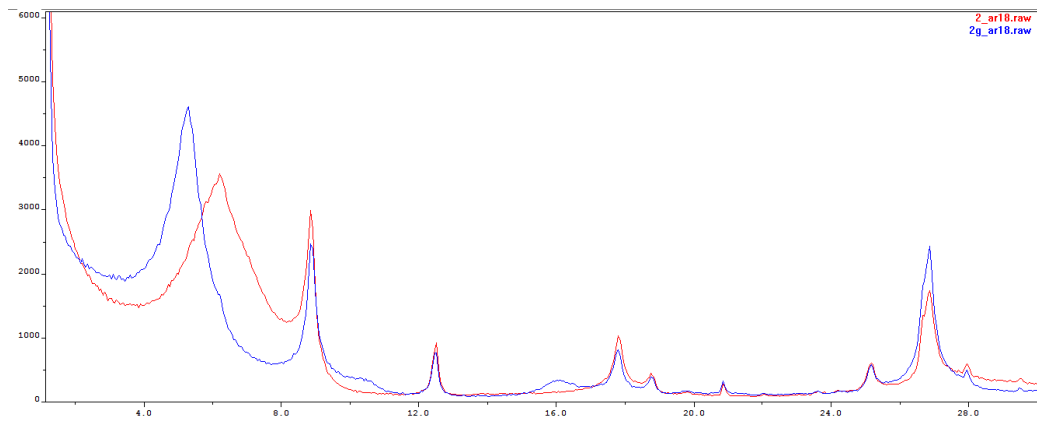
AR16



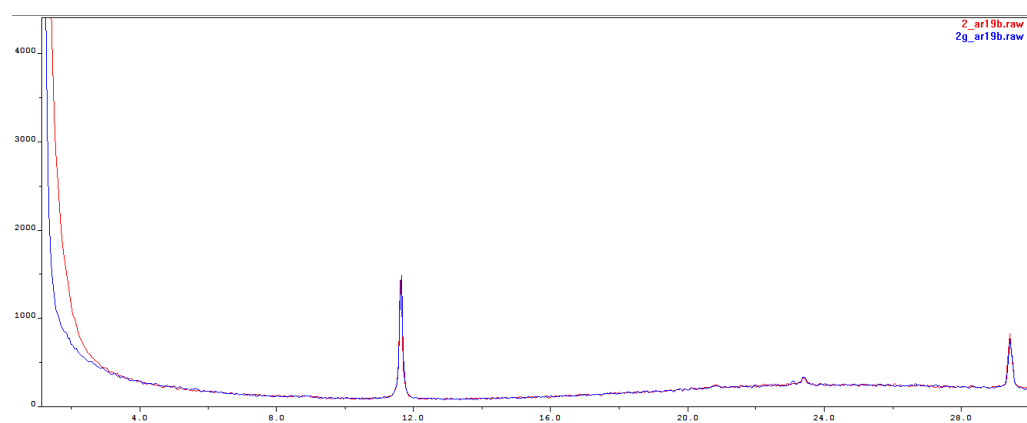
AR17



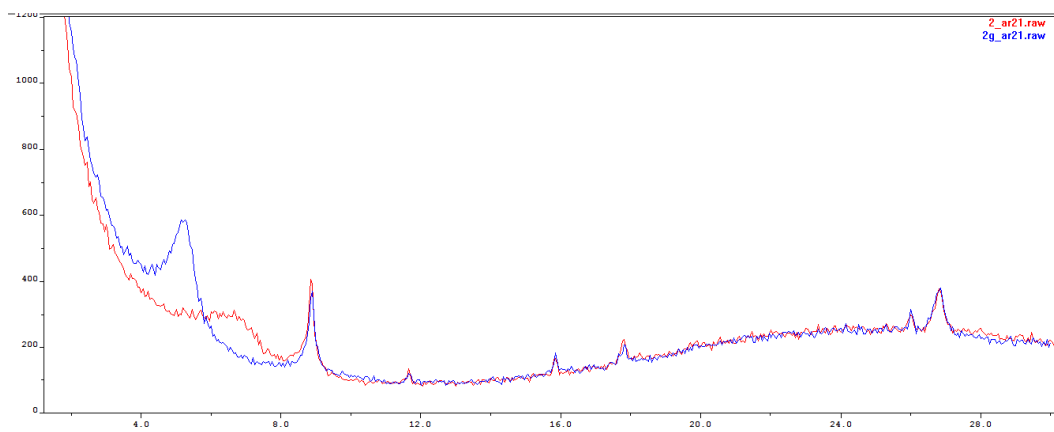
AR18



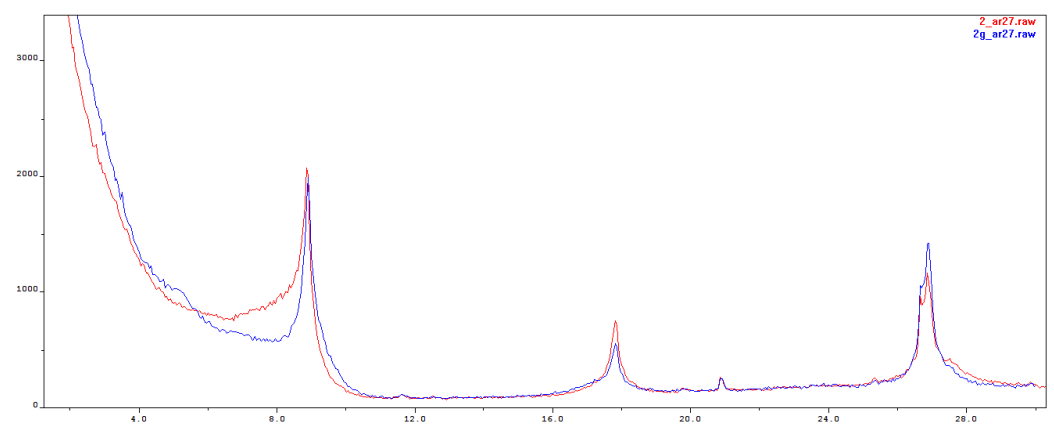
AR19b



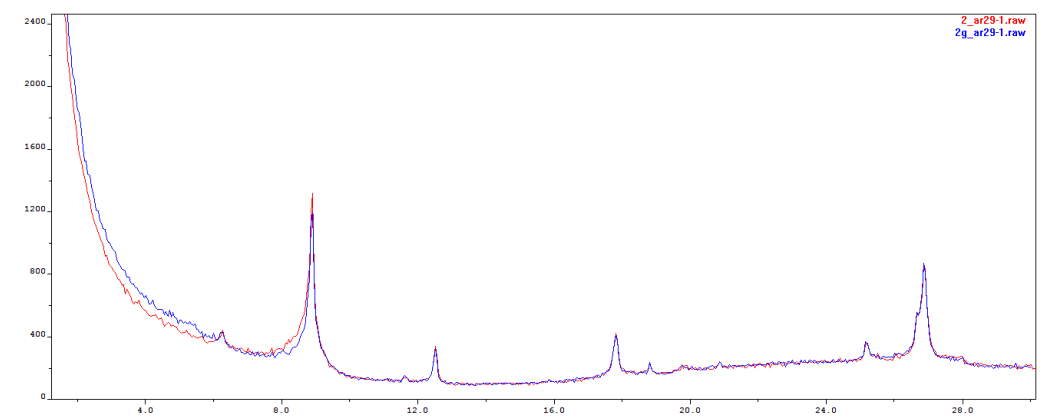
AR21



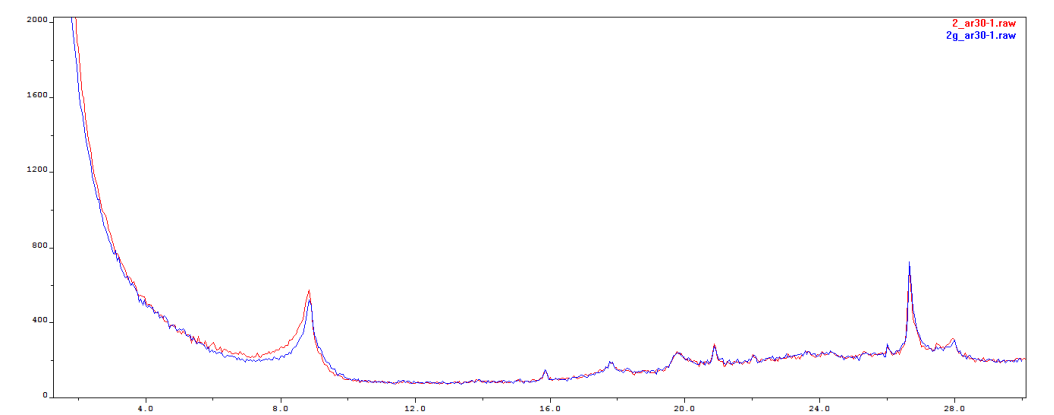
AR27



AR29



AR30.1



AR30.2

